ON THE QUANTIFICATION OF ARTERIAL WALL MECHANICAL PROPERTIES USING INVASIVE AND NON-INVASIVE EXPERIMENTAL INVESTIGATIONS AND ANALYTICAL TECHNIQUES

A thesis submitted for the degree of doctor of philosophy

By

Alessandro Giudici

Biomedical Engineering Research Theme

Department of Mechanical and Aerospace Engineering

Brunel University London

March 2021

Contents

Acknowledgements **V**

Abstract **VII**

List of figures **XI**

List of tables **XIV**

Notations and abbreviations **XV**

1 Introduction **1**

1.1 Background 2

1.2 The arterial wall 5

1.2.1 Macro and micro-structure 5

1.2.2 Arterial wall mechanics 9

1.2.3 Relation between structure and function in arteries 12

1.3 The evaluation of arterial stiffness *in vivo* 16

1.3.1 Pulse Wave Velocity 16

1.3.2 Exponential relationship between pressure and diameter/area 19

1.4 Project aims and objectives 20

1.4.1 Thesis outline 20

2 Theoretical background **23**

2.1 Introduction 24

2.2 *Ex vivo* evaluation of arterial mechanics 24

2.2.1 Kinematics 24

2.2.2 Definitions of stress 25

2.2.3 Definitions of stiffness 27

2.2.4 Mathematical description of the wall behaviour: strain-energy functions . 28

2.3 Characterisation of arterial mechanics *in vivo* 29
2.3.1 PU-loop method and wave intensity analysis 29
2.3.2 $\ln DU$-loop method and the non-invasive wave intensity 32
2.3.3 D^2P-loop 33
2.3.4 The relationship between γ and c 34

3 The mechanical behaviour of the pig and lamb tri-layered aortic wall *ex vivo* 37
3.1 Introduction 38
3.2 Methods 40
3.2.1 Experimental methods 40
3.2.2 Layer-specific constitutive modelling 43
3.2.3 Tri-layered wall model 44
3.2.4 Parameter estimation 47
3.2.5 Statistical analysis 50
3.3 Results 52
3.3.1 Wall and layer-specific geometry and residual deformations 52
3.3.2 The wall and layer-specific mechanics 54
3.3.3 Tri-layered wall model 61
3.4 Discussion 72
3.4.1 Aortic wall and layer-specific structural features 73
3.4.2 Wall and layer-specific mechanics 74
3.4.3 Tri-layered wall model 75
3.5 Chapter conclusions 79

4 The mechanical behaviour of the human aortic wall *ex vivo* 81
4.1 Introduction 82
4.2 Methods 83
4.2.1 Arterial samples 83
4.2.2 Mechanical testing 83
4.2.3 Data analysis 83
4.2.4 Constitutive modelling and parameter fitting 85
4.2.5 Statistical analysis 87
4.3 Results 88
4.4 Discussion 92
4.5 Chapter conclusions 96

5 Non-invasive evaluation of viscoelasticity in the human carotid artery 99

5.1 Introduction . . . 100

5.2 Methods . . . 101

5.2.1 Study population . . . 101

5.2.2 Data acquisition . . . 102

5.2.3 Data analysis . . . 103

5.2.4 Statistical analysis . . . 109

5.3 Results . . . 110

5.3.1 Ageing in healthy people . . . 110

5.3.2 Hypertension and type 2 diabetes . . . 118

5.4 Discussion . . . 124

5.4.1 Ageing . . . 125

5.4.2 Hypertension and type 2 diabetes . . . 126

5.4.3 Pressure-normalisation of local wave speed . . . 128

5.5 Chapter conclusions . . . 130

6 Non-invasive investigation of the impact of bariatric surgery on the carotid haemodynamics 131

6.1 Introduction . . . 132

6.2 Methods . . . 133

6.2.1 Study population . . . 133

6.2.2 Ultrasound acquisitions . . . 133

6.2.3 Data analysis . . . 134

6.2.4 Statistical analysis . . . 135

6.3 Results . . . 136

6.3.1 Treatment outcome . . . 136

6.3.2 Local wave speed . . . 137

6.3.3 Wave intensity . . . 138

6.4 Discussion . . . 138

6.5 Chapter conclusions . . . 141

7 Non-invasive determination of pressure using cuff pressure and local D and U 143

7.1 Introduction . . . 144

7.2 Methods . . . 146

7.2.1 Study population and acquisition protocol . . . 146
7.2.2 Non-invasive wave speed ${}_{\mathrm{n}}c$ and exponential gain ${}_{\mathrm{n}}\gamma$ . . . 146
7.2.3 Non-invasive estimation of pressure . . . 147
7.2.4 Tonometer-based local wave speed c and exponential gain γ . . . 148
7.2.5 Statistical analysis . . . 149
7.3 Results . . . 149
7.3.1 Effect of ageing . . . 150
7.4 Discussion . . . 152
7.4.1 Considerations on the age-effect . . . 160
7.5 Chapter conclusions . . . 162

8 General discussion and conclusions **163**
8.1 General discussion . . . 164
8.1.1 Methodological considerations . . . 164
8.1.2 Clinical considerations . . . 167
8.2 Limitations and experimental considerations . . . 168
8.2.1 *Ex vivo* studies . . . 168
8.2.2 *In vivo* studies . . . 169
8.3 Conclusions . . . 171
8.3.1 Future directions . . . 172

Appendix **175**
A1 The relationship between $\mathscr{C}_{\theta\theta\theta\theta}$ and $\mathscr{K}_{\theta\theta\theta\theta}$ . . . 175
A2 Supplementary tables . . . 176
A3 Supplementary figures . . . 188

List of publications **189**

Acknowledgements

While this PhD journey officially started 'just' three and a half years ago, its true beginning traces back to long before that. Several people I had the luck to meet on my way played an important role, whether on an academic level, human level or a combination of both.

First and foremost, I would like to express my sincere gratitude to my supervisor Prof. Ashraf W. Khir for his mentoring and support, for exposing me to different projects during these years, for his patience during our long meetings, and for allowing me to steer my research in the direction of my interests. I also would like to thank the other members of my supervisory team at Brunel University, Dr. Quan Long and Dr. Tze Pei Chong. Furthermore, I am truly grateful to Prof. Ian B. Wilkinson for the mentoring and supervision throughout my PhD and to Addenbrooke's hospital for funding my studies.

During these years, I had the opportunity to collaborate with many inspiring researchers in the cardiovascular mechanics and haemodynamics field; this thesis would not be the same without their valuable contribution, support and advice. I wish to warmly thank Prof. Carlo Palombo and his group at the University of Pisa for making your data available to me (Chapters 5-6), for your support and for our long discussions on the development of our projects, Prof. J. Kennedy Cruickshank for his competent clinical outlook, for his inspiring drive and for always pushing me to do a 'little more analysis' to improve our work (I might have not always felt this way, but I immensely appreciate it now!!), and Prof. Alun D. Hughes for his competent advice. I also would like to thank Prof. Ian B. Wilkinson and his group at the University of Cambridge, and Dr. Ye Li for for their support in the experimental work conducted on the human aorta (Chapter 4). A huge 'thank you' also goes to Prof. Bart Spronck for his help in developing the tri-layered arterial wall model of Chapter 3, for making me feel at home during my time at Yale University, and for our great times on the snow; I look forward to working with you in Maastricht. Furthermore, this collaboration could not have taken place if Prof. Jay D. Humphrey had not welcomed me to his laboratory at Yale University; I will always be extremely grateful for this great opportunity and for his support throughout my stay (in the mid of a pandemic...). A special mention goes to

Prof. Maria Laura Costantino for always supporting me and because none of this would have happened if she had not introduced me to Prof. Khir.

I wish to thank all the friends (and colleagues) in the Biomedical Engineering Theme at Brunel University: Femke, Angel, Naumann, Ioana, Aya, Giovanni, Lorenzo, Rune, Sebaastian, Vera, Enrico, Clarissa, Wisam, Jenny, and Viktor; my time at Brunel would not have been the same without you all. Among these, a special thank you to Femke, Lorenzo and Ioana for allowing me to supervise their work during their MSc studies; what I learend from you is certainly much more that what you did from me!

Finally, I will always be grateful to my family; my desire for knowledge, my curiosity find their roots in what you thought and showed me throughout my life, long before I started my PhD journey. Nonno Nino and Nonna Luisa, your regret for not being able to study as much as you would have wanted to has thought me since my childhood the importance of education and learning. Nonno Nino how many hours did you spend studying when I was a kid? Nonna Marta, would I enjoy reading as much as I do if you had not read me countless books when I was a child? Dad, would I be an engineer if I had not experienced first hand your passion and devotion? Would I be where I am without your never-ending support? Gigio, I am the eldest, but I learned countless lessons from you (including how to use Latex... my thesis would not look nearly as good as it does if it were not for your help). Layla, words have no value to you... but I am certain you know. Shima, you above all have been close to me during my PhD, first as a friend and colleague and then as part of my family. I simply have no words to describe and acknowledge the support and inspiration you gave me, and I really look forward to all the new 'adventures' that will come in *our* future. Last but certainly not least, I would like to dedicate this thesis to my Mum; you did not have the chance to see me start this journey, but what you taught me resonates in every decision I took along the way.

Abstract

Cardiovascular diseases are the leading cause of death worldwide. Therefore, understanding their aetiology and development is a fundamental goal for biomedical research. Large arteries play a pivotal role in cardiovascular physiology; their elastic properties allow transforming the intermittent heart pulsation into a relatively steady flow. However, age-related microstructural changes of the arterial wall impair their compliant function, with negative consequences on the heart and other organs, including the brain. For this reason, arterial stiffness, assessed clinically by pulse wave velocity (PWV), has gained a central role in the prediction of cardiovascular risk. This thesis aimed to advance our understanding of the performance of the arterial wall, devising effective methods for the characterisation of its complex mechanical behaviour and, more specifically, stiffness both *in vivo* and *ex vivo*.

The first part of this work comprises invasive *ex vivo* studies on arterial mechanics. The formulation of a novel tri-layered model of the arterial wall allowed investigating the layer-specific contribution to the macroscopic behaviour of arteries, providing a structural explanation to the pressure-dependence of arterial stiffness. Furthermore, the effects of the age-related remodelling of the wall microstructure on its non-linear behaviour were directly assessed via analysis of mechanical data of human donors' aortae.

The second part of this work consisted of the development and application of non-invasive techniques for the clinical assessment of arterial mechanics. First, the hysteresis area and the different slopes of the systolic and diastolic arms of the carotid pressure-diameter loops were used to quantify arterial viscoelasticity in a cohort of healthy people and hypertensive and diabetic patients. Second, exponential modelling of the carotid pressure-area relationship was used to define the relationship between local PWV, exponential parameters and blood pressure. This allowed assessing arterial stiffness independently of acute inter-subject differences in blood pressure. Furthermore, the viability of a new technique using ultrasound-based PWV to operate an exponential conversion of local diameter distension waveform into non-invasive pressure has been evaluated.

List of Figures

1.1 Wiggers diagram representing typical pressure traces of the left ventricle, aorta, and left atrium. . . . 3

1.2 Cross sectional view of the media obtained with Scanning Electron Microscopy (SEM). . . . 6

1.3 Volume fraction of elastin, collagen and Smooth Muscle Cell (SMC) in different regions along the aorta. . . . 9

1.4 Stress-stretch relationships of the pig aortic wall in the circumferential and longitudinal direction. . . . 11

1.5 Stress-strain relationships of the arterial wall with and without collagenase or elastase treatments. . . . 13

1.6 Histological cross-sectional images of the arterial media fixed at increasing level of distending pressure. . . . 14

1.7 Example of PU-loop in the in the human pulmonary artery. . . . 18

3.1 Schematic representation of the arterial tree. . . . 41

3.2 Schematic representation of cut-open configuration of a circumferential strip of arterial wall and definition of the opening angle (OA). . . . 42

3.3 Schematic representation of the mapping flow linking the different configurations analysed in this study. . . . 44

3.4 Schematic representation of the mapping between the flat wall sample and the cylindrical vessel. . . . 45

3.5 Schematic representation of the mapping between the unloaded cylindrical vessel and the pressurised longitudinally stretched vessel. . . . 46

3.6 Schematic representation of the workflow used for the parameters estimation for the tri-layered model of the arterial wall. . . . 48

3.7 Geometrical features of the lamb and pig ascending aorta, upper thoracic aorta, and lower thoracic aorta. . . . 51

3.8 Regional changes of the wall and layer-specific opening angles for the lamb and pig aorta. 53

3.9 Examples of wall and layers Cauchy stress-stretch relationships of the ovine and swine ascending aorta. 55

3.10 Examples of wall and layers Cauchy stress-stretch relationships of the ovine and swine upper thoracic aorta. 56

3.11 Examples of wall and layers Cauchy stress-stretch relationships of the ovine and swine lower thoracic aorta. 57

3.12 Comparison between the fitting obtained with single-layered and tri-layered modellings of a lamb lower thoracic aorta. 62

3.13 Average simulated pressure-diameter relationship of the ascending aorta, upper thoracic aorta and lower thoracic aorta of lambs and pigs. 63

3.14 Circumferential ($t_{\theta\theta}$) and longitudinal (t_{zz}) stress, tangential elastic modulus ($\mathscr{K}_{\theta\theta\theta\theta}$) and small-on-large circumferential stiffness stiffness ($\mathscr{C}_{\theta\theta\theta\theta}$), structural stiffness calculated with $\mathscr{K}_{\theta\theta\theta\theta}$ and $\mathscr{C}_{\theta\theta\theta\theta}$ in the ascending aorta of lambs at the reference pressures of 100 and 160 mmHg. 65

3.15 Cicrumferential ($t_{\theta\theta}$) and longitudinal (t_{zz}) stress, tangential elastic modulus ($\mathscr{K}_{\theta\theta\theta\theta}$) and small-on-large circumferential stiffness stiffness ($\mathscr{C}_{\theta\theta\theta\theta}$), structural stiffness calculated with $\mathscr{K}_{\theta\theta\theta\theta}$ and $\mathscr{C}_{\theta\theta\theta\theta}$ in the ascending aorta of pigs at the reference pressures of 100 and 160 mmHg. 66

3.16 Circumferential ($t_{\theta\theta}$) and longitudinal (t_{zz}) stress, tangential elastic modulus ($\mathscr{K}_{\theta\theta\theta\theta}$) and small-on-large circumferential stiffness stiffness ($\mathscr{C}_{\theta\theta\theta\theta}$), structural stiffness calculated with $\mathscr{K}_{\theta\theta\theta\theta}$ and $\mathscr{C}_{\theta\theta\theta\theta}$ in the upper thoracic aorta of lambs at the reference pressures of 100 and 160 mmHg. 67

3.17 Circumferential ($t_{\theta\theta}$) and longitudinal (t_{zz}) stress, tangential elastic modulus ($\mathscr{K}_{\theta\theta\theta\theta}$) and small-on-large circumferential stiffness stiffness ($\mathscr{C}_{\theta\theta\theta\theta}$), structural stiffness calculated with $\mathscr{K}_{\theta\theta\theta\theta}$ and $\mathscr{C}_{\theta\theta\theta\theta}$ in the upper thoracic aorta of pigs at the reference pressures of 100 and 160 mmHg. 68

3.18 Circumferential ($t_{\theta\theta}$) and longitudinal (t_{zz}) stress, tangential elastic modulus ($\mathscr{K}_{\theta\theta\theta\theta}$) and small-on-large circumferential stiffness stiffness ($\mathscr{C}_{\theta\theta\theta\theta}$), structural stiffness calculated with $\mathscr{K}_{\theta\theta\theta\theta}$ and $\mathscr{C}_{\theta\theta\theta\theta}$ in the lower thoracic aorta of lambs at the reference pressures of 100 and 160 mmHg. 69

3.19 Circumferential ($t_{\theta\theta}$) and longitudinal (t_{zz}) stress, tangential elastic modulus ($\mathscr{K}_{\theta\theta\theta\theta}$) and small-on-large circumferential stiffness stiffness ($\mathscr{C}_{\theta\theta\theta\theta}$), structural stiffness calculated with $\mathscr{K}_{\theta\theta\theta\theta}$ and $\mathscr{C}_{\theta\theta\theta\theta}$ in the lower thoracic aorta of pigs at the reference pressures of 100 and 160 mmHg. 70

3.20 Simulated circumferential stress-stretch relationships of tension-inflation test at the *in vivo* axial stretch. 71

3.21 Effect of neglecting wall prestretches in the stress distribution among arterial layers. 78

4.1 Schematic representation of the deformation characterising ring tensile tests. . . 84

4.2 Average pressure-diameter (A) and Cauchy stress-stretch (B) relationship of the human thoracic aorta in each of the six age groups considered in this study. . . . 88

4.3 Changes with age of the tangential elastic modulus $\mathscr{K}_{\theta\theta\theta\theta}$ of the thoracic aorta at the luminal pressure of 60 and 100 mmHg. 89

4.4 Changes with age of the pressure-dependence of the tangential elastic modulus of the human thoracic aorta. 90

4.5 HGO-SEF model parameters as a function of age; elastin/matrix stiffness-like parameter μ, collagen fibre stiffness-like k_1 and exponential k_2 parameters. Anisotropy parameters were assumed constant with age: $\alpha = 44.5°$ and $\tau = 0.20$. 91

4.6 HGO-SEF model parameters as a function of age; elastin/matrix stiffness-like parameter μ, collagen fibre stiffness-like k_1 and exponential k_2 parameters. Anisotropy parameters were given age-dependent values taken from the literature, as detailed in Table 4.1. 92

4.7 Changes in stored elastic energy over the pressure range 120-80 mmHg with age. 93

5.1 Example of pressure heartbeat and its second derivative. 105

5.2 Example of the calculation of the systolic and diastolic distensibility. 106

5.3 Example of the calculation of the hysteresis index. 107

5.4 Systolic and diastolic blood pressure and carotid diameter as a function of age in heathy people. 111

5.5 c, c_{T}, γ, γ_0, Ds in systole and diastole, and $\mathscr{K}_{\theta\theta\theta\theta}$ as a function of age in healthy people. 113

5.6 Comparison between P_c, $\mathrm{SBP_{CCA}}$ and DBP. 114

5.7 Linear correlation and Bland-Altman plots between P_c and DBP, and between P_c and DBP + $0.15\mathrm{PP_{CCA}}$. 114

5.8 Examples of PD-loops for three healthy controls: 26, 55, and 78 years (left, middle and right respectively). 117
5.9 Hysteresis area (H_{A}) and index (H_{I}) as a function of age. 117
5.10 Examples of PD-loops for a healthy control, a hypertensive patient, and a T2DM patient (all >60 years). 123

6.1 Example of non-invasive wave intensity graph in the common carotid artery chosen from one of the patients included in this study. 135
6.2 Evolution during the treatment of the lnDU-loop of a representative patient included in this study. 137
6.3 Average forward compression wave (FCW), backward compression wave (BCW) and forward expansion wave (FEW) area at baseline, post-diet and post-surgery. 138

7.1 Graphical representation of the process used to non-invasively estimate the pressure from acquisition of blood flow velocity U and diameter distension D. 148
7.2 Correlation analysis and Bland-Altman plot between c estimated with D^2P-loop and ${}_{\mathrm{n}}c$ estimated with the lnDU-loop, and between the fitted γ and ${}_{\mathrm{n}}\gamma$ estimated from ${}_{\mathrm{n}}c$. 151
7.3 Correlation analysis and Bland-Altman plot between tonometer MBP and ${}_{\mathrm{n}}$MBP, and between tonometer $\mathrm{SBP}_{\mathrm{CCA}}$ and ${}_{\mathrm{n}}\mathrm{SBP}_{\mathrm{CCA}}$. 152
7.4 Correlation analysis and Bland-Altman plot between c estimated with D^2P-loop and ${}_{\mathrm{n}}c$ estimated with the lnDU-loop in young people, middle-aged adults and older adults. 155
7.5 Correlation analysis and Bland-Altman plot between the fitted γ and ${}_{\mathrm{n}}\gamma$ estimated from ${}_{\mathrm{n}}c$ in young people, middle-aged adults and older adults. 156
7.6 Correlation analysis and Bland-Altman plot between tonometer MBP and ${}_{\mathrm{n}}$MBP in young people, middle-aged adults and older adults. 157
7.7 Correlation analysis and Bland-Altman plot between tonometer $\mathrm{SBP}_{\mathrm{CCA}}$ and ${}_{\mathrm{n}}\mathrm{SBP}_{\mathrm{CCA}}$ in young people, middle-aged adults and older adults. 158

A1 Effect of changes in HGO-SEF model parameters on the modelled behaviour of the arterial wall. 188

List of Tables

3.1 Experimentally determined layer-specific pre-stretches. 53

3.2 Layer-specific model parameters of the ovine and swine ascending aorta. 58

3.3 Layer-specific model parameters of the ovine and swine upper thoracic aorta. . . 59

3.4 Layer-specific model parameters of the ovine and swine upper thoracic aorta. . . 60

3.5 Fitted layer-specific pre-stretches. 61

3.6 Layer-specific circumferential and axial components of the deformation gradient $\mathbf{F}_1$. 63

4.1 Age-specific values of the fibre orientation and dispersion parameters in the two fitting routines used in this study. 87

4.2 Donors demographic and ring geometrical features in the 6 age groups. 88

4.3 Tangential elastic modulus of the human thoracic aorta: differences between decade age-groups. 97

4.4 Age-group-specific model parameters of the human thoracic aorta. 98

5.1 Number of subjects included in this study organised by type of recording (simultaneous and sequential pressure and diameter acquisition) and clinical group. . . 102

5.2 Demographic, HR and brachial pressure of the healthy population included in this study. 111

5.3 Pressure normalisation of local wave speed c in healthy controls: comparison between statistical (ANCOVA) and analytical methods. 115

5.4 Drug treatment of the people included in this study. 118

5.5 Comparison in haemodynamic characteristics between healthy controls $\geq$35 years and hypertensive and T2DM patients. 120

5.6 Adjusted haemodynamic characteristics between healthy controls $\geq$35 years and hypertensive and T2DM patients. 121

5.7 Pressure normalisation of local wave speed c in the three clinical groups. 122

5.8 Comparison in viscous parameters between healthy controls ≥35 years, plain hypertensive, plain T2DM (N-T2DMs), and hypertensive T2DM (H-T2DMs) patients. 124

6.1 Participant characteristics and carotid haemodynamic indices at baseline, post-diet, and post-surgery. 136

7.1 Measured and non-invasively estimated haemodynamic characteristics of the people included in the study. 150

A1 HGO-SEF intact wall and layer-specific parameters of the ascending aortae of the lambs included in this study. 176

A2 HGO-SEF intact wall and layer-specific parameters of the upper thoracic aortae of the lambs included in this study. 177

A3 HGO-SEF intact wall and layer-specific parameters of the lower thoracic aortae of the lambs included in this study. 178

A4 HGO-SEF intact wall and layer-specific parameters of the ascending aortae of the pigs included in this study. 179

A5 HGO-SEF intact wall and layer-specific parameters of the upper thoracic aortae of the pigs included in this study. 180

A6 HGO-SEF intact wall and layer-specific parameters of the lower thoracic aortae of the pigs included in this study. 181

A7 Inter-regional differences in the HGO-SEF parameters of the intact wall and isolated layers of the lamb aorta 182

A8 Inter-regional differences in the HGO-SEF parameters of the intact wall and isolated layers of the pig aorta 183

A9 Inter-layer differences in the HGO-SEF parameters of the three regions of the lamb aorta 184

A10 Inter-layer differences in the HGO-SEF parameters of the three regions of the pig aorta 185

A11 Comparison between local carotid wave speed (c) calculated using the sequential and simultaneous analysis protocol. SD: standard deviation. 186

A12 Comparison in viscous parameters between healthy controls ≥35 years, plain hypertensive, plain T2DM (N-T2DMs), and hypertensive T2DM (H-T2DMs) patients recruited in the hospital of Pisa. All diameter data acquisitions were performed with Aloka Prosound 10 (Hitachi). 187

Notations and abbreviations

Abbreviations

AA	Ascending aorta
ANCOVA	Analysis of covariance
ANOVA	Analysis of variance
BP	Blood pressure
BMI	Body mass index
BRA	Brachial artery
BSA	Body surface area
CCA	Common carotid artery
CVD	Cardiovascular disease
DBP	Diastolic blood pressure
EC	Endothelial cell
ECG	Electrocardiogram
EEL	External elastic lamina
FF	Form factor
$_{n}$FF	Non-invasive form factor
HGO	Holzapfel-Gasser-Ogden

HR	Heart rate
IEF	Inter-lamellar elastic fibre
IEL	Internal elastic lamina
IMT	Intima-media thickness
LTA	Lower thoracic aorta
OA	Opening angle
PP_i	Pulse pressure in the artery i
PWV	Regional pulse wave velocity
cfPWV	Carotid-femoral PWV
baPWV	Brachial-ankle PWV
SBP_i	Systolic blood pressure of the artery i
SEF	Strain energy function
T1DM	Type 1 diabetes mellitus
T2DM	Type 2 diabetes mellitus
TF	Transfer function
US	Ultrasound machine
UTA	Upper thoracic aorta
VSMC	Vascular smooth muscle cell

Arterial mechanics variables

α	Fibre (collagen) orientation parameter of the HGO SEF
$\boldsymbol{\mathcal{B}}$	Stiffness tensor in the reference configuration

$\boldsymbol{\mathcal{C}}$	Small-on-large stiffness tensor
$\mathbf{C}$	Right Cauchy-Green tensor
$d\mathbf{f}$	Differential force vector in κ_t
$d\tilde{\mathbf{f}}$	Fictitious differential force vector in κ_0
dA	Differential area in κ_0
da	Differential area in κ_t
$\not{d}$	Radius of the holding pins for the ring test
$\mathbf{E}$	Green strain tensor
$\boldsymbol{\epsilon}$	Linearised strain tensor
$\mathbf{F}$	Deformation gradient
$\mathbf{F}_1$	Deformation gradient from $\kappa_{\text{composite}}$ to κ_{unloaded}
$\mathbf{F}_2$	Deformation gradient from κ_{unloaded} to $\kappa_{\text{tension-inflation}}$
$\mathbf{F}_3^k$	Layer-specific deformation gradient from κ_{isolated} to $\kappa_{\text{uniaxial test}}$ with $k = \{\text{intima}, \text{media}, \text{adventitia}\}$
$\mathbf{F}_3^{\text{wall}}$	Wall's deformation gradient from κ_{isolated} to $\kappa_{\text{uniaxial test}}$
F	Applied force in the uniaxial/ring test
F_z	Reduced axial force in $\kappa_{\text{tension-inflation}}$
$\mathbf{G}^k$	Laye-specific deformation gradient from κ_{isolated} to $\kappa_{\text{composite}}$ with $k = \{\text{intima}, \text{media}, \text{adventitia}\}$
$\mathbf{H}$	Displacement gradient
h^k	Sample thickness with $k = \{\text{intima}, \text{media}, \text{adventitia}\}$
h_0	Undeformed sample thickness
$\mathbf{I}$	Identity tensor
$\boldsymbol{\mathcal{K}}$	Tangential elastic modulus tensor

$\dot{\mathscr{K}}_{\theta\theta\theta\theta}$	Slope of the $\mathscr{K}_{\theta\theta\theta\theta}$-pressure relationship
κ_0	Generic reference configuration
κ_t	Generic current configuration
κ_{isolated}	Isolated layer configuration in Cartesian coordinates ($\mathscr{X}$,$\mathscr{Y}$,$\mathscr{Z}$)
$\kappa_{\text{composite}}$	Tri-layered flat wall configuration in Cartesian coordinates (x,y,z)
κ_{unloaded}	Tri-layered cylindrical vessel configuration in cylindrical coordinates (Θ,R,Z)
$\kappa_{\text{tension-inflation}}$	Tension-inflated tri-layered cylindrical vessel configuration in cylindrical coordinates (θ,r,z)
$\kappa_{\text{uniaxial test}}$	Uniaxial tensile test configuration in Cartesian coordinates ($\mathbb{X}$,$\mathbb{Y}$,$\mathbb{Z}$)
k_1	Fibre (collagen) stiffness-like parameter of the HGO-SEF
k_2	Fibre (collagen) exponential parameter of the HGO-SEF
L_i	Layer dimension in the i^{th} direction in κ_{isolated} with $i = \{\mathscr{X}, \mathscr{Z}\}$
l_i	Layer dimension in the i^{th} direction in $\kappa_{\text{composite}}$ with $i = \{x, z\}$
L_Z	Axial length of the vessel segment in κ_{unloaded}
l_z	Axial lenght of the vessel segment in $\kappa_{\text{tension-inflation}}$
$\mathscr{L}$	Deformed inter-jaws/pins distance in uniaxial/ring tests
$\mathscr{L}_0$	Undeformed inter-jaws/pins distance in uniaxial/ring tests
Γ	Deformed length of the arterial ring circumference
Γ_0	Undeformed length of the arterial ring circumference
Λ_i	$i^{\text{th}}i^{\text{th}}$ component of $\mathbf{F}_1$ with $i = \{\Theta, Z\}$
λ_i	$i^{\text{th}}i^{\text{th}}$ component of $\mathbf{F}_2$ with $i = \{\theta, z\}$

λ_z	*in vivo* axial stretch
$\overline{\lambda}_i^k$	$i^{\text{th}}i^{\text{th}}$ component of $\mathbf{F}_3$ with $i = \{\mathbb{X}, \mathbb{Z}\}$
$\hat{\lambda}_i^k$	$i^{\text{th}}i^{\text{th}}$ component of $\mathbf{G}^k$ with $i = \{\mathit{x}, \mathit{z}\}$
μ	Matrix (elastin) stiffness-like parameter of the HGO-SEF
p	Lagrange multiplier
Ψ	Strain energy function
$\Psi_{\text{isotropic}}$	Isotropic part of Psi
$\Psi_{\text{anisotropic}}$	Anisotropic part of Psi
R	Radial coordinate in κ_{unloaded}
R_{internal}	Luminal radius in κ_{unloaded}
r	Radial coordinate in $\kappa_{\text{tension-inflation}}$
r_{internal}	Luminal radius in $\kappa_{\text{tension-inflation}}$
$\mathbf{S}$	Second Piola-Kirchhoff stress tensor
$\mathbf{t}$	Cauchy stress tensor
$\mathbf{t}_{\text{exp}}^k$	Experimental Cauchy stress tensor fir the sample $k = \{$wall, intima, media, adventitia$\}$
$\mathbf{t}^k$	Modelled Cauchy stress tensor for the sample $k = \{$wall, intima, media, adventitia$\}$
$\boldsymbol{T}^{(\boldsymbol{i})}$	Traction vector with orientation of the vector $\boldsymbol{i}$
$\tilde{\boldsymbol{T}}^{(\boldsymbol{i})}$	Fictitious traction vector with orientation of the vector $\boldsymbol{i}$
τ	Fibre (collagen) dispersion parameter of the HGO-SEF
$\boldsymbol{u}$	Displacement vector
w_0	Undeformed sample width
$\boldsymbol{X}$	Position vector in κ_0

$\boldsymbol{x}$	Position vector in κ_t

Haemodynamic variables

A	Luminal area of the artery
A_{d}	Luminal area of the artery at diastolic pressure
β	Pressure dependent exponential parameter of the P-D relationship
β_0	Pressure independent exponential parameter of the P-D relationship
c	Local wave speed
${}_{\mathrm{n}}c$	Non-invasive local wave speed (lnDU-loop)
D	Arterial diameter
D_{d}	Diameter at diastolic pressure
D_{ref}	Diameter at the reference pressure P_{ref}
D_{s}	Diameter at systolic pressure
ΔD	Difference between diameter at systolic and diastolic pressures
Ds	Distensibility
${}_{\mathrm{d}}Ds$	Distensibility in diastole
${}_{\mathrm{s}}Ds$	Distensibility in systole
ΔDs	Percent difference between distensibility in systole and diastole
η	Viscous coefficient
γ	Pressure-dependent exponential parameter of the P-D^2 relationship

γ_0	Pressure-independent exponential parameter of the P-D^2 relationship
${}_{\mathrm{n}}\gamma$	Non-invasively determined exponential parameter of the P-D^2 relationship
$\mathrm{d}I$	Wave intensity
H_{A}	Hysteresis area in the pressure diameter loop
H_{I}	Hysteresys index
P	Pressure
${}_{\mathrm{n}}P$	Non-invasively estimated pressure
P_{elastic}	Elastic component of P
P_c	Pressure at which wave speed is determined
P_{ref}	Reference pressure
P_{viscous}	Viscous component of P
Q	Blood flow rate
ρ	*Blooddensity*
Δt	Transit time for the determination of PWV
U	Blood flow velocity

CHAPTER 1

Introduction

Part of this Chapter was published in:

Giudici, A., Wilkinson, I.B., & Khir, A.W. (2020). Review of the techniques used for investigating the role elastin and collagen play in arterial mechanics. *Reviews in Biomedical Engineering*, *15*, 256-259.

1.1 Background

Cardiovascular diseases (CVDs) are the leading cause of death worldwide. In 2017, almost 18 million people died of CVDs, nearly twice as much as the second most deadly pathology: cancers. This corresponds to approximately 2.3% of the world population and 31% of the total number of deaths (Ritchie & Roser, 2019). While in North America and Western Europe the burden of CVDs is considerably lower (1-1.5%) than worldwide and steadily decreased over the years (in 1990 the percentage of people dying of CVDs was approximately twice as much as in 2017), in poorer and less developed regions of the world, like Asia and Africa, cardiovascular-related deaths account for 2-3% of the population and numbers seemed less keen on improving over the years (Ritchie & Roser, 2019). In 2010 alone, CVDs cost 863 billion dollars worldwide, corresponding to approximately 30% of the total expenditure for non-communicable diseases that, in turn, accounted for approximately 63% of the total number of deaths. This cost is expected to rise by 22% by 2030 (Bloom et al., 2011). The message transpiring from these data is twofold: first, these statistics clearly point out the urge in identifying effective solutions to reduce the mortality associated to CVDs, and, second, that scientific advances did effectively reduce mortality in the last three decades, but this has been the case only in rich highly developed countries (World Health Organization, 2017). Therefore, the scientific community has the crucial goal of finding effective and, more importantly, cost-effective solutions to address the issue of CVDs worldwide.

Most of the deaths related to CVDs are classified as heart pathologies (approx. 614 thousand in the USA in 2014) (GBD 2015 Mortality and Causes of Death Collaborators, 2016). However, arteries and the heart are both parts of the cardiovascular system, so that heart failure often reflects problems downstream in the circulation, mainly in arteries. In fact, coronary heart disease and stroke were the leading cause of death in the UK in 2016 (British Heart Foundation, 2020) and high blood pressure (BP) is considered the risk factor associated with the highest level of mortality (Ritchie & Roser, 2019). In a simplistic view, the cardiovascular system can be considered as composed of a pump, the heart, connected to a system of flexible conduits. Therefore, vessel and, specifically arteries, determine the impedance that heart faces when performing its function, hence, they play a key role in determining the cardiac risk factor. For this reason, understanding arterial functioning and how it is impaired with pathologies is of crucial importance to reduce mortality.

Arteries are typically classified in elastic and muscular; the firsts are located in proximity to the heart and owe their name to their high compliance. The function of elastic arteries consists in distending in systole to take in the blood volume ejected from the ventricles and elastically

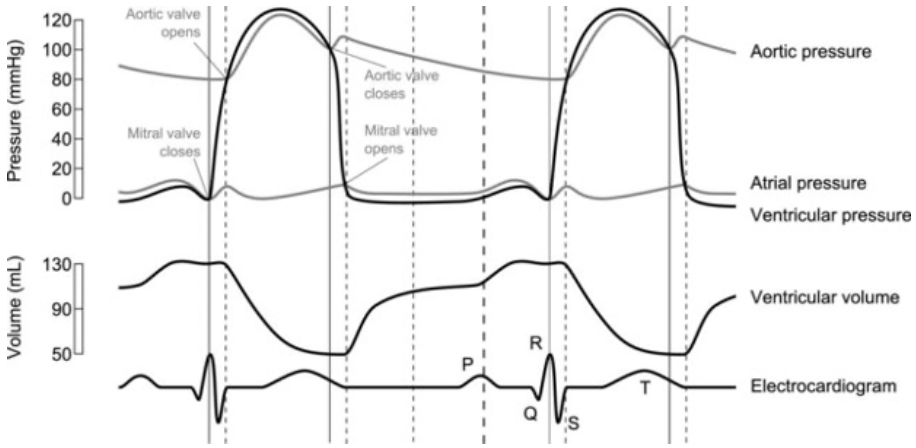

Figure 1.1: *Wiggers diagram representing typical pressure traces of the left ventricle, aorta, and left atrium. While the pressure in the left ventricle cyclically oscillates between ∼0 mmHg and the systolic pressure of 120 mmHg, thanks to its elastic properties the aorta is able to store elastic energy and accommodate blood volume in systole, and then slowly recoil in diastole pushing the blood downstream in the circulation. This process results in the damping of the ventricle pressure pulse, with pressure in the aorta oscillating between 80 and 120 mmHg (Krug et al., 2013).*

recoil during diastole, pushing the blood downstream in the systemic, pulmonary and coronary circulations. The main outcome of the compliant action of elastic arteries is the damping of the intermittent blood flow produced by the heart into a relatively continuous flow (Figure 1.1). On the other hand, muscular arteries owe their name to the higher concentration of smooth muscle cells in their wall and play a different role in the circulation; through their contraction or dilation such arteries control arterial resistance and, hence, the distribution of blood in different district of the body.

Historically, in clinical practice, the health of the cardiovascular and arterial system has been quantified via measurements of arterial pressure waves. The first instruments allowing the measurement of arterial BP were developed in the mid 19th century (Mahomed, 1872; Marey, 1863), evolved at the beginning of the 20th century (Korotkoff, 1905; Riva-Rocci, 1896), and, in more refined versions, are still largely used today in clinical practice (Williams et al., 2018). However, to more careful analysis, arterial BP is not the only variable involved in the functioning of arteries; in fact, the rise of pressure is caused by the ejection of a fluid volume from the heart into a confined space (i.e. the arterial system). Therefore, blood flow rate and arterial geometry are equally crucial in determining the arterial response. Considering a more practical example, the elastic behaviour of a rubber band cannot be described only in terms of the force necessary to obtain its elongation. In fact, the entity of the elongation itself and the size of the cross-sectional area of the rubber band are equally important in determining its elastic properties; at a given

force level, the smaller the elongation the stiffer the rubber band is. Similarly, BP alone is not sufficient to effectively describe the mechanical behaviour of the arterial wall, as this is intrinsically related to blood flow and changes in arterial geometry (e.g. diameter or lumen area).

Furthermore, the measurement of BP is an invasive procedure in most locations of the arterial tree, while can be measured non-invasively through cuff-based measurement or applanation tonometry only in superficial arteries (typically brachial, radial, carotid and femoral arteries). On the contrary, central BP (CBP), the pressure in the aorta, can be measured directly only via catheterisation, a highly invasive technique unsuitable for standard routine checks. For this reason, peripheral BP is currently used as a surrogate of arterial BP (Williams et al., 2018). However, BP (especially systolic BP (SBP), the peak pressure in a cardiac cycle) is not constant along the arterial tree (Reference Values for Arterial Measurements Collaboration, 2014) and a growing number of researchers and clinicians support the idea that, since the heart, kidneys and cerebral arteries are exposed to pressure levels similar to that in the aorta, CBP may predict more effectively CV events than the more widely used brachial BP (Cheng et al., 2012; Sharman et al., 2008).

To address this issues, during the 20th century, researchers, first, and clinicians, later, started borrowing old metrics from continuum mechanics and fluid dynamics and applied them to the field of arterial mechanics (Burton, 1954; Dobrin, 1978; Learoyd & Taylor, 1966), thus mathematically relating blood pressure, flow and arterial distension, and introducing the concept of 'arterial stiffness': i.e., the distending resistance arteries exert in response to the increase in blood pressure induced by the ventricular ejection. Today, Pulse Wave Velocity (PWV) represents the gold standard of the clinical evaluation arterial stiffness (Laurent et al., 2016). PWV is the speed at which a perturbation (i.e., changes in pressure, flow, geometry) propagates in a conduit and is commonly estimated as the ratio between the distance between two sites along the arterial tree and the time the wave takes in travelling from one to the other (typically the carotid to the femoral artery). Clinical studies proved that PWV is a powerful predictor of mortality and cardiovascular risk in hypertensive (Laurent et al., 2003) and diabetic patients (Cruickshank et al., 2002), development of hypertension (Najjar et al., 2008), and cognitive decline (Chiesa et al., 2019; Laugesen et al., 2013), and effectively characterises the ageing process of the arteries (The Reference Values for Arterial Stiffness' Collaboration, 2010).

Nevertheless, in 2018 the guidelines for the management of hypertension of the European Society of Cardiology and European Society of Hypertension stated that "routine use of PWV measurement is not practical and is not recommended for routine practice" (Williams et al., 2018),

matter-of-factly downgrading PWV with respect of 2013 guidelines that had indicated that "The additive value of PWV above and beyond traditional risk factors (...) has been quantified in a number of studies. In addition, a substantial proportion of patients at intermediate risk could be reclassified into higher or lower cardiovascular risk, when arterial stiffness is measured" (Mancia et al., 2013). Different reasons can be attributed to this change in direction indicated by the guidelines: first, although the foot-to-foot PWV represents the gold standard for the evaluation of arterial stiffness in clinical practice, several PWV estimation methods have been devised over the years, each one characterised by different underlying assumptions and requiring analysis of varying levels of complexity. Second, each method can be applied on distinct regions of the arterial tree and is characterised by different level of location-specificity (i.e., provide information on a single artery or an entire region of the arterial tree). Third, even when considering a single metric (e.g. carotid-to-femoral PWV (cfPWV)), medical companies produced several devices for the estimation of PWV, based on different algorithms for the analysis of the arterial waveforms (Salvi et al., 2008; Sánchez Muñoz-Torrero et al., 2018; Ueda et al., 2008). Fourth, arterial stiffness, and consequently PWV, is intrinsically pressure-dependent (Gavish & Izzo, 2016). All these factors contribute to making comparison across studies and across pathologies extremely complex, so that providing reference values to stratify the degree of cardiovascular risk is not trivial. Additionally, measurement of PWV is, even in its simplest form, considerably more complex than measurement of brachial SBP and diastolic BP (DBP), hence less appealing in daily medical practice.

Overall, the CVDs diagnostic and risk stratification potential of arterial stiffness, and PWV more specifically, is, to date, largely underexploited, and more work is currently needed to make this powerful predictor of the risk associated to the highest cause of mortality worldwide more useful in clinical practice, This PhD work has to be considered as part of this broader effort. The following sections will, first, describe the macro and microstructure and mechanical properties of the wall of elastic arteries, as well as its structure-function relationship. Finally, a summary of the techniques currently used to study arterial mechanics *in vivo* will be provided.

1.2 The arterial wall

1.2.1 Macro and micro-structure

The arterial wall presents a complex three-layered structure: the innermost layer is the intima, the middle layer is the media, and the outermost is the adventitia. Each layer is characterised by different structural features and composition, reflecting its specific function. Therefore, given that

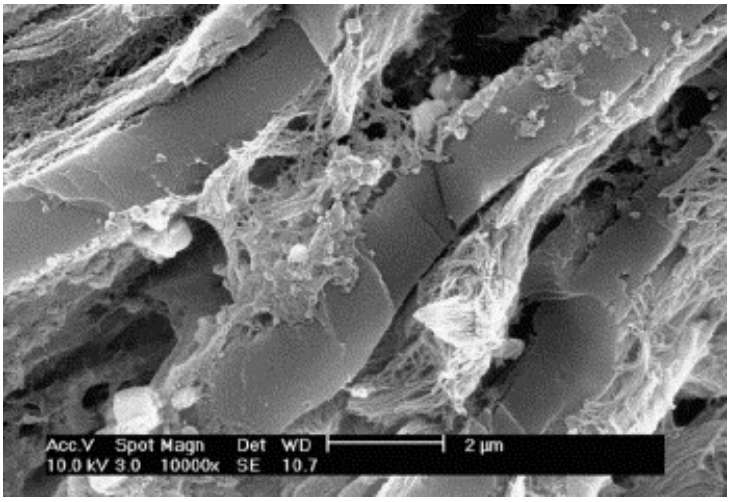

Figure 1.2: *Cross sectional view of the media obtained with Scanning Electron Microscopy (SEM). The structural organisation of the tissue can be noticed, with the elastic lamellae showing a regular sheet-like structure, and the more complex intra-lamellar regions (Raspanti et al., 2006)*

different arteries play specific roles in the cardiovascular system, the composition, structure and relative dimension of the arterial layers vary in different locations of the arterial tree (Halloran et al., 1995; Sugita & Matsumoto, 2013; Wolinsky & Glagov, 1969). The description provided in this chapter refers to large elastic arteries, typically the aorta. The intima is composed by two sublayers; the innermost one is composed mainly by endothelial cells (ECs), a thin basement membrane, a proteoglycan rich matrix and few axially (i.e., along the vessel axis) oriented collagen fibres (O'Connell et al., 2008; Schriefl et al., 2013). It forms the lumen and thus has the function to interface directly with blood, but plays a negligible role in determining the elastic properties of the arterial wall (Burton, 1954). The outermost sublayer is constituted mainly by elastin fibres and individual vascular smooth muscle cells (VSMCs) (Azinfar et al., 2017; O'Connell et al., 2008; Timmins et al., 2010). Experimental results have proven that the intima has a negligible effect on the overall arterial wall mechanics (Butcher, 1960).

The media is highly rich in elastin and organised in concentric structural units, namely medial lamellar units (MLUs) that repeat through its whole thickness. Each MLU is composed of an elastic lamella and an inter-lamellar layer (Figure 1.2). Circumferentially oriented elastin (71% of the total medial elastin) constitutes the elastic lamellae forming regular sheet-like structures with small fenestrations (Boulesteix et al., 2006; O'Connell et al., 2008; Wasano & Yamamoto, 1983) and showing an undulated pattern in both the circumferential and axial direction in the unloaded condition (Fonck et al., 2007; Raspanti et al., 2006; Wolinsky & Glagov, 1964). These sheet-like structures develop mainly in the circumferential direction but show branching and radial connections between adjacent MLUs (Clark & Glagov, 1985; Shimada et al., 1993). Fenestrations in the elastic lamellae allow cell signalling between adjacent MLUs (Boulesteix et al., 2006). The internal and external elastic laminae (IEL and EEL, respectively) separate the media from the other arterial layers. These elastin structures present larger fenestration

with respect to the elastic lamellae, thus a less regular shape (Wasano & Yamamoto, 1983). On the other hand, the inter-lamellar layer has a complex internal structure made by two families of elastin fibres, VSMCs, collagen fibres and mucopolysaccharide gel. In particular, inter-lamellar elastin fibres (IEFs) (27% of the total elastin content) form a connection between elastic lamellae and VSMCs (Dingemans et al., 2000; O'Connell et al., 2008), having a tilt angle with respect to the circumferential direction of approximately 19° (circumferential-radial plane) and a circumferential orientation in the longitudinal-circumferential plane (Dingemans et al., 2000). VSMCs are characterized by elongated elliptic nuclei sharing the same tilt angle of IEFs and seem to interact with both collagen fibrils and elastin lamellae (Dingemans et al., 2000; O'Connell et al., 2008; Bezie et al., 1998a). The second family of elastin fibres, elastin struts (ES) (2% of the total elastin content), form a connection between adjacent elastin lamellae. Wavy collagen fibres surround VSMCs and represent the principal constituent, in terms of volumetric fraction, of the inter-lamellar layer (Krasny et al., 2017b; O'Connell et al., 2008; Shimada et al., 1993). Collagen orientation in the circumferential (0°)-longitudinal plane (90°) has been shown to slightly change through the thickness of the media, with an almost completely circumferential direction in the inner media and a 10-25° (approx.) in the outer media (Polzer et al., 2015; Schriefl et al., 2013). Also, elastin orientation changes through the media thickness, being circumferential in the central portion and assuming a more longitudinal orientation near IEL and especially the EEL (Timmins et al., 2010; Zou & Zhang, 2009).

The adventitia, the outermost arterial layer, is relatively acellular and mainly constituted by collagen (Akhtar et al., 2009). The innermost part of the adventitia (30-40% of its thickness) has a layered structure, and similar volume fractions of collagen and elastin (∼30%). The external part of the adventitia has a higher content of collagen (∼35%) and a lower content of elastin (∼20%). Adventitial collagen is organised in crimped bundles of fibres in the unloaded artery; its waviness is frequently quantified as the ratio between the fibre end-point distance and the fibre length (∼0.8 in the unloaded configuration) (Rezakhaniha et al., 2012). The orientation of fibres in the arterial adventitia has been investigated by means of different microscopy techniques, such as polarised light microscopy (Canham et al., 1989; Schriefl et al., 2012), Diffusion Tensor Imaging (Flamini et al., 2010), and Confocal Laser Scanning Microscopy (Chen et al., 2011; Rezakhaniha et al., 2012; Schrauwen et al., 2012). It is relevant to consider, however, that the collagen's wavy structure complicates the angle estimation. A wider angular distribution of collagen fibres is commonly accepted in the adventitia with respect to the media. In fact, both longitudinally (0°), circumferentially (90°), and diagonally ($\pm 35 - 45°$) running adventitial collagen fibres have been detected in animal models (Chen et al., 2011; Flamini et al., 2013;

Rezakhaniha et al., 2012; Schrauwen et al., 2012; Wan et al., 2012) and human arteries (Cavinato et al., 2017). In the inner adventitia, each layer is characterized by a preferential orientation of collagen fibres, while elastin is organised in two families of fibres: the first sharing the same orientation as collagen fibres and the second displaying a different principal orientation (Chen et al., 2011, 2013). A change in directionality of collagen fibres through the thickness of the adventitia has been reported by several authors; circumferential-diagonal in the inner portion, and longitudinal with higher spread in the angular distribution towards the external part of the artery (Polzer et al., 2015; Schriefl et al., 2013; Wan et al., 2012).

Elastin and collagen

Collagen and elastin are two major constituents of the arterial wall; these proteins contribute to the 50 (aorta)-70% (other arteries) of the total dry weight of the arterial wall, which correspond to the 15-22.5% of the total hydrated weight. Their relative content varies significantly in different regions of the arterial tree, with elastin being preponderant over collagen only in the more proximal region of the aorta and decreasing quite abruptly in the abdominal aorta (Figure 1.3) (Apter et al., 1966; Cox, 1978; Fischer & Llaurado, 1966; Harkness et al., 1957). Elastin and collagen are the major passive mechanical components of soft tissues; their molecular structure is consequently fundamental in characterizing the mechanical behaviour of tissues. Elastin is a mostly hydrophobic protein that constitutes 90% of the elastic fibre. It presents a helical structure at both the microscopic and sub-microscopic levels, and this is thought to be one of the reasons for its elastic properties (Burton, 1954; Urry et al., 1995). At a molecular level, plausible mechanisms explaining elastin elasticity are entropy changes providing elastic recoiling force as seen in the classical theory of rubber elasticity and the highly dynamic behaviour of the hydrophobic domain of elastin (Li & Daggett, 2002).

Collagen, on the other hand, defines a broad family of proteins, characterised by repeating -Gly-X-Y- sequences and a triple right-handed helical structure constituted by three left-handed helical polypeptide chains. Collagen types differ for their structures and consequently for their biological functions. Three types of collagen are present in the arterial wall: type I and III, belonging to the fibril sub-family, and type IV, that forms network-like structures. The degree of collagen crosslinking is a key determinant of the mechanical properties of collagenous tissues, and its alteration, as occurs in pathology and ageing, dramatically alters the mechanical behaviour of arteries (Greenwald, 2007).

Collagen and elastin present markedly different mechanical properties, reflecting their different functions in the arterial wall mechanics (Prockop & Kivirikko, 1995). The modulus of elasticity of collagen is approximately 400 times greater than that of elastin: 100-130 MPa and 200-500

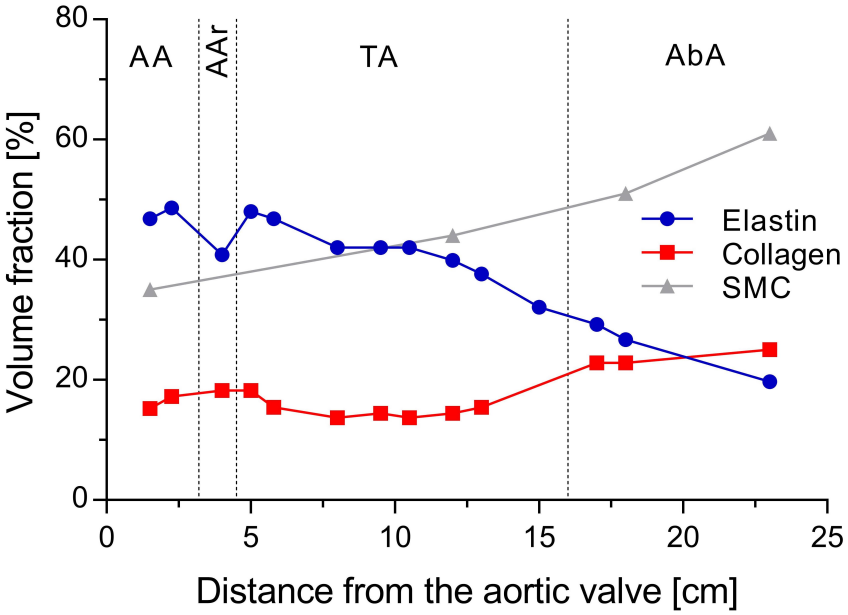

Figure 1.3: *Volume fraction of elastin, collagen and Smooth Muscle Cell (SMC) in different regions along the aorta. Elastin volume fraction is approximately 50% in proximal regions and drops to 20% in the abdominal aorta. On the contrary, collagen volume fraction rises from 15% to 25%. Different protein concentrations are related to the different functions played by the specific arterial segment (Apter et al., 1966; Harkness et al., 1957). AA: Ascending aorta, AAr: Aortic Arch, TA: Descending Thoracic Aorta, AbA=Descending Abdominal Aorta.*

kPa, respectively (Armentano et al., 1991; Burton, 1954; Cox, 1978). Therefore, while elastin provides elasticity and compliance to the tissue, collagen limits the wall stretch and prevents mechanical rupture. Nevertheless, knowing the intrinsic mechanical properties of collagen and elastin is not sufficient to determine the mechanical properties of the whole arterial wall. Indeed, both isolated collagen and elastin fibres maximum strain is lower than the strain that arterial tissue undergoes *in vivo* (Dobrin, 1978). This implies that the spatial organisation of these structural proteins, described in the previous section, plays a key role in determining the tissue mechanical properties. These will be described in the following section.

1.2.2 Arterial wall mechanics

The arterial wall has been defined as "an incompressible nonlinearly elastic orthotropic material subjected to finite deformation" (Greenwald et al., 1997). The first major implication of this definition is that stresses and strains must be defined with reference to the stress-free state. Until 1983, researchers had identified the load-free state (i.e. the configuration in which both the internal pressure and the axial stretch are released) as the stress-free configuration. In 1983,

two different studies introduced a revolution in arterial mechanics observing that, when cut radially, the arterial wall opens and assumes the shape of a circular arch (Chuong & Fung, 1986; Vaishnav & Vossoughi, 1983). The latter was, then, identified as the stress-free configuration. This indicates that the arterial wall in the unloaded configuration (zero internal pressure and no axial stretch) presents residual strains and stresses due to the deformation, or closing, of the open circular arch in the arterial ring (Rachev & Greenwald, 2003). The cut-open configuration is quantitatively described through the opening angle (OA), namely the angle defined by the extremes of the radially cut vessel ring and the middle point of the circular arch. While more recent experimental results have shown that residual stresses are still present in the cut-open configuration (Greenwald et al., 1997; Peña et al., 2015), results in the porcine aorta showed that a multi-layered stress-free state definition does not introduce a significant change in the estimation of stresses and strains (Stergiopulos et al., 2001).

From a physiology perspective, several studies have proved that the residual strains are crucial in guaranteeing an almost uniform distribution of stresses through the thickness of the arterial wall (Alastrué et al., 2007; Humphrey & Na, 2002; Rachev & Greenwald, 2003). Indeed, Holzapfel et al. (2007) developed a more in-depth layer-specific mathematical description of the residual stresses in arteries considering not only the circumferential residual stresses but also the axial and radial ones. Empirical results showed bending of the media in the axial direction and constitutive modelling has demonstrated that this residual deformation furtherly homogenises the distribution of stresses in the arterial media (Zheng & Ren, 2016). It is commonly assumed that a uniform distribution of stresses is optimal for the wall mechanics and that the arterial remodelling aims at preserving this condition (Alford et al., 2008; Driessen et al., 2004; Humphrey et al., 2009; Tsamis & Stergiopulos, 2007). In agreement with this theory, empirical results have proven that wall remodelling, i.e. the alteration of the wall structure, takes place in response to alteration of the physiological level and configuration of stresses (Wang et al., 2017).

The arterial wall can be accounted as orthotropic because arteries are subjected to negligible torsion *in vivo* and, thus, to very low value of shear strains. An exception can be found in the ascending aorta that, due to its proximity to the left ventricle, is subjected to higher and cyclical longitudinal stretches and twist along the vessel main axis (Wittek et al., 2016). Nevertheless, with the exception of the ascending aorta, all relevant arterial wall strains are oriented along the three axes of a cylindrical reference system centred on the vessel longitudinal axis (Dobrin, 1978).

The arterial wall is commonly described as a non-linear elastic material. It is worth noting, however, that defining a biological soft tissue elastic is, in principle, incorrect. In fact, these

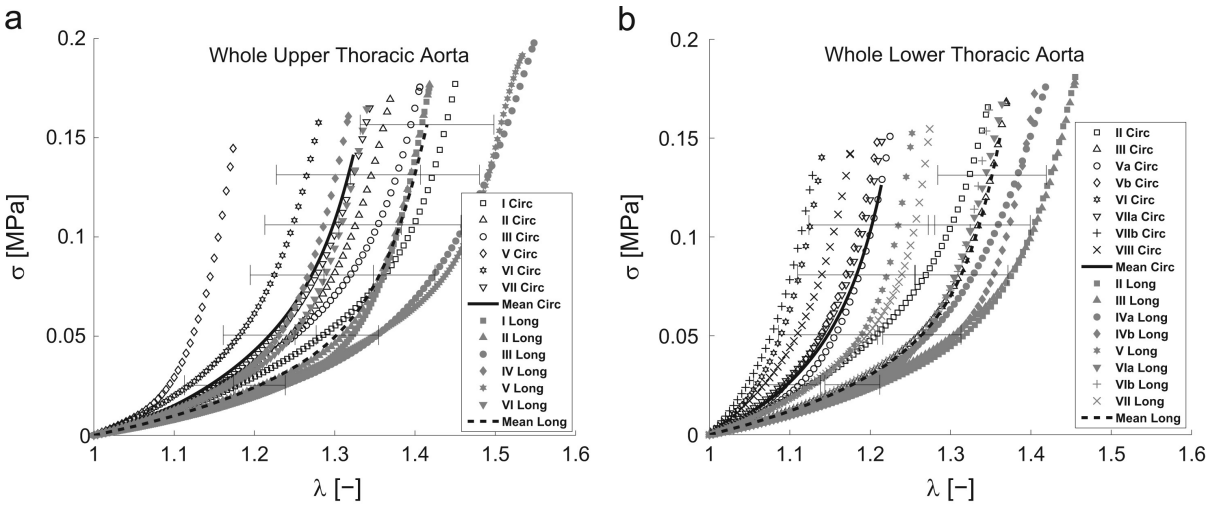

Figure 1.4: *Stress-stretch relationships of the pig aortic wall in the circumferential and longitudinal direction. The non-linear response is evident in both directions, but the non-linearity is higher in the circumferential direction. Moreover, the wall is more compliant axially than circumferentially. Finally, the left graph (panel a) refers to the upper thoracic aorta, while the right one to the lower thoracic aorta (panel b); a stiffening can be observed in both directions when moving from proximal to distal regions (Peña et al., 2015).*

tissues show typical viscoelastic features, including softening in response to cyclic loading, rate dependent behaviour, and an area of hysteresis between the loading and unloading arms of the stress-strain relationship (Cox, 1972; Remington, 1954). Worth of notice is the study of Learoyd & Taylor (1966) that, performing dynamic testing on human arteries, showed not only that the arterial wall stiffness with increasing loading frequency, but also that this frequency-related stiffening appears to be different in different locations of the arterial tree. These findings suggest that the arterial composition plays an important role in determining the viscous properties of the tissue. Furthermore, it has been hypothesised that arterial viscosity could possibly function as a high-frequency filter to protect the arterial wall integrity from sudden changes in arterial pressure (Valdez-Jasso et al., 2009). Nevertheless, several experimental studies show that after a finite number of repeated loading cycles (preconditioning) the wall stress-strain relationship becomes repeatable, thus showing what has been defined as a pseudoelastic behaviour; it means, two different elastic relationships can be identified for the loading and unloading arms of the stress-strain response (Bergel, 1961; Fung et al., 1979; Weisbecker et al., 2013). The majority of studies concentrate on the loading curve after appropriate preconditioning, thus considering the arterial wall as a non-linear elastic material. The stress-strain relationship can, then, be described as formed by two distinct portions: a first compliant region at low strains, followed by a transition region and a final second stiff region at high strains (Figure 1.4) (Burton, 1954; Cox,

1978; Fonck et al., 2007; Sokolis et al., 2006).

Arterial anisotropicity has been shown in a number of experimental works; in the physiological range of pressures, arteries show a higher stiffness in the circumferential direction than in the longitudinal one due to preferential fibres orientation (Shafigh et al., 2013; Vande Geest et al., 2004; Weisbecker et al., 2013). Moreover, the stress-strain curves show a higher dispersion in the longitudinal direction indicating a higher variability in mechanical properties.

Finally, given the strong relation between structure and function in arteries, mechanical properties change significantly between different positions in the arterial tree; in general, a stiffening can be observed moving from proximal to distant regions (Patel et al., 1963; Peña et al., 2015). Moreover, considering a given location in the arterial tree, arterial mechanical properties, as well as geometrical features, change in different circumferential position (anterior, left lateral, right lateral, posterior region). Similar observations have been made in terms of residual strains, with the opening angle that varies according to the quadrant in which the radial cut is performed. It has been hypothesised that these differences may be related to the different level of curvature of aorta in different regions (Sokolis et al., 2017).

1.2.3 Relation between structure and function in arteries

The mechanical behaviour of arteries is generally classified into passive and active responses. Passive response refers to arterial components whose behaviour cannot be modulated (i.e., the extracellular matrix constituted mainly of proteins). Conversely, active mechanics refers to the behaviour conferred to the arterial wall by active components (i.e., VSMCs) that affect the vascular tone through their activation. It is commonly accepted that collagen and elastin are the major determinants of the passive mechanical behaviour of arteries (Burton, 1954; Dobrin, 1978). In fact, they constitute a large portion of the dry weight of arteries, and other wall components, such as VSMCs, have negligible values of passive stiffness if compared to those of collagen and elastin (Burton, 1954; Cox, 1978; Wolinsky & Glagov, 1964). However, the contraction of VSMCs can significantly alter the stress distribution across the wall and, therefore, the distribution of stresses between collagen and elastin, so that, *in vivo*, passive and active responses are strongly interrelated (Matsumoto et al., 1996). Nevertheless, understanding the role of collagen and elastin on the passive mechanical properties of the arterial wall is of great interest as it provides a solid basis for studying more complex active mechanisms characterising the arterial wall *in vivo*.

In a review on arterial mechanics, Burton (1954) described the different roles that elastin and collagen play in the arterial mechanics: “elastic fibres, with their great range of extensibility

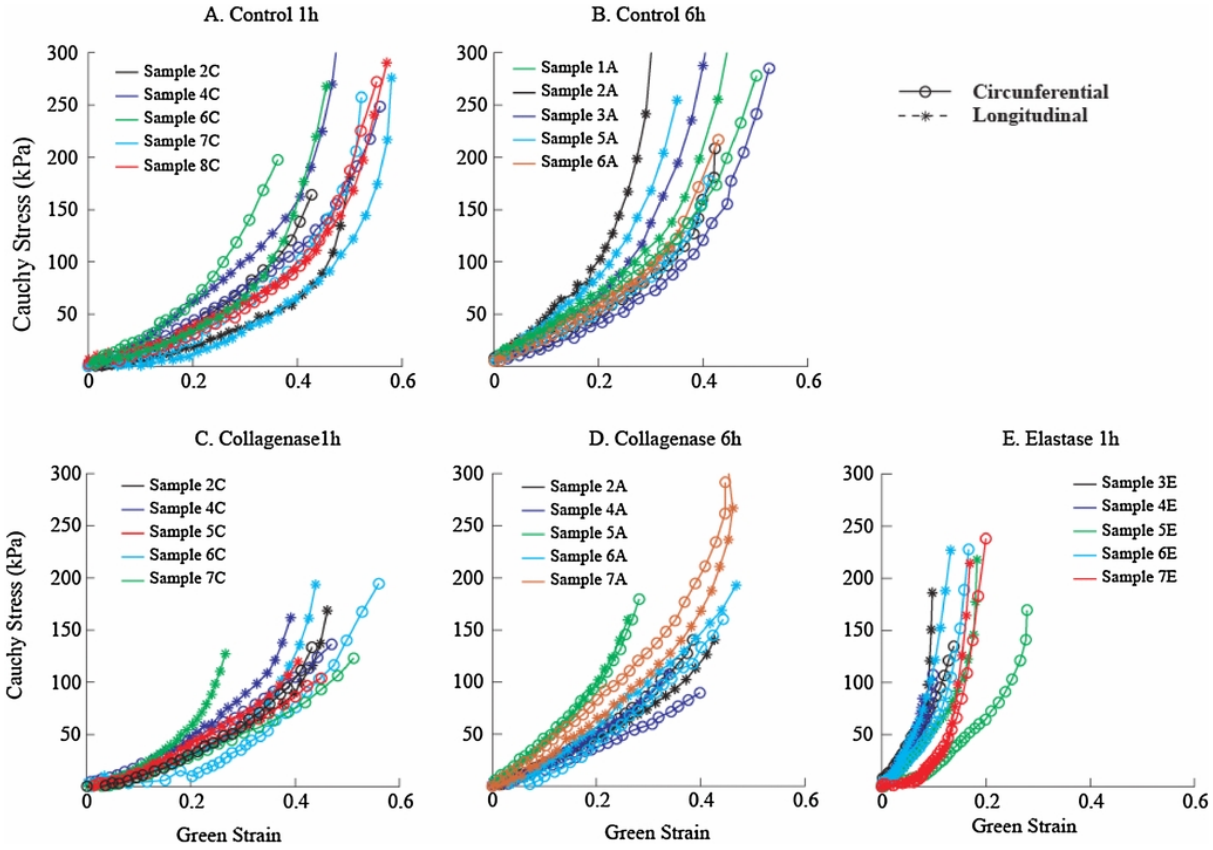

Figure 1.5: *Stress-strain relationships of the arterial wall with and without collagenase or elastase treatments. After collagen digestion, the curve shows a higher linearity, proving the linear behaviour of elastin. Moreover, the relationship at low level of strain is remarkably similar to the one of the intact tissue. On the other hand, elastase treatment significantly alters the initial portion of the curve, while the stiffening at high pressure is still present (Gundiah et al., 2013)*

before elastic limit is reached, have the function of producing maintenance against the normal blood pressure fluctuation. The collagenous fibres, because of the architecture of the wall, are stretched only at higher than normal pressures and have a protective supporting role".

Driven by the strikingly different mechanical properties of these two structural proteins, early works tried correlating the stiffness of arteries with their collagen to elastin ratio. Interestingly, this ratio has been shown to be a good predictor of the mechanical response of arteries at a given location in the arterial tree (e.g. in response structural changes with arterial ageing and hypertension), but it was not when comparing different arterial sites. These findings imply that knowing the relative quantities of collagen and elastin is not sufficient to predict the wall mechanical properties (Apter et al., 1966; Cox, 1978, 1977, 1982).

Selective enzymatic digestion of collagen (collagenase) or elastin (elastase) helped in further

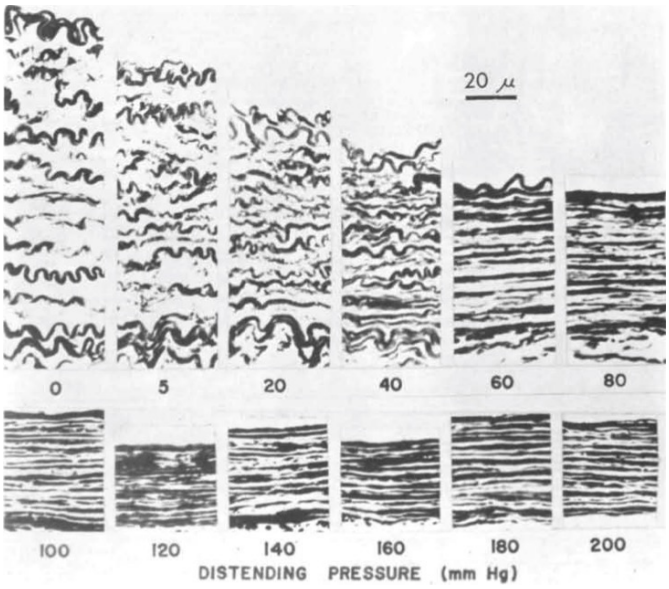

Figure 1.6: *Histological cross-sectional images of the arterial media fixed at increasing level of distending pressure. At low level of pressure, the lamellar structures show a high level of waviness that decreases when the pressure is increased. At 80 mmHg, lamellae appear as completely straightened, and as the pressure is increased further the inter-lamellar spaces become thinner (Wolinsky & Glagov, 1964).*

unveiling the different role these two structural proteins play in arterial mechanics, as well as the importance of their interaction (Figure 1.5). Elastin seems to retain most of the residual strains in the wall as elastase, but not collagenase, treatment significantly affects the artery OA (Fonck et al., 2007; Greenwald et al., 1997). Further, digestion of elastin produces a change in the stress-diameter curve over the whole range of diameters and preserved the tissue anisotropicity and viscoelastic behaviour (Fonck et al., 2007; Schriefl et al., 2015; Weisbecker et al., 2013; Gundiah et al., 2013). Conversely, collagenase-treated samples exhibit a different behaviour compared to untreated samples only for higher levels of transmural pressure (>60 mmHg) and exhibit an almost elastic and isotropic response (Chow et al., 2014; Dobrin & Canfield, 1984; Fonck et al., 2007; Gundiah et al., 2013; Schriefl et al., 2015; Weisbecker et al., 2013). These results suggest that at low pressures the load is borne entirely by elastin, while collagen contributes to arterial mechanics only at high levels of arterial pressure. It has, also, been proven that, in the physiological range of pressures, the percentage of load-bearing of collagen remains significantly lower with respect to elastin (Lillie et al., 2012).

Similar deductions on the relationship between structure and function in arteries have been achieved through microscopy; in the pioneering work of Wolinsky and Glagov (Wolinsky & Glagov, 1964), light and electron microscopies on animal aortae fixed at different distending pressures aided the understanding of the structural reasons behind the static mechanical properties of the aortic media (Figure 1.6). In the unloaded configuration, the elastic lamellae present a wavy structure in both axial and circumferential directions, but straightening is observed when a stretch is applied. In the circumferential direction, the straightening of elastic lamellae takes palce between 0 and 80-100 mmHg of luminal pressure with increasing alignment of the elastin

fibrils. Little further change is observed at higher pressures. On the other hand, collagen fibres were present in the form of bundles with no consistent arrangement for pressures below 80 mmHg. When rising the pressure to 100-150 mmHg, collagen showed a circumferential orientation and it was organised in separated uniformly distributed fibres. Similar results were confirmed in more recent works (Cavinato et al., 2017; Farand et al., 2007; Raspanti et al., 2006; Sokolis et al., 2006), proving that the straightening and alignment process of elastin and collagen in the media takes place at two different ranges of pressures and explaining the biphasic stress-strain relationships of the arterial wall.

Recent studies, coupling uniaxial and biaxial tensile testing with multi-photon microscopy, revealed even more complex recruitment and behaviour of collagen fibres, suggesting that this might not only differ between the media and adventitia, but also among fibres with different functions within the media (Chow et al., 2014; Krasny et al., 2017b; Sugita & Matsumoto, 2016). It was shown that collagen fibres in the adventitia display increased alignment in response to loads in both circumferential and axial directions and delayed recruitment compared to medial collagen fibres whose structural organisation was affected only when loaded circumferentially (Chow et al., 2014; Krasny et al., 2017b). It is crucial to consider, however, that tensile tests require the flattening of the arch-shaped arterial sample into a strip, introducing tensile and compressive strains in the inner and outer part of the artery, respectively. Therefore, this process inevitably induces change in the crimping level of collagen fibres in the media and adventitia, thus affecting the recruitment timing. Further, Sugita & Matsumoto (2016) identified two families of circumferentially oriented collagen fibres in the media, associated with VSMCs and elastic lamellae, respectively. Elastic lamellae associated collagen fibres showed a delayed uncrimping starting at 80-100 mmHg with respect to VSMCs related fibres (40 mmHg).

Collagen and elastin are often considered the main players in arterial mechanics, and most studies focus on the passive response of arteries. Nevertheless, active contraction of the VSMCs significantly affects the stress-strain and pressure-diameter relationship of both muscular and elastic arteries (Jerius et al., 2000; Zhou et al., 2018). Furthermore, researchers agree in identifying the VSMCs as the main determinant of arterial viscosity; Zatzman et al. Zatzman et al. (1954) found profound differences in the relaxation behaviour of the carotid and umbilical arteries, with the first being a musco-elastic artery and showing a 25% of relaxation, and the second being almost completely composed of smooth muscle and showing a relaxation higher than 90%. Apter et al. (1966) found a positive correlation between VSMCs concentration and viscous parameters obtained by fitting the stress-strain relationship using viscoelastic models. Similar mechanical observations were made by Learoyd & Taylor (1966), who observed higher

viscous moduli in the femoral and carotid arteries compared to the aorta.

1.3 The evaluation of arterial stiffness *in vivo*

If the experimental characterisation of the properties of arteries relies on the evaluation stresses and strains through mechanical testing, arterial waveforms (blood pressure, blood velocity, and diameter distension) represent the source of information on arterial mechanics *in vivo*. The ejection of blood from the ventricles in systole produces a wave that propagates downstream in the systemic and pulmonary circulation. The resulting increase in blood pressure distends the elastic arteries whose function consists in dampening the intermittent blood flow generated by heart by storing blood during systole and elastically recoiling and pushing blood downstream in diastole. Further, if the arterial system were a uniform tube of infinite length and the blood were an inviscid fluid, the systolic wave would propagate unaltered. On the contrary, the complex structure of the arterial tree, with its bifurcations and both geometrical and mechanical tapering, gives rise to wave reflections (Abdullateef et al., 2020); at any discontinuity point , the incident wave is decomposed in a transmitted wave, that keeps travelling downstream in the circulation, and a reflected wave, that travels back upstream. Moreover, both transmitted and reflected waves can then be regarded as a new incident wave that will be partially transmitted and reflected when encountering another discontinuity. The amalgamation of all the waves transiting at a given arterial location determines, therefore, the shape of the pressure, velocity and diameter waveforms. This section will introduce the main metrics researcher have defined to quantify the mechanical properties of arteries *in vivo* by means of arterial waveforms.

1.3.1 Pulse Wave Velocity

PWV, defining the velocity of propagation of a wave in a system, is the most commonly used biomarker of arterial stiffness *in vivo* (Laurent et al., 2006; Salvi et al., 2008). In the case of the arterial system, PWV describes the velocity at which the pulse produced by the ventricles propagates in the systemic and pulmonary circulation and must not to be confused with the convective velocity of blood. Several methods have been devised to estimate PWV *in vivo*; these can be classified into regional and local depending on the spatial specificity of the information they provide. In the context of this thesis, the term PWV will be used to indicate regional PWV metrics, while the term wave speed (c) will indicate local PWV values.

Regional estimation of arterial stiffness: PWV

PWV, estimated using the foot-to-foot technique, represent the gold standard for the estimation

of arterial stiffness *in vivo* (Laurent et al., 2016). Two arterial waveforms (pressure, diameter or flow) are recorded at two sites along the arterial tree, the distance between the recording sites (Δx) is measured, and the transit time (Δt) between the feet of the systolic upstroke in the two signals is determined. PWV is then defined as the ratio between Δx and Δt.

However, both the determination of Δx and Δt need further clarification. The transit time can either be directly calculated from two signals acquired simultaneously or by using the electrocardiographic (ECG) signal as reference to synchronise two sequentially recorded signals. The distance Δx consists, theoretically, in the exact length of the arterial pathway bounded by the two acquisition points. Given the non-invasivity of the foot-to-foot PWV and the tortuous and complex architecture of the arterial tree, Δx cannot be measured precisely and is approximated using external measurements of the distance between the acquisition points. For this reason, the higher the distance between the recording sites, the lower the relative error in the estimation of Δx, making PWV an estimate of the average speed at which waves propagate along long arterial pathways. The most widely used recording sites are the carotid-femoral (cfPWV), carotid-brachial (cbPWV) and femoral-dorsalis pedis (Laurent et al., 2006, 2016).

Local estimation of arterial stiffness: c

Although cfPWV still represents the gold standard for the clinical evaluation of arterial stiffness, regional PWV presents evident limits in terms of the spatial resolution of the information provided. For this reason, new techniques have been devised to obtain local estimates of the wave speed c. The PU-loop method, formulated by Parker et al. (1988), relies on the observation that, in early systole, waves are unidirectional (travelling from the heart towards the periphery) because reflected waves have not had the time yet to travel back from the reflection site. For this reason, in this cardiac phase pressure (P) and velocity (U) waveforms are linearly related and the slope of the relationship is proportional to c ('water-hammer' equation) (Figure 1.7).

The PU-loop technique, however, presents two major limitations: first, the recording of pressure is an invasive procedure in most locations of the arterial tree and is therefore unsuitable for routine examinations. Second, the closer the reflection site is to the acquisition site, the shorter the duration of the reflection-free phase in the cardiac cycle (Khir et al., 2001), so that in some arterial locations (e.g. the coronaries) no linear portion can be identified in the PU-loop. More recent local methods aimed at addressing these two limitations but none, to date, successfully solved both simultaneously.

The lnDU-loop (Feng & Khir, 2010) and the QA-loop (Rabben et al., 2004) methods aimed at solving the first of the two limitations mentioned above. Indeed, in their formulation, pressure is substituted by the vessel area (A) or diameter (D) that can be acquired non-invasively

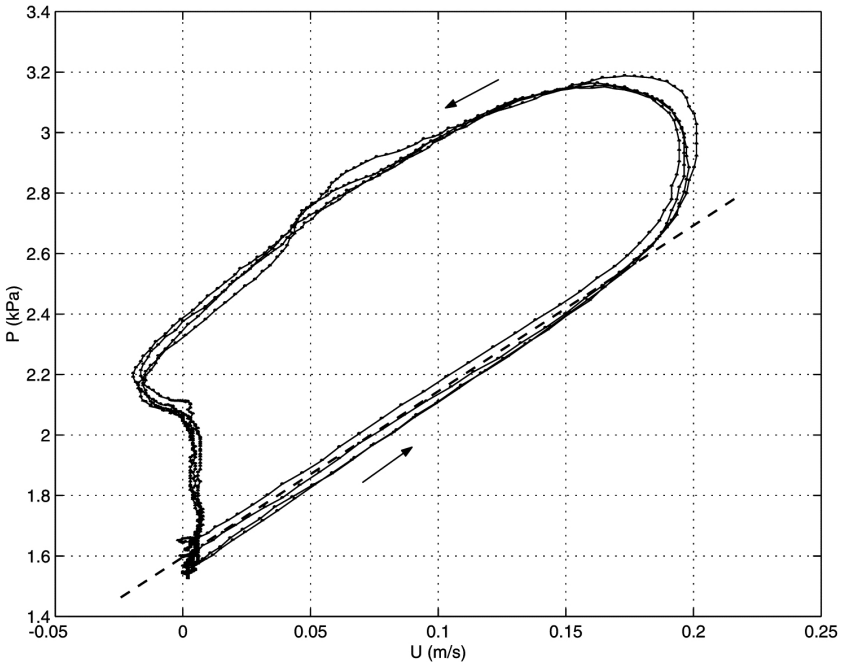

Figure 1.7: *Example of PU-loop in the in the human pulmonary artery. The dashed line indicates the slope of the linear portion in early systole (Khir et al., 2001).*

by ultrasound scanning or magnetic resonance imaging (MRI). The QA-loop and lnDU-loop methods estimate c from the slope of the linear relationship between blood flow ($Q = U/A$) and A and between the natural logarithm of D (ln$D$) and U, respectively, in early systole. As both techniques still rely on the assumption of the absence of reflections in early systole, it is clear that neither of them overcomes the issue of the proximity to the reflection site.

Davies et al. (2005) developed the sum of squares method that extends the principle of the PU-loop technique to allow the determination of c in the coronary arteries by minimising the net wave energy over an entire cardiac cycle. Finally, the D^2P-method (Alastruey, 2011), deriving from the Bramwell-Hill equation (Bramwell et al., 1923), is based on the assumption that the mechanical behaviour of the arterial wall can be described as a Voigt-type viscoelastic material and on the observation that, in late diastole, the viscous term in the model becomes constant and negligible, and the D^2-P relationship is approximately linear. The slope of this relationship is, then, proportional to c. While eliminating the necessity of a reflection-free phase in early systole, both techniques require the acquisition of the pressure waveform and are therefore invasive methods in all but superficial arteries.

The pressure dependence of PWV/c

As described in Section 1.2.3, the mechanical behaviour of soft biological tissues, including the arterial wall, is highly non-linear. Therefore, arterial stiffness, that can be visualised as the slope of the tangent to the stress-strain relationship, is highly dependent on the strain level, which, in turns, is determined by the level of distending pressure. Considering that PWV, as well as c, is an index of arterial stiffness, this fact has obvious repercussion on the *in vivo* metric as well.

Indeed, the Moens-Kortweg equation (Kortweg, 1878; Moens, 1878) relates c in of cylindrical structure to its mechanical properties and geometrical features, indicating that c is proportional to the square root of wall's elastic modulus.

The pressure-dependence of c was also empirically demonstrated in a clinical study where the wave speed of a population of hypertensive subjects was assessed before and after 3 months of pressure-lowering drug treatment (Spronck et al., 2015). The results showed a ∼10% decrease in local wave speed that, given the short follow-up time, could not be explained by actual remodelling of the arterial wall structure and had to be related to the 15% and 13% decreased in SBP and DBP, respectively. As suggested by the authors, the pressure-dependence of c has important clinical implications; indeed, stiffness, as PWV, is commonly used as a marker of healthiness of the arterial wall, but differences in PWV could either be caused by actual differences in wall mechanical properties (reflecting changes in wall structure and composition), in distending pressure only (no change in wall structure and composition) or a combination of the two factors. This fact gains particular importance when evaluating the vascular damage in response to hypertension, when that acute and chronic arterial stiffening are hard to discern.

1.3.2 Exponential relationship between pressure and diameter/area

As detailed in the previous paragraph, the pressure-dependence represents a major limitation of PWV, making this metric comparable to a narrow window through which we cannot fully capture the complex non-linear mechanical behaviour of the arterial wall. In the attempt to address this issue, Hayashi et al. (1980) observed that, in the physiological range of pressures, the relationship between pressure and diameter closely resembles an exponential function and introduced the exponential parameter β_0 as index of arterial stiffness that, in contrast with c, describes the elastic behaviour of arteries over the entire physiological range of pressures and defines their stiffening with increasing pressure (Hayashi et al., 1980). Further, if the exponential function is referred to the same reference pressure P_{ref} for all subject in the study cohort, the resulting β_0 is a pressure-normalised index of arterial stiffness that can be compared without accounting for inter-subjects differences in BP (note that β_0 should not be defined pressure-independent because affected by the arbitrary choice of P_{ref}).

Later, Kawasaki et al. (1987) introduced a simplified version of Hayashi's formula where P_{ref} is substituted by DBP. This simplification allows an easier application of Hayashi's method in clinical studies were D_{ref} is unknown if P_{ref} falls outside the patient-specific SBP-DBP range. However, in doing so, the newly defined exponential constant β (note that $\beta \neq \beta_0$) is intrinsically dependent on the patient-specific DBP. Therefore, while still providing information on the

pressure-related arterial stiffening, β, as PWV, cannot be compared across subjects/group without accounting for their BP differences. It can be shown, however, that β_0 can analytically be calculated knowing β, DBP and P_{ref} (Segers, 2017).

More recently, Meinders & Hoeks (2004) applied a similar modelling framework to the relationship between pressure and area that, under the assumption of circular cross-section, is proportional to D^2.

1.4 Project aims and objectives

This thesis aimed to provide a better understanding of the performance of the arterial wall, devising effective methods for the characterisation of its complex behaviour both *in vivo* and *ex vivo*. Given the importance and fundamental effect of intra-luminal pressure on arterial stiffness, this thesis sought to understand further the structural basis of the nonlinear behaviour of the arterial wall and how this is affected by ageing and pathologies, such as hypertension, diabetes and obesity.

The main objectives of this work were: 1) developing an experimental/modelling technique to study the complex tri-layered behaviour of the arterial wall, 2) devising a method for the characterisation of arterial viscoelasticity *in vivo* and its consequences on arterial stiffness, 3) addressing the issue of the pressure-dependence of PWV/c, and 4) developing a method for the non-invasive estimation of pressure in arteries from local acquisitions of diameter and blood velocity waveforms and peripheral cuff pressure.

1.4.1 Thesis outline

To achieve the stated aims and objectives, this work has been structured in two parts: 1) *ex vivo* work and 2) *in vivo* non-invasive studies. The experimental methods gradually moved from highly invasive and destructive testing of animal and then human arterial samples *ex-vivo* (Chapters 3 and 4) to non-invasive techniques that could be used in clinical practice (Chapters 5, 6 and 7).

A summary of the of the contents of all Chapters is provided below:

- Chapter 2, entitled '*Theoretical background*', provides the mathematical basis for the methods that are used throughout the thesis. Following the structure of this thesis, the first section of this Chapter provides a general introduction to continuum mechanics and its application to the arterial wall. The second section focuses on the analytical methods used for the analysis of arterial haemodynamics and mechanics *in vivo*, including wave intensity analysis, the estimation of local c, and the exponential modelling of the pressure-area

relationship of arteries.

- Chapter 3, entitled '*The mechanical behaviour of the pig and lamb tri-layered aortic wall ex vivo*', consists of the first of two experimental *ex vivo* studies providing a basis for the interpretation of the results of the subsequent non-invasive *in vivo* studies. In this Chapter, the information on the layer-specific mechanical response of the pig and lamb aorta to uniaxial tensile loading will be used to develop a tri-layered model of the arterial wall allowing the simulation of physiological loads (pressurisation and axial extension of the artery). This study will illustrate how shifting from the normotensive to the hypertensive pressure ranges affects the layer-specific engagement and, consequently, the macroscopic wall behaviour. This analysis will allow to understand the structural basis of the pressure-dependence of arterial stiffness.

- Chapter 4, entitled '*The mechanical behaviour of the human aortic wall ex vivo*', is an experimental *ex vivo* study on the human thoracic aorta. Following from the work conducted in Chapter 3 where animal samples are used to perform an in-depth analysis of the 'young' aortic wall mechanical behaviour, this chapter will investigate the effects arterial ageing has on aortic mechanics, with particular interest, once more, on the pressure-dependence of arterial stiffness.

- Chapter 5, entitled '*Non-invasive evaluation of viscoelasticity of the human carotid artery, normalised to pressure variations*', represents the first of the *in vivo* studies. Focusing on the non-invasive quantification of the mechanical properties of the carotid artery from pressure-diameter/area loops, this chapter will address two of the main objectives of this doctoral work: first, establishing a method for the evaluation of the effect of arterial wall viscosity on arterial stiffness *in vivo* and, second, determining the relationship between c and pressure-area exponential constant γ to devise an effective method to address the issue of the pressure-dependence of arterial stiffness *in vivo*. The proposed methods will be tested on a large cohort of healthy people and patients affected by hypertension and type 2 diabetes mellitus (T2DM), pathologies that contribute to increasing the cardiovascular risk, thus evaluating the effects of ageing and pathologies in the specific context of the proposed metrics.

- Chapter 6, entitled '*Non-invasive investigation of the impact of bariatric surgery on the human carotid haemodynamics*', focuses on another important cardiovascular risk factor: obesity. This Chapter represents a case study investigating the consequences of intensive weight loss on arterial mechanics in morbidly obese people in a short/medium-time

framework. Using non-invasive methods for the quantification of relevant haemodynamic parameters, results will be interpreted in light of the findings described in the chapters above.

- Chapter 7, entitled '*Non-invasive estimation of pressure using cuff pressure and local vessel diameter and blood velocity*'. Following from the work on the exponential pressure-area modelling of Chapter 5, the Chapter addresses the fourth proposed objective of this thesis: namely, devising a new method for the non-invasive estimation of pressure in arteries. Central aortic pressure carries physiologically valuable information on the cardiac afterload and cardiovascular risk but can only be directly measured via highly invasive catheterisation. Therefore, the development of effective techniques to non-invasively estimate aortic pressure is of pivotal importance to improve cardiovascular risk assessment in daily clinical practice.

- Chapter 8, entitled '*General discussion and conclusions*', will critically analyse the results and validity of the methods proposed in this project, while providing directions for future work.

Chapter 2

Theoretical background

2.1 Introduction

As described at the end of the previous chapter, this doctoral work can be considered as constituted of two parts, reflecting different approaches used to investigate arterial mechanics: experimental *ex vivo* studies (Chapters 3 and 4) and clinical non-invasive *in vivo* studies (Chapters 5, 7 and 6). Following this classification, the present 'Theoretical background' chapter consists of two parts introducing the analytical methods that will be used throughout this thesis in both *ex vivo* and *in vivo* investigations. Section 2.2 will provide a brief overview of continuum mechanics and on the mathematical description of the mechanical behaviour of the arterial wall. Section 2.3 will cover the analytical methods that will be used in the characterisation of arterial mechanics *in vivo*.

2.2 *Ex vivo* evaluation of arterial mechanics

Despite modern physics proved that matter is discrete, the 'continuum hypothesis' states that the macroscopic response of a body can be approximated by assuming locally averaged properties, which are defined at every point in a body, when the scale of the investigated problem is much larger than dimension of a microstructure in the material. This is the case of the macroscopic behaviour of the arterial wall, where the size of fibres and cells is in the order of μm while the wall thickness is in the order of mm.

2.2.1 Kinematics

Kinematics defines the motion of a body, with the word 'motion' assuming a wider connotation compared to the more general meaning and describing changes in the position of the particles within the body from the reference to a particular perturbed configuration. Hence, a body is a collection of particles and a configuration is a specification of the position of such particles at a given time t. Let κ_0 be a reference configuration (i.e., at $t = 0$) and κ_t a current configuration at time t. The position vector $\boldsymbol{X}$ locates a particle in κ_0, while $\boldsymbol{x}$ defines the position of that particle in κ_t (note that it is generally convenient to refer $\boldsymbol{X}$ and $\boldsymbol{x}$ to different coordinate systems, preferably sharing the same origin). The particle displacement vector can then be defined as $\boldsymbol{u} = \boldsymbol{x} - \boldsymbol{X}$. A rigid body motion, coinciding with the more common meaning of the word motion, is obtained when all particles within a body experience the same $\boldsymbol{u}$. However, this is generally not the case, and every particle can, indeed, experience a different $\boldsymbol{u}$.

The position vector $\boldsymbol{x}$ can be defined as a function of the position vector $\boldsymbol{X}$ and time

$$\boldsymbol{x} = \boldsymbol{x}(\boldsymbol{X}, t) \ , \tag{2.1}$$

so that $\boldsymbol{u}$ becomes

$$\boldsymbol{u} = \boldsymbol{x}(\boldsymbol{X}, t) - \boldsymbol{X} \ . \tag{2.2}$$

Further, defining $d\boldsymbol{x}$ as a generic differential line segment in κ_t with its corresponding $d\boldsymbol{X}$ in κ_0, the deformation gradient $\mathbf{F}$, which is a second-order two-points (i.e. operating a transformation from the coordinate system of κ_0 to that of κ_t) tensor, maps the deformation of $d\boldsymbol{X}$ into $d\boldsymbol{x}$.

$$d\boldsymbol{x} = \mathbf{F} d\boldsymbol{X} = \frac{\partial \boldsymbol{x}}{\partial \boldsymbol{X}} d\boldsymbol{X} \ . \tag{2.3}$$

Combining Eq. 2.2 and Eq. 2.3 the following relationship can also be written

$$\mathbf{F} = \mathbf{I} + \frac{\partial \boldsymbol{u}}{\partial \boldsymbol{X}} = \mathbf{I} + \mathbf{H} \ , \tag{2.4}$$

where $\mathbf{I}$ is the identity tensor and $\mathbf{H}$ is a displacement gradient. Two remarks are worth noting: first, the incompressibility condition, that is often assumed for the arterial wall tissue (see Section 1.2.2), translates to the following relationship

$$J = \det \mathbf{F} = 1 \ . \tag{2.5}$$

Second, as stated in Section 1.2.2, the arterial wall is generally considered orthotropic because subjected to negligible torsion *in vivo*. The same applies to most of the loading conditions applied in ex vivo experiments. In this particular case, only the diagonal components of $\mathbf{F}$ are non-zero, considerably simplifying the analysis.

The right Cauchy-Green tensors ($\mathbf{C}$) is an alternative descriptor of the deformation that, unlike $\mathbf{F}$, is symmetric and independent from rigid body motions.

$$\mathbf{C} = \mathbf{F}^{\mathrm{T}} \mathbf{F} \ . \tag{2.6}$$

Then, the Green strain tensor is defined as

$$\mathbf{E} = \frac{1}{2}(\mathbf{C} - \mathbf{I}) = \frac{1}{2}(\mathbf{H} + \mathbf{H}^{\mathrm{T}} + \mathbf{H}^{\mathrm{T}}\mathbf{H}) \ . \tag{2.7}$$

If deformations and rigid body rotations are small, the quadratic terms in Eq. 2.7 can be neglected, leading to the definition of the linearised strain $\boldsymbol{\epsilon}$.

$$\boldsymbol{\epsilon} = \frac{1}{2}(\mathbf{H} + \mathbf{H}^{\mathrm{T}}) \ . \tag{2.8}$$

2.2.2 Definitions of stress

Important are also the different definitions of stress, whose general description is that of a force acting on an oriented area. To do so, it is useful to first introduce the traction vector $\boldsymbol{T}^{(\boldsymbol{n})}$:

$$\boldsymbol{T}^{(\boldsymbol{n})} = \frac{\mathrm{d}\boldsymbol{f}}{\mathrm{d}a} \ , \tag{2.9}$$

where $\mathrm{d}\boldsymbol{f}$ is a differential force vector and $\mathrm{d}a$ a differential area whose orientation is defined by the perpendicular outward unit vector $\boldsymbol{n}$, both defined in κ_t. Then, the Cauchy stress $\mathbf{t}$ can be defined as the tensor that transforms the orientation $\boldsymbol{n}$ of the area $\mathrm{d}a$ into the traction vector $\boldsymbol{T}^{(\boldsymbol{n})}$.

$$\boldsymbol{T}^{(\boldsymbol{n})} = \boldsymbol{n}\mathbf{t}, \quad T_j^{(\boldsymbol{n})} = n_i t_{i,j} \ . \tag{2.10}$$

Therefore, the subscript, i denotes the orientation of the area on which the force acts and j the orientation of the applied force. As both $\boldsymbol{n}$ and $\mathrm{d}\boldsymbol{f}$ are defined in the current configuration, the Cauchy stress is defined in terms of the actual force that acts on the current area. It is worth noting that for an incompressible material the Cauchy stress can also be written as

$$\mathbf{t} = -p\mathbf{I} + \hat{\mathbf{t}} \ , \tag{2.11}$$

where p is the Lagrange multiplier enforcing incompressibility and $\hat{\mathbf{t}}$ is the extra stress.

However, the current 'deformed' area is not always known, and it can be, therefore, useful to introduce an alternative definition of stress that refers to the area corresponding to $\mathrm{d}a$ in the reference configuration κ_0. Similarly to what has been done above, we, therefore, introduce an infinitesimal area $\mathrm{d}A$ whose orientation is defined by the vector $\boldsymbol{N}$ in κ_0 and a new traction vector $\boldsymbol{T}^{(\boldsymbol{n})}$ so that

$$\boldsymbol{T}^{(\boldsymbol{N})} = \frac{\mathrm{d}\boldsymbol{f}}{\mathrm{d}A} \ . \tag{2.12}$$

Then, the first Piola-Kirchhoff stress tensor $\mathbf{P}$ is defined as

$$\boldsymbol{T}^{(\boldsymbol{N})} = \boldsymbol{N}\mathbf{P} \ . \tag{2.13}$$

It is worth noting that, as $\mathbf{F}$, $\mathbf{P}$ is a two-points vector, hence generally non-symmetric. Therefore, it is useful to introduce a third definition of stress, the second Piola-Kirchhoff stress, that is entirely defined in the reference configuration. We need to introduce a fictitious force $\mathrm{d}\tilde{\boldsymbol{f}}$ satisfying the relationship

$$\mathrm{d}\tilde{\boldsymbol{f}} = \mathbf{F}^{-1}\mathrm{d}\boldsymbol{f} \ , \tag{2.14}$$

and corresponding traction vector

$$\tilde{\boldsymbol{T}}^{(\boldsymbol{N})} = \frac{\mathrm{d}\tilde{\boldsymbol{f}}}{\mathrm{d}A} \ . \tag{2.15}$$

Then, the second Piola-Kirchhoff stress is defined as

$$\tilde{\boldsymbol{T}}^{(\boldsymbol{N})} = \boldsymbol{N}\mathbf{S} \ . \tag{2.16}$$

While benefiting from the advantage of being defined in the reference configuration, $\mathbf{S}$ is defined in terms of a fictitious force and is, hence, of difficult physical interpretation.

Before moving to the definitions of stiffness, it is worth considering that all definitions of stress are mathematically related. Combining Eqs. 2.13 - 2.16 leads to

$$\mathbf{S} = \mathbf{F}^{-1}\mathbf{P} \quad \text{and} \quad \mathbf{P} = \mathbf{S}\mathbf{F}^{\mathrm{T}} \ . \tag{2.17}$$

Also, combining Eqs. 2.9 - 2.10 and Eqs. 2.12 - 2.13 and considering the Nenson's equation for the mapping of surface areas

$$\boldsymbol{N}\mathrm{d}A = \frac{1}{J}\boldsymbol{n}\mathrm{d}a\mathbf{F} \ , \tag{2.18}$$

the following relationship can be obtained

$$\mathbf{t} = \frac{1}{J}\mathbf{F}\mathbf{P} \ , \tag{2.19}$$

so that

$$\mathbf{t} = \frac{1}{J}\mathbf{F}\mathbf{S}\mathbf{F}^{\mathrm{T}} \ . \tag{2.20}$$

2.2.3 Definitions of stiffness

Following from the different definitions of stress described above, the material stiffness can be defined using different metrics. The first stiffness tensor $\boldsymbol{\mathcal{B}}$, defined in the reference configuration κ_0, is calculated as the partial derivative of the second Piola-Kirchhoff stress tensor with respect to the Green strain tensor and its component $\mathscr{B}_{ABCD}$ can be visualised as the tangent to the relationship between $\mathbf{S}_{AB}$ and $\mathbf{E}_{CD}$.

$$\boldsymbol{\mathcal{B}} = \frac{\partial \mathbf{S}}{\partial \mathbf{E}} \ . \tag{2.21}$$

However, as stated above, $\mathbf{S}$ is defined in terms of a fictitious force and is, hence, not convenient in experimental work.

Commonly used in arterial mechanics, the tangential elastic modulus $\boldsymbol{\mathcal{K}}$ defined as the derivative of the Cauchy stress with respect to the Green strain tensor (Kim & Baek, 2011).

$$\boldsymbol{\mathcal{K}} = \frac{\partial \mathbf{t}}{\partial \mathbf{E}} \ , \quad \text{with} \quad \mathscr{K}_{ijAB} = \frac{\partial t_{ij}}{\partial E_{AB}} \ . \tag{2.22}$$

As shown in Eq. 2.15, $\mathscr{K}_{ijAB}$ can be visualised as the slope to the relationship between $\mathbf{t}_{ij}$ and $\mathbf{E}_{AB}$. While commonly used, $\boldsymbol{\mathcal{K}}$ is a two-points vector (operating a transformation between the reference and current configuration) and is, hence, of difficult physical interpretation.

Finally, Baek et al. (2007) introduced the concept of small-on-large, allowing the definition of a stiffness tensor in the current configuration. The small-on-large framework is based on the observation that the deformation that the arterial wall experiences *in vivo* can be considered as the superimposition of a small (cyclic) deformation within the cardiac cycle over a large

deformation from the stress-free configuration κ_0 to the that at physiological pressure κ_*. This allows the introduction of the small-on-large stiffness tensor $\boldsymbol{\mathcal{C}}$ as

$$\mathscr{C}_{ijkl} = \delta_{i,j}\hat{t}^*_{l,j} + \hat{t}^*_{i,l}\delta_{j,k} + 4F^*_{iA}F^*_{jB}F^*_{kC}F^*_{lD}\mathscr{B}_{ABCD}|_{\kappa_*} \ , \tag{2.23}$$

where $\delta_{i,k} = 1$ if $i = k$ and $\delta_{i,k} = 0$ if $i \neq k$, $\hat{\mathbf{t}}^*$ is the extra Cauchy stress in κ_*, $\mathbf{F}^*$ maps the deformation from κ_0 to κ_*. While $\boldsymbol{\mathcal{K}}$ assumes that the non-linear behaviour of the arterial wall can be linearised around the relatively small deformation occurring within the cardiac cycle, the small-on-large stiffness $\boldsymbol{\mathcal{C}}$ was introduced to connect the linearised arterial stiffness with complex features of the constitutive relations, such as residual stress, anisotropy, and nonlinear behaviours. The mathematical relationship between the circumferential components of $\boldsymbol{\mathcal{C}}$ and $\boldsymbol{\mathcal{K}}$ is detailed in the Appendix A1.

2.2.4 Mathematical description of the wall behaviour: strain-energy functions

The mechanical behaviour of incompressible hyperelastic materials, such as the arterial wall when considering only the loading part of the stress-strain relationship after preconditioning, can be defined in term of a strain-energy function $\Psi = \Psi(\mathbf{C})$, describing the energy per unit volume stored in the deformed elastic continuum and satisfying the condition $\Psi(\mathbf{I}) = 0$ (Gasser et al., 2006). As Ψ describes the behaviour of a fully elastic material, the internal dissipation is null and the Clausius-Planck form of the second law of thermodynamics reduces to

$$w_{\text{internal}} - \frac{d\Psi}{dt} = 0 \ . \tag{2.24}$$

It can be shown that Eq. 2.24 leads to the following relationship:

$$\mathbf{S} = -p\mathbf{C}^{-1} + 2\frac{\partial\Psi(\mathbf{C})}{\partial\mathbf{C}} \ . \tag{2.25}$$

Further, combining Eq. 2.20 and Eq. 2.25 allows the definition of the Cauchy stress as a function of Ψ (note that due to incompressibility $J = 1$).

$$\mathbf{t} = -p + 2\mathbf{F}\frac{\partial\Psi(\mathbf{C})}{\partial\mathbf{C}}\mathbf{F}^{\mathrm{T}} \ . \tag{2.26}$$

The Holzapfel-Gasser-Ogden's strain energy function

In this thesis, the Holzapfel-Gasser-Ogden (HGO) two fibre family hyperelastic strain SEF has been used to mathematically describe the wall and layer-specific behaviour (Gasser et al., 2006). The HGO-SEF is based on the assumption that the passive response of the arterial wall

is determined by two main constituents: the first is a compliant matrix, typically associated with elastin, that exhibits an isotropic behaviour, and the second a fibrous component, collagen, whose behaviour is anisotropic. Therefore, the SEF of the arterial wall is defined as the sum of an isotropic and an anisotropic component:

$$\Psi = \Psi_{\text{isotropic}} + \Psi_{\text{anisotropic}} \ , \tag{2.27}$$

where

$$\Psi_{\text{isotropic}} = \mu(I_1 - 3) \qquad \text{and} \tag{2.28}$$

$$\Psi_{\text{anisotropic}} = \sum_{i=1}^{2} \frac{k_1}{2k_2}(e^{k_2[\tau I_1 + (1-3\tau)I_{4,i} - 1]^2} - 1) \ . \tag{2.29}$$

where μ is a matrix/elastin stiffness-like parameter, k_1 is a collagen stiffness-like parameter, k_2 is a dimensionless collagen exponential parameter, and $\tau \in [0, 1/3]$ is a fibre dispersion coefficient describing the angular dispersion of collagen fibres. I_1 and $I_{4,i}$ are the first and fourth invariants of the right Cauchy-Green tensor ($\mathbf{C}$) defined as

$$I_1 = C_{AA} + C_{BB} + C_{CC}; \ I_{4,i}(\mathbf{C}) = C_{AA}\cos{\alpha_i}^2 + C_{CC}\sin{\alpha_i}^2 \ , \tag{2.30}$$

with A, B and C corresponding to the circumferential, radial and axial orientation of the vessel, respectively, $\alpha_i = \{-\alpha, \alpha\}$ the collagen fibres' principal orientation with respect to the circumferential orientation. Symmetry ($\alpha_1 = -\alpha_2$) results in $I_{4,1} = I_{4,2}$, and, hence, Eq. 2.29 can be simplified to (Gasser et al., 2006)

$$\Psi_{\text{anisotropic}} = \frac{k_1}{k_2}(e^{k_2[\tau I_1 + (1-3\tau)I_{4,i} - 1]^2} - 1) \ . \tag{2.31}$$

2.3 Characterisation of arterial mechanics *in vivo*

2.3.1 *PU*-loop method and wave intensity analysis

Wave intensity analysis (WIA) is a method for the time-domain analysis of waves propagation in the arterial system introduced by Parker et al. (1988) and based on the one dimensional model of fluid propagation formulated by Euler (1775). WIA assumes that the arterial P and U waveforms are generated by the summed contribution of forward travelling (from the heart to the periphery of the circulation) and backward travelling (vice versa) waves. In the systemic circulation, the contraction of the left ventricle produces a compression and acceleration forward wave in early systole that travels from the aortic valve to the periphery. Conversely, backward waves consist in reflections that generate when a travelling wave faces a discontinuity in the circulation: a change in tube geometry (e.g., bifurcation) or mechanical properties. Clearly,

reflections can also be regarded as travelling waves and hence can be re-reflected into a forward wave, so that arterial waveforms are made by a complex composition of forward and backward travelling waves (Abdullateef et al., 2020; Parker, 2009). WIA provides an analytical method for the separation of forward and backward components of the arterial waves, thus allowing a detailed analysis of the propagation of waves in the arterial system.

WIA is based on three main assumptions: 1) blood is incompressible and 2) inviscid, and 3) blood flow is governed by equations of conservation of mass and momentum. The conservation of mass equation states that the mass variation in time in a system must be equal to the net inflow/outflow of an incompressible fluid, since mass cannot be created or destroyed.

$$\frac{\partial A}{\partial t} + \frac{\partial AU}{\partial x} = 0 \ , \tag{2.32}$$

where A is the luminal area and U is the blood velocity. The momentum equation derives from Newton's second law:

$$\frac{\partial U}{\partial t} + U\frac{\partial U}{\partial x} + \frac{1}{\rho}\frac{\partial P}{\partial x} = 0 \ , \tag{2.33}$$

where P is the intraluminal pressure and ρ is the blood density. Under the above-cited assumptions, and considering arteries as uniform elastic tubes with constant properties, the luminal area can be considered as a function of pressure only, and conservation of mass and momentum equations can be expressed in matrix form

$$\frac{\partial}{\partial t}\begin{bmatrix} P \\ U \end{bmatrix} + \begin{bmatrix} U & \frac{A}{\frac{\partial A}{\partial P}} \\ \frac{1}{\rho} & U \end{bmatrix} \frac{\partial}{\partial x}\begin{bmatrix} P \\ U \end{bmatrix} = 0 \ . \tag{2.34}$$

This system of first order hyperbolic differential equation was solved by Riemann (1860) using the method of characteristics. The eigenvalues of the x derivative matrix are:

$$\lambda_{\pm} = U \pm \sqrt{\frac{A}{\rho\frac{\partial A}{\partial P}}} = U \pm c \ , \tag{2.35}$$

and indicate the speed at which the perturbations propagate in the vessel. Since in arteries $c > U$, any perturbation will travel downstream at a speed $U + c$ (forward wave) and upstream at a speed $U - c$ (backward wave). As it can be seen from Eq. 2.35, c is a function of $P(x, t)$ and this significantly complicates the analytical solution of the problem. If c is assumed to be independent of P, then Eq. 2.34 can be solved in terms of the Riemann variables:

$$dR_{\pm} = dU \pm \frac{dP}{\rho c} \ , \tag{2.36}$$

where R_+ and R_- are Riemann variables for the forward and backward waves, respectively, dP and dU are changes in pressure and blood velocity over an infinitesimal time dt.

The 'water hammer' equation constitutes the basis of the PU-loop method and easily follows from the definition of the forward and backward Riemann variables (Eq. 2.36). Assuming that dP and dU can similarly be separated into forward and backward components

$$\mathrm{d}P = \mathrm{d}P_+ + \mathrm{d}P_- \quad \text{and } \mathrm{d}U = \mathrm{d}U_+ + \mathrm{d}U_- \ . \tag{2.37}$$

In the presence of unidirectional waves (either forward or backward) the Riemann variable corresponding to the other direction of travel equals 0. For instance, for a forward wave

$$dRm_- = 0 = dU_+ - \frac{dP_+}{\rho c} \ . \tag{2.38}$$

Rearranging Eq. 2.38 leads to the 'water-hammer' equation that, as seen in Section 1.3.1, allows estimating c from the linear relationship between P and U in the early systolic phase of the cardiac cycle when waves are unidirectional: i.e., the PU-loop method.

$$\mathrm{d}P_\pm = \rho c \ \mathrm{d}U_\pm \ . \tag{2.39}$$

Further, combing Eqs. 2.37 with Eq. 2.39 leads to

$$\mathrm{d}P_\pm = \frac{1}{2}(\mathrm{d}P \pm \rho c \ \mathrm{d}U) \ , \quad \text{and} \tag{2.40}$$

$$\mathrm{d}U_\pm = \frac{1}{2}\left(\mathrm{d}U \pm \frac{\mathrm{d}P}{\rho c}\right) \ . \tag{2.41}$$

Therefore, the forward and backward pressures and velocities at any time instant $\hat{t} \in [0, T]$ can be calculated as

$$P_\pm(\hat{t}) = \sum_{t=0}^{\hat{t}} \mathrm{d}P_\pm(t) + P_0 \ , \quad \text{and} \tag{2.42}$$

$$U_\pm(\hat{t}) = \sum_{t=0}^{\hat{t}} \mathrm{d}U_\pm(t) + U_0 \ . \tag{2.43}$$

where P_0 and U_0 are integration constants conventionally set to $P(t = 0)$ and $U(t = 0)$, respectively, and T is the duration of a cardiac cycle. Note that this choice contradicts Eq. 2.37 and a more mathematically sound choice would be $P_0 = P(t = 0)/2$ and $U_0 = U(t = 0)/2$. However, the conventional choice above allows for an easier comparison between forward and backward waves.

Finally, wave intensity is defined as the product between $\mathrm{d}P$ and $\mathrm{d}U$, and its forward and backward components can be calculated as:

$$\mathrm{d}I_\pm = \mathrm{d}P_\pm \mathrm{d}U_\pm \ . \tag{2.44}$$

The forward and backward components of the wave intensity have the property of being always positive and negative, respectively, implying that a forward travelling wave will always produce a positive contribution to dI, and vice versa.

2.3.2 lnDU-loop method and the non-invasive wave intensity

One of the limitations of the standard WIA consists of requiring invasive measurements for all the non-superficial arterial locations where P cannot be acquired via tonometry. Feng & Khir (2010) provided a non-invasive alternative to the standard WIA formulation by substituting P with the diameter D.

The wave speed can be expressed as a function of the arterial distensibility Ds.

$$c^2 = \frac{1}{\rho Ds} = \frac{A_d \, \mathrm{d}P}{\rho \, \mathrm{d}A} \ , \tag{2.45}$$

where A_d is the diastolic luminal area and dA is a small increment of the luminal area. Considering a circular cross-sectional area and neglecting the second order terms in infinitesimal dD, the following relationship can be written:

$$\frac{\mathrm{d}A}{A_\mathrm{d}} = \frac{2\mathrm{d}D}{D_\mathrm{d}} \ . \tag{2.46}$$

Therefore, substituting Eq. 2.46 into Eq. 2.45 leads to the following relationship between pressure and diameter incremental changes can be obtained:

$$\mathrm{d}P = \rho c^2 \frac{2\mathrm{d}D}{D_\mathrm{d}} \ . \tag{2.47}$$

Similarly to what has been described for the pressure and diameter waves in Section 2.3.1, variations in pressure and diameter are determined by the arrival of forward and backward travelling waves. Therefore Eq. 2.47 can be rewritten as a sum of backward and forward incremental changes in pressure and diameter:

$$(\mathrm{d}P_+ + \mathrm{d}P_-) = \rho c^2 \frac{2(\mathrm{d}D_+ + \mathrm{d}D_-)}{D_\mathrm{d}} \ . \tag{2.48}$$

Using the water hammer equation (Eq. 2.39), we can substitute $\mathrm{d}P_+$ and $\mathrm{d}P_-$ in Eq. 2.48 with the forward and backward incremental changes of velocity:

$$c = \frac{D}{2} \frac{(\mathrm{d}U_+ + \mathrm{d}U_-)}{(\mathrm{d}D_+ + \mathrm{d}D_-)} \ , \tag{2.49}$$

and considering $\mathrm{d}D/D = \mathrm{d}(lnD)$, the following expression for the non-invasive wave speed ${}_nc$ can be written:

$${}_\mathrm{n}c = \pm \frac{1}{2} \frac{\mathrm{d}U_\pm}{\mathrm{d}(\ln D_\pm)} \ . \tag{2.50}$$

Given Eq. 2.50, the separation of wavefronts described in Eqs. 2.40 and 2.41 in terms of pressure and velocity can be reformulated in terms of diameter and velocity as follows:

$$\mathrm{d}D_\pm = \frac{1}{2} \left(\mathrm{d}D \pm \frac{D_\mathrm{d}}{2 \ {}_\mathrm{n}c} \mathrm{d}U \right), \quad \text{and} \tag{2.51}$$

$$\mathrm{d}U_{\pm} = \frac{1}{2}\left(\mathrm{d}U \pm \frac{2\ {}_{\mathrm{n}}c}{D_{\mathrm{d}}}\mathrm{d}P\right) \ . \tag{2.52}$$

The forward and backward components of the diameter and velocity waveforms can then be calculated as the linear summation of wavefronts in time:

$$D_{\pm}(\hat{t}) = \sum_{t=0}^{\hat{t}} \mathrm{d}D_{\pm}(t) + D_0, \quad \text{and} \tag{2.53}$$

$$U_{\pm}(\hat{t}) = \sum_{t=0}^{\hat{t}} \mathrm{d}U_{\pm}(t) + U_0 \ . \tag{2.54}$$

where D_0 and U_0 are integration constants conventionally set to $D(t=0)$ and $U(t=0)$, respectively, and $\hat{t} \in [0, T]$.

Finally, the non-invasive wave intensity can be formulated as follows:

$${}_{\mathrm{n}}\mathrm{d}I = \mathrm{d}D_{\pm}\mathrm{d}U_{\pm} = \frac{2\ {}_{\mathrm{n}}c}{4D_{\mathrm{d}}}\left(\mathrm{d}D \pm \frac{D_{\mathrm{d}}}{2\ {}_{\mathrm{n}}c}\mathrm{d}U\right)^2 \ . \tag{2.55}$$

2.3.3 D^2P-loop

The D^2P-loop method was introduced by Alastruey (2011). As seen in Section 1.3.1, the arterial wall exhibits a typical viscoelastic behaviour. Alastruey postulated that such behaviour could be described through Voigt-type viscoelastic model where the total pressure waveform is considered as the sum of an elastic and a viscous component.

$$P = P_{\mathrm{elastic}} + \eta\frac{\mathrm{d}D}{\mathrm{d}t} \ , \tag{2.56}$$

where P_{elastic} is the purely elastic component of P, η is a viscosity coefficient, and $\mathrm{d}D/\mathrm{d}t$ is the time derivative of the diameter waveform D. In late diastole, the elastic recoil of the arterial wall is relatively slow, so that $\mathrm{d}D/\mathrm{d}t$ is much smaller in this phase of the cardiac cycle than during systolic ejection. Over the small range of pressure characterising late diastole, the 'nearly' elastic relationship between P and D^2 is nearly linear and its slope can be used to estimate an 'elastic' wave speed c.

Considering the Bramwell-Hill equation (Bramwell et al., 1923)

$$c = D\sqrt{\frac{\mathrm{d}P}{\rho\ \mathrm{d}(D^2)}} \ , \tag{2.57}$$

and applying a linearisation over the 'elastic' late diastolic part of the P-D^2 relationship, the local wave speed can then be calculated as

$$c = D_{\mathrm{d}}\sqrt{\frac{\mathrm{d}P}{\rho\ \mathrm{d}(D^2)}} \ , \tag{2.58}$$

where D_d is the diameter at DBP and the derivative term is approximated with the slope of the linear regression of the P-D^2 relationship in late diastole.

2.3.4 The relationship between γ and c

Section 1.3.1 introduced the concept of pressure-dependence of c, highlighting the impact this relationship has on the clinical application of c, as well as PWV. Section 1.3.2 showed how the observation that, in the physiological pressure range, the arterial P-A relationship closely resembles an exponential function allows defining a stiffness metric (γ) capable of describing the entire P-A in the physiological pressure range.

$$P(D) = \mathrm{DBP} e^{\gamma\left(\frac{D^2}{D_\mathrm{d}^2}-1\right)} , \tag{2.59}$$

where DBP is the diastolic pressure. Further, if Eq. 2.59 is generalised to an arbitrary reference pressure P_ref, the resulting γ_0 is a pressure-normalised metric of arterial stiffness; i.e., despite still depending on the subjective choice of P_ref, if the same P_ref is chosen for all subjects, γ_0 is unaffected by inter-subject differences in BP.

$$P(D) = P_\mathrm{ref} e^{\gamma_0\left(\frac{D^2}{D_\mathrm{ref}^2}-1\right)} . \tag{2.60}$$

Combining Eq. 2.59 and Eq. 2.60 leads to

$$\gamma_0 = \gamma - \ln\left(\frac{\mathrm{DBP}}{P_\mathrm{ref}}\right) . \tag{2.61}$$

The Bramwell-Hill equation (Eq. 2.57) states that, at any BP level, c can be determined as a function of the slope of the P-D^2 relationship. Therefore, for any c metrics (i.e., determined using any local method) there must exist a pressure level P_c and corresponding diameter D_c that satisfies Eq. 2.57. Eq. 2.57 can then be rewritten as

$$c = D_c \sqrt{\frac{\mathrm{d}P}{\rho\ \mathrm{d}(D^2)}\Big|_{P_c}} . \tag{2.62}$$

Inverting Eq. 2.59 to express the diameter as a function of pressure leads to

$$D_c = D_\mathrm{d} \sqrt{1 + \frac{\ln\left(\frac{P_c}{\mathrm{DBP}}\right)}{\gamma}} . \tag{2.63}$$

Using Eq. 2.59, the derivative term of Eq. 2.62 can be rearranged as follows:

$$\frac{\mathrm{d}P}{\mathrm{d}D^2} = \frac{\mathrm{d}}{\mathrm{d}D^2}\left[\mathrm{DBP} e^{\gamma\left(\frac{D^2}{D_\mathrm{d}^2}-1\right)}\right] = \frac{\gamma\ \mathrm{DBP}}{D_\mathrm{d}^2} e^{\gamma\left(\frac{D^2}{D_\mathrm{d}^2}-1\right)} , \tag{2.64}$$

so that

$$\frac{\mathrm{d}P}{\mathrm{d}D^2}\Big|_{P_c} = \frac{\gamma\ \mathrm{DBP}}{D_\mathrm{d}^2} e^{\gamma\left(\frac{D_c^2}{D_\mathrm{d}^2}-1\right)} , \tag{2.65}$$

and substituting D_c with the relationship in Eq. 2.63, the derivative term is manipulated further into:

$$\frac{\mathrm{d}P}{\mathrm{d}D^2}\Big|_{P_c} = \frac{\gamma\ \mathrm{DBP}}{D_\mathrm{d}^2} e^{\gamma\left[\frac{\ln\left(\frac{P_c}{\mathrm{DBP}}\right)}{\gamma}\right]} = \frac{\gamma\ \mathrm{DBP}}{D_\mathrm{d}^2} e^{\ln\left(\frac{P_c}{\mathrm{DBP}}\right)} = \frac{\gamma\ P_c}{D_\mathrm{d}^2}\ . \tag{2.66}$$

Substituting Eq. 2.66 into Eq. 2.62 leads to the relationship between γ and c:

$$c^2 = \frac{D_c^2\ \gamma\ P_c}{D_\mathrm{d}^2\ \rho}\ , \tag{2.67}$$

and then substituting Eq. 2.63 into Eq. 2.67, leads to

$$\gamma = \frac{\rho\ c^2}{P_c} - \ln\left(\frac{P_c}{\mathrm{DBP}}\right)\ . \tag{2.68}$$

Eq. 2.68 indicates that γ can be estimated from c if the corresponding pressure level P_c is known and using a reasonable value of blood density ρ. However, P_c is, per se, unknown and depends on the method used to estimate the wave speed.

Given the assumptions behind the PU-loop (Parker et al., 1988) and the lnDU-loop methods (Feng & Khir, 2010), that estimate c from a linear regression of the pressure-velocity and diameter-velocity loop in early systole, and the D^2P-loop method (Alastruey, 2011), that estimates the wave speed from linear regression of the pressure-area relationship late diastole, it may be reasonable to assume that, for these methods, P_c is close to DBP. If the assumptions were to be verified, then Eq. 2.68 would be simplified to

$$c^2 = \frac{\gamma\ \mathrm{DBP}}{\rho} \qquad \text{and} \qquad \gamma = \frac{c^2\ \rho}{\mathrm{DBP}}\ . \tag{2.69}$$

If the diastolic pressure is assumed to be approximately constant along the arterial tree (Nichols et al., 2005), Eq. 2.69 allows estimating γ from c and a brachial/femoral measurement of diastolic pressure.

Non-invasive estimation of arterial pressure

Among the loop methods for the estimation of c, the lnDU-loop and QA-loop techniques present the advantage of being non-invasive as they require the acquisition of arterial D and U/Q, both achievable though MRI or ultrasound imaging. Therefore, the first major implication of the new proposed formulation is that γ can be determined non-invasively if P_c is known for the lnDU-loop or QA-loop methods. As a result, under the assumption that DBP is approximately the same throughout the arterial tree and, hence, can be measured using brachial/femoral cuffs, Eq. 2.58 can be used to convert the D waveform into P.

Pressure-normalisation of c

Using Eq. 2.61, Eq. 2.68 can be expressed in terms of the pressure-normalised exponential coefficient γ_0, leading to

$$\gamma_0 = \frac{\rho\, c^2}{P_c} - \ln\left(\frac{P_c}{P_{\text{ref}}}\right), \quad \text{and} \tag{2.70}$$

$$c^2 = \frac{\left[\gamma_0 + \ln\left(\frac{\text{DBP}}{P_{\text{ref}}}\right)\right] P_c}{\rho} + \frac{P_c}{\rho}\ln\left(\frac{P_c}{\text{DBP}}\right). \tag{2.71}$$

Let us consider now two different BP levels: the *in vivo* patient-specific SBP-DBP pressure interval and a target pressure interval SBP_T-DBP_T to which we want to convert an estimate of c. For the target pressure interval, there will be a c_T that given P_{c_T} satisfies Eq. 2.71.

$$c_\text{T}^2 = \frac{\left[\gamma_0 + \ln\left(\frac{\text{DBP}_\text{T}}{P_{\text{ref}}}\right)\right] P_{c_\text{T}}}{\rho} + \frac{P_{c_\text{T}}}{\rho}\ln\left(\frac{P_{c_\text{T}}}{\text{DBP}_\text{T}}\right). \tag{2.72}$$

Note that both γ_0 and P_{ref} are independent from the chosen pressure interval. Substituting γ_0 in Eq. 2.72 with the expression in Eq. 2.70, leads to

$$c_\text{T} = \sqrt{c^2\frac{P_{c_\text{T}}}{P_c} + \frac{P_{c_\text{T}}}{\rho}\ln\frac{P_{c_\text{T}}}{P_c}}, \tag{2.73}$$

where c indicates the wave speed in the patient-specific SBP-DBP pressure interval and c_T is the wave speed in the target pressure interval SBP_T-DBP_T. Eq. 2.73 allows converting c to a desired BP level if P_c for the method used for the estimation c is known. If the same target pressure interval is chosen for a cohort of subjects, c_T becomes a pressure-normalised wave speed metric. It is worth considering that since c and c_T are calculated using the same method, P_{c_T} and P_c correspond to the same pressure level in the systolic-diastolic pressure interval (i.e., if P_c is the DBP in the measured systolic-diastolic pressure interval, similarly, P_{c_T} is the DBP_T in the target systolic-diastolic pressure interval).

CHAPTER 3

The mechanical behaviour of the pig and lamb tri-layered aortic wall *ex vivo*

Part of this Chapter was published in:

Giudici, A., Khir, A.W., Szafron, J.M. & Spronck, B. (2021). From uniaxial testing of isolated layers to a tri-layered arterial wall: A novel constitutive modelling framework. *Annals of Biomedical Engineering* (accepted).

3.1 Introduction

As illustrated in Chapter 1.2, the arterial wall is a highly complex tri-layered structure whose mechanical properties are highly influenced by the structural arrangement of its constituents. Elastin and collagen are commonly considered the major determinants of the passive mechanical response of arteries, as smooth muscle cells have a relatively low passive stiffness (Burton, 1954; Cox, 1978; Wolinsky & Glagov, 1964). As reported in several studies, the relative amount, as well as the spatial organisation, of elastin and collagen fibres vary significantly across the arterial wall thickness (Krasny et al., 2017b; O'Connell et al., 2008; Timmins et al., 2010), conferring different mechanical properties and function to intima, media and adventitia.

The mechanical testing of isolated arterial layers is a technique used for investigating the impact of the different layer microstructures on arterial mechanics. This method has been used in several locations along the arterial tree as well as in different species, including the human (Weisbecker et al., 2012) and swine (Peña et al., 2015) thoracic aorta, aneurysmal human ascending aorta (Sassani et al., 2015; Deveja et al., 2018), human carotid arteries (Sommer et al., 2010), and human coronary arteries (Holzapfel et al., 2005; Hollander et al., 2011a,b). By fitting structurally motivated hyperelastic SEF (i.e. constitutive models whose parameters reflect the behaviour of the components of the arterial wall) on the experimental data, such studies (Sassani et al., 2015; Peña et al., 2017; Weisbecker et al., 2012; Holzapfel et al., 2005) have shown how the different microstructural features of the three layers strongly affect their mechanical properties, including the degree of anisotropy and the rate of recruitment of collagen fibres.

While characterising the mechanical response of isolated layers is of scientific interest, understanding the individual layers' respective roles in the overall mechanical behaviour of the arterial wall is required to further the understanding of (patho)physiology. As described in Section 1.2.2, an unloaded artery is obviously subjected to null average stresses in all three principal directions (i.e., circumferential, axial and radial), but local stresses at any generic point within the arterial wall volume are, in general, non-zero due to the presence of residual deformations (Holzapfel & Ogden, 2010b; Chuong & Fung, 1986). Therefore, the mechanical behaviour of the isolated layers does not necessarily match their response when part of the wall as these might be subjected pre-compression or pre-extension in all three principal directions. The implementation of multi-layered models of the arterial wall is, hence, necessary to fully comprehend the complex tri-layered behaviour of the arterial wall.

The standard approach to multi-layer modelling consists in formulating complex SEFs that account for the contribution of each wall constituent (e.g., collagen, elastin, and VSMCs) in each

modelled arterial layer and fitting their parameters to the experimental whole-wall mechanical behaviour (Polzer et al., 2015; Wang et al., 2016). However, the number of constitutive parameters increases with the complexity of the model, increasing the risk of overfitting. More fundamentally, a stress split between the individual layers cannot be inferred from whole-wall mechanical testing without additional structural information and assumptions (Bellini et al., 2014).

Histological images of the wall cross-section are often used to infer structural features of the wall constituents and constrain model parameters. For example, Polzer et al. (2015) implemented a two-layered model of the arterial wall with an isotropic neo-Hookean SEF in the media reinforced by medial and adventitial collagen fibres with anisotropic SEFs. The collagen fibre orientation was inferred from histological images, and the probability functions describing the collagen recruitment were postulated from the literature and qualitative observation of collagen waviness across the wall thickness. Fata et al. (2012, 2014) chose anisotropic SEFs for modelling both collagen and elastin and used multi-photon fluorescence of the ovine pulmonary artery wall tissue subjected to biaxial testing to determine collagen and elastin orientation distributions. Moreover, the waviness of the adventitial collagen was used to define a probabilistic recruitment function describing its delayed response. Wang et al. (2016) and Chow et al. (2014) extended this approach to multi-layer modelling, including contribution of medial elastin and medial and adventitial collagen fibres. Further, Rego & Sacks (2017) combined layer-specific biaxial mechanical testing and tissue imaging (Stella & Sacks, 2007), allowing the quantification of the transmural variation of constituent volumetric fractions and of the fibre orientation distribution function, to develop a multi-layered model of the aortic valve leaflet.

While these studies represent comprehensive approaches to multi-layer modelling, they also present technical and practical limitations; first, the need for detailed microstructural information from complex and expensive imaging techniques (e.g. multiphoton microscopy) makes wide adoption of these methods infeasible and limits the scope of available data. It is also worth noting that the opacity of the arterial wall tissue limits the penetration depth of most microscopy techniques, so that, in human-like arteries, only superficial regions ($\sim$100 μm) of the samples can be imaged (Krasny et al., 2017b; Chow et al., 2014). Second, these models are typically applied to planar biaxial tensile mechanical data (Chow et al., 2014; Polzer et al., 2015; Rego & Sacks, 2017). Indeed, tension-inflation tests, that more closely mimic the physiological loading condition arteries are subjected to *in vivo*, require specialised apparatus, whose size is compatible with microscopy imaging only when designed to test arteries of small calibre (i.e., human coronary arteries or small animal models) (Krasny et al., 2017b; Chen et al., 2011, 2013). Conversely, biaxial testing requires subjecting the wall to artificial deformations to flatten its

natural arch-shape, so that the ability of these models to predict the behaviour of the arterial wall *in vivo* is limited. Furthermore, biaxial testing requires specialised equipment that is not available in several biomechanics laboratories.

Holzapfel & Ogden (2010b) proposed a different approach to multi-layer modelling; using empirical observation of the layer-specific stress-free configuration, they introduced a tri-layered thick-walled model of the arterial wall accounting for the three-dimensional layer-specific residual deformations. Therefore, in contrast with the approaches presented above, this method allowed for the first time to use the mechanical data obtained from direct mechanical testing of isolated layers to estimate the behaviour of the tri-layered wall. As described in Section 1.2.2, the stress-free configuration of arteries (and layers) has been typically quantified via the OA which defines the idealised arch-shaped configuration an arterial ring assumes after being cut radially (Chuong & Fung, 1986). Holzapfel & Ogden (2010b) extended the characterisation of the stress-free configuration also to the axial direction, by quantifying the curvature layers isolated from axially oriented wall strips assumed when left to equilibrate in saline solution. This allowed achieving a more complete characterisation of the layer-specific residual deformations. However, the full implementation of this model is non-trivial, requiring the idealisation of complex layer-specific three-dimensional stress-free configurations, and its use has been, so far, limited (Zheng & Ren, 2016).

The aim of this study was to develop a testing/modelling framework that integrates layer-specific uniaxial testing data into a tri-layered model of the arterial wall, thereby enabling study of layer-specific mechanics under realistic (patho)physiological conditions using simple, widely available and inexpensive experimental techniques. In contrast with previous works (Holzapfel & Ogden, 2010a; Zheng & Ren, 2016), the arterial wall was assumed to comprise three thin-walled concentric layers, thus simplifying the definition of residual deformations to average values across the layer thickness which were inferred directly from the mechanical data rather than from the complex geometry of the stress-free configuration. The proposed method was used to study the regional differences in the tri-layered behaviour of the pig and lamb aorta.

3.2 Methods

3.2.1 Experimental methods

Arterial samples

N=18 ovine and swine plucks (i.e. the content of the thorax) (age 6-12 months, sex unknown) were purchased from a local abattoir (Samples for school, UK). Animal organs were delivered

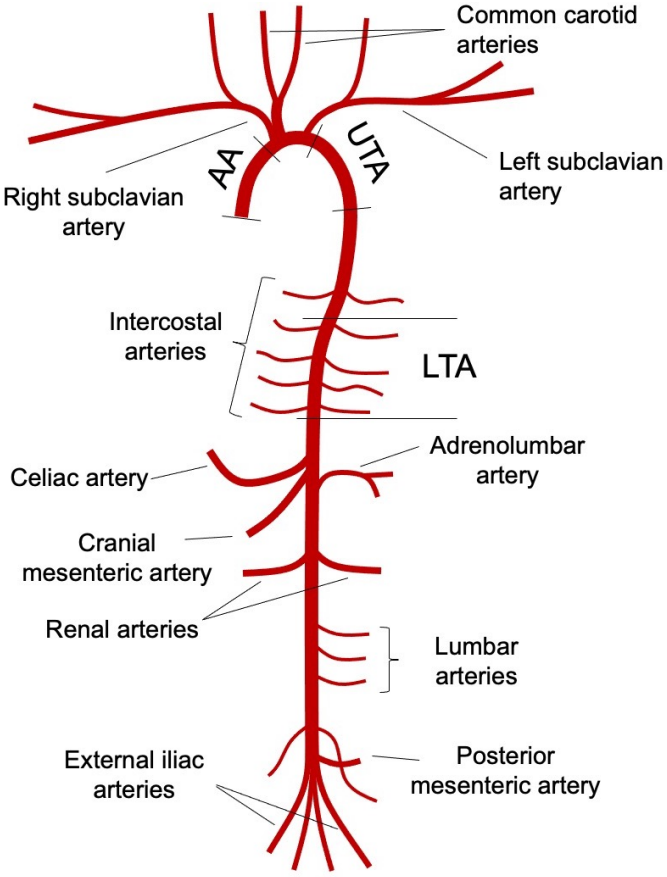

Figure 3.1: *Schematic representation of the arterial tree. The three aortic regions tested in this study are indicated as AA = ascending aorta, UTA = upper thoracic aorta, and LTA = lower thoracic aorta.*

frozen and immediately stored at −20°C in a laboratory freezer. The pluck was left to thaw at room temperature for approximately four hours and then the aorta was carefully dissected from the rest of the organs using a scalpel. Three aortic regions were isolated for testing: 1) the ascending aorta (AA), between the heart and the first bifurcation in the aortic arch, 2) the upper thoracic aorta (UTA), the first segment of descending thoracic aorta after the left subclavian artery, and 3) the lower thoracic aorta (LTA), at the level of the intercostal arteries (Figure 3.1). Each isolated region was then refrozen until the day of testing.

For each aortic region, at least two circumferentially and two longitudinally oriented ∼5 mm wide and ∼25 cm long strips were cut using a scalpel. Undeformed width (w_0) and thickness (h_0) were measured three times along the strip length using a high precision digital calliper. For each region, two strips were uniaxially tested in the circumferential and longitudinal directions. After testing, each strip was carefully peeled into its three anatomical layers (intima, media and adventitia) using tweezers (Peña et al., 2015; Weisbecker et al., 2012) and each layer was uniaxially tested separately. In case the peeling process resulted in the rupture of the layer, when available, said layer was obtained from an adjacent arterial strip.

Opening angle and layer-specific prestretches

The opening angle experiments were performed on N=8 swine and ovine plucks. To evaluate

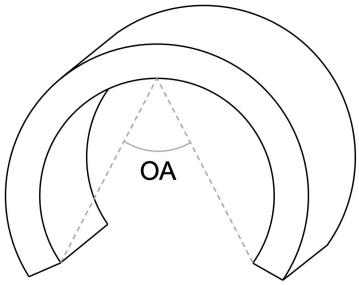

Figure 3.2: *Schematic representation of cut-open configuration of a circumferential strip of arterial wall and definition of the opening angle (OA).*

the layer-specific residual deformations, two parameters were assessed: first, the intact wall strip length and the layers length after peeling were measured using a digital calliper. The measurements were performed on both circumferentially and axially oriented strips. The ratio wall-to-layer length provided an experimental measure of the circumferential ($\hat{\lambda}_x^k$) and axial ($\hat{\lambda}_z^k$) prestretches layers are subjected to when part of a flat wall sample. Note that this corresponds to the configuration of the wall at the beginning of an planar uniaxial or biaxial tensile test.

Second, the wall and layer-specific OAs were measured on circumferentially oriented strips only. Arterial rings were placed in Petri dishes filled with saline solution (NaCl 0.9%) kept at the constant body temperature of 37°C. Then, a single radial cut was performed to release the ring residual stresses. Cut-open rings were let to equilibrate for 30 minutes in saline solution at 37°C (Holzapfel et al., 2002; Sokolis, 2019) and then photographed from the top (cross-sectional view) using a Nikon 5600D equipped with a Sigma 18-200 mm zoom lens. After the layers separation, individual layers were also let to equilibrate for 30 minutes in saline solution at 37°C before shooting photographs in the cross-sectional view. Finally, the OA was measured as the angle formed by connecting the two open ends of the arch-shaped cut-open ring to its midpoint (Figure 3.2) using the images processing software ImageJ.

Mechanical testing

The mechanical testing experiments were performed on N=10 swine and ovine plucks. Wall and layers circumferential and axial strips were tested following the same protocol. The strip was mounted on the uniaxial tensile device (MFS Stage equipped with 20N load cell, Linkam Scientific Ltd., UK), blocking its ends by means of serrated jaws. The initial inter-jaw distance was set to 15 mm to ensure an initial aspect ratio (inter-jaw distance/sample width) above 2 which has been shown to minimise the local distortions in uniaxial tests (Duprey et al., 2010). This distance was then adjusted until the sample had assumed a flat configuration (this required an initial force below 0.020N), and the final inter-jaw distance was set to be the unloaded sample length $\mathscr{L}_0$. Samples were cyclically tested to a peak Cauchy stress value of 250 kPa, and the loading part of the sixth cycle was used for the analysis. Preliminary testing indicated that five preconditioning cycles were sufficient to obtain a repeatable force-elongation curve.

In a uniaxial tensile test, for any sample k (with $k = \{\text{wall,i,m,a}\}$ and i=intima, m=media, and a=adventitia), the stretch $\overline{\lambda}_i^k$ in the loading direction i can be easily calculated as

$$\overline{\lambda}_i^k = \frac{\mathscr{L}}{\mathscr{L}_0} \ , \tag{3.1}$$

where $\mathscr{L}$ is the deformed inter-jaw distance and $i = \{\mathbb{X}, \mathbb{Z}\}$, with $\mathbb{X}$ and $\mathbb{Z}$ indicating the circumferential and axial direction of the sample. The linearised strain ϵ_i^k is defined as

$$\epsilon_i^k = \overline{\lambda}_i^k - 1 \ . \tag{3.2}$$

On the contrary, the other in-plane (i.e., circumferential and axial for axial and circumferential tensile tests, respectively) and the out of plane (radial) stretches and strains are, generally, unknown. However, since the arterial wall is assumed to be incompressible (Chuong & Fung, 1984; Carew et al., 1968), the sample volume throughout the uniaxial tensile test must be preserved. This leads to

$$V_0 = A_0 \mathscr{L}_0 = A \mathscr{L} = V \ , \tag{3.3}$$

where V and V_0 are the deformed and undeformed sample volumes, respectively, and A and A_0 are its deformed and undeformed cross-sectional areas. Substituting Eq. 3.1 loads to

$$A = \frac{A_0}{\overline{\lambda}_i^k} \ , \tag{3.4}$$

where $\overline{\lambda}_i^k$ is the stretch in the loading direction i. Hence, the experimental Cauchy stress for any sample k was calculated as:

$$t_{ii_{\text{exp}}}^k = \frac{F}{A} = \frac{F}{A_0} \overline{\lambda}_i^k \ . \tag{3.5}$$

Note that F/A_0 is the first Piola-Kirchhoff (or engineering) stress, so that Eq. 3.5 coincides with Eq. 2.13. All the other components of the Cauchy stress tensor $\mathbf{t}_{\text{exp}}$ are equal to 0.

3.2.2 Layer-specific constitutive modelling

The mechanical behaviour of the individual layers was modelled using the HGO-SEF, whose complete formulation has been detailed in Section 2.2.4. Briefly, the passive mechanical response of each layer is assumed to be determined by the contribution of an isotropic matrix (typically associated with elastin), exhibiting a linear elastic behaviour, reinforced by two families of fibres (collagen) that are simmetrically oriented with respect to the vessel circumferential direction and whose behaviour is, generally, nonlinear. Previous study have shown that, although the intimal microstructure and composition considerably differs from that of the other layers (See Section 1.2.1), the HGO-SEF is able to accurately predict the mechanical behaviour of all three layers (Weisbecker et al., 2012; Peña et al., 2017).

The definition of constitutive models capable of capturing the layers' behaviour represents a crucial building-block for the development of the tri-layered model of the arterial wall, as these will be used to predict the layers' behaviour when subjected to the simulated *in vivo* deformations. Furthermore, although the aim of this study consists in developing a tri-layered model of the arterial wall, the same single-layer modelling approach was also applied to the arterial wall as a whole to provide a means of comparison for the accuracy of tri-layered model.

3.2.3 Tri-layered wall model

The wall is considered as constituted of three adequately spaced membranes corresponding to the three arterial layers. The wall composition process, from the isolated layer to a pressurised cylindrical vessel, requires three mapping steps as represented in Figure 3.3.

First, considering a flat rectangular slab of arterial wall tissue, each layer can be in a compressed or stretched state in both circumferential and axial directions. Therefore, when isolated from the wall, the layer deforms to release such prestresses, leading to a layer-specific deformation gradient $\mathbf{G}^k$ (where $k = \{\text{i,m,a}\}$, where i=intima, m=media, and a=adventitia) mapping the deformation from κ_{isolated} to $\kappa_{\text{composite}}$. It is assumed that the layer separation induces negligible shear deformations and, hence, the only non-zero components of $\mathbf{G}^k$ are those

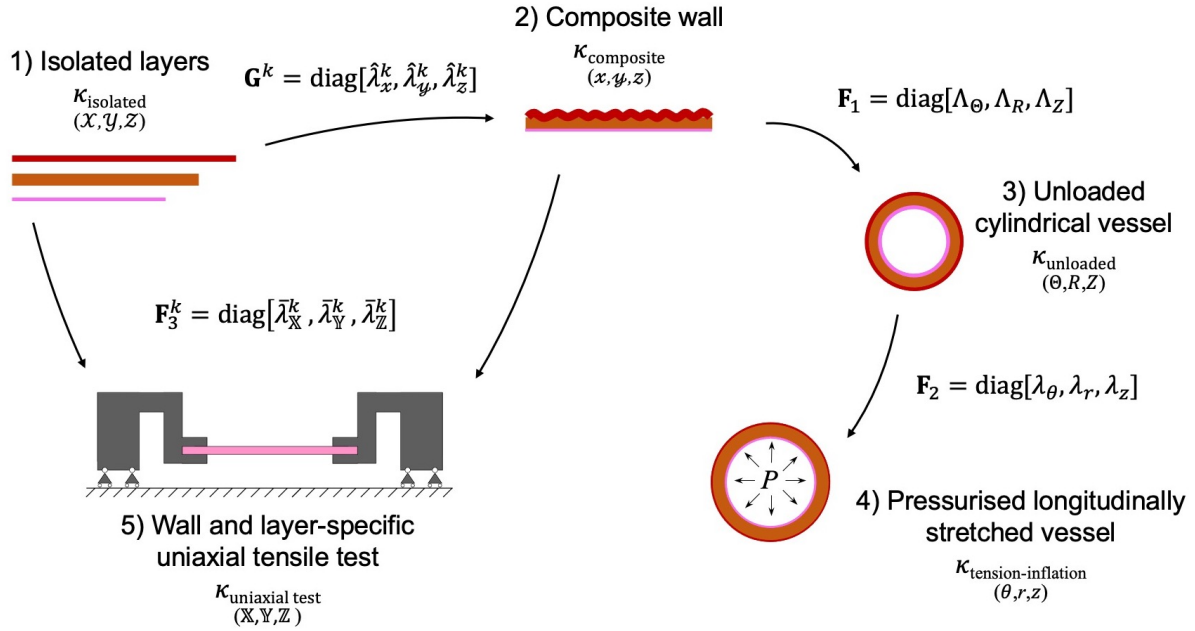

Figure 3.3: *Schematic representation of the mapping flow linking the different configurations analysed in this study: 1) isolated layers* (κ_{isolated})*, 2) composite wall* ($\kappa_{\text{composite}}$)*, 3) unloaded cylindrical vessel* (κ_{unloaded})*, 4) pressurised longitudinally stretched cylindrical vessel* ($\kappa_{\text{tension-inflation}}$)*, and 5) uniaxial testing* (κ_{uniaxial}).

in the three principal directions (circumferential, axial and radial). Using Cartesian coordinates $(\mathcal{X}, \mathcal{Y}, \mathcal{Z})$ and (x, y, z) for κ_{isolated} and $\kappa_{\text{composite}}$, the mapping between the isolated layers and the composite wall configuration is given by

$$\mathbf{G}^k = \text{diag}\left[\frac{\partial x}{\partial \mathcal{X}}, \frac{\partial y}{\partial \mathcal{Y}}, \frac{\partial z}{\partial \mathcal{Z}}\right] . \tag{3.6}$$

For each layer k, $\mathbf{G}^k$ translates into

$$\mathbf{G}^k = \text{diag}\left[\frac{l_x}{L^k_{\mathcal{X}}}, \frac{L^k_{\mathcal{X}} L^k_{\mathcal{Z}}}{l_x l_z}, \frac{l_z}{L^k_{\mathcal{Z}}}\right] = \text{diag}\left[\hat{\lambda}^k_x, \frac{1}{\hat{\lambda}^k_x \hat{\lambda}^k_z}, \hat{\lambda}^k_z\right] , \tag{3.7}$$

where $L^k_{\mathcal{X}}$ and $L^k_{\mathcal{Z}}$ are the circumferential and axial length of isolated layer k, l_x and l_z are the circumferential and axial length of the composite wall, $\hat{\lambda}^k_x = l_x / L^k_{\mathcal{X}}$ and $\hat{\lambda}^k_z = l_z / L^k_{\mathcal{Z}}$ are the stretches in the circumferential and axial direction, and the radial component is determined from incompressibility. While no study directly investigated the (in)compressibility of isolated layers, the arterial wall is commonly considered nearly incompressible (Chuong & Fung, 1984; Carew et al., 1968). Therefore, the hypothetical compressible properties of the three layers would need to compensate one another to guarantee the incompressibility of the wall. As this eventuality is unlikely, in agreement with previous studies (Weisbecker et al., 2012; Peña et al., 2017; Díaz et al., 2021), the incompressibility assumption is extended to the individual layers. Note, due to the thin-wall approached chosen herein, $\mathbf{G}^k$ is homogeneous through the thickness of each layer.

The second deformation gradient $\mathbf{F}_1$ maps the flat composite wall ($\kappa_{\text{composite}}$) into a (closed) cylindrical vessel (κ_{unloaded}) (Figure 3.4). It is assumed that, in the axial direction, the entire wall is subjected to the same level of stretch $\Lambda_Z = L_Z / l_z$. The circumferential stretch can be determined by enforcing conservation of volume:

$$V_{\kappa_{\text{unloaded}}}(R) = \pi \left(R^2 - R^2_{\text{internal}}\right) L_Z = l_x l_z y = V_{\kappa_{\text{composite}}}(y) . \tag{3.8}$$

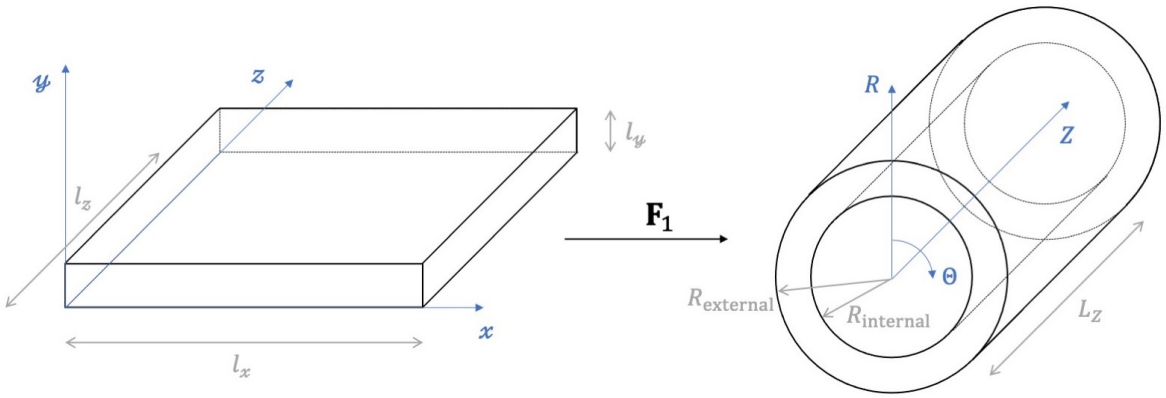

Figure 3.4: *Schematic representation of the mapping between the flat wall sample and the cylindrical vessel. Both configurations are assumed to be uniform in thickness, and the deformation in the $z - Z$ direction is assumed to be uniform across the wall thickness.*

Expressing R as a function of the flat wall geometry and Λ_Z

$$R = \sqrt{R_{\text{internal}}^2 + \frac{l_x \mathcal{V}}{\pi \Lambda_Z}} \ , \tag{3.9}$$

the circumferential stretch becomes

$$\Lambda_\Theta = \frac{2\pi R}{l_x} = \sqrt{\frac{4\pi^2 R_{\text{internal}}^2}{l_x^2} + \frac{4\pi \mathcal{V}}{l_x \Lambda_Z}} \ . \tag{3.10}$$

The deformation gradient $\mathbf{F}_1$ is therefore defined as

$$\mathbf{F}_1 = \text{diag}\left[\Lambda_\Theta, \frac{1}{\Lambda_\Theta \Lambda_Z}, \Lambda_Z\right] \ . \tag{3.11}$$

The third deformation gradient $\mathbf{F}_2$ maps the tension-inflation of the vessel to its in vivo configuration ($\kappa_{\text{tension-inflation}}$) (Figure 3.4). The general form of $\mathbf{F}_2$ is

$$\mathbf{F}_2 = \text{diag}\left[\frac{r\partial\theta}{R\partial\Theta}, \frac{\partial r}{\partial R}, \frac{\partial z}{\partial Z}\right] \ . \tag{3.12}$$

Once more, the axial deformation for this motion, $\lambda_z = l_z/l_Z$, is assumed to be constant throughout the wall thickness, and the circumferential deformation can be inferred from conservation of volume:

$$V_{\kappa_{\text{tension-inflation}}}(r) = \pi(r^2 - r_{\text{internal}}^2) l_z = \pi(R^2 - R_{\text{internal}}^2) L_Z = V_{\kappa_{\text{unloaded}}}(R) \ , \tag{3.13}$$

$$\lambda_\theta = \frac{r}{R} = \sqrt{\left(\frac{r_{\text{internal}}}{R}\right)^2 + \frac{R^2 - R_{\text{internal}}^2}{R^2 \lambda_z}} \ . \tag{3.14}$$

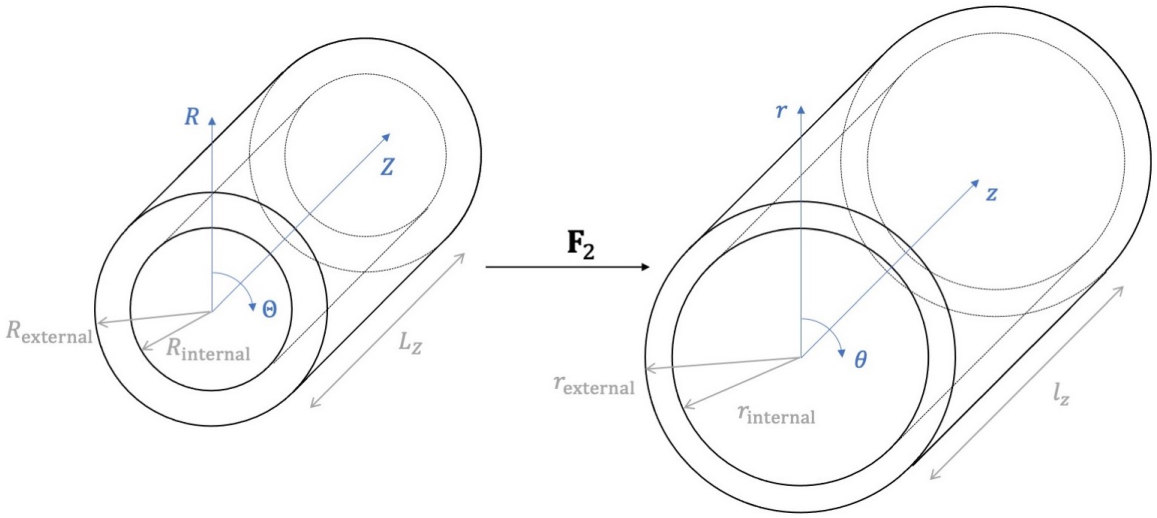

Figure 3.5: *Schematic representation of the mapping between the unloaded cylindrical vessel and the pressurised longitudinally stretched vessel. Both configurations are assumed to be uniform in thickness, and the deformation in the $Z - z$ direction is assumed to be uniform across the wall thickness.*

Therefore, $\mathbf{F}_2$ can be reformulated as

$$\mathbf{F}_2 = \text{diag}\left[\lambda_\theta, \frac{1}{\lambda_\theta \lambda_z}, \lambda_z\right] \ . \tag{3.15}$$

The total deformation from κ_{isolated} to $\kappa_{\text{tension-inflation}}$ for a layer k is given by

$$\mathbf{F}^k_{\text{total}} = \mathbf{F}_2\mathbf{F}_1\mathbf{G}^k = \text{diag}\left[\lambda_\theta \Lambda_\Theta \hat{\lambda}^k_x, \frac{1}{\lambda_\theta \Lambda_\Theta \hat{\lambda}^k_x \lambda_z \Lambda_Z \hat{\lambda}^k_z}, \lambda_z \Lambda_Z \hat{\lambda}^k_z\right] \ . \tag{3.16}$$

Finally, an additional layer and wall-specific deformation gradient maps the deformation from κ_{isolated} to $\kappa_{\text{uniaxial test}}$ and from $\kappa_{\text{composite}}$ to $\kappa_{\text{uniaxial test}}$ during the uniaxial test, respectively.

$$\mathbf{F}^k_3 = \text{diag}\left[\overline{\lambda}^k_{\mathbb{X}}, \frac{1}{\overline{\lambda}^k_{\mathbb{X}} \overline{\lambda}^k_{\mathbb{Z}}}, \overline{\lambda}^k_{\mathbb{Z}}\right] \ , \tag{3.17}$$

where $k = \{\text{wall,i,m, a}\}$, $\overline{\lambda}^k_i$ with $i = \mathbb{X}, \mathbb{Z}$ is the stretch.

3.2.4 Parameter estimation

Figure 3.6 presents the diagram of the methods used for the fitting of the model parameters. First, the layer-specific constitutive parameters of HGO-SEF were fitted to minimise the error between the measured (Eq. 3.5) and estimated stress in the loading direction for both the $\mathbb{X}$ and $\mathbb{Z}$ uniaxial test simultaneously (cost function Π). To give the same weight to the stress-stretch relationships resulting from the uniaxial test in the $\mathbb{X}$ and $\mathbb{Z}$ directions, each stress-stretch relationship was resampled at 50 equally-spaced increments between $\overline{\lambda}^k_i = 1$ and the maximum stretch (i.e., the stretch at ∼250 kPa).

$$\Pi = \sum_{i=1}^{50} \left(t_{\mathbb{X}\mathbb{X}_{\text{exp}}} - t_{\mathbb{X}\mathbb{X}}\right)^2 + \sum_{i=1}^{50} \left(t_{\mathbb{Z}\mathbb{Z}_{\text{exp}}} - t_{\mathbb{Z}\mathbb{Z}}\right)^2 \ . \tag{3.18}$$

From Eqs. 2.26-2.29 and Eq. 2.31, the modelled Cauchy stresses in the $\mathbb{X}$ and $\mathbb{Z}$ directions are

$$\begin{aligned} t^k_{\mathbb{X}\mathbb{X}} = {} & 2\mu^k \left[\left(\overline{\lambda}^k_{\mathbb{X}}\right)^2 - \frac{1}{\left(\overline{\lambda}^k_{\mathbb{X}} \overline{\lambda}^k_{\mathbb{Z}}\right)^2}\right] + \\ & + 4k^k_1 \left\{\tau^k \left[\left(\overline{\lambda}^k_{\mathbb{X}}\right)^2 - \frac{1}{\left(\overline{\lambda}^k_{\mathbb{X}} \overline{\lambda}^k_{\mathbb{Z}}\right)^2}\right] + (1 - 3\tau^k)\left(\overline{\lambda}^k_{\mathbb{X}}\right)^2 \cos\left(\alpha^k\right)^2\right\} \cdot \\ & \cdot \left[\tau^k I_1 + (1 - 3\tau^k) I_4 - 1\right] e^{k^k_2 \left[\tau^k I_1 + (1-3\tau^k) I_4 - 1\right]} \ , \end{aligned} \tag{3.19}$$

$$\begin{aligned} t^k_{\mathbb{Z}\mathbb{Z}} = {} & 2\mu^k \left[\left(\overline{\lambda}^k_{\mathbb{Z}}\right)^2 - \left(\frac{1}{\overline{\lambda}^k_{\mathbb{X}} \overline{\lambda}^k_{\mathbb{Z}}}\right)^2\right] + \\ & + 4k^k_1 \left\{\tau^k \left[\left(\overline{\lambda}^k_{\mathbb{Z}}\right)^2 - \left(\frac{1}{\overline{\lambda}^k_{\mathbb{X}} \overline{\lambda}^k_{\mathbb{Z}}}\right)^2\right] + (1 - 3\tau^k)\left(\overline{\lambda}^k_{\mathbb{Z}}\right)^2 \sin\left(\alpha^k\right)^2\right\} \cdot \\ & \cdot \left[\tau^k I_1 + (1 - 3\tau^k) I_4 - 1\right] e^{k^k_2 \left[\tau^k I_1 + (1-3\tau^k) I_4 - 1\right]} \ . \end{aligned} \tag{3.20}$$

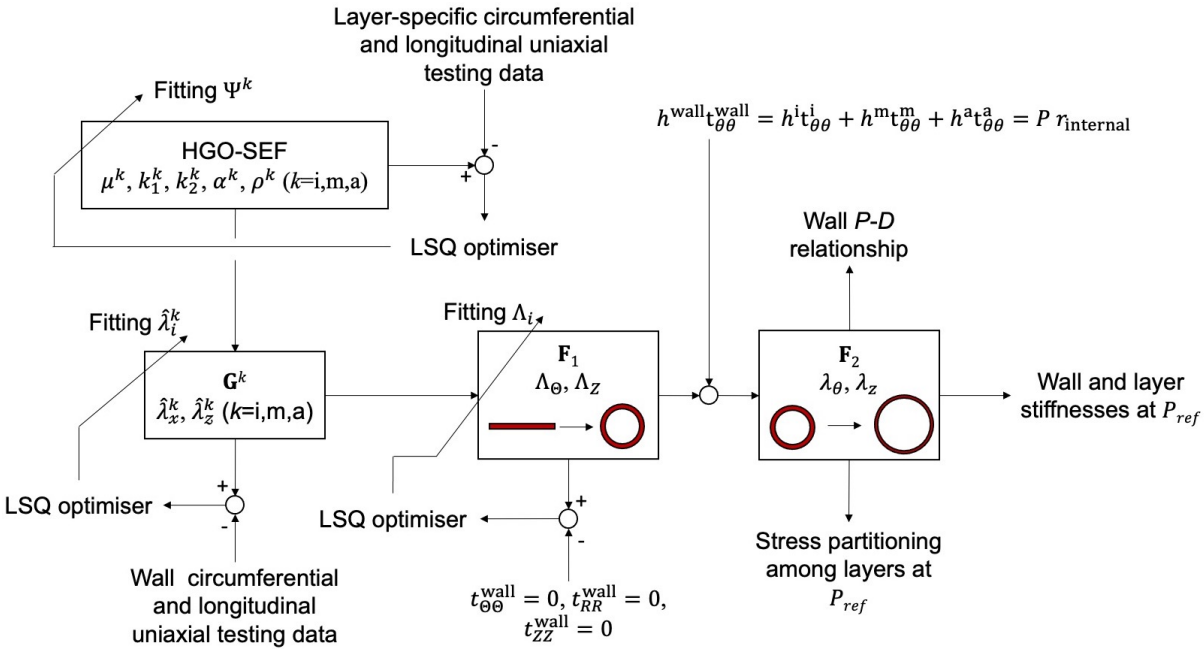

Figure 3.6: *Schematic representation of the workflow used for the parameters estimation for the tri-layered model of the arterial wall, starting to the determination of the layer-specific parameter in the HGO-SEF and then moving to the wall parameters.*

where μ^k, k_1^k, k_2^k, α^k, and τ^k are the layer-specific HGO-SEF model parameters. As mentioned above, in a uniaxial tensile test, the only non-zero component of the Cauchy stress tensor is that corresponding to the loading direction $\overline{\lambda}_i^k$. $\overline{\lambda}_j^k$ is determined by imposing the off-axis stress $t_{jj}^k = 0$ and enforcing incompressibility.

The deformation tensors $\mathbf{G}^k$, $k = \{\text{i,m,a}\}$ requires the estimation of a total of six stretches $\hat{\lambda}$ (three layers times two stretches) defining the axial and circumferential prestretches that each layer is subjected to when part of the wall. $\hat{\lambda}$ was estimated by minimising the error between the experimental and modelled wall stresses in the circumferential and axial direction simultaneously (i.e., minimising the cost function Π). The average Cauchy stress of the composite wall ($\kappa_{\text{composite}}$) was calculated as

$$\mathbf{t}^{\text{wall}} = \frac{h^{\text{i}}\mathbf{t}^{\text{i}} + h^{\text{m}}\mathbf{t}^{\text{m}} + h^{\text{a}}\mathbf{t}^{\text{a}}}{h^{\text{wall}}}\,, \tag{3.21}$$

with layer wall thicknesses h^k determined using the layer thickness in κ_{isolated} and enforcing incompressibility. Additionally, the search for the six $\hat{\lambda}$ was constrained to ranges measured experimentally on the separate cohort of arterial samples used for the estimation of residual deformations (See Section 3.2.1). Mounting the samples on the uniaxial tensiometer requires setting its unloaded length. Since the components of $\mathbf{G}^k$ were fitted on the basis of the mechanical data, the modelled $\hat{\lambda}_i^k$ refers to the ratio between the lengths of the wall and the layer at the

beginning of the uniaxial test and might not correspond exactly to that measured experimentally due to the possible under- or over-estimation of the sample's unloaded length. For this reason, the constrains were set to mean ± 3 standard deviations of the experimental values (Table 3.1).

$\mathbf{F}_1$ maps the deformation of a generic point in the $\kappa_{\text{composite}}$ configuration to the κ_{unloaded} configuration. However, in a thin-walled modelling framework, each layer is considered to be a membrane located at the midpoint of the layer thickness. This introduces a complication as the midpoint through the layer thickness in κ_{unloaded} does not match the midpoint through the layer thickness in $\kappa_{\text{composite}}$. It can be shown that the y coordinate providing the layer-specific Λ_Θ corresponding to the mid-wall point depends on deformed configuration itself, and, therefore, Λ_Θ has to be estimated iteratively by imposing zero average stress in all three principal directions ($t^{\text{wall}}_{\Theta\Theta} = 0$, $t^{\text{wall}}_{RR} = 0$, $t^{\text{wall}}_{ZZ} = 0$) and satisfying the geometrical constraints determined by the interaction between layers. It is worth noting that, in κ_{unloaded}, while the circumferential stress is expected to be compressive in the inner portion of the wall and tensile in the outer regions, its average is also expected to be null. In fact, if the average circumferential stress was positive (tensile), the wall radius would decrease to reach equilibrium and *vice versa*.

Previous studies have shown that the *in vivo* λ_z is the axial stretch that results in an approximately constant axial force in the physiological range of pressures (Van Loon et al., 1977). In practice, λ_z can be estimated as the crossover point between reduced axial force-longitudinal stretch relationships at different levels of distending pressure, where the reduced axial force is calculated as:

$$F_z = \pi t^{\text{wall}}_{zz} \left(r^2_{\text{external}} - r^2_{\text{internal}} \right) - \pi r^2_{\text{internal}} P \ , \tag{3.22}$$

where t^{wall}_{zz} is the wall axial stress, and P is the luminal pressure. In this work, λ_z was estimated as the average of the cross-over points between the reduced axial force-axial stretch relationships in simulations of the axial extension of the artery at three constant pressure level: $P = 60$, 100, and 140 mmHg. r_{internal} is estimated iteratively so that the desired P is achieved and estimating pressure from the Laplace equation (Burton, 1954).

$$P = t^{\text{wall}}_{\theta\theta} \frac{r_{\text{external}} - r_{\text{internal}}}{r_{\text{internal}}} = t^{\text{wall}}_{\theta\theta} \frac{h^{\text{wall}}}{r_{\text{internal}}} \ . \tag{3.23}$$

Once all the model parameters required for the overall mapping from κ_{isolated} to $\kappa_{\text{tension-inflation}}$, the tension-inflation of the vessel at *in vivo* length and physiological pressure was simulated. Two reference pressure levels were taken into consideration: $P_{\text{ref}} = 100$ mmHg representing the average physiological pressure, and $P_{\text{ref}} = 160$ mmHg as high physiological (hypertensive) pressure level. At these pressure levels, layers stresses in the circumferential and axial directions were calculated using Eqs. 3.19 and 3.20 (opportunely adjusted for the $\kappa_{\text{tension-inflation}}$ configuration), while wall

stresses were calculated from the layers stresses using Eq. 3.21. The tangential elastic modulus $\boldsymbol{\mathcal{K}}$ and the small-on-large stiffness $\boldsymbol{\mathcal{C}}$ were used to evaluate the wall and layer circumferential stiffnesses at P_{ref}. The tangential elastic modulus in the circumferential direction $\mathscr{K}_{\theta\theta\theta\theta}$ was calculated as

$$\mathscr{K}^k_{\theta\theta\theta\theta} = \frac{\partial t^k_{\theta\theta}}{\partial \epsilon^k_{\theta\theta}}\bigg|_{P=P_{\text{ref}}} . \tag{3.24}$$

The small-on-large circumferential stiffness $\mathscr{C}_{\theta\theta\theta\theta}$ was

$$\mathscr{C}^k_{\theta\theta\theta\theta} = 2\left(t^k_{\theta\theta} + p\right) + 4\left(\lambda^k_\theta\right)^4 \frac{\partial^2 \Psi}{\partial\left[\left(\lambda^k_\theta\right)^2\right]^2} . \tag{3.25}$$

The structural stiffness was calculated as the product between the layer/wall material stiffness and its respective loaded thickness ($\mathscr{C}^k_{\theta\theta\theta\theta}h^k$ and $\mathscr{K}^k_{\theta\theta\theta\theta}h^k$ with $k = \{\text{wall,i,m,a}\}$). Additionally, the contribution of each layer to the load bearing was calculated as the ratio between the force per unit length of the layer and the wall:

$$\text{Load bearing } \% = \frac{t^k_{\theta\theta}h^k}{t^{\text{wall}}_{\theta\theta}h^{\text{wall}}} . \tag{3.26}$$

In order to illustrate the role of the total layers prestretches (i.e., composition of $\mathbf{F}_1$ and $\mathbf{G}^k$), the load-bearing when both $\mathbf{F}_1$ and $\mathbf{G}^k$ and when $\mathbf{G}^k$ only equal the spatial second-order identity tensor $\mathbf{I}$ were also evaluated.

3.2.5 Statistical analysis

On each aorta, tensile tests were conducted in duplicate on two adjacent circumferential and two adjacent axial strips, as were the layer tests. For each artery, the layer-specific constitutive and tri-layered modelling was then conducted in pairs (i.e. circumferential strip 1 with axial strip 1 and circumferential strip 2 with axial strip 2). For each output variable, the average was considered as the representative value for that artery and used in further group statistical analysis.

Results are presented as mean ± standard deviation of the 10 arteries (8 for the residual deformation experiments). Differences in output variables (constitutive parameters, stresses, stiffnesses) among arterial layers were first evaluated using a permissive repeated-measures analysis of variance (ANOVA) followed by paired student's t-tests for the pairwise comparisons. Similar analysis was also conducted to compare intact wall and layer-specific output variables at the three different aortic locations. Finally, inter-species differences at the three arterial locations were tested using unpaired student's t-tests. $p<0.05$ was take as statistically significant.

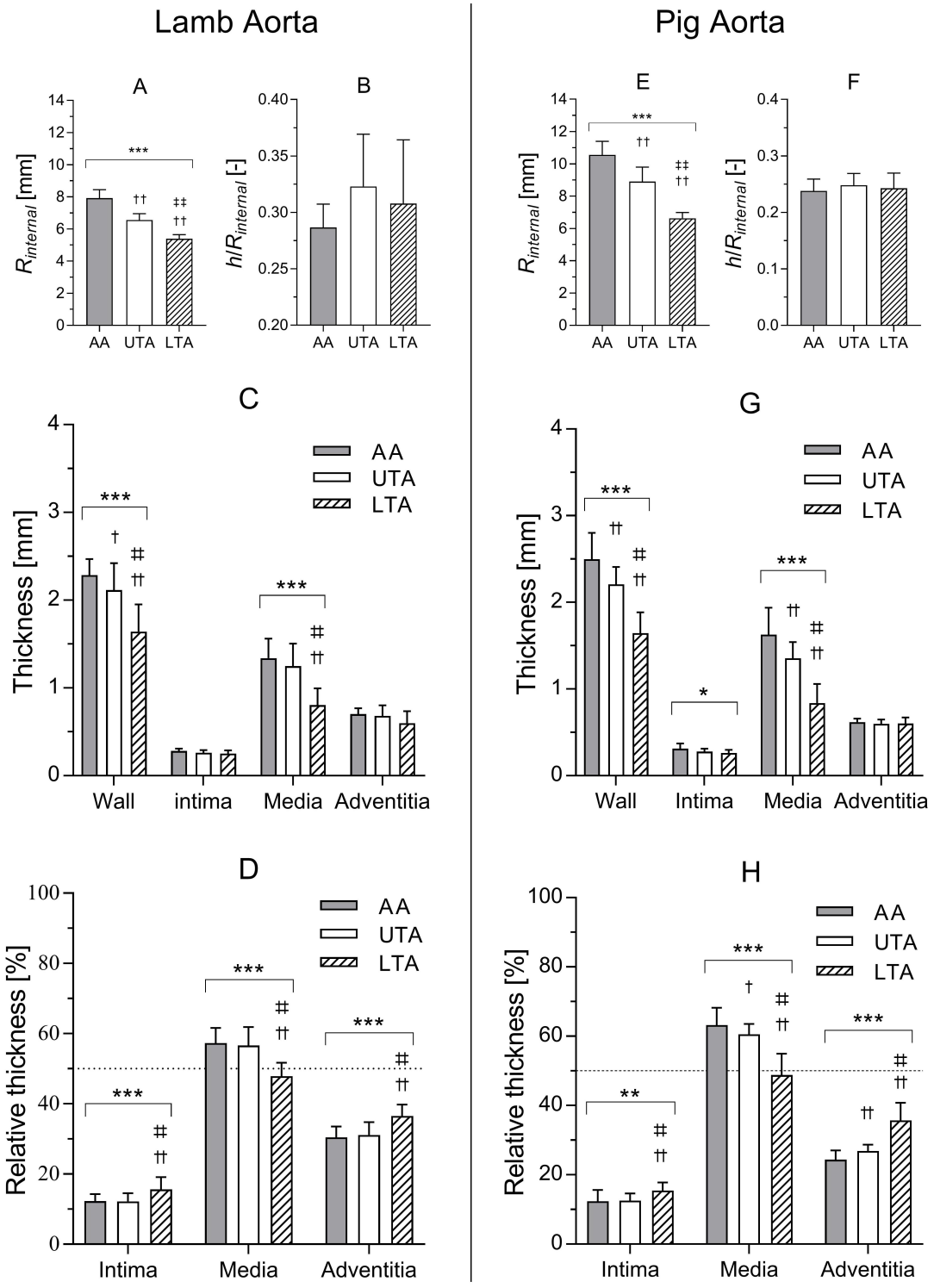

Figure 3.7: *Geometrical features of the ovine (A, B, C, D) and swine (E, F, G, H) ascending aorta (AA), upper thoracic aorta (UTA), and lower thoracic aorta (LTA). The relative thickness was calculated as the ratio between layer thickness and wall thickness (calculated as sum of the layers). Data are presented as mean ± standard deviation. Repeated measures ANOVA: $^{*}p<0.05$,$^{**}p<0.01$, $^{***}p<0.001$. Pairwise comparison AA-UTA: $^{\dagger}p<0.05$, $^{\dagger\dagger}p<0.01$, $^{\dagger\dagger\dagger}p<0.001$. Pairwise comparison UTA-LTA: $^{\ddagger}p<0.05$, $^{\ddagger\ddagger}p<0.01$, $^{\ddagger\ddagger\ddagger}p<0.001$.*

3.3 Results

3.3.1 Wall and layer-specific geometry and residual deformations

The geometrical features of the lamb and pig aortae are summarised in Figure 3.7 (A-D and E-H for lambs and pigs, respectively). The pig aorta was characterised by a significantly higher radius than the lamb aorta independently on the aortic region ($p<0.001$), decreasing from 10.28±1.08 mm at the AA to 6.90±0.49 mm at the LTA in pigs and from 7.86±0.48 mm to 5.40±0.27 mm in lambs. On the contrary, wall and layer-specific thicknesses were comparable in the two species (except for the adventitia and media of the AA that were significantly thicker and thinner, respectively, in lambs than pigs, $p<0.01$), leading to a significantly higher thickness to radius ratio in the lamb aorta, independently of the region ($p<0.001$) (overall 0.25±0.03 in pigs and 0.30±0.07 in lambs). In both species, changes in wall thickness mainly reflected changes in the thickness of the media, as intimal and adventitial thicknesses remained relatively constant along the aorta.

On the contrary the relative thickness of all layers showed region-dependence in both animals, with the media decreasing from 57±4% to 48±4% in labs and 62±7% to 49±5% in pigs moving from the AA to the LTA ($p<0.001$ for both). Both the intima and adventitia showed an opposite trend (intima: 12±2% to 16±3% in lambs, $p<0.01$, and 15±5% to 18±4% in pigs, $p<0.001$, and adventitia 30±3% to 37±3% in lambs and 23±3% to 33±4% in pigs, $p<0.001$ for both).

Figure 3.8A and B present the wall and layer-specific OAs for the three different aortic regions of the lamb and pig aorta, respectively. Independently on the region, the wall OA was higher in lambs than in pigs ($p<0.01$ at the AA and UTA, and $p<0.001$ at the LTA), as well as characterised by different regional changes in the two species; in lambs, the wall OA was similar at 185.5±47.4 and 192.4±44.1 in the AA and LTA, respectively, but significantly lower at 130.9±34.0 at the UTA (Figure 3.8A). Conversely, the wall OA decreased monotonically from 140.7±22.1 at AA to 51.6±13.9 at the LTA in pigs (Figure 3.8B). Interestingly, both species shared similar intima and media OAs, with the only exception of the media of the LTA where the OA was higher in lambs than pigs ($p<0.001$). While in both species, the intima OA decreased when moving distally (from 293.0±60.3 at the AA to 193.3±17.6 at the LTA and from 296.4±46.5 to 190.5±39.4 in lambs and pigs, respectively) and was characterised by the highest OAs, the OA of the media followed a similar trend to that shown by the wall, thus, explaining the difference found at the LTA. The OA of the adventitia was significantly higher in lambs than in pigs ($p<0.001$ at the AA and UTA, $p<0.05$ at the LTA). Further, while no regional changes were observed in lambs, an increasing trend was observed in pigs when moving from proximal to

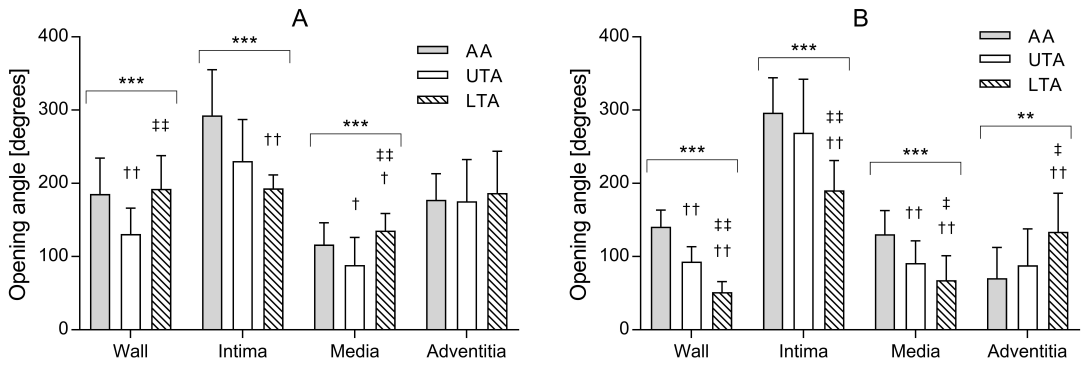

Figure 3.8: *Regional changes of the wall and layer-specific opening angles for the lamb (A) and pig (B) aorta. Data are presented as mean ± standard deviation. Repeated measures ANOVA:* $^{\dagger}p<0.05$, $^{\dagger\dagger}p<0.01$, $^{\dagger\dagger\dagger}p<0.001$. *Pairwise comparison UTA-LTA:* $^{\ddagger}p<0.05$, $^{\ddagger\ddagger}p<0.01$, $^{\ddagger\ddagger\ddagger}p<0.001$.

distal regions (70.3±40.7 at the AA to 133.9±50.8 at the LTA).

Table 3.1 reports the prestretches layers are subjected to when part of the wall. While OAs are crucial in determining the distribution of residual strains across the wall and layer thicknesses, prestretches provide information on their average across the thickness. It is worth noting that the layer prestretches were measured on flat wall strips and, hence, do not correspond to the state of deformation layers are subjected to in the wall 'stress-free' OA configuration. On the contrary, these values provide valuable information to interpret the results of the uniaxial test which are carried out on flattened samples. As for the OA, differences were observed between species; the intima was always in a compressed state in both circumferential and axial directions in lambs but not in pigs where residual strains were small except for an average 0.97±0.01 circumferential compression AA and 1.02±0.01 extension in the LTA. Prestretches in the media

Table 3.1: *Experimentally determined layer-specific pre-stretches. Data are presented as mean ± standard deviation.*

		Intima		**Media**		**Adventitia**	
		$\hat{\lambda}_x^{\mathrm{i}}$	$\hat{\lambda}_z^{\mathrm{i}}$	$\hat{\lambda}_x^{\mathrm{m}}$	$\hat{\lambda}_z^{\mathrm{m}}$	$\hat{\lambda}_x^{\mathrm{a}}$	$\hat{\lambda}_z^{\mathrm{a}}$
Lamb	AA	0.97 ± 0.02	0.97 ± 0.03	0.99 ± 0.01	0.99 ± 0.01	0.95 ± 0.03	0.99 ± 0.03
	UTA	0.98 ± 0.01	0.97 ± 0.02	0.99 ± 0.01	0.99 ± 0.01	0.90 ± 0.02	1.00 ± 0.03
	LTA	0.97 ± 0.02	0.95 ± 0.01	0.98 ± 0.01	0.98 ± 0.01	0.95 ± 0.03	1.02 ± 0.02
Pig	AA	0.97 ± 0.01	1.00 ± 0.02	1.00 ± 0.01	1.05 ± 0.02	0.97 ± 0.01	0.98 ± 0.03
	UTA	1.00 ± 0.01	1.00 ± 0.01	1.00 ± 0.01	0.98 ± 0.02	0.93 ± 0.02	1.01 ± 0.01
	LTA	1.02 ± 0.01	0.99 ± 0.02	1.00 ± 0.01	0.97 ± 0.01	0.93 ± 0.01	1.03 ± 0.03

were relatively small and similar in the two species, except for the pig AA where the media was subjected to a 1.05±0.02 axial stretch. Finally, in both pigs and lambs and in all regions the adventitia elongated in the circumferential direction when peeled from the wall, indicating that, in flat strips, this layer is always subjected to compression. Conversely, adventitial residual deformation in the axial direction were slightly compressive in the AA and shifted to tensile while moving distally along the aorta.

3.3.2 The wall and layer-specific mechanics

Figures 3.9, 3.10 and 3.11 present examples of Cauchy stress-stretch relationships of wall and layers of the AA, UTA and LTA, respectively. Independently of the region, the pig intact wall and layers were stiffer than the corresponding lamb samples, exhibiting significantly lower $\overline{\lambda}_{\mathbb{X}}$ and $\overline{\lambda}_{\mathbb{Z}}$ at any stress level, in all aortic regions and for both the intact wall and isolated layers. Furthermore, while, as clearly visible in the stress-stretch graphs, all tissues exhibited a pronounced nonlinear behaviour, this was more pronounced in adventitial samples compared to both intimal and medial strips.

Inter-species differences

Tables 3.2, 3.3, and 3.4 present the average wall (when modelled as a single uniform layer) and layer-specific model parameters of the AA, UTA, and LTA, respectively, of pigs and lambs (model parameters for each artery are reported in Appendix Tables A1-A6). The stiffness-like parameters (both the isotropic μ and the anisotropic k_1) were, in general, significantly higher (approximately 2-fold) in pig aortae than in those of lambs. In the intact wall of lambs, μ was 7.45±2.79, 10.41±3.74, and 12.65±4.09 kPa at the AA, UTA and LTA, respectively. Corresponding values for the pig aorta were significantly higher at the AA (21.34±3.09 kPa, $p<0.001$) and UTA (21.07±6.12 kPa, $p<0.001$), but not at the LTA (16.34±6.26 kPa). Similar differences in μ were also found for the isolated layers, except for the intima where μ differed significantly among species only at the UTA (Tables 3.2-3.4).

k_1 of the intact wall of lambs and pigs was 42.44±6.16 and 118.81±24.33 kPa at the AA ($p<0.001$), 56.93±40.37 and 137.87±45.49 kPa at the UTA ($p<0.001$), and 81.61±57.13 and 203.55±55.24 kPa at the LTA ($p<0.001$). Similar differences in k_1 were also found for the isolated layers (Tables 3.2-3.4). Inter-species differences in the fibre exponential parameter k_2 were even more marked than those found for the stiffness-like parameters, ranging from ∼5 to 10 folds. k_2 of the intact wall of lambs and pigs were 1.41±1.86 and 5.31±2.62 at the AA ($p<0.01$), 2.27±1.94 and 17.11±9.14 at the UTA ($p<0.001$), and 5.98±5.50 and 33.05±20.04 at the LTA ($p<0.001$). On the contrary, the intact wall and layer-specific degree of anisotropy was

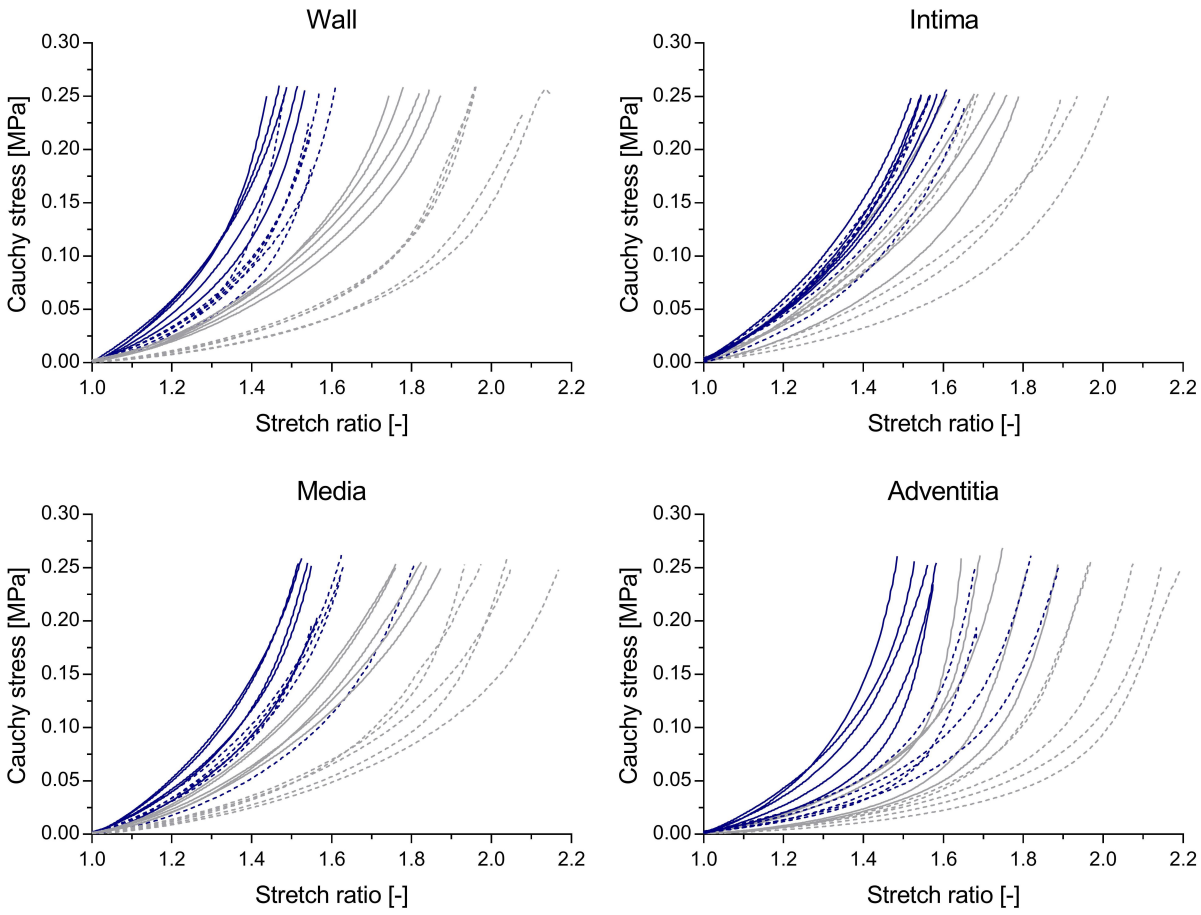

Figure 3.9: *Examples of wall and layers Cauchy stress-stretch relationships of the ovine (gray) and swine (blue) ascending aorta. Circumferential uniaxial tests are presented as continuous lines, while longitudinal tests as dashed lines.*

remarkably similar in pigs and lambs (the only inter-species significant difference was found in the adventitia of the AA, $p<0.05$).

Inter-regional differences

The statistical analysis of the inter-regional variations of constitutive parameters can be found in the Appendix (Tables A7 and A8 for lambs and pigs, respectively). In both animals, μ exhibited modest non-significant changes along the aorta, except for a small but significant decrease in the pig intact wall ($p=0.01$) and increase in the lamb adventitia ($p<0.05$) when moving from proximal to distal regions. On the contrary, both k_1 and k_2 were higher in distal regions of the pig aorta compared to proximal regions (except k_1 in the adventitia and k_2 in the media), signifying a significant wall stiffening along the aorta. Interestingly, regional changes in k_1 and k_2 along the lamb aorta were mostly non-significant. Only the adventitia showed a marked increase of k_2 when moving downstream in the circulation ($p<0.01$).

When considering the intact wall, fibres presented a preferential circumferential orientation

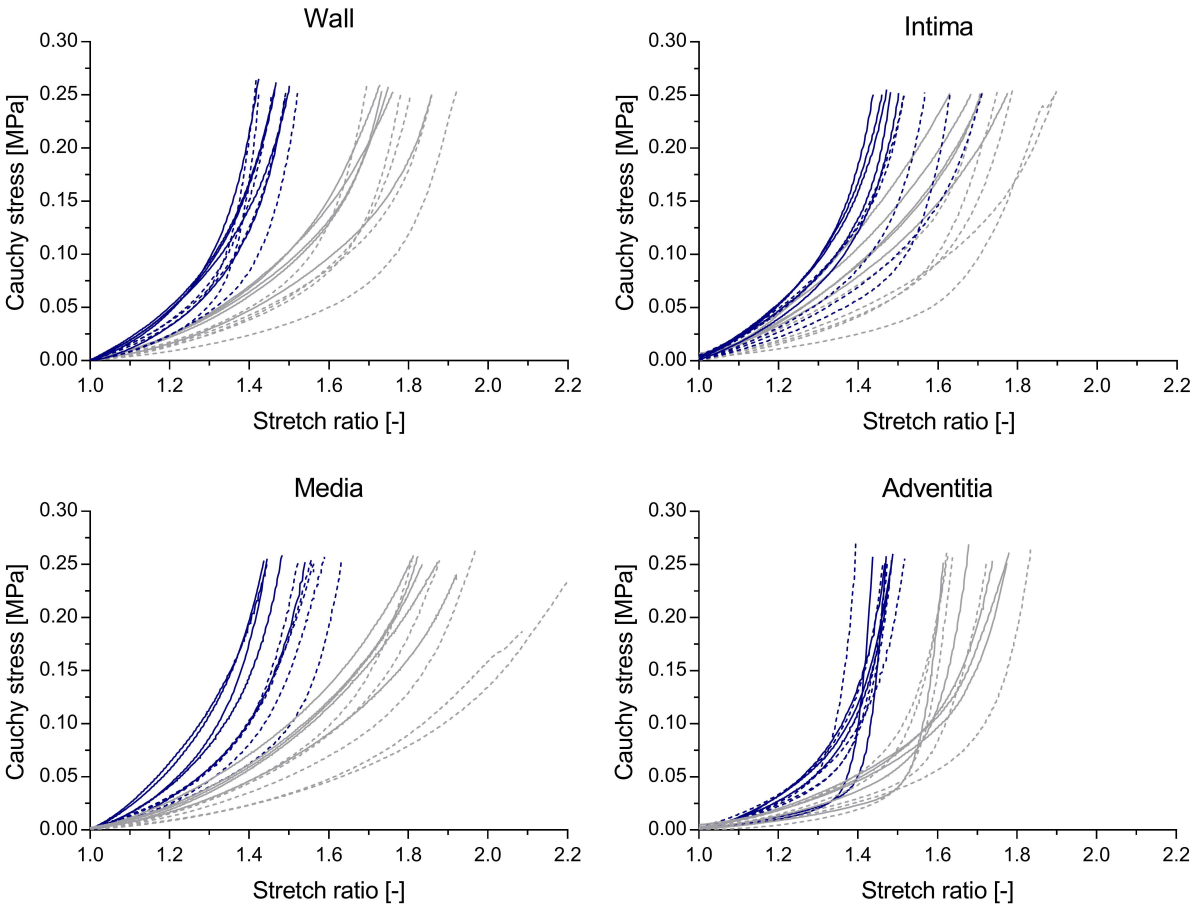

Figure 3.10: *Examples of wall and layers Cauchy stress-stretch relationships of the ovine (gray) and swine (blue) upper thoracic aorta. Circumferential uniaxial tests are presented as continuous lines, while longitudinal tests as dashed lines.*

in the AA (35.81±5.29° in lambs and 36.57±3.48° in pigs), while displaying an approximately isotropic behaviour in both UTA and LTA (lambs: 43.12±12.74° at UTA and 44.31±5.17° at LTA, and pigs 43.49±3.08° at UTA and 43.43±2.38° at LTA). However, as for the other model parameters, changes in wall fibre orientation were not significant in lambs. The shift in fibre orientation was driven by a shift of fibre direction in the adventitia from a strong preferential circumferential orientation in the AA (19.73±9.83° in lambs and 28.92±6.20° in pigs) to a diagonal orientation in the thoracic aorta (lambs: 40.31±10.93° at UTA and 44.55±3.79° at LTA, and pigs 44.55±3.60° at UTA and 42.55±3.54° at LTA, $p<0.01$ for all). On the contrary, the orientation of fibres in the intima gradually shifted from diagonal in the AA (40.71±8.97° in lambs and 46.91±6.72° in pigs) to preferentially circumferential in the LTA (33.66±4.25° in lambs, $p<0.05$, and 35.02±6.55° in pigs, $p<0.01$). Changes of fibres orientation in the media were milder (although still significant in pigs) than in the other layers, displaying a preferential circumferential orientation in the range 30-35° throughout the aorta.

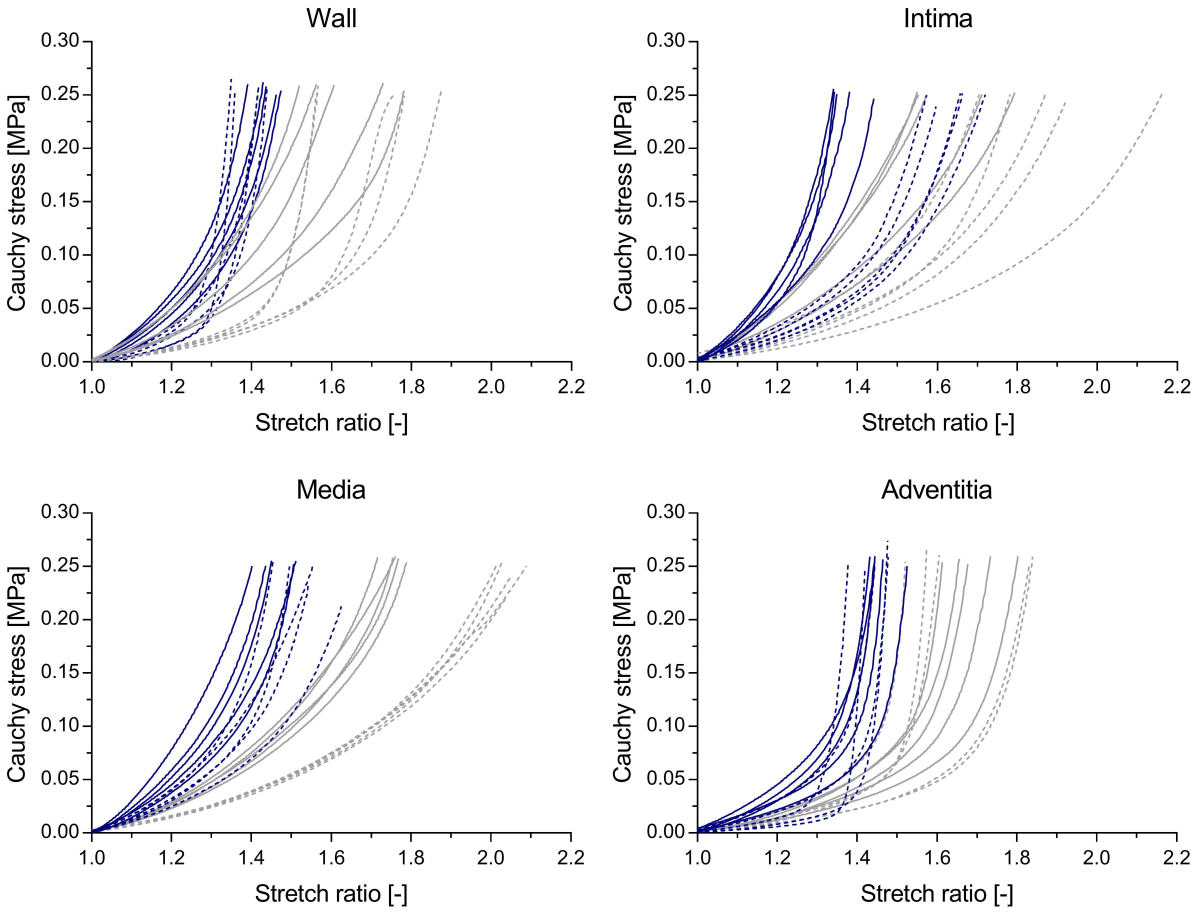

Figure 3.11: *Examples of wall and layers Cauchy stress-stretch relationships of the ovine (gray) and swine (blue) lower thoracic aorta. Circumferential uniaxial tests are presented as continuous lines, while longitudinal tests as dashed lines.*

Inter-layer differences

The statistical analysis of the inter-layer differences in HGO-SEF constitutive parameters can be found in the Appendix (Tables A9 and A10 for lambs and pigs, respectively). Overall, the intima exhibited higher μ values than both adventitia and media, except for the pig UTA where intima-media differences were not significant and the pig LTA where μ was significantly higher in the media than in the intima ($p<0.01$). Conversely, the fibre stiffness-like parameter k_1 and non-linearity parameter k_2 were on average lower and markedly higher, respectively, in the adventitia than in both intima and media, although inter-layer differences in k_1 were not always significant. As shown in the appendix (Figure A1), this signifies a delayed but abrupt stiffening of the adventitia, that is clearly visible in Figures 3.9-3.11.

Table 3.2: *Layer-specific model parameters of the ovine and swine ascending aorta. Data are presented as mean ± standard deviation. The average curve columns report the model parameters fitted on the average of the modelled stress-stretch relationships of the n=10 lamb and n=9 pig aortae, respectively. Artery-specific model parameters are reported in tables A1 and A4, respectively.*

		Ascending aorta				
		Lamb (n=10)	Average curve	Pig (n=10)	Average curve	
Wall	μ [kPa]	7.45 ± 2.79	7.62	21.34 ± 3.09	22.38	p<0.001
	k_1 [kPa]	42.44 ± 6.17	49.59	118.81 ± 24.33	122.16	p<0.001
	k_2 [-]	1.41 ± 1.87	2.09	5.31 ± 2.62	7.05	p<0.01
	α [°]	35.81 ± 5.29	30.20	36.57 ± 3.48	34.63	N.S.
	τ [-]	0.22 ± 0.04	0.27	0.24 ± 0.02	0.26	N.S.
	R^2 [-]	0.99 ± 0.01		1.00 ± 0.00		
Intima	μ [kPa]	22.18 ± 6.56	22.64	27.78 ± 6.02	28.21	N.S
	k_1 [kPa]	56.91 ± 13.20	72.38	97.43 ± 31.15	106.39	p<0.01
	k_2 [-]	1.21 ± 1.35	1.27	2.10 ± 1.97	2.06	N.S.
	α [°]	40.71 ± 8.97	33.72	46.91 ± 6.72	49.66	N.S.
	τ [-]	0.25 ± 0.05	0.29	0.24 ± 0.01	0.27	N.S.
	R^2 [-]	1.00 ± 0.00		1.00 ± 0.00		
Media	μ [kPa]	9.44 ± 2.23	9.50	21.86 ± 4.47	22.84	p<0.001
	k_1 [kPa]	45.15 ± 10.92	58.28	113.80 ± 21.41	124.68	p<0.001
	k_2 [-]	0.33 ± 0.52	0.26	2.47 ± 1.40	3.33	p<0.001
	α [°]	35.29 ± 7.13	24.35	35.18 ± 4.66	30.83	N.S.
	τ [-]	0.18 ± 0.03	0.27	0.22 ± 0.02	0.24	N.S.
	R^2 [-]	0.99 ± 0.01		1.00 ± 0.00		
Adventitia	μ [kPa]	6.22 ± 1.05	6.29	11.79 ± 3.08	12.92	p<0.001
	k_1 [kPa]	26.22 ± 12.73	27.96	81.92 ± 28.35	84.23	p<0.001
	k_2 [-]	4.41 ± 1.42	7.04	5.78 ± 3.18	6.89	N.S.
	α [°]	19.73 ± 9.83	20.98	28.92 ± 6.19	24.10	p<0.05
	τ [-]	0.27 ± 0.02	0.29	0.25 ± 0.02	0.27	N.S.
	R^2 [-]	0.99 ± 0.01		0.99 ± 0.00		

Table 3.3: *Layer-specific model parameters of the ovine and swine upper thoracic aorta. Data are presented as mean ± standard deviation. The average curve columns report the model parameters fitted on the average of the modelled stress-stretch relationships of the n=10 lamb and n=10 pig aortae, respectively. Artery-specific model parameters are reported in tables A2 and A5, respectively.*

		Upper thoracic aorta				
		Lamb (n=10)	Average curve	Pig (n=10)	Average curve	
Wall	μ [kPa]	10.41 ± 3.74	10.88	21.07 ± 6.12	21.26	p<0.001
	k_1 [kPa]	56.93 ± 40.37	59.24	137.87 ± 45.49	141.64	p<0.001
	k_2 [-]	2.27 ± 1.94	2.79	17.11 ± 9.14	20.01	p<0.001
	α [°]	43.12 ± 12.74	41.86	43.49 ± 3.08	44.51	N.S.
	τ [-]	0.26 ± 0.06	0.29	0.22 ± 0.03	0.23	N.S.
	R^2 [-]	0.98 ± 0.02		0.98 ± 0.01		
Intima	μ [kPa]	15.89 ± 4.48	17.19	26.89 ± 5.64	26.64	p<0.001
	k_1 [kPa]	69.62 ± 11.73	97.02	101.56 ± 31.37	109.99	p=0.01
	k_2 [-]	0.12 ± 0.22	0.00	11.33 ± 4.97	12.86	p<0.001
	α [°]	38.93 ± 1.73	27.36	40.25 ± 5.05	40.14	N.S.
	τ [-]	0.20 ± 0.03	0.29	0.24 ± 0.02	0.25	p<0.01
	R^2 [-]	0.98 ± 0.01		0.99 ± 0.01		
Media	μ [kPa]	8.51 ± 2.28	9.18	20.34 ± 6.45	22.51	p<0.001
	k_1 [kPa]	43.74 ± 12.38	58.49	146.27 ± 34.40	132.29	p<0.001
	k_2 [-]	0.26 ± 0.24	0.33	5.84 ± 4.55	9.67	p<0.01
	α [°]	32.17 ± 10.77	17.42	34.60 ± 4.14	33.74	N.S.
	τ [-]	0.23 ± 0.04	0.29	0.23 ± 0.02	0.24	N.S.
	R^2 [-]	0.99 ± 0.01		1.00 ± 0.00		
Adventitia	μ [kPa]	9.31 ± 4.08	11.35	18.51 ± 5.62	21.11	p<0.001
	k_1 [kPa]	19.62 ± 13.55	17.17	61.62 ± 26.75	16.60	p<0.001
	k_2 [-]	9.37 ± 3.48	25.03	42.35 ± 23.63	76.05	p<0.001
	α [°]	40.31 ± 10.37	48.52	44.55 ± 3.60	42.76	N.S.
	τ [-]	0.24 ± 0.07	0.26	0.23 ± 0.02	0.18	N.S.
	R^2 [-]	0.98 ± 0.02		0.98 ± 0.01		

Table 3.4: *Layer-specific model parameters of the ovine and swine upper thoracic aorta. Data are presented as mean ± standard deviation. The average curve columns report the model parameters fitted on the average of the modelled stress-stretch relationships of the n=10 lamb and n=10 pig aortae, respectively. Artery-specific model parameters are reported in tables A3 and A6, respectively.*

		Lower thoracic aorta				
		Lamb (n=10)	Average curve	Pig (n=10)	Average curve	
Wall	μ [kPa]	12.65 ± 4.09	14.71	16.34 ± 6.26	14.90	N.S.
	k_1 [kPa]	81.61 ± 57.13	92.34	203.55 ± 55.24	223.48	p<0.001
	k_2 [-]	5.98 ± 5.50	15.19	33.05 ± 20.04	41.29	p<0.01
	α [°]	44.31 ± 5.17	47.05	43.43 ± 2.39	44.26	N.S.
	τ [-]	0.16 ± 0.08	0.27	0.19 ± 0.02	0.19	N.S.
	R^2 [-]	0.95 ± 0.02		0.96 ± 0.01		
Intima	μ [kPa]	16.50 ± 6.09	17.57	21.09 ± 3.79	19.99	N.S
	k_1 [kPa]	68.73 ± 18.74	93.11	132.78 ± 33.23	140.22	p<0.001
	k_2 [-]	0.21 ± 0.47	0.02	12.65 ± 8.06	16.74	p<0.001
	α [°]	33.66 ± 4.25	22.64	35.02 ± 6.55	36.59	N.S.
	τ [-]	0.18 ± 0.03	0.26	0.23 ± 0.01	0.22	p<0.05
	R^2 [-]	0.99 ± 0.01		0.99 ± 0.01		
Media	μ [kPa]	10.82 ± 2.65	11.55	28.31 ± 8.25	30.34	p<0.001
	k_1 [kPa]	44.40 ± 10.41	63.81	155.19 ± 31.06	147.90	p<0.001
	k_2 [-]	0.17 ± 0.19	0.11	9.83 ± 9.73	16.48	p<0.01
	α [°]	33.93 ± 2.26	14.26	31.97 ± 4.23	29.47	N.S.
	τ [-]	0.18 ± 0.03	0.27	0.22 ± 0.02	0.24	p<0.01
	R^2 [-]	1.00 ± 0.00		1.00 ± 0.00		
Adventitia	μ [kPa]	10.14 ± 3.86	10.34	12.39 ± 5.68	13.13	N.S.
	k_1 [kPa]	20.48 ± 16.93	16.04	90.35 ± 84.48	57.32	p<0.05
	k_2 [-]	16.60 ± 7.10	21.05	71.93 ± 21.33	91.92	p<0.001
	α [°]	42.40 ± 8.44	39.69	42.55 ± 3.54	42.59	N.S.
	τ [-]	0.24 ± 0.06	0.29	0.21 ± 0.03	0.19	N.S.
	R^2 [-]	0.98 ± 0.02		0.97 ± 0.03		

Table 3.5: *Fitted layer-specific pre-stretches. Data are presented as mean ± standard deviation.*

		Intima		**Media**		**Adventitia**	
		$\hat{\lambda}_x^{\mathrm{i}}$	$\hat{\lambda}_z^{\mathrm{i}}$	$\hat{\lambda}_x^{\mathrm{m}}$	$\hat{\lambda}_z^{\mathrm{m}}$	$\hat{\lambda}_x^{\mathrm{a}}$	$\hat{\lambda}_z^{\mathrm{a}}$
Lamb	AA	0.99 ± 0.01	0.98 ± 0.02	1.03 ± 0.02	0.97 ± 0.06	0.94 ± 0.04	0.98 ± 0.11
	UTA	1.00 ± 0.01	0.97 ± 0.03	1.02 ± 0.03	0.99 ± 0.03	0.93 ± 0.05	1.02 ± 0.08
	LTA	0.99 ± 0.01	0.97 ± 0.02	1.03 ± 0.02	0.99 ± 0.04	0.94 ± 0.05	1.08 ± 0.04
Pig	AA	0.96 ± 0.02	1.01 ± 0.05	1.03 ± 0.01	1.03 ± 0.01	1.00 ± 0.01	0.99 ± 0.02
	UTA	1.01 ± 0.02	0.99 ± 0.04	1.02 ± 0.02	0.99 ± 0.02	0.95 ± 0.04	1.04 ± 0.02
	LTA	1.03 ± 0.03	1.01 ± 0.03	1.02 ± 0.01	0.97 ± 0.03	0.91 ± 0.03	1.05 ± 0.05

3.3.3 Tri-layered wall model

Tri-layered model of the flattened arterial tissue

Table 3.5 presents the fitted layer-specific prestretches of the AA, UTA and LTA of lambs and pigs. As shown in Section 3.2.3, these prestretches determine the layer-specific deformation gradient $\mathbf{G}^k$ mapping the deformation from $\kappa_{\mathrm{isolated}}$ to $\kappa_{\mathrm{composite}}$. The accuracy of fitting of the tri-layered model did not show region-dependence; R^2 was 0.98±0.01, 0.99±0.02 and 0.99±0.01 in the AA, UTA and LTA of lambs and 0.99±0.01, 0.99±0.01 and 0.98±0.02 in pigs, respectively. On the contrary, the accuracy of the single-layer modelling of the intact arterial wall, whose results were presented in Tables 3.2-3.4, slightly decreased moving from proximal to distal regions of the aorta (from 0.99±0.01 and 1.00±0.00 in the AA of lambs and pigs, respectively, to 0.95±0.03 and 0.96±0.01 at the LTA). This finding can be explained by looking at the regional differences in the stress-stretch relationships; at the AA, the wall tissue was stiffer in the circumferential than axial direction throughout the entire range of investigated stresses (0.00-0.25 MPa) (Figure 3.9). Conversely, when moving distally, the complexity of the wall biaxial behaviour increases, with samples being stiffer in the circumferential than axial direction at low stress, while showing increasingly isotropic behaviour at high stresses (Figures 3.10-3.11). Therefore, while a two-fiber family SEF (i.e., modelling the behaviour of two families of fibres oriented symmetrically with respect to the circumferential direction) is sufficient to effectively capture the wall behaviour at the AA, the accuracy of fitting with single-layered model decreased in the UTA and LTA. Indeed, as shown in Tables 3.2-3.4 layers exhibited different degrees of anisotropicity and speed of recruitment of collagen fibres, so that the composite wall may exhibit a different level of anisotropic behaviour depending on the acting stretch level.

Figure 3.12 shows an example of single-layered and tri-layered fitting of the behaviour of

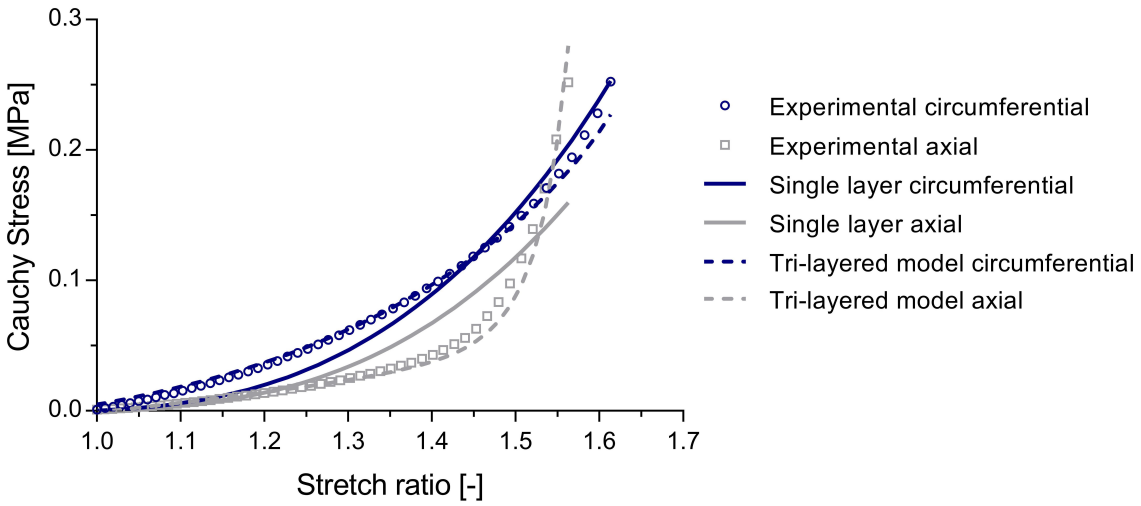

Figure 3.12: *Comparison between the fitting obtained with single-layered and tri-layered modellings of a lamb lower thoracic aorta.*

lamb LTA. The wall was stiffer circumferentially than axially for stress levels below ∼0.18 MPa, while the opposite behaviour was observed above that stress level. The single-layered model failed in effectively predicting the wall stress-stretch relationship (R^2=0.90), under- and overestimating the circumferential and axial stresses, respectively, below ∼0.12 MPa, and largely underestimating axial stresses in the high range (>0.12 MPa). Conversely, the tri-layered model provided a good fit of the experimental data over the entire stress range and in both loading directions (R^2=0.99). Indeed, the stiffer circumferential behaviour at low stresses was provided by the fast recruitment of fibres in the intima and media displaying a preferential circumferential orientation (α=31.82° and α=32.33°, respectively). On the other side, the delayed recruitment of the adventitia, whose behaviour was approximately isotropic in the isolated strip (α=48.77°), explains the stiffer response in the axial than circumferential direction for stresses above 0.18 MPa.

Simulated tension-inflation of the tri-layered aorta

Table 3.6 reports the deformation each layer is subjected to when the flat wall ($\kappa_{\text{composite}}$) is deformed into an unloaded cylindrical vessel (κ_{unloaded}) (i.e. deformation gradient $\mathbf{F}_1$). As expected, the closure of the flat wall model into a cylindrical vessel introduced compressive and tensile circumferential stretches at the intima and adventitia, respectively. The media is subjected to a small compression, reflecting the fact that the radial coordinate of mid-layer of media is lower that of the mid-wall.

Figure 3.13 presents the average simulated pressure-diameter relationship of the ovine and porcine aortae. The estimated *in vivo* axial stretch, determined as that stretch guaranteeing an

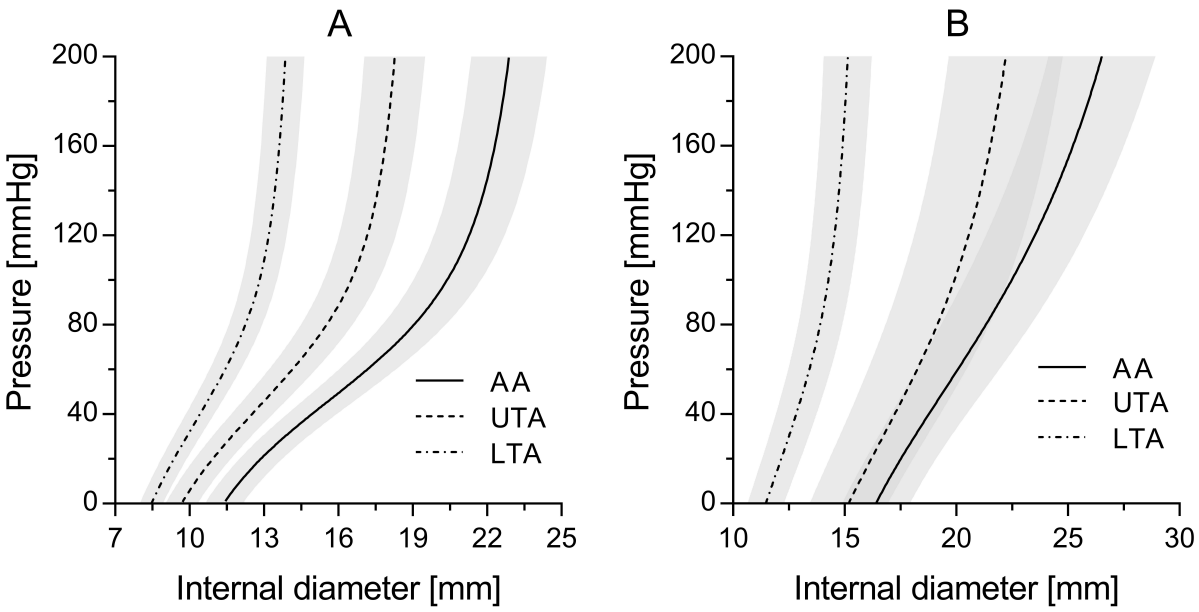

Figure 3.13: *Average simulated pressure-diameter relationship of the ascending aorta, upper thoracic and lower thoracic aorta of lambs (A) and pigs (B). The gray area surrounding each curve represents ± standard deviation.*

approximately constant reduced axial force in the physiological pressure range, was 1.23±0.05, 1.10±0.03 and 1.08±0.04 in the pig AA, UTA and LTA, respectively, and higher in lambs at 1.41±0.09, 1.28±0.09 and 1.17±0.08, respectively ($p<0.001$). In the ascending aorta, the pressure-diameter relationships present the S-shape typical of hyperelastic materials. Such feature became less visible when moving from proximal to distal regions along the aorta, especially in pigs. Furthermore, in the physiological pressure range (i.e., above 50 mmHg), the pressure-diameter relationships resembled exponential functions. As expected, lamb aortae underwent much higher

Table 3.6: *Layer-specific circumferential and axial components of the deformation gradient* $\boldsymbol{F}_1$. *Data are presented as mean ± standard deviation.*

		Intima		**Media**		**Adventitia**	
		Λ_Θ	Λ_Z	Λ_Θ	Λ_Z	Λ_Θ	Λ_Z
Lamb	AA	0.87 ± 0.01	1.04 ± 0.05	0.98 ± 0.02	1.04 ± 0.05	1.11 ± 0.02	1.04 ± 0.05
	UTA	0.85 ± 0.02	1.02 ± 0.02	0.97 ± 0.01	1.02 ± 0.02	1.12 ± 0.01	1.02 ± 0.02
	LTA	0.87 ± 0.03	1.01 ± 0.02	0.98 ± 0.01	1.01 ± 0.02	1.10 ± 0.02	1.01 ± 0.02
Pig	AA	0.89 ± 0.02	0.98 ± 0.01	0.98 ± 0.01	0.98 ± 0.01	1.09 ± 0.01	0.98 ± 0.01
	UTA	0.89 ± 0.01	1.01 ± 0.01	0.99 ± 0.00	1.01 ± 0.01	1.09 ± 0.01	1.01 ± 0.01
	LTA	0.90 ± 0.02	1.02 ± 0.01	0.98 ± 0.01	1.02 ± 0.01	1.08 ± 0.01	1.02 ± 0.01

dilatation to reach the *in vivo* pressure range of approximately 120-80 mmHg.

Figures 3.14-3.19 present wall and layer stresses and stiffnesses when the modelled vessel was inflated at 100 mmHg and 160 mmHg of arterial pressure and stretched at the *in vivo* axial length. Wall circumferential and axial stresses were generally higher in lambs than in pigs ($p<0.01$), reflecting a lower *in vivo* h/R_{internal} ratio (Eq. 3.23). Only the LTA axial stress was similar in the two species. In both species, the circumferential stresses were highest at the AA (0.117±0.020 MPa in lambs and 0.085±0.016 MPa in pigs at 100 mmHg) and dropped at the UTA (0.092±0.017 and 0.076±0.009 MPa) and LTA (0.087±0.015 and 0.072±0.009), although regional differences were significant only in lambs ($p<0.01$). Similar trends were also observed for the axial wall stress.

In both species, circumferential stresses at 100 mmHg were similar in the media and adventitia and comparable to the wall stresses. $t_{\theta\theta}$ was significantly lower in the adventitia than in the media only in the pig AA ($p<0.05$). However, while medial and adventitial circumferential stresses were still similar at 160 mmHg in the pig aorta, this was not the case in the lamb UTA and LTA where $t_{\theta\theta}$ becomes significantly higher in the adventitia than in the media. Interestingly, further inter-species differences were found in the behaviour of the intima; in lambs $t_{\theta\theta}$ at the intima was comparable to that of both media and adventitia, while the former was approximately half $t_{\theta\theta}$ of the media and adventitia in pigs, independently on the region and pressure level ($p<0.01$). In the axial direction, the average stress was higher in the media than in the adventitia in the AA region ($p<0.01$ in pigs and $p<0.05$ in lambs), while in more distal regions the adventitia was subjected to higher stresses than the media (significant only at the UTA, $p<0.05$).

At the AA, $\mathscr{K}_{\theta\theta\theta\theta}$ at 100 mmHg was similar in the two species (0.41±0.09 MPa in lambs and 0.41±0.07 in Pigs), as was $\mathscr{C}_{\theta\theta\theta\theta}$ (0.57±0.13 and 0.49±0.09 MPa, respectively). However, the pressure-related stiffening was significantly stronger in lambs than pigs, with $\mathscr{K}_{\theta\theta\theta\theta}$ rising by 142% and $\mathscr{C}_{\theta\theta\theta\theta}$ by 170% in the former compared to 93% and 114% in the latter (Figures 3.14 and 3.15). This difference can be explained by looking at the layer-specific stiffening over the 60 mmHg pressure increase; in pigs, $\mathscr{K}_{\theta\theta\theta\theta}$ increased by 33%, 80% and 139% for intima, media, and adventitia, respectively. On the contrary, these values were 81%, 66%, and 253% in lambs. Similar changes were also observed for $\mathscr{C}_{\theta\theta\theta\theta}$. As a result, the circumferential stress partitioning between layers was only marginally affected by the 60 mmHg pressure increase in pigs (6±3%-71±8%-23±7% at 100 mmHg vs 6±2%-69±8%-25±7% at 160 mmHg for intima-media-adventitia) (Figure 3.20B). Conversely, in lambs, the adventitial load bearing increased from 26±10% at 100 mmHg to 36±13% at 160 mmHg, while that of the media dropped from 59±7% to 50±9% (Figure 3.20A). Indeed, the structural stiffness of the adventitia was significantly lower than that

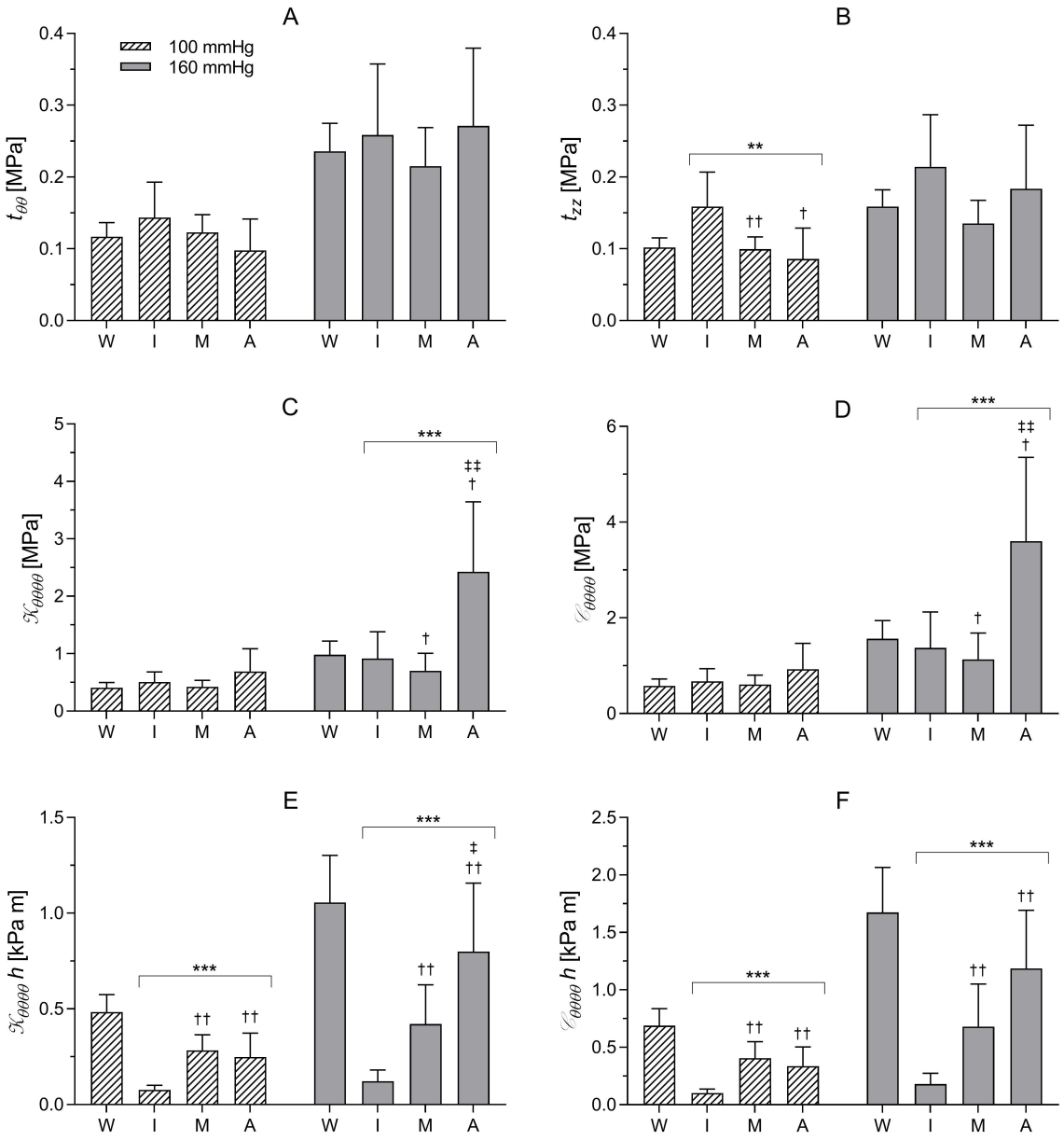

Figure 3.14: *Circumferential ($t_{\theta\theta}$) (A) and longitudinal (t_{zz}) stress (B), tangential elastic modulus ($\mathscr{K}_{\theta\theta\theta\theta}$) (C) and small-on-large circumferential stiffness stiffness ($\mathscr{C}_{\theta\theta\theta\theta}$) (D), structural stiffness calculated with $\mathscr{K}_{\theta\theta\theta\theta}$ (E) and $\mathscr{C}_{\theta\theta\theta\theta}$ (F) in the ascending aorta of lambs at the reference pressures of 100 and 160 mmHg. W=intact wall, I=intima, M=media, and A=adventitia. ANOVA: $^{*}p<0.05$,$^{**}p<0.01$, $^{***}p<0.001$. Pairwise comparison UTA-LTA: $^{\ddagger}p<0.05$, $^{\ddagger\ddagger}p<0.01$, $^{\ddagger\ddagger\ddagger}p<0.001$.Inter-layers pairwise comparison: $^{\dagger}p<0.05$, $^{\dagger\dagger}p<0.01$ with intima, $^{\ddagger}p<0.05$, $^{\ddagger\ddagger}p<0.01$ with media.*

of the media at both reference pressure levels in pig (Figure 3.15E-F), while was comparable to and significantly higher than the structural stiffness of the media at 100 mmHg and 160 mmHg, respectively, in lambs (Figure 3.14E-F).

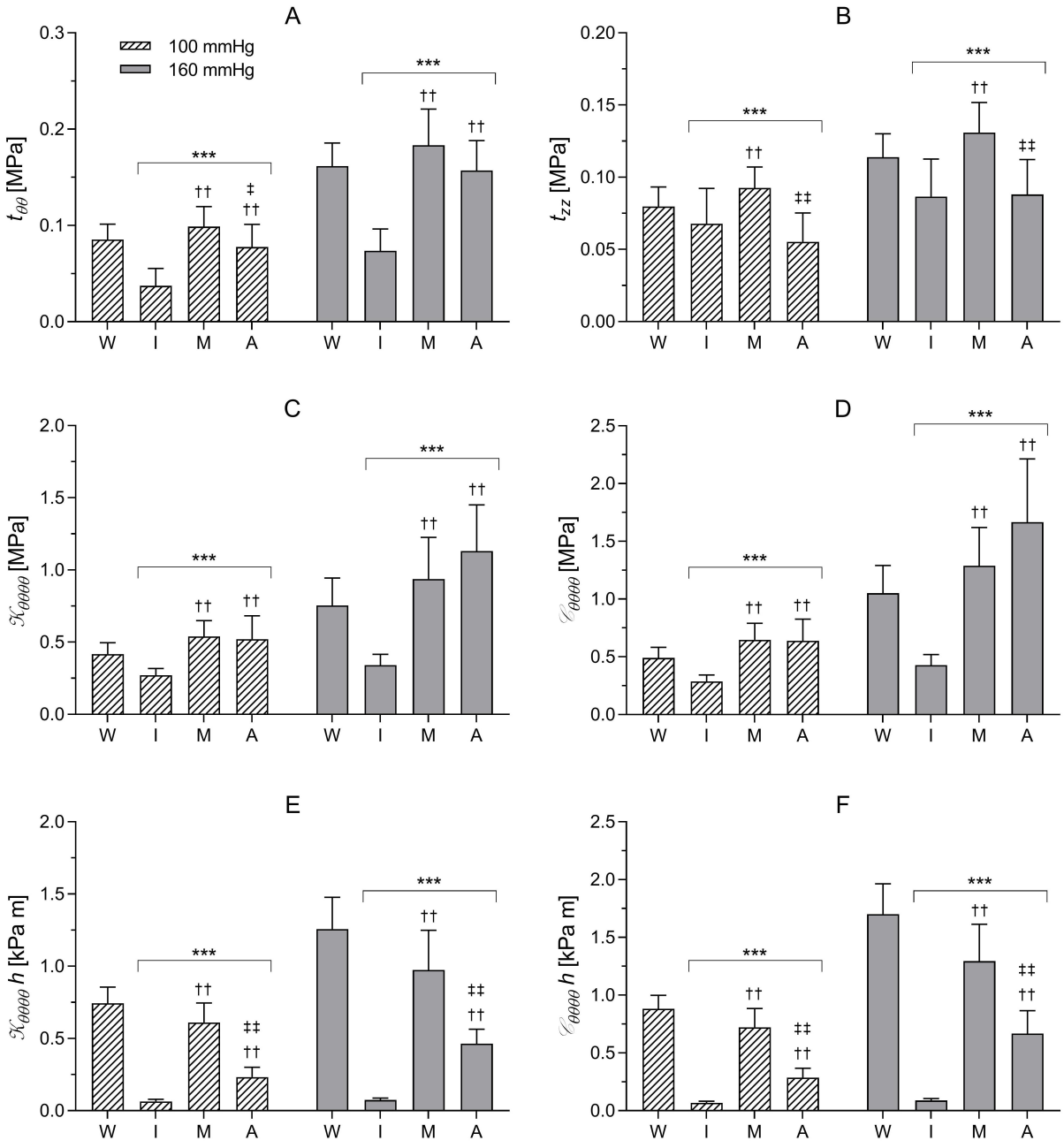

Figure 3.15: *Circumferential ($t_{\theta\theta}$) (A) and longitudinal (t_{zz}) stress (B), tangential elastic modulus ($\mathscr{K}_{\theta\theta\theta\theta}$) (C) and small-on-large circumferential stiffness stiffness ($\mathscr{C}_{\theta\theta\theta\theta}$) (D), structural stiffness calculated with $\mathscr{K}_{\theta\theta\theta\theta}$ (E) and $\mathscr{C}_{\theta\theta\theta\theta}$ (F) in the ascending aorta of pigs at the reference pressures of 100 and 160 mmHg. W=intact wall, I=intima, M=media, and A=adventitia. ANOVA: $^{*}p<0.05$,$^{**}p<0.01$, $^{***}p<0.001$. Pairwise comparison UTA-LTA: $^{‡}p<0.05$, $^{‡‡}p<0.01$, $^{‡‡‡}p<0.001$.Inter-layers pairwise comparison: $^{†}p<0.05$, $^{††}p<0.01$ with intima, $^{‡}p<0.05$, $^{‡‡}p<0.01$ with media.*

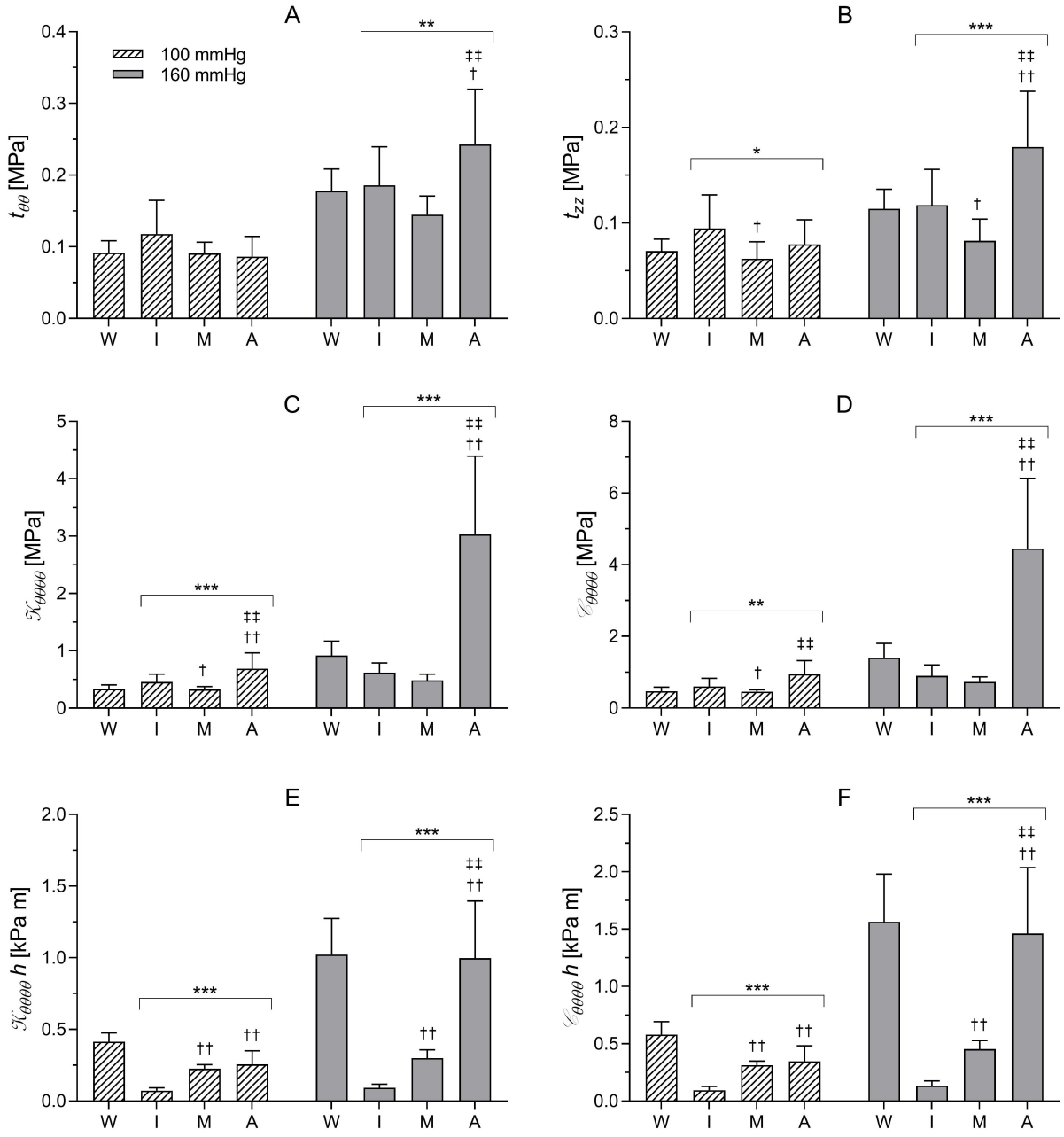

Figure 3.16: *Circumferential ($t_{\theta\theta}$) (A) and longitudinal (t_{zz}) stress (B), tangential elastic modulus ($\mathcal{K}_{\theta\theta\theta\theta}$) (C) and small-on-large circumferential stiffness stiffness ($\mathscr{C}_{\theta\theta\theta\theta}$) (D), structural stiffness calculated with $\mathcal{K}_{\theta\theta\theta\theta}$ (E) and $\mathscr{C}_{\theta\theta\theta\theta}$ (F) in the upper thoracic aorta of lambs at the reference pressures of 100 and 160 mmHg. W=intact wall, I=intima, M=media, and A=adventitia. ANOVA: $^{*}p<0.05$,$^{**}p<0.01$, $^{***}p<0.001$. Pairwise comparison UTA-LTA: $^{‡}p<0.05$, $^{‡‡}p<0.01$, $^{‡‡‡}p<0.001$.Inter-layers pairwise comparison: $^{†}p<0.05$, $^{††}p<0.01$ with intima, $^{‡}p<0.05$, $^{‡‡}p<0.01$ with media.*

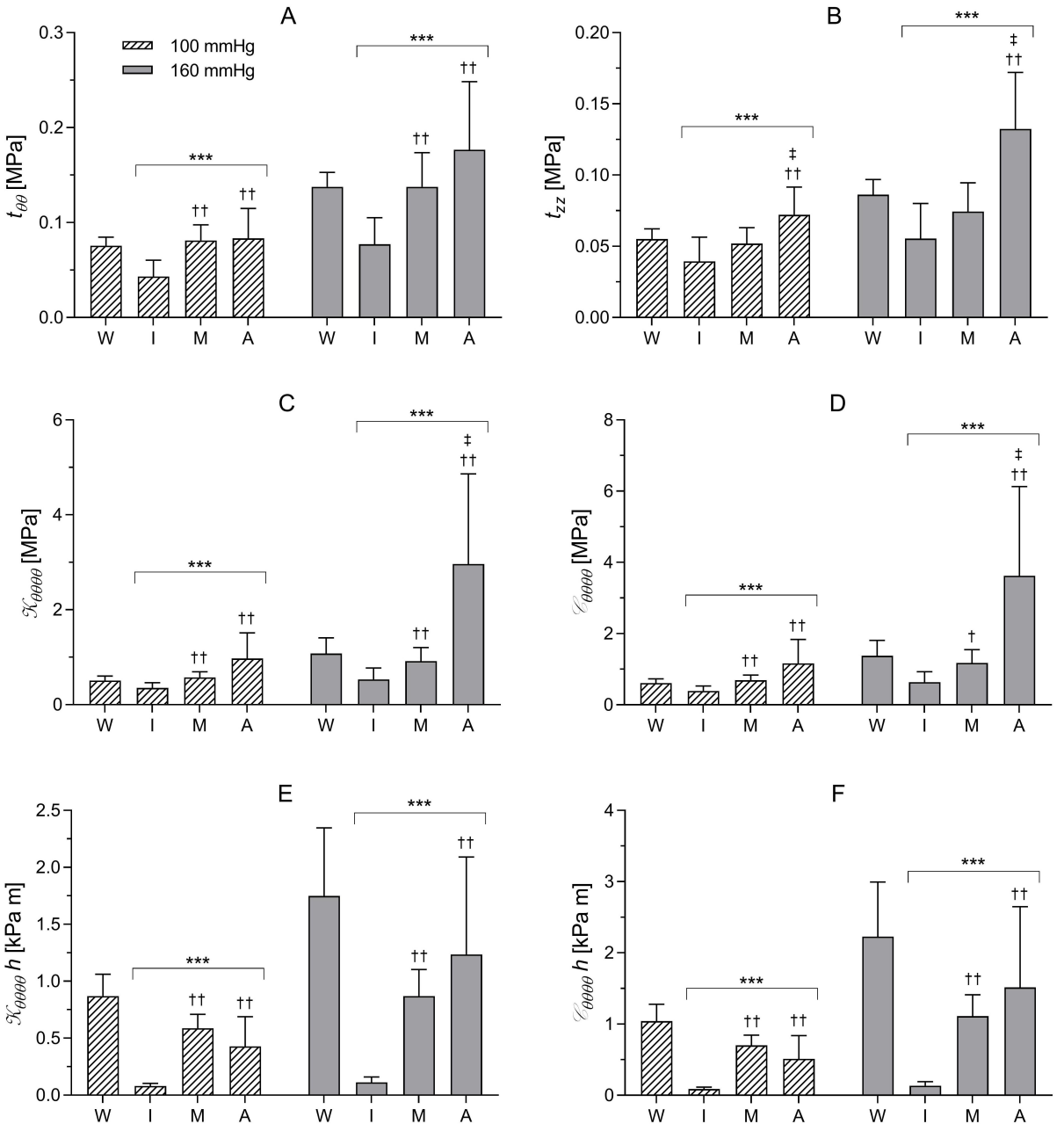

Figure 3.17: *Circumferential ($t_{\theta\theta}$) (A) and longitudinal (t_{zz}) stress (B), tangential elastic modulus ($\mathscr{K}_{\theta\theta\theta\theta}$) (C) and small-on-large circumferential stiffness stiffness ($\mathscr{C}_{\theta\theta\theta\theta}$) (D), structural stiffness calculated with $\mathscr{K}_{\theta\theta\theta\theta}$ (E) and $\mathscr{C}_{\theta\theta\theta\theta}$ (F) in the upper thoracic aorta of pigs at the reference pressures of 100 and 160 mmHg. W=intact wall, I=intima, M=media, and A=adventitia. ANOVA: $^{*}p<0.05$,$^{**}p<0.01$, $^{***}p<0.001$. Pairwise comparison UTA-LTA: $^{‡}p<0.05$, $^{‡‡}p<0.01$, $^{‡‡‡}p<0.001$.Inter-layers pairwise comparison: $^{†}p<0.05$, $^{††}p<0.01$ with intima, $^{‡}p<0.05$, $^{‡‡}p<0.01$ with media.*

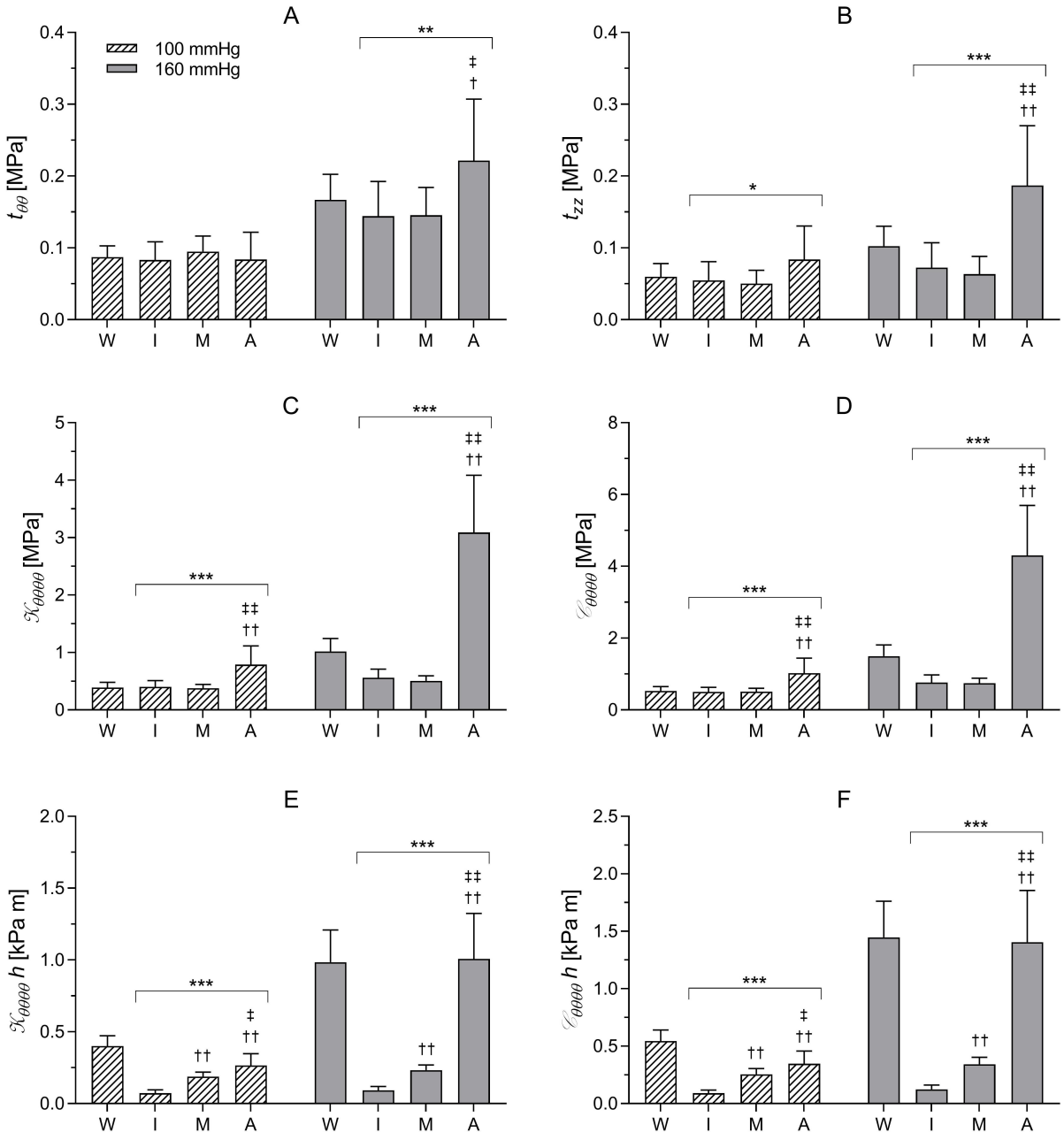

Figure 3.18: *Circumferential ($t_{\theta\theta}$) (A) and longitudinal (t_{zz}) stress (B), tangential elastic modulus ($\mathscr{K}_{\theta\theta\theta\theta}$) (C) and small-on-large circumferential stiffness stiffness ($\mathscr{C}_{\theta\theta\theta\theta}$) (D), structural stiffness calculated with $\mathscr{K}_{\theta\theta\theta\theta}$ (E) and $\mathscr{C}_{\theta\theta\theta\theta}$ (F) in the lower thoracic aorta of lambs at the reference pressures of 100 and 160 mmHg. W=intact wall, I=intima, M=media, and A=adventitia. ANOVA: $^{*}p<0.05$,$^{**}p<0.01$, $^{***}p<0.001$. Pairwise comparison UTA-LTA: $^{\ddagger}p<0.05$, $^{\ddagger\ddagger}p<0.01$, $^{\ddagger\ddagger\ddagger}p<0.001$.Inter-layers pairwise comparison: $^{\dagger}p<0.05$, $^{\dagger\dagger}p<0.01$ with intima, $^{\ddagger}p<0.05$, $^{\ddagger\ddagger}p<0.01$ with media.*

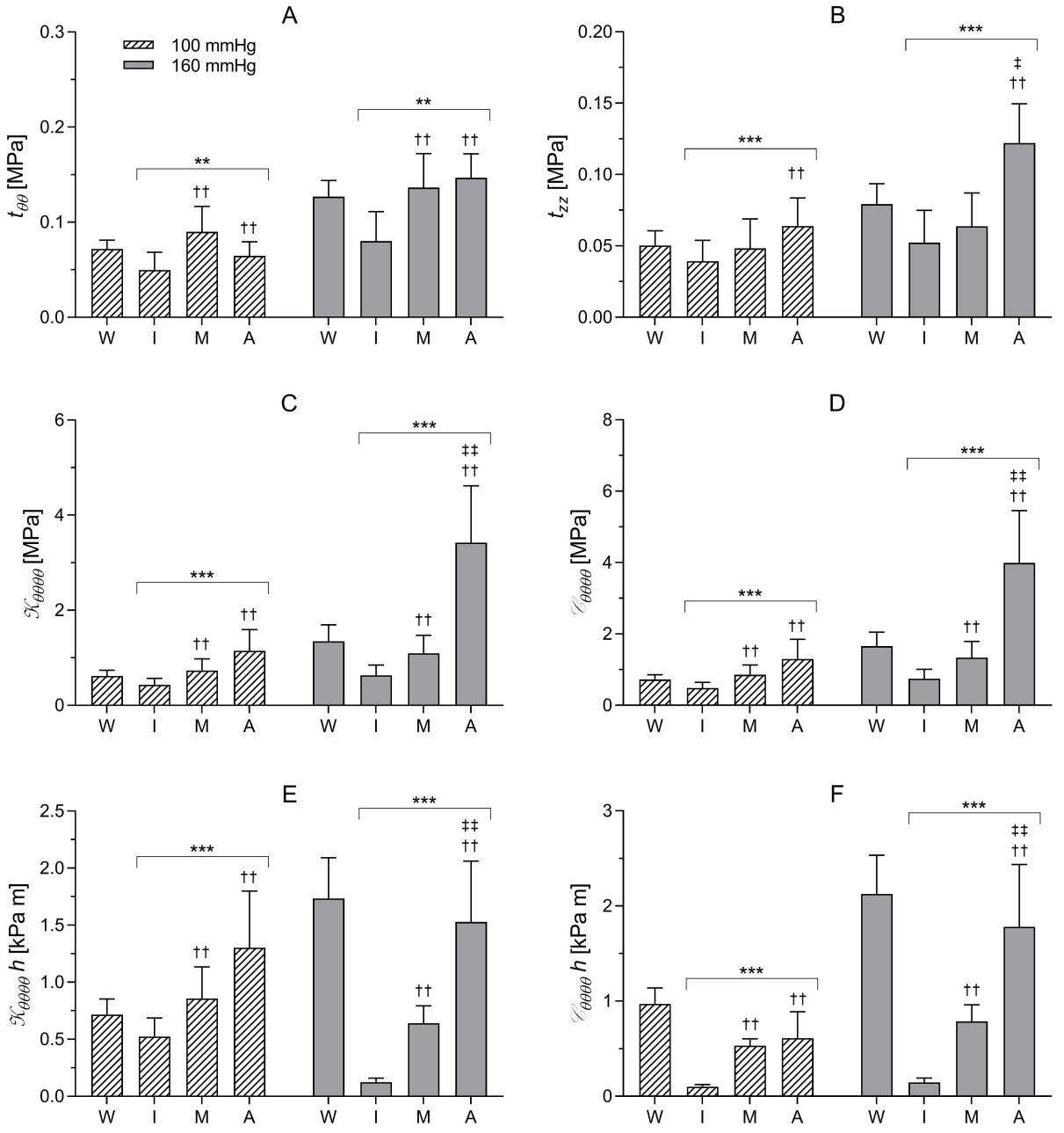

Figure 3.19: *Circumferential ($t_{\theta\theta}$) (A) and longitudinal (t_{zz}) stress (B), tangential elastic modulus ($\mathscr{K}_{\theta\theta\theta\theta}$) (C) and small-on-large circumferential stiffness stiffness ($\mathscr{C}_{\theta\theta\theta\theta}$) (D), structural stiffness calculated with $\mathscr{K}_{\theta\theta\theta\theta}$ (E) and $\mathscr{C}_{\theta\theta\theta\theta}$ (F) in the lower thoracic aorta of pigs at the reference pressures of 100 and 160 mmHg. W=intact wall, I=intima, M=media, and A=adventitia. ANOVA: $^{*}p<0.05$,$^{**}p<0.01$, $^{***}p<0.001$. Pairwise comparison UTA-LTA: $^{\ddagger}p<0.05$, $^{\ddagger\ddagger}p<0.01$, $^{\ddagger\ddagger\ddagger}p<0.001$.Inter-layers pairwise comparison: $^{\dagger}p<0.05$, $^{\dagger\dagger}p<0.01$ with intima, $^{\ddagger}p<0.05$, $^{\ddagger\ddagger}p<0.01$ with media.*

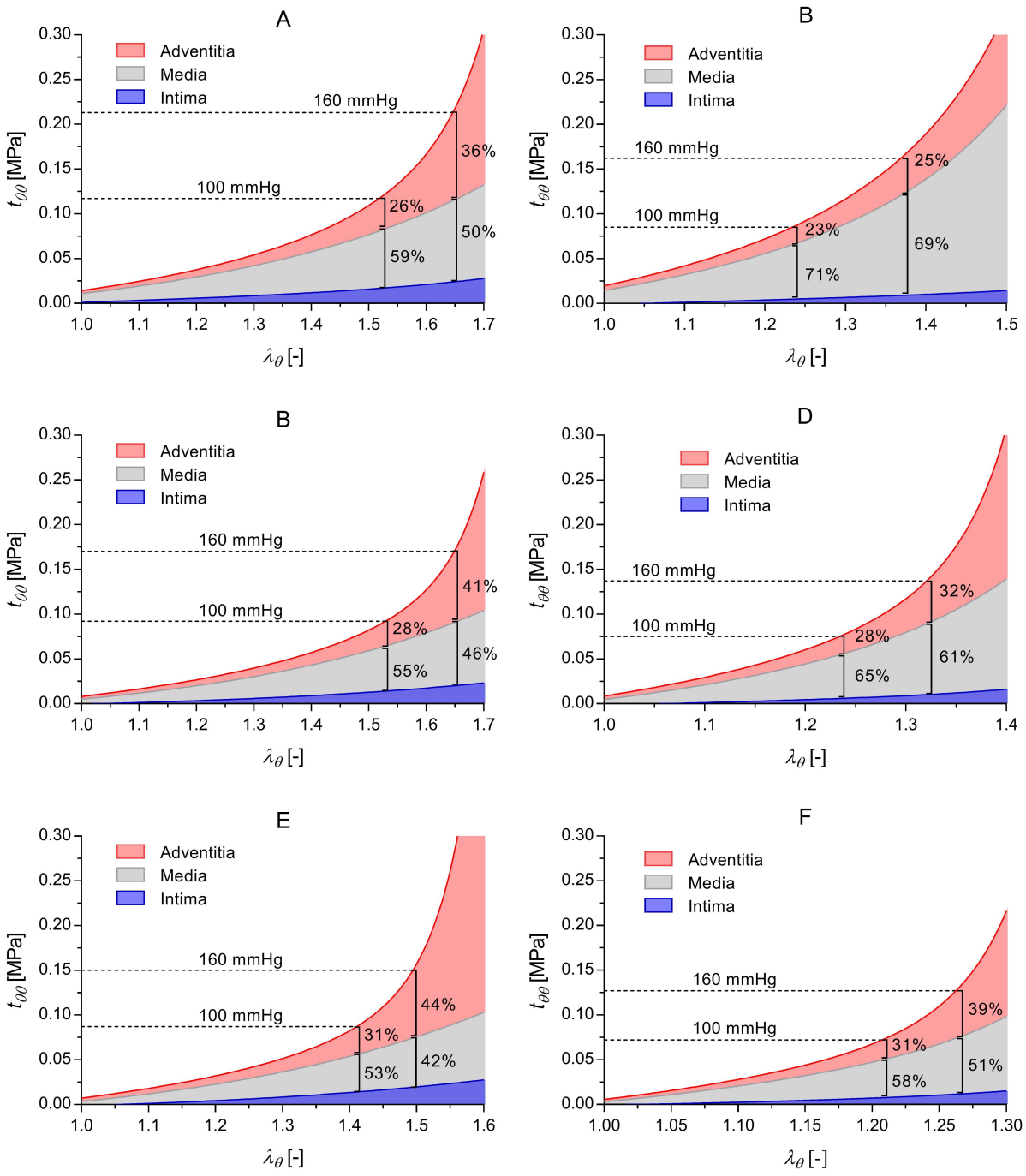

Figure 3.20: *Simulated circumferential stress-stretch relationships of tension-inflation test at the in vivo axial stretch. The blue, grey, and red areas indicate the contribution to the total wall stress provided by the intima, media, and adventitia, respectively. Panels correspond to the ovine ascending aorta (A), upper thoracic aorta (C), and lower thoracic aorta (E) and swine ascending aorta (B), upper thoracic aorta (D), and lower thoracic aorta (F).*

At the UTA, $\mathscr{K}_{\theta\theta\theta\theta}$ and $\mathscr{C}_{\theta\theta\theta\theta}$ at 100 mmHg were 0.34±0.07 and 0.48±0.11 MPa, respectively, in lambs and significantly higher at 0.51±0.09 ($p<0.001$) and 0.60±0.12 MPa ($p<0.05$) in pigs (Figures 3.16C-D and 3.17C-D). Only, $\mathscr{K}_{\theta\theta\theta\theta}$ in pigs was significantly different from corresponding values at the AA. Rising pressure by 60 mmHg produced, on average, a 150% and 112% wall stiffening in lambs and pigs, respectively, that was mainly driven by a 4-folds and 2-folds increase in stiffness of the adventitia. Conversely, stiffening of both intima and media were marginal at ∼30-40% in lambs and ∼50-60% in pigs. In pigs, the media contributed to 65±10% of the total wall stress at 100 mmHg, more than 2-folds more than the adventitia (28±9%). These per cent changed to 61±14 and 32±14 at 160 mmHg. As at AA, shifts in load-bearing were much more accentuated in lambs than pigs, moving from 56±9% for the media and 28±7% for the adventitia at 100 mmHg to 46±8% and 41±8%, respectively, at 160 mmHg (Figure 3.19C-D). In both species, structural stiffnesses were comparable in the media and adventitia at 100 mmHg, while that of the adventitia became significantly higher than in the media at 160 mmHg in lambs only (Figures 3.16E-F and 3.17E-F).

As for the UTA, LTA $\mathscr{K}_{\theta\theta\theta\theta}$ and $\mathscr{C}_{\theta\theta\theta\theta}$ at 100 mmHg were significantly lower in lambs than pigs (0.39±0.09 vs 0.62±0.12 MPa, $p<0.001$, and 0.53±0.11 and 0.72±0.13 MPa, $p<0.001$) (Figures 3.18C-D and 3.18C-D). Further, distal stiffening (i.e. increase in wall stiffness moving downstream in the aorta) was observed only in pigs ($p<0.001$). Changes in wall stiffness with further pressurisation to 160 mmHg were comparable to those observed at the UTA: 160% and 118% in lambs and pigs, respectively, as was the layer-specific stiffening, with marginal stiffening for the intima and media (∼30-40% in lambs and ∼40-50% in pigs) and larger changes for the adventitia (292% and 198%, respectively). Wall stress partitioning was 16±5%-53±9%-31±5% in lambs and 11±3%-58±7%-31±7% in pigs (intima-media-adventitia) at 100 mmHg and shifted to 14±4%-42±7%-44±5% and 10±3%-51±7%-39±8% at 160 mmHg, with the adventitia carrying most of the circumferential load in lambs (Figure 3.20E-F).

3.4 Discussion

Arterial structure and function are strongly related. As described in Section 1.2, arteries are tri-layered vessels, where the composition and structural organisation strongly depends on the location in the arterial tree. This chapter aimed to introduce a new simple and inexpensive experimental and computational approach for the characterisation of the passive mechanical response of arteries starting from the mechanical behaviour of its isolated layers (the intima, the media, and the adventitia), and to provide insight on the role each layer plays in the load-bearing at different levels of arterial BP. As the proposed approach relies solely on wall and

layer-specific mechanical data obtained from inexpensive and widely available uniaxial testing and does not involve expensive imaging and multi-axial testing techniques, it could potentially make multi-layered modelling of the arterial wall accessible to a broad audience. The model indicated that, as expected, at the mean physiological pressure of 100 mmHg the media bears most of the circumferential load. When pressure increases to the hypertensive range, the rapid stiffening of the adventitia generates a shift of the load-bearing from the compliant media to the outermost layer, considerably affecting the wall stiffness.

3.4.1 Aortic wall and layer-specific structural features

Aortic tapering was significant in both species; taking the ascending aorta as a reference, reductions in calibre at the upper and lower thoracic aorta were 17% and 31% in lambs, and 16% and 33% in pigs, in agreement with changes reported previously (Han & Fung, 1991; Peña et al., 2015). In both species, the thickness to internal radius ratio did not change along the thoracic aorta but was significantly higher in lambs due to an approximately 22-25% smaller diameter compared to pigs with no difference in wall thickness. It is worth noting, however, that the lamb aortic wall was much softer than that of pigs and experienced higher deformations to reach the simulated *in vivo* loading condition. Therefore, the simulated *in vivo* thickness to internal radius ratio was lower in lambs (ranging 0.11-0.15) compared to pigs (0.16-0.19) as indicated by the higher circumferential and axial stresses found in lambs.

The isolation of the arterial wall anatomical layers is not a new technique, and several works have shown how the concentric structure of the wall makes this process relatively simple, causing little damage to the isolated structures. Any peeling-induced damage has been shown to be limited to the interconnective tissue between adjacent layers and, hence, will have negligible effects on the layers' macroscopic behaviour (Holzapfel et al., 2007; Peña et al., 2015; Holzapfel et al., 2005). Here, the intima accounted for approximately 10-15% of the wall thickness, the adventitia for 25 to 35%, and the media for 45-65%, depending on the species and on the location along the aorta, in agreement with values of isolated layers thickness reported for the porcine proximal and distal thoracic aorta (Peña et al., 2015; Sokolis, 2019) and human lower thoracic aorta (Holzapfel et al., 2007). However, previous measurements of the medial and adventitial thicknesses from light-microscopy histological images seem to indicate that the adventitial layer obtained via peeling might be thicker than the anatomical adventitia (Sokolis, 2007). Nevertheless, Peña et al. (2015) reported that the per cent of the number of MLU wrongly included in both the intima and adventitia were minimal and, therefore, this errors in the layer separation are not expected to largely influence the results.

3.4.2 Wall and layer-specific mechanics

The lamb and pig aorta showed significantly different mechanical properties, with the pig aorta exhibiting a significantly stiffer response to deformation in both circumferential and longitudinal directions in all the investigated regions but the AA. Similar results have been found when investigating the biaxial mechanical properties of the carotid artery of different mammals (Prim et al., 2018). This difference was also visible in terms of stiffness-like and fibre exponential model parameters that were significantly lower in lambs compared to pigs. Circumferential tangential elastic modulus in the simulate *in vivo* loading condition ranged from ∼0.3-0.4 MPa at 100 mmHg to ∼0.8-1.0 MPa at 160 mmHg in lambs and from ∼0.4-0.6 MPa to ∼0.8-1.3 MPa in pigs, in agreement with values reported previously in tension-inflation experiments in pigs (Kim & Baek, 2011; Lillie et al., 2012, 2010) and sheep (Bia et al., 2005; Wells et al., 1998).

In contrast, the constitutively determined degree of anisotropy of the wall at different locations along the aorta was impressively similar in the two species: markedly anisotropic in the ascending aorta and almost isotropic in the descending thoracic aorta (both UTA and LTA). Using a similar testing and fitting protocol Weisbecker et al. (2012) found a similar diagonal orientation of fibres in the human thoracic and abdominal aorta (α=51° and 38.8°, respectively). Further, several studies on the AA of both humans (Haskett et al., 2010) and other mammals (Deplano et al., 2016) reported higher stretches in the axial than the circumferential direction in equibiaxial tensile tests. These findings suggest the level of anisotropy might purely reflect functional differences between regions, regardless of the inter-species differences in aortic wall mechanical properties. Indeed, compared to other locations of the aorta and, in general, of the arterial tree that are subjected to negligible torsion and variation of the axial stretch throughout the cardiac cycle, the ascending aorta experienced cyclic longitudinal extension and torsion due to its proximity to the heart (Wittek et al., 2016). The different function of the ascending aorta might, thus, explain its higher anisotropy compared to other locations along the aorta. Further, Ferruzzi et al. (2018) hypothesised the existence of an 'exertion reserve' allowing the axial stretch of the ascending aorta to increase with increasing level of exercise, allowing to store more elastic energy and augment blood flow in diastole.

Changes in the degree of anisotropy of the wall tissue found here were mostly related to a shift in fibres direction in the adventitia, showing strong preferential circumferential orientation only in the ascending aorta. Conversely, the media exhibited anisotropic behaviour in all three regions. This finding suggested that, independently on the aortic region, the function of the media consists mainly in providing elasticity in the circumferential direction, while marginally contributing in the axial direction, in agreement with previous findings (Zheng & Ren, 2016).

Finally, the intima showed higher isotropy in the ascending aorta compared to the descending thoracic aorta, hence following an opposite trend compared to that of the intact wall. The functional reason behind this shift is unclear and, to the extent of author's knowledge, unreported before.

Interestingly, Peña et al. (2015, 2017) and colleagues found that fibres in both the intact wall and isolated layers leaned more towards the circumferential direction compared to results reported here for both the UTA and LTA. The reason for these differences is likely attributable to the different target stress used in the fitting process; model parameters in this study were obtained by fitting stress-stretch relationships up to a Cauchy stress level of 250kPa. Peña et al. (2015) tested samples up to a stress of first Piola-Kirchhoff stress of 60 and 120 kPa (∼150-170 kPa in terms of Cauchy stress). As fibres are gradually recruited while the wall deformation increases (Chow et al., 2014; Krasny et al., 2017b), fitting the wall behaviour up to a lower target stress might capture only part of the process, when fibres are still not completely engaged. Indeed, Peña et al. (2015) reported that the fibre orientation shifted from a preferentially circumferential direction towards a 45° diagonal direction when fitting stress-stretch relationship of the same arteries up to 60 and 120 kPa first Piola-Kirchhoff stress. Ultimately, the choice of the fitting target stress is dictated by the objective of the study and the type of wall behaviour that has to be modelled, balancing the trade-off between the accuracy of the fit in the desired stress range and amplitude of the range itself.

3.4.3 Tri-layered wall model

The development of a tri-layered wall model allowed investigating the role each layer plays in the overall wall mechanics in simulated *in vivo* physiological and pathological (i.e., increased BP) axial tension and pressurisation. Since aortae were not directly excised from the euthanised animals, the *in vivo* axial stretch λ_z to be used in the tension-inflation simulations was estimated as the stretch that guarantees a pressure-independent reduced axial force (Van Loon et al., 1977). It has, indeed, been postulated that arterial remodelling aims at satisfying this structurally efficient condition which prevents the risk of buckling and aortic occlusion. λ_z was significantly higher in lambs than pigs, ranging from 1.1 to 1.5 in lambs and 1.0-1.3 in pigs. Han & Fung (1995) experimentally determined λ_z in the porcine aorta as a function of the axial position, reporting values ranging ∼1.1-1.3 in the proximal thoracic aorta, as also confirmed in more recent studies (Peña et al., 2015). Similar values were also reported for the ovine thoracic aorta (Bia et al., 2005; Wells et al., 1998). Interestingly, in disagreement with previous findings (Han & Fung, 1995), in both species λ_z decreased when moving downstream along the aorta.

It has been shown in mice, however, that λ_z determined as the cross-over point in the axial stretch-reduced axial force curves at different distending pressures significantly overestimates the *in vivo* axial stretch in the ascending aorta (Ferruzzi et al., 2018), possibly reflecting an unique functional feature of the ascending aorta that is capable of increasing the stored elastic energy by increasing the axial stretch in response to increased cardiac output during exercise. Therefore, λ_z imposed here in the tension-inflation simulations of the ascending aorta might overestimate the physiological λ_z at rest.

Tri-layered modelling of the arterial wall showed that, as expected, at the physiological mean pressure of 100 mmHg the media bears more than half of the total circumferential load, independently on the species and aortic location. Further, the average load bearing per cent of adventitia was comparable, if not lower, than its relative thickness. These findings support the generally accepted hypothesis that, in the physiological range of pressures, the media determines the elastic function of conduit arteries (Fonck et al., 2007; Zheng & Ren, 2016). When P_{ref} rose to 160 mmHg, representing a hypothetical hypertensive condition, the aortic wall stiffened by a factor that ranged from 1.9 to 2.6 depending on the aortic region (pressure-related stiffening was enhanced in distal compared to proximal regions) and on the species (higher in lambs than pigs). This stiffening was accompanied by a shift in load-bearing from the compliant media to the stiffer collagen-rich adventitia. Reflecting changes in wall stiffness, this shift was more pronounced in lambs (on average −9-11% for the media and +11-13% for the adventitia) than in pigs (on average −2-7% for the media and +2-8% for the adventitia). Indeed, while intimal and medial stiffening over the 60 mmHg was relatively small, the adventitial circumferential stiffness was 2 to 3-folds and 3 to 4-folds higher at 160 than 100 mmHg in pigs and lambs, respectively. Figures 3.9 to 3.11 show that, compared to intima and media, the adventitia was characterised by a delayed but abrupt recruitment of collagen fibres, mechanically translating in an initial highly compliant behaviour at low stretches followed by a rapid stiffening at higher deformations. The results presented in this study suggest that the microstructure of the adventitia is finely tuned so that its *in vivo* working point coincides with the transition point in this biphasic behaviour, thus guaranteeing compliance at mean physiological pressure and protection against supra-physiological loads.

Previous studies have shown that residual deformations are fundamental to guarantee a homogeneous distribution of stresses across the wall thickness, counterbalancing the gradient of circumferential deformation induced by the inflation of a cylindrical vessel (i.e., maximum at the internal radius and minimum at the external radius as suggested by Eq. 3.9). The results presented here confirm this hypothesis; at 100 mmHg the circumferential stress was always not

significantly different between media and adventitia. This was also the case for the intima but in lambs only. Recently, Díaz et al. (2021) found different load distributions for the arterial layers with a similar animal model; the media contributed marginally to the wall behaviour both at physiological and supraphysiological pressures. It is worth considering that they used a thick-walled modelling approach with parameters from a single sample, which highlighted the difficulty in identifying and including layer-specific opening angles in the wall model (Holzapfel & Ogden, 2010a). Further, uniaxial testing, as well as planar biaxial testing, requires flattening of the samples so that the layer-specific model parameters do not necessarily describe the layer behaviour in its stress-free configuration. Due to the simplified thin-layered modelling approach chosen in this study, each layer is considered as a membrane and residual deformations are considered as average values across the layer thickness. The layer-specific residual deformation in κ_{unloaded} can be determined by a multiplicative combination of the deformation gradients $\mathbf{F}_1\mathbf{G}^k$ (Tables 3.5 and 3.5); where $\mathbf{G}^k$ describes residual deformations layers are subjected to when part of the wall and at the beginning uniaxial test and $\mathbf{F}_1$ maps the deformation into a cylindrical vessel. Interestingly, combing $\mathbf{F}_1$ and $\mathbf{G}^k$ shows that residual deformations were location-dependent in pigs; the residual compressive strain of the intima decreased from 15% at the AA to 10% at the UTA, and reached 8% at the LTA. Similarly, the residual tensile strain of the adventitia was 10% at the AA, 3% at the UTA and became compressive at the LTA (−1%). Conversely, the residual deformations remained relatively constant throughout the length of the thoracic aorta in lambs; the intima was subjected to a 14%, 15% and 13% compressive residual strain at the AA, UTA, and LTA, respectively, while the tensile residual strain of the adventitia was 4% at the AA and UTA and 3% at the LTA. These results are in agreement with the opening angle experiments, where pigs, but not lambs, showed a proximal to distal decrease of wall OA.

Accounting for the residual deformations is a complex procedure, and these are frequently neglected in studies on arterial mechanics, potentially leading to wrong interpretation of the results. For example, de Lucio et al. (2020) developed a thick-walled tri-layered model of the aneurysmal aorta neglecting residual deformation. Their results, showing circumferential stresses monotonically decreased across the wall thickness, lead to the conclusion that the intima plays a major role in the mechanical behaviour of the aneurysmal aorta. Similarly, recent studies, coupling mechanical testing with 'live' multiphoton microscopy, observed that the untangling of collagen in the adventitia happens at higher deformations compared to that of collagen fibres in the media and hypothesised the former exhibit delayed recruitment in response to high pressure levels only (Chow et al., 2014; Krasny et al., 2017b). However, flattening of the arterial wall in biaxial tensile test necessarily introduced artificial deformation of the three layers, compressing

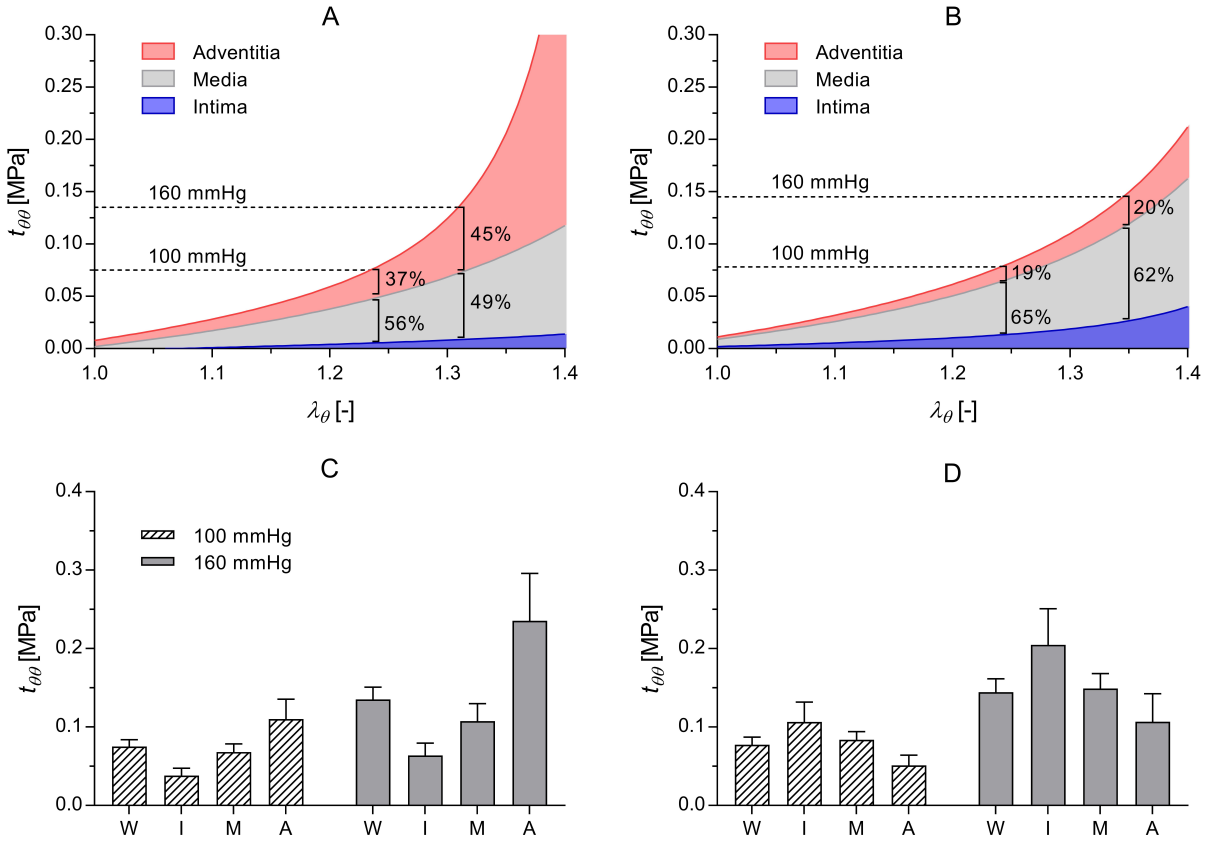

Figure 3.21: *Effect of neglecting wall prestretches in the stress distribution among arterial layers. In panels A and C, the layer-specific prestretches defined by the deformation gradient* $\mathbf{G}^k$ *are neglected, leading to over-stretching of the adventitia when closing the flat strip into a ring. In panels B and D, both* $\mathbf{G}^k$ *and* $\mathbf{F}_1$ *are neglecting and the oppsoite effect is obtained; over-stretching of the intima. In both cases, the media is largely unaffected bcause of its middle-location through the wall thickness.*

the adventitia. Figure 3.21 illustrates wall circumferential stress and layer-specific load-bearing in the swine UTA when $\mathbf{G}^k = \mathbf{I}$, i.e. the flat wall is stress-free, and when both $\mathbf{G}^k = \mathbf{F}_1 = \mathbf{I}$, the closed cylinder is stress-free. Assuming that the flat wall is stress-free implies that the deformation gradient $\mathbf{F}_1$ alone defines the residual deformation in κ_{unloaded}. As clear from Table 3.6, $\mathbf{F}_1$ determines a 10-15% circumferential compression strain for the intima and a 8-12% tensile deformation for the adventitia. The latter is normally compensated by an circumferential compression of the adventitia in $\mathbf{G}^k$ (Table 3.5). Therefore, as shown in Figure 3.21B-D, assuming $\mathbf{G}^k = \mathbf{I}$ results in the circumferential stress monotonically increasing from the intima to the adventitia and an early recruitment of the adventitia (see Figures 3.16A and 3.19D for comparison with the complete model). Opposite effects are achieved when residual deformation are completely neglected ($\mathbf{G}^k = \mathbf{F}_1 = \mathbf{I}$); as mentioned above inflation of a cylindrical structure

produces circumferential deformation that decrease moving outward across the wall thickness. Therefore, if layer-specific residual deformations are neglected, the circumferential stress also follows a similar trend, leading to an overestimation and underestimation of the contributions of the intima and adventitia, respectively, to the wall mechanics (Figure 3.20B-D) as in study of de Lucio et al. (2020).

Study limitations

The constitutive parameters of the isolated layers were estimated by fitting simultaneously the stress-stretch relationships resulting from the uniaxial tensile testing in the circumferential and axial directions as done previously (Holzapfel et al., 2005; Weisbecker et al., 2012). The deformation in the other principal direction (i.e. axial and circumferential, respectively) was not measured but determined by enforcing incompressibility and zero traction in all principal directions except that of the load. Peña et al. (2015) found that the biaxial response of the arterial wall inferred from constitutive modelling of uniaxial relationships poorly represented the experimental biaxial response of arteries. However, when fitting uniaxial stress-stretch relationships, they assumed the deformation in the other two principal directions (e.g., axial and radial in circumferential uniaxial tests) to be equal, but this is not the case in an isotropic matrix reinforced by fibres located in the circumferential-longitudinal plane of the artery.

Furthermore, a thin-walled modelling approach was used here, hence, neglecting the bending stiffness and opening angles of the isolated layers. The application of a thick-walled modelling framework would likely improve the accuracy of the estimation of the composite wall mechanical behaviour, but the complexity of the model and data required would also increase considerably.

3.5 Chapter conclusions

While developing methods to accurately assess arterial wall mechanical properties *in vivo* represents the ultimate goal of cardiovascular mechanics research, *ex vivo* techniques and animal studies are useful to further our understanding of the behaviour of the arterial wall. Indeed, they allow to evaluate wall properties to a level of detail that is hardly achievable *in vivo*. In most *ex vivo* investigations, the arterial wall is assumed to be a material with uniform mechanical properties, thus neglecting its complex tri-layered nature. Some studies have attempted to address this issue by directly quantifying microstructural features of the layer-specific wall constituents via advanced microscopy techniques. While this approaches might provide more accurate information on arterial mechanics at a constituents level, their high cost and limited availability makes adoption of these methods infeasible to most laboratories and researchers.

This study proposed a novel experimental/computational approach to study arterial mechanics where layer-specific mechanical properties, determined experimentally via simple, inexpensive and widely available uniaxial testing, are used to formulate a tri-layered model of an artery. The model allowed for the in-depth analysis of the contribution of each layer to the overall wall behaviour, highlighting a gradual shift in load-bearing from the compliant media to the stiffer adventitia with increasing luminal pressure. This process results in the well-known exponential pressure-diameter relationship of arteries in the physiological pressure range. The application of the proposed modelling framework to human arterial samples could provide valuable insight into the impact of layer-specific remodelling associated with ageing and pathologies on the wall mechanics. Furthermore, the limited amount of tissue required in uniaxial tensile tests makes the proposed methodology highly advantageous for human *ex vivo* studies.

Chapter 4

The mechanical behaviour of the human aortic wall *ex vivo*

4.1 Introduction

Ageing has important consequences on the macro- and microstructure of human arteries, involving all constituents that determine their mechanical response. VSMCs migrate from the media, where they are substituted by collagen fibres, to the intima, where they proliferate, thus generating a considerable intimal thickening (Graham et al., 2011; Harvey et al., 2016; Tesauro et al., 2017). Further, the organization of elastin, undergoing very limited turnover *in vivo*, becomes sparser and fragmented, thus losing its functionality (Greenwald, 2007; Harvey et al., 2016; Kohn et al., 2015). On the other hand, collagen crosslinking increases with age, as does the degree of alignment of its fibres (Kohn et al., 2015; Tsamis et al., 2013; Haskett et al., 2010). Furthermore, the concentrations of arterial wall components are also altered with age; collagen volume fraction rises with age, while those of elastin and VSMCs decrease (Greenwald, 2007; Spina et al., 1983; Tsamis et al., 2013). Since the elastin content remains unchanged, these changes have to be attributed to enhanced synthesis of collagen fibres (Graham et al., 2010; Harvey et al., 2016; Spina et al., 1983; Tesauro et al., 2017; Tsamis et al., 2013).

These structural changes result in a gradual stiffening of the arterial wall with age, with the circumferential tangential elastic modulus of the thoracic aorta at mean arterial pressure (100 mmHg) typically more than doubling across the life-span of an individual (Haskett et al., 2010; Jadidi et al., 2020). Further, the pioneering study on the effect of ageing on arterial mechanics of Learoyd & Taylor (1966) showed that ageing enhances the pressure-dependence of arterial stiffness in elastic arteries. In Chapter 3, tri-layered modelling of the healthy aortic wall of young animals has allowed in-depth analysis of the effects of increased BP on layer-specific arterial mechanics and wall stiffness, indicating that BP-related stiffening is not associated with a uniform stiffening across the wall thickness but with a shift of load-bearing from the compliant media to the rapidly stiffening adventitia.

The present chapter aimed to understand how age-related remodelling of the aortic wall affect the stiffness of the healthy human thoracic aorta, first, providing reference value of the wall tangential elastic modulus in the circumferential direction, the most relevant to the pulsatile blood flow. Second, this chapter seeks to determine how age-related remodelling affects the pressure-dependence of arterial stiffness. Finally, using constitutive modelling of experimental data, this study aims to provide a plausible microstructural interpretation of the mechanical data, including insight into the timing of arterial remodelling by discerning between alterations in the structure-mechanics of elastin and collagen (i.e., collagen and elastin stiffness-like parameters and collagen exponential constant, see Chapter 2.2.4), and evaluating consequences on arterial

function.

4.2 Methods

4.2.1 Arterial samples

This study was approved by the Brunel Research Ethics Committee (Reference: 11502-TISS-Jun/2019-19421-6). Aortae were obtained from 127 human organ donors following Research Ethics Committee (REC) and family consent, and stored at −80°C. A 10 mm wide ring was cut from each arterial segment in the thoracic region and the connective tissues surrounding the vessel carefully removed before testing. The presence of atherosclerotic plaques, calcification or side branches was verified. Unloaded wall thickness (h_0^{wall}), ring internal diameter (D_0) and width (w_0) were measured using a digital calliper. Rings were subdivided into six groups according to the donor's age (Table 4.1).

4.2.2 Mechanical testing

Aortic rings underwent uniaxial tensile ring testing. Each ring was mounted on an Instron (Norwood, MA, USA) tensile device equipped with a 100 N load cell and tissue holder suitable for ring tests. The diameter of each holding pin $\mathscr{d}$ was 5 mm (Figure 3.1). The ring was first preloaded at 0.05 N to ensure that the two sides of the ring were parallel to the loading direction, then tested according to the following protocol: 1) cycled three times between 0 and 30 mmHg equivalent force, 2) cycled three times between 30 and 80 mmHg equivalent force, and 3) cycled three times between 15 and 100 mmHg equivalent force at a speed of 10 mm/min. The pressure-equivalent load was estimated as previously reported (Burton, 1954):

$$F = PD_0w_0 \ , \tag{4.1}$$

where F is the force applied by the tensile device and P is the arterial pressure. The loading phase of the last load cycle from 15-100 mmHg was considered for the analysis. Samples were kept wet throughout the test by spraying saline solution. All tests were run in duplicate and reported data are the average of both.

4.2.3 Data analysis

The experimental circumferential Cauchy stress ($t_{\theta\theta_{\text{exp}}}$) was calculated as (see section 3.2.1):

$$t_{\theta\theta_{\text{exp}}} = \frac{F}{A} = \frac{F}{2h_0^{\text{wall}}w_0}\lambda_\theta \ , \tag{4.2}$$

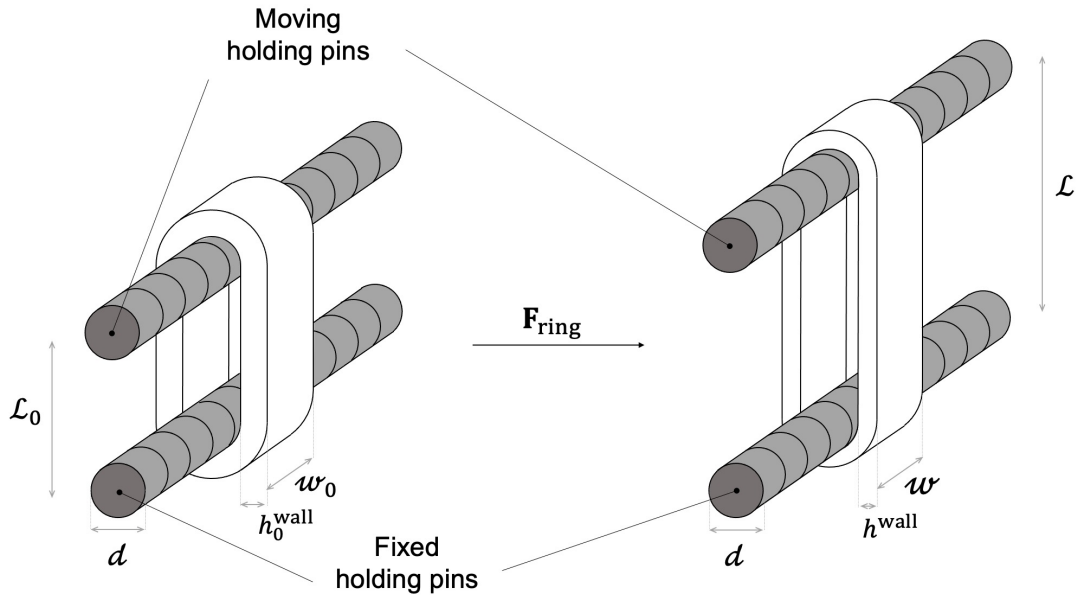

Figure 4.1: *Schematic representation of the deformation characterising ring tensile tests.*

where A is the deformed cross-sectional area and λ_θ is the circumferential component of the deformation gradient $\mathbf{F}_{\text{ring}}$ mapping the deformation characterising the ring test (Figure 3.1). While in uniaxial tensile tests the induced deformation is uniform throughout the thickness of the specimen, in ring tests, the curvilinear shape of the sample around the holding pins makes all stretches component dependent on the radial coordinate (i.e., through the sample thickness). Hence, the exact definition of the deformation gradient is not trivial. However, the circumferential stretch can be approximated by considering the deformation of the lumen.

With reference to Figure 4.1, the undeformed length of the lumen Γ_0 can be calculated as the sum of the length of the two parallel sides of the ring and the length of the two circular semi circumferences at the holding pins.

$$\Gamma_0 = 2\mathscr{L}_0 + 2\left(\frac{\pi d}{2}\right) = 2\mathscr{L}_0 + \pi d \ , \tag{4.3}$$

where $\mathscr{L}_0$ is the initial distance between the holding pins. Similarly, the deformed length of the lumen Γ is

$$\Gamma = 2\mathscr{L} + 2\left(\frac{\pi d}{2}\right) = 2\mathscr{L} + \pi d \ . \tag{4.4}$$

Hence, the circumferential deformation of the lumen can be calculated as

$$\lambda_\theta = \frac{\Gamma}{\Gamma_0} = \frac{2\mathscr{L} + \pi d}{2\mathscr{L}_0 + \pi d} \tag{4.5}$$

and the linearised circumferential strain becomes

$$\epsilon_{\theta\theta} = \lambda_\theta - 1 = \frac{2\mathscr{L} - 2\mathscr{L}_0}{2\mathscr{L}_0 + \pi d} \ . \tag{4.6}$$

The tangential elastic modulus in the circumferential direction was calculated as

$$\mathscr{K}_{\theta\theta\theta\theta} = \frac{\partial t_{\theta\theta}}{\partial \epsilon_{\theta\theta}}\Big|_{P=P_{\mathrm{ref}}} , \tag{4.7}$$

indicating the tangent to the circumferential Cauchy stress-circumferential strain relationship at the stress level equivalent to the pressure P_{ref}. The pressure-equivalent stress level can be determined using the Laplace equation

$$t_{\theta\theta_P} = \frac{P_{\mathrm{ref}} R}{h^{\mathrm{wall}}} , \tag{4.8}$$

where R and h^{wall} are the deformed radius and thickness, respectively. While R can easily be determined as the product between the undeformed radius R_0 and λ_θ, changes in wall thickness were not measured throughout the test. Hence, h was approximated with the undeformed thickness h_0, so that Eq. 4.8 reduces to

$$t_{\theta\theta_P} \approx \frac{P_{\mathrm{ref}} R_0}{h_0^{\mathrm{wall}}} \lambda_\theta . \tag{4.9}$$

$\mathscr{K}_{\theta\theta\theta\theta}$ was calculated for $P_{\mathrm{ref}} = 60$, 80, and 100 mmHg. Note that $t_{\theta\theta_P}$ for $P_{ref} = 100$ mmHg corresponds to the peak stress reached during the ring test.

As shown in Chapter 3 and reported in several studies (Gavish & Izzo, 2016; Bergel, 1961; Burton, 1954), the stress-strain relationship of arteries is approximately exponential in the physiological range of pressure. This entails an approximately linear $\mathscr{K}_{\theta\theta\theta\theta}$-$P$ relationship and its slope quantifies the pressure-related arterial stiffening

$$\dot{\mathscr{K}}_{\theta\theta\theta\theta} = \frac{\mathrm{d}\mathscr{K}_{\theta\theta\theta\theta}}{\mathrm{d}P} . \tag{4.10}$$

$\dot{\mathscr{K}}_{\theta\theta\theta\theta}$ was determined as the slope of the linear regression between $\mathscr{K}_{\theta\theta\theta\theta}$ and P for $P_{\mathrm{ref}} = 60$, 80, and 100 mmHg.

4.2.4 Constitutive modelling and parameter fitting

Determination of $\mathscr{K}_{\theta\theta\theta\theta}$ and $\dot{\mathscr{K}}_{\theta\theta\theta\theta}$ allows characterising the effects age-related arterial remodelling has on the mechanical properties of the arterial wall, but does not provide insight into the microstructural changes that are at their basis. Structurally-motivated constitutive models are mathematical descriptions of the wall behaviour that account for the mechanical contribution of its constituents. Therefore, fitting the model parameters on mechanical data can provide insight into age-related constituent-specific remodelling determining the observed changes in the macroscopic wall behaviour. As for the *ex vivo* test on animal aortae, the hyperelastic behaviour of the human thoracic aortic wall was modelled using the HGO-SEF Ψ described in Chapter 2.2.4,

which accounts for the contribution of an isotropic matrix (typically associated with elastin) reinforced by two symmetrically-oriented families of fibres (collagen). As in Chapter 3, the model parameters were determined by minimising the cost function Π corresponding to the error between the modelled and experimental stresses:

$$\Pi = \sum \left(t_{\theta\theta_{\text{exp}}} - t_{\theta\theta}\right)^2 + \sum \left(t_{zz_{\text{exp}}} - t_{zz}\right)^2 \ . \tag{4.11}$$

where z indicates the axial direction. It is worth noting, however, that unlike in Chapter 3 where uniaxial tests were performed in both circumferential and axial directions, ring tests quantify the arterial behaviour in circumferential direction only. Therefore Π reduces to

$$\Pi = \sum \left(t_{\theta\theta_{\text{exp}}} - t_{\theta\theta}\right)^2 \ . \tag{4.12}$$

The modelled circumferential Cauchy stress $t_{\theta\theta}$ was calculated as

$$t^k_{\theta\theta} = 2\mu\left(\lambda_\theta^2 - \frac{1}{\lambda_\theta^2\lambda_z}\right) + 8k_1\left[\tau\left(\lambda_\theta^2 - \frac{1}{\lambda_\theta^2\lambda_z^2}\right) + (1-3\tau)\lambda_\theta^2\cos\alpha^2\right] \\ [\tau I_1 + (1-3\tau)I_4 - 1]\, e^{k_2[\tau I_1 + (1-3\tau)I_4 - 1]} \ , \tag{4.13}$$

with λ_z determined iteratively by enforcing incompressibility and ensuring that stresses equal 0 in the sample axial t_{zz} and radial t_{rr} directions.

The absence of information on the mechanical behaviour in the axial direction does not allow the evaluation of the degree of anisotropicity of the tissue which, from the constitutive modelling perspective, is determined by the fibre orientation and dispersion parameters α and τ, respectively (see Figure A1). As α and τ cannot be accurately determined, including these parameters in the fitting routine would lead to overfitting, implying that multiple combinations of model parameters similarly minimise Π and the estimated parameters lose their physical meaning. Therefore, α and τ were fixed to values previously reported in the literature. Using a similar model Haskett et al. (2010) found that the fibre orientation shifted towards the axial direction with progressing age, in agreement with findings reported by Weisbecker et al. (2012) in older adults. Similar results were reported by Jadidi et al. (2020), although their model did not include a fibre dispersion parameter τ. Therefore, α was set to 44.5° for people <60 years and 50.0° in older adults (Haskett et al., 2010; Weisbecker et al., 2012). It is worth noting that similar fibre orientations were observed in the thoracic aorta of young pigs and lambs (see Chapter 3). Similarly, τ was set to 0.10 for young arteries (donor's age <30 years) and 0.20 for middle-aged and older donors (Haskett et al., 2010; Weisbecker et al., 2012). Further, since imposing step-wise changes to α and τ could possibly lead to abrupt variation of the fitted μ, k_1 and k_2 with age, parameters were also estimated assuming age-independent $\alpha = 44.5°$ and

Table 4.1: *Age-specific values of the fibre orientation and dispersion parameters in the two fitting routines used in this study. In the age-dependent routine, different values α and τ were used according to the donor's age-group. In the age-independent routine, α and τ were set to fixed values, independently of the donor's age.*

Age-group		**<30**	**30-39**	**40-49**	**50-59**	**60-69**	**≥70**
Age-independent	α	44.5	44.5	44.5	44.5	44.5	44.5
	τ	0.20	0.20	0.20	0.20	0.20	0.20
Age-dependent	α	44.5	44.5	44.5	44.5	50.0	50.0
	τ	0.10	0.20	0.20	0.20	0.20	0.20

$\tau = 0.20$. The age-specific α and τ for the two fitting routines described above are summarised in Table 4.1.

Finally, the ability of the thoracic aorta to store elastic energy during systole was evaluated as the difference between the HGO-SEF Ψ at 120 and 80 mmHg (Spronck et al., 2020):

$$\Delta\Psi_{120\text{-}80\ \text{mmHg}} = \Psi|_{120\ \text{mmHg}} - \Psi|_{80\ \text{mmHg}}\ , \tag{4.14}$$

where Ψ is Eq. 2.27 evaluated at stress level corresponding to P_{ref}=120 mmHg and P_{ref}=80 mmHg (Eq. 4.9).

4.2.5 Statistical analysis

The statistical analysis was carried out using SPSS 23 (IBM corporation, Chicago, IL, USA), considering age both as a continuous and as a categorical variable by grouping samples in decade age-groups (except for the youngest group that included all donors <30 years and the oldest group that included those ≥70 years due to the limited number of donors belonging to these two categories). Differences between age groups were first evaluated using analysis of covariance (ANCOVA) test with sex as confounder, followed by post-hoc pairwise comparisons when statistical significance was reached. Further, Pearson's test has been used to evaluate the correlation between age and outcomes variables where appropriate.

Data in tables are presented as mean ± standard deviation. The average curves have been built by averaging the stress-strain and pressure-diameter relationships of the subjects in each age group. The value of $p<0.05$ has been taken as statistical significance.

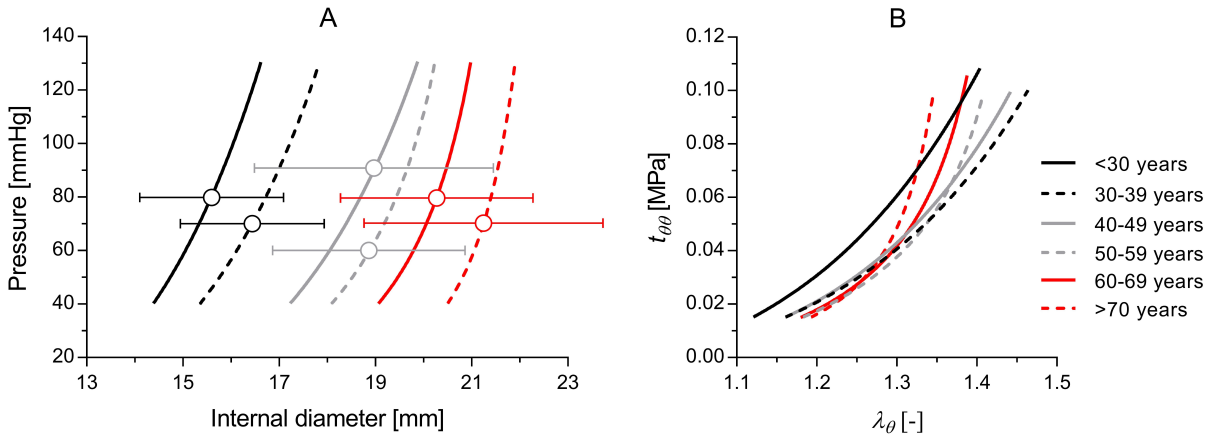

Figure 4.2: *Average pressure-diameter (A) and Cauchy stress-stretch (B) relationship of the human thoracic aorta in each of the six age groups considered in this study. Bars indicate ± standard deviation.*

4.3 Results

Donor demographics can be seen in Table 4.2. All age groups except <30 years and 40-49 years presented an even distribution of men and women. Under 30 years there were men only and 40-49 years there were more men (77%). There was a significant increase in both aortic diameter (r=0.70, p<0.001) and wall thickness with age (r=0.37, p<0.001). However, while the increase in aortic diameter was steady throughout the investigated age range, changes in wall thickness were significant only before 50 years (p<0.01).

The average pressure-diameter and circumferential Cauchy stress-stretch relationships are shown in Figure 4.2. The increase in diameter with age can clearly be observed in Figure 4.2A where pressure-diameter relationships shift rightward with progressing age, as did the stress-stretch relationships, requiring a higher level of stretch to reach a given level of wall stress. Indeed, λ_θ at 80 kPa of Cauchy stress was significantly lower at 1.35±0.05 in <30 years rings

Table 4.2: *Age, sex, and ring size in the 6 age groups. Data are presented as mean ± standard deviation.*

Age-group	**<30**	**30-39**	**40-49**	**50-59**	**60-69**	**≥70**
Men:Women	11:0	5:5	20:6	22:14	15:15	5:9
Age [years]	23 ± 4	34 ± 3	44 ± 3	55 ± 3	63 ± 3	74 ± 4
R_0 [mm]	5.8 ± 0.5	6.2 ± 0.5	6.6 ± 0.9	7.3 ± 1.2	7.6 ± 1.2	9.0 ± 1.7
h_0^{wall} [mm]	1.1 ± 0.3	1.3 ± 0.2	1.3 ± 0.2	1.5 ± 0.3	1.5 ± 0.3	1.6 ± 0.3

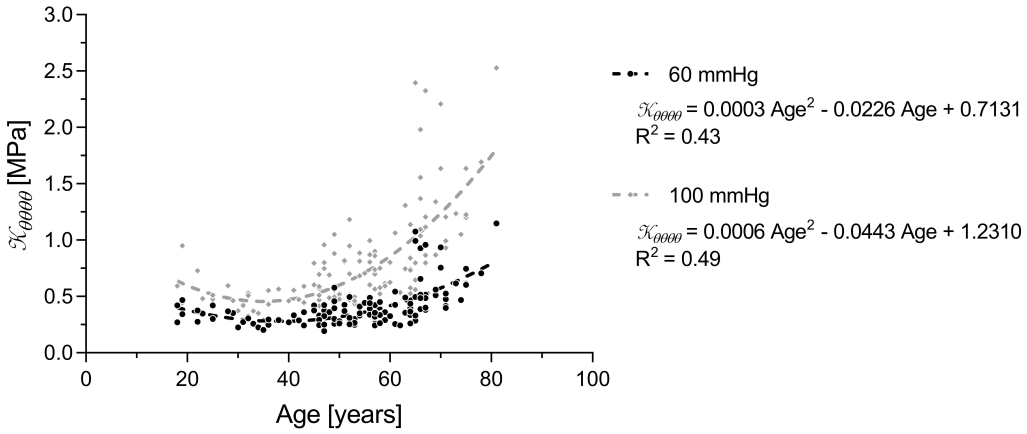

Figure 4.3: *Changes with age of the tangential elastic modulus $\mathcal{K}_{\theta\theta\theta\theta}$ of the thoracic aorta at the luminal pressure of 60 and 100 mmHg.*

than rings harvested from middle-aged donors (1.43±0.05, 1.42±0.05, and 1.43±0.05 in 30-39, 40-49, and 50-59 years, respectively, $p<0.05$). Up to 50-59 years, the average stress-stretch relationships in all age groups were below that of the youngest age group, which crossed the curve of the oldest age group only at $\lambda_\theta = \sim 1.32$.

Figure 4.3 presents $\mathcal{K}_{\theta\theta\theta\theta}$ calculated at the pressure-equivalent stress levels of 60 and 100 mmHg as a function of age. Age-group averages are reported in Table 4.3. As shown in Figure 4.3, age-differences in the slope of the stress-stretch relationships ($\mathcal{K}_{\theta\theta\theta\theta}$) were more accentuated at mean pressure (i.e. 100 mmHg) than at low physiological pressure (60 mmHg). At 100 mmHg, $\mathcal{K}_{\theta\theta\theta\theta}$ was 0.55±0.16 MPa in donors below 30 years, did not change significantly until 60-69 years, and almost tripled in donors above 70 years (157% increase). On the contrary, $\mathcal{K}_{\theta\theta\theta\theta}$ at 60 mmHg was 0.36±0.06 MPa in donors <30 years, significantly different only than that in arteries above 70 years (80% increase).

As expected, $\mathcal{K}_{\theta\theta\theta\theta}$ increased linearly with pressure (average $r \geq 0.95$, $p<0.001$ for all age-groups) (Figure 4.4A), reflecting the exponential nature of the stress-stretch relationship of arteries (Figure 4.2B). The pressure-related arterial stiffening $\dot{\mathcal{K}}_{\theta\theta\theta\theta}$, corresponding to the slope of the linear $\mathcal{K}_{\theta\theta\theta\theta}$-$P$ relationship in Figure 4.4A, was 4.72±2.95 kPa/mmHg in young donors and approximately four times higher at 19.06±6.82 kPa/mmHg in older adults (≥70 years), signifying an enhanced sensitivity to pressure changes (Figure 4.4B). This result implies that, in agreement with Figure 4.3, the higher the pressure level the more pronounced are age-related differences in $\mathcal{K}_{\theta\theta\theta\theta}$. Interestingly, changes in $\dot{\mathcal{K}}_{\theta\theta\theta\theta}$ appeared relatively small before 50 years of age, followed by a steep increase in late middle-aged and older adults.

Constitutive modelling of the arterial wall behaviour was used to provide a plausible microstructural interpretation of the age-related changes observed in the mechanical data. Figure 4.5

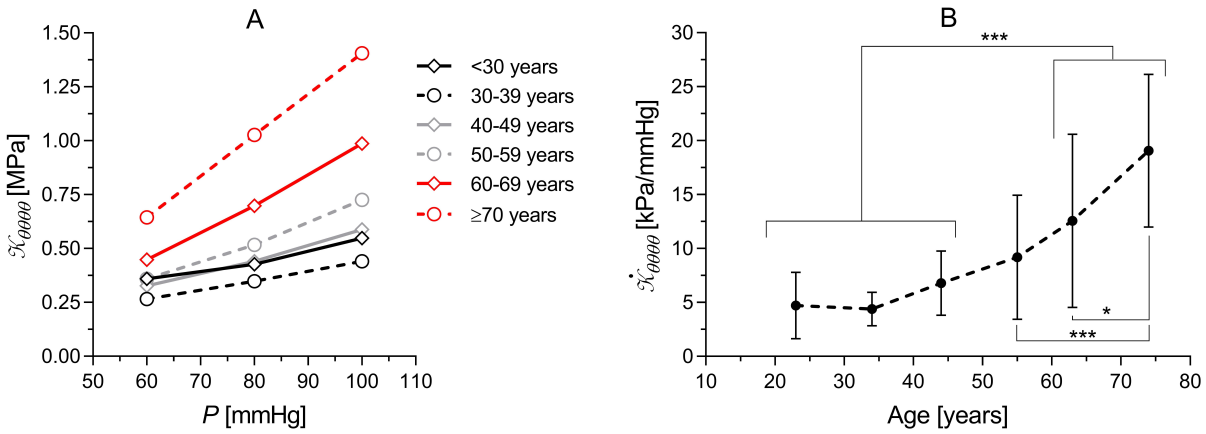

Figure 4.4: *Changes with age of the pressure-dependence of the tangential elastic modulus of the human thoracic aorta. Panel A: $\mathcal{K}_{\theta\theta\theta\theta}$ as a function of pressure for all the age-groups included in the study. Data are presented as mean without standard deviation (SD) for clarity (see Table 4.2 for SD). Panel B: the slope of the $\mathcal{K}_{\theta\theta\theta\theta}$-pressure relationship $\dot{\mathcal{K}}_{\theta\theta\theta\theta}$ indicate the elastic modulus sensitivity to changes in intraluminal pressure. Data are presented as mean ± standard deviation. $^{*}p<0.05$ and $^{***}p<0.001$.*

presents trends of the constitutive model parameters with age when α and τ were assumed to be age-independent as shown in Table 4.1 (top). Their age-group averages are presented in Table 4.4 (top). The matrix stiffness-like parameter μ showed a decreasing trend that resembled a quadratic function (Panel A, R^2=0.34), ranging from 16.37±4.12 kPa in young donors (<30 years) to 6.93±2.56 kPa after 70 years. Age-groups ANCOVA analysis revealed that μ dropped by 31 (2 to 60)% between <30 and 30-39 years ($p<0.05$) and did not change thereafter. The collagen fibre stiffness-like parameter k_1 mildly correlated with age (Panel B, $r=-0.23$, $p<0.01$), falling from 143.63±42.92 kPa to 95.92±43.84 kPa across the investigate age-range, and was significantly different from <30 years only for 50-59 years and older people. Conversely, the fibre exponential constant k_2 rose exponentially with age (Panel C, R^2=0.42), growing from 0.61±1.84 in people <30 years to more than 50-times as much after 70 years (34.74±18.06). Age-groups ANCOVA analysis indicated that changes in k_2 were not significant until 60-69 years ($p<0.01$), despite k_2 being already on average 10-folds higher at 50-59 years compared to <30 years, likely reflecting the high inter-subject variability of this parameter.

Interestingly, assigning age-dependent values to α and τ only mildly affected the trends of μ and k_2 with age (Figure 4.6). Their age-group averages are presented in Table 4.4 (bottom). μ decreased quadratically with age (Panel A, R^2=0.26), ranging from 15.94±3.96 kPa in young donors (<30 years) to 8.31±2.88 kPa after 70 years. k_2 grew exponentially from 2.88±5.43 in people <30 years to more than 20-times as much after 70 years (55.43±26.03) (Panel C,

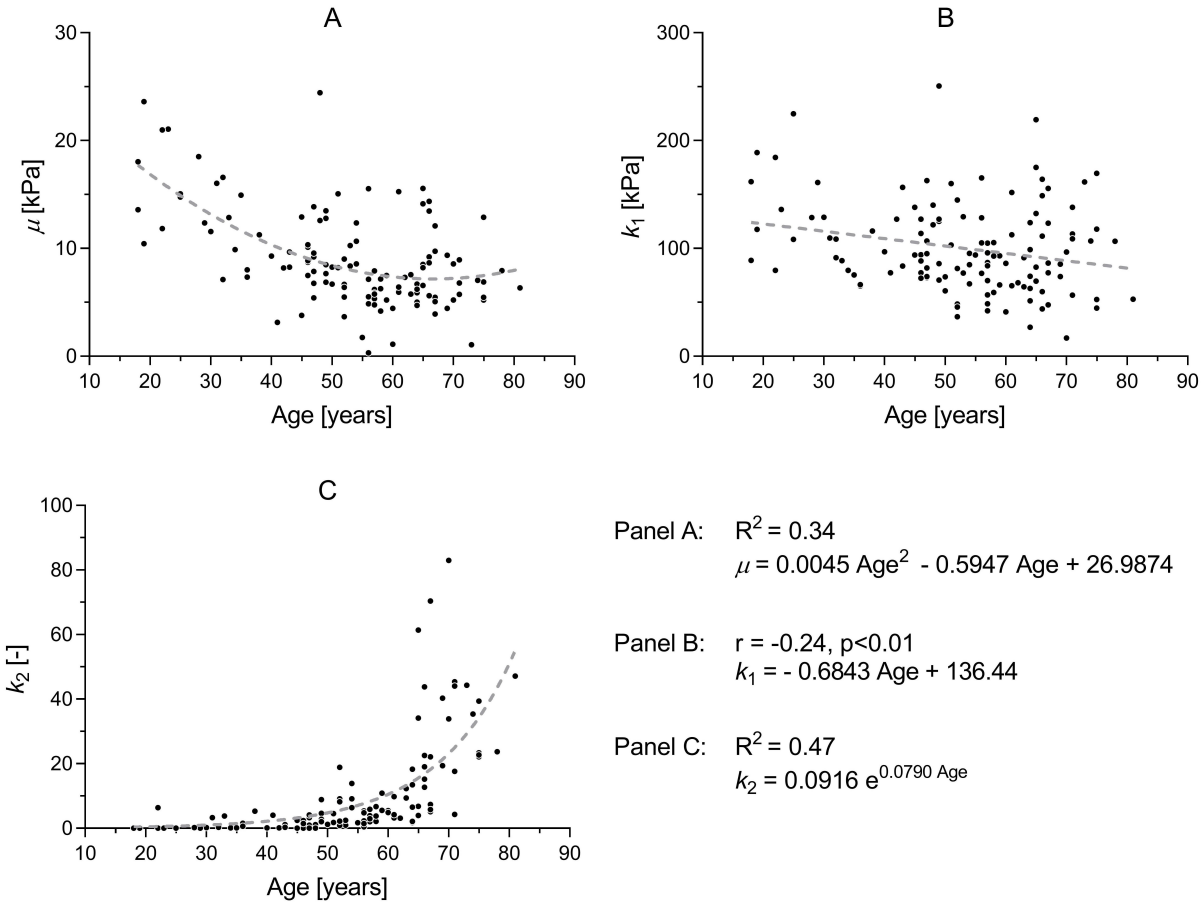

Figure 4.5: *HGO-SEF model parameters as a function of age; elastin/matrix stiffness-like parameter μ (A), collagen fibre stiffness-like k_1 (B) and exponential k_2 (C) parameters. Anisotropy parameters were assumed constant with age: $\alpha = 44.5°$ and $\tau = 0.20$. Dashed lines represent the best-fit functions: quadratic, linear, and exponential, respectively.*

R^2=0.56). On the contrary, k_1, that appeared to be linearly decreasing with age when assuming constant α and τ, quadratically increased with age when assigning age-group-specific values to α and τ. Similarly to k_2, k_1, 99.44±27.14 in young individuals, did not change significantly until after 60 years and was almost double in arteries of donors ≥70 years.

Finally, Figure 4.7 shows changes in stored elastic energy over the physiological pressure range 120-80 mmHg. The modelling choices on α and τ only slightly affected $\Delta\Psi_{120\text{-}80\ \text{mmHg}}$ that was 6.93±1.43 kPa in rings <30 years, did not change significantly in the first three decades analysed in this study, and started decreasing by the age of 50 years reaching 2.49±1.21 kPa after 70 years ($p<0.001$).

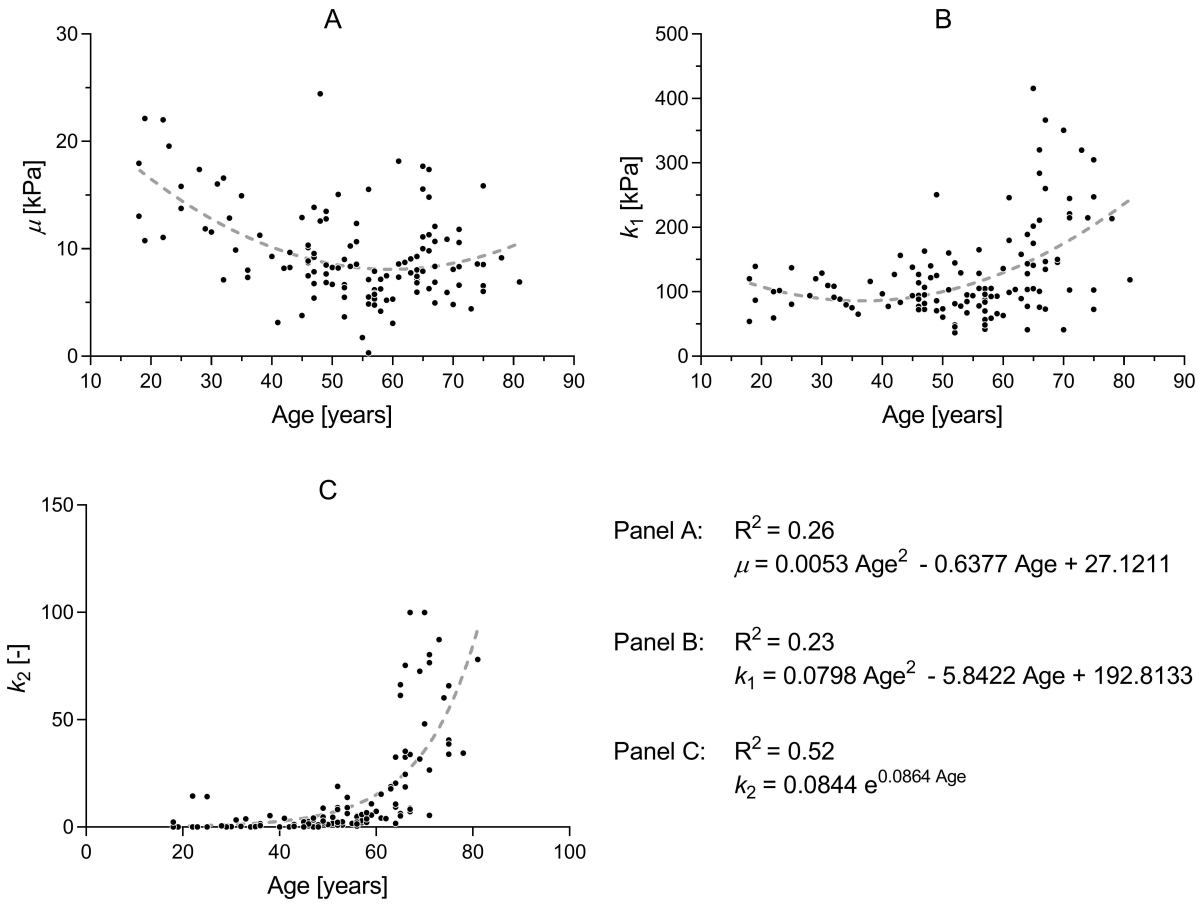

Figure 4.6: *HGO-SEF model parameters as a function of age; elastin/matrix stiffness-like parameter μ (A), collagen fibre stiffness-like k_1 (B) and exponential k_2 (C) parameters. Anisotropy parameters were given age-dependent values taken from the literature, as detailed in Table 4.1. Dashed lines represent the best-fit functions: quadratic for both μ and k_1, and exponential for k_2.*

4.4 Discussion

The strong relationship between arterial structure and function has long been known (Burton, 1954). Therefore, it not surprising that structural alterations that characterise the ageing process of large arteries largely affects their mechanical properties. This study evaluated changes with age of the circumferential mechanical properties of the human thoracic aorta *ex vivo* in a cohort of unprecedented size. Further, constitutive modelling of the wall behaviour was used to provide a microstructural interpretation of the mechanical data, inferring changes in the mechanical behaviour of the two wall constituents that determine the passive mechanical response of arteries: collagen and elastin.

Values of tangential elastic modulus at the mean physiological pressure of 100 mmHg found here are in agreement with those reported previously for the descending thoracic aorta of humans, ranging from ~0.4-0.5 MPa in young people (<30 years) to ~0.8-1.8 MPa in older

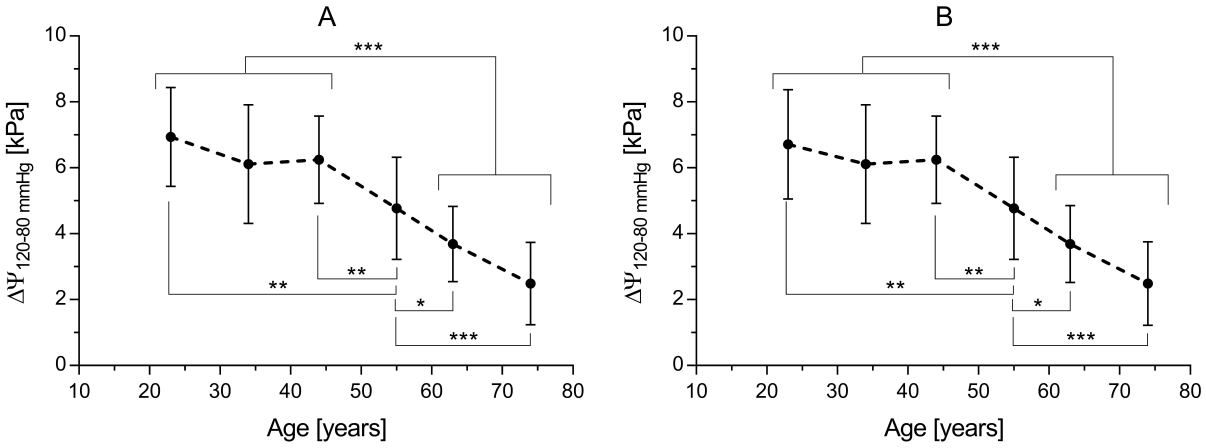

Figure 4.7: *Changes in stored elastic energy over the pressure range 120-80 mmHg with age. Panel A: α and τ were assumed independent of age. Panel B: α and τ were given age-group-specific values as shown in Table 4.1. Data are presented as mean ± standard deviation. $^{*}p<0.05$, $^{**}p<0.01$, $^{***}p<0.001$.*

adults (>60 years) (Haskett et al., 2010; Jadidi et al., 2020). Interestingly, despite $\mathscr{K}_{\theta\theta\theta\theta}$ significantly correlated with age at all pressure levels, the onset of age-related arterial stiffening differed between the three considered pressure levels: 60-69 years at both 80 and 100 mmHg, but higher at ≥70 years when P_{ref}=60 mmHg. Indeed, the slope of the $\mathscr{K}_{\theta\theta\theta\theta}$-$P$ relationship with age ($\dot{\mathscr{K}}_{\theta\theta\theta\theta}$) increased by 300% across the investigated age range (with onset at 60-69 years), suggesting that, in line with the development of a highly collagenous tissue (Fonck et al., 2007), age differences in stiffness are enhanced at high pressures.

To further quantify structural changes in the arterial wall, the Cauchy stress-stretch relationships were fitted with the HGO-SEF which models the superimposed contributions of a compliant isotropic matrix, commonly associated with elastin, and an anisotropic fibrous component, typically associated with collagen. Absence of mechanical data in the axial direction required making assumptions on the model parameters determining the anisotropicity of the tissue: the fibre orientation parameter, α, and the fibre dispersion parameter, τ (Weisbecker et al., 2012; Haskett et al., 2010). In a first analysis, these parameters were assumed to be age-independent. However, previous studies have shown that the human thoracic aorta, exhibiting an almost isotropic behaviour in aortae of young and middle-age donors, tends to become stiffer axially than circumferentially in older adults (Weisbecker et al., 2012; Haskett et al., 2010). Therefore, the parameters estimation was also repeated using age-dependent values of α and τ. Independently of the modelling choices for the anisotropy parameters, the elastin stiffness-like parameter was highest in the <30 years age group and significantly dropped by ∼27-31% at 30-39 years with little further change thereafter, in agreement with previous

quantification of the elastin density in the human thoracic aorta from histological images of the wall cross-section (Jadidi et al., 2020). This finding is also consistent with the observation that elastase treatment (i.e., digestion of the elastin matrix) affects the stress-strain relationship of arteries independently on the level of strain (Fonck et al., 2007). Indeed, the average stress-strain relationships of the age groups 30-39 and 40-49 years appeared to be consistently below that of the youngest age group (<30 years) (see Figure A1A for a graphical representation of the effect of varying the parameter μ). Changes in collagen exponential parameter, affecting the wall behaviour at high stresses (see Figure A1C), happened later with age (≥60 years), concomitantly with the observed increase in $\dot{\mathscr{K}}_{\theta\theta\theta\theta}$. This result was also independent of fitting protocol (i.e., age-dependent or age-independent α and τ). These findings suggest different time courses for the elastin degradation and collagen remodelling with age, the former occurring in young adults and the latter from middle-age onwards possibly in response to the first.

It is worth considering, however, that these results need to be taken with caution for several reasons; first, despite being formulated on the basis of empirical observations, the constitutive model parameters may not necessarily match the behaviour of the wall constituents *in vivo*. Indeed, several mathematical descriptions of the behaviour of the human arterial wall constituents have been proposed previously (Zulliger & Stergiopulos, 2007; Jadidi et al., 2020; Haskett et al., 2010), and all showed good ability in predicting the macroscopic wall's mechanical response. Further, modelling choices for α and τ might have affected the outcomes of the analysis. The collagen stiffness-like parameter k_1 was the only parameter largely affected by the modelling assumptions; indeed, while k_1 negatively correlated with age when α and τ were assumed constant for all age-groups, the former increased quadratically when using age-specific α and τ. It is worth noting, however, that the exponential parameter k_2 dominates the response of the fibrous component of the SEF, so that observed differences in the age-trends of k_1 do not change the overall message of the analysis: i.e., loss of integrity of the elastin network in early middle-aged people is followed by a gradual stiffening of collagen fibres in late middle-aged people, likely reflecting enhanced synthesis and increased cross-linking (Graham et al., 2010; Harvey et al., 2016; Tsamis & Stergiopulos, 2007; Kohn et al., 2015).

As described in Chapter 1, the function of large arteries consists of transforming the intermittent blood flow generated by the cyclic action of the heart into a continuous flow. Arteries absolve this function by distending in systole to accommodate a high volume of blood and store elastic energy to be used in diastole to push the blood downstream in the circulation. In order to assess the impact of aortic ageing on its function, the elastic energy per unit volume stored within a hypothetical cardiac cycle where pressure ranged between 120 and 80 mmHg was

estimated; $\Delta\Psi_{120\text{-}80\ \mathrm{mmHg}}$ started declining at the age of 50 years and the physiological elastic function of the thoracic aorta was reduced by 64% over the investigated age range, in agreement with previous findings (Jadidi et al., 2020) and with the increase in pulse pressure observed in elastic arteries with age (Gurven et al., 2012; Shimura & Kubo, 2019; Wang et al., 2019).

Study limitations

In this study, the mechanical properties of the human thoracic aorta have been evaluated using ring tests, hence assessing the wall response to deformation in the circumferential direction only. This choice was dictated by the necessity of preserving the samples' integrity and limiting the amount of tissue required for the experiments. *In vivo*, the thoracic aorta, as most arteries, is subjected to a complex loading configuration, consisting in the superimposition of cyclic circumferential deformation and a constant axial stretch. Hence, the full characterisation of the wall behaviour requires testing in both axial and circumferential direction simultaneously. Based on previous experimental results (Weisbecker et al., 2012; Haskett et al., 2010) and findings of Chapter 3, the behaviour of the thoracic aorta was assumed to be almost isotropic in young and middle-aged donors and slightly stiffer in the axial than circumferential direction in older adults. Further, it was verified that assuming age-independent anisotropy parameters did not largely affect the results of the analysis. Therefore, assumptions on the wall anisotropy unlikely affected the conclusion of this study.

Second, as discussed in Chapter 3, uniaxial, ring and planar biaxial tensile tests require flattening a typically arch-shaped (or circular in the case of ring tests) sample into a strip (double-sided in the case of ring tests), thus introducing pre-deformations that vary throughout the sample thickness. Considering the unloaded ring as reference configuration, these pre-deformations can be quantified into an approximately 10-15% extension for the intima and 8-12% compression for the adventitia (see deformation gradient $\mathbf{F}_1$ in Chapter 3). Contrarily to Chapter 3 where the tri-layered modelling allowed accounting for these pre-deformations, here the aortic wall has been modelled as a material with homogeneous mechanical properties (i.e., independent on the radial coordinate) so that inclusion of the pre-deformations would not result in a change in the mechanical behaviour. Therefore, the age-related stiffening observed in this study mainly reflects structural changes in the intima and media layers, rather than in the adventitia. It is worth considering, however, that arterial remodelling with age mostly interest the intima and media so that, once more, conclusions reached here are unlikely to be affected by the testing protocol.

4.5 Chapter conclusions

This study showed that the human thoracic aorta undergoes significant stiffening during our life-course, with increased steepness of the pressure-stiffness relationship. At the physiological mean pressure, the onset of the age-related arterial stiffening was approximately 60 years. This change in mechanical properties impacts the ability of the arterial wall to exert its compliant function, which steadily declines from 50 years onward. Decreased compliance will, in turn, contribute to increasing BP and, hence, the cardiac afterload.

Table 4.3: *Tangential elastic modulus $\mathscr{K}_{\theta\theta\theta\theta}$ of the human thoracic aorta at 60, 80, and 100 mmHg of pressure-equivalent Cauchy stress for the 6 age-groups included in this study. Data are presented as mean ± standard deviation. Post-hoc pairwise comparison between age-groups after sex adjustments: $^{*}p<0.05$, $^{**}p<0.01$ and $^{***}p<0.001$ with <30 years; $^{\dagger}p<0.05$ with 30-39 years; $^{\ddagger}p<0.05$, $^{\ddagger\ddagger}p<0.01$ and $^{\ddagger\ddagger\ddagger}p<0.001$ with 60-69 years.*

Age-group		**<30**	**30-39**	**40-49**	**50-59**	**60-69**	**≥70**
$\mathscr{K}_{\theta\theta\theta\theta}$	60 mmHg [MPa]	0.36 ± 0.06 ***	0.27 ± 0.04 ***††	0.33 ± 0.10 ***††	0.36 ± 0.13 ***†	0.47 ± 0.20 **	0.64 ± 0.20
	80 mmHg [MPa]	0.43 ± 0.08 ***†††	0.35 ± 0.06 ***†††	0.44 ± 0.15 ***†††	0.52 ± 0.22 ***††	0.71 ± 0.29 ***	1.03 ± 0.35
	100 mmHg [MPa]	0.55 ± 0.16 ***†††	0.44 ± 0.09 ***†††	0.59 ± 0.22 ***†††	0.73 ± 0.34 ***†	0.97 ± 0.43 ***	1.41 ± 0.46

Table 4.4: *Age-group-specific model parameters of the human thoracic aorta. The top part of the table reports model parameters obtained when setting α and τ to 44.5° and 0.20, respectively, independently on the age-group. The bottom part of the table displays results when using age-dependent α and τ as detailed in Table 4.1. Data are presented as mean ± standard deviation. Post-hoc pairwise comparison between age-groups after sex adjustments: $^{*}p<0.05$, $^{**}p<0.01$ and $^{***}p<0.001$ with <30 years; $^{\dagger}p<0.05$ with 30-39 years; $^{\ddagger}p<0.05$, $^{\ddagger\ddagger}p<0.01$ and $^{\ddagger\ddagger\ddagger}p<0.001$ with 60-69 years; $^{\#}p<0.01$ and $^{\#\#}p<0.001$ with ≥70 years.*

Age-group		**<30**	**30-39**	**40-49**	**50-59**	**60-69**	**≥70**
Age-independent α *and* τ	μ [kPa]	16.37 ± 4.12	11.56 ± 3.34 *	9.56 ± 3.98 ***	7.31 ± 3.36 ***†	7.47 ± 3.06 ***†	6.93 ± 2.56 ***†
	k_1 [kPa]	143.63 ± 42.92	93.00 ± 20.87 *	110.06 ± 38.70	88.94 ± 33.67 ***	93.36 ± 42.79 **	95.92 ± 43.84 *
	k_2 [-]	0.61 ± 1.84 $^{\ddagger\ddagger\#\#}$	1.54 ± 1.80 $^{\ddagger\#\#}$	1.73 ± 2.02 $^{\ddagger\ddagger\ddagger\#\#}$	6.25 ± 10.09 $^{\ddagger\#\#}$	14.46 ± 15.00 $^{\#\#}$	34.74 ± 18.06
Age-dependent α *and* τ	μ [kPa]	15.94 ± 3.96	11.56 ± 3.34	9.56 ± 3.98 ***	7.31 ± 3.36 ***†	9.30 ± 3.66 ***	8.31 ± 2.88 ***
	k_1 [kPa]	99.44 ± 27.14 $^{\#}$	93.00 ± 20.87 $^{\ddagger\#\#}$	110.06 ± 38.70 $^{\ddagger\#\#}$	88.94 ± 33.67 $^{\ddagger\ddagger\ddagger\#\#}$	162.99 ± 89.81	197.77 ± 92.70
	k_2 [-]	2.88 ± 5.43 $^{\ddagger\ddagger\#\#}$	1.54 ± 1.80 $^{\ddagger\ddagger\#\#}$	1.73 ± 2.02 $^{\ddagger\ddagger\ddagger\#\#}$	6.25 ± 10.09 $^{\ddagger\ddagger\ddagger\#\#}$	22.89 ± 24.51 $^{\#\#}$	55.43 ± 26.03

CHAPTER 5

Non-invasive evaluation of viscoelasticity in the human carotid artery, normalised to pressure variations

Part of this Chapter was published in:

Giudici A., Palombo C., Kozakova M., Morizzo C., Penno G., Jamagidze G., Della Latta D., Chiappino D., Cruickshank J.K. & Khir A.W. (2021). Non-invasive Carotid Pressure-Diameter Loops to Identify Viscoelastic Properties in Ageing, Hypertension and Type 2 Diabetes. *Journal of Hypertension* (In press).

5.1 Introduction

Arterial stiffness, estimated by aortic PWV, is a powerful predictor of mortality independent of known risk factors including BP (Ben-Shlomo et al., 2014; The Reference Values for Arterial Stiffness' Collaboration, 2010). Arterial ageing and cardiovascular pathologies, such hypertension and diabetes, have been associated with arterial stiffening as measured by PWV (Chirinos et al., 2013; Cruickshank et al., 2002; Mitchell et al., 2004; Najjar et al., 2008; Zhang et al., 2011). Despite several studies indicate that these changes in PWV are independent of BP (Mattace-Raso et al., 2010; Zhang et al., 2011), results on local wall stiffness are more controversial; Armentano et al. (1995a) and Laurent et al. (1994) found that carotid stiffness in human did not differ significantly between normotensive and hypertensive subjects when compared at a given pressure level. Similar observations have been made in animal models of hypertension (Bezie et al., 1998b,a; Cohuet et al., 2001; Marque et al., 1999).

Several factors could explain these controversial findings; first, as detailed in section 1.3.1, regional PWVs describe average mechanical properties which correspond poorly with local changes in arterial stiffness. Second, pressure-normalisation of PWV and c using statistical methods (the most commonly used approached in clinical studies (Desamericq et al., 2015; Valbusa et al., 2019; Vogel et al., 2013)) presents noteworthy limitations, including the lack of patient-specific corrections based on mechanistic model of the wall behaviour, the inability in discerning between the short-term (shift in the working point on the non-linear behaviour of the wall, see Chapter 3) and long-term (i.e., vascular damage/remodelling) effects of increased BP, and the arbitrary choice of the normalising pressure (SBP and MBP are commonly chosen as confounders for statistical adjustments) (Desamericq et al., 2015; Valbusa et al., 2019; Vogel et al., 2013). Indeed, mechanistic approaches have been introduced to apply patients-specific corrections to both regional PWV (Shirai et al., 2006; Spronck et al., 2017b,a), although the choice of the normalising pressure is still object of debate for some PWV metrics (Shirai et al., 2018; Spronck, 2018; Shirai et al., 2019), and local c (Spronck et al., 2015, 2017c), although its application requires measurement of the arterial pressure waveform and is, therefore, not applicable to ultrasound based c (Feng & Khir, 2010; Rabben et al., 2004).

Third, the complex mechanical behaviour of the arterial wall and consequent arterial stiffening result from the interaction of viscous and elastic elements. Soft tissues are known to exhibit a typical viscoelastic behaviour from *ex vivo* experiments (Dobrin, 1978; Remington, 1954); this implies a load frequency-dependent behaviour and different loading and unloading paths in stress-strain and pressure-diameter/area relationships. Nevertheless, arterial wall viscoelasticity

has been investigated *in vivo* only in a handful of studies (Armentano et al., 1995a; Boutouyrie et al., 1998; Hermeling et al., 2010). Interestingly, however, both *in vivo* and *ex vivo* studies have reported changes in wall viscosity with ageing and hypertension (Armentano et al., 1995a; Learoyd & Taylor, 1966). Viscous forces, depending on smooth muscle cell content (Apter et al., 1966; Zatzman et al., 1954), acts in response to abrupt changes in BP so are high during the systolic upstroke and relatively small during arterial wall recoil when luminal pressure decreases in diastole. Therefore, foot-to-foot PWV (e.g. cfPWV, baPWV, carotid-ankle PWV) and local c (e.g. PU-loop and lnDU-loop methods) measured in systole might reflect a combination of both viscous and elastic wall properties, while wall elasticity would be better detectable in diastole.

Centred on the analysis of PD-loops and D^2P-loops (pressure-area loops), this Chapter aimed to investigate the viscoelastic properties of the human common carotid artery (CCA) in both healthy individuals and people affected by hypertension and T2DM. The main objectives were 1) to quantify the viscous properties of the arterial wall and how these may affect differences in arterial distensibility in systole and diastole, and 2) to introduce a method for the subject-specific pressure-normalisation of local c (See section 2.3.4), allowing to evaluate age- and pathology-induced effects on the carotid wall elasticity independently of BP. The performance of the proposed method was compared with that of commonly used statistical methods, also evaluating the impact of the choice of the normalising pressure.

5.2 Methods

5.2.1 Study population

Participants to this study were recruited at the Pisa University Hospital (Pisa, Tuscany, Italy) and the hospital of Massa (Tuscany, Italy) by Prof. C. Palombo's group (Department of Surgical, Medical, Molecular Pathology and Critical Area Medicine, University of Pisa, Pisa, Italy). The protocol of the study followed the principles of the Declaration of Helsinki and was approved by the institutional ethics committee 'Comitato Etico di Area Vasta Nord Ovest' (reference number: 3146/2010). Also, the analysis of non-invasive human data was approved by the Brunel Research Ethics Committee (Reference: 6124-LR-Feb/2017-6443-1). The study population included healthy controls (N=114, Age range 18-80, average 57±10 years, 57 men) and patients with hypertension (N=69, Age range 38-80, average 65±10 years, 40 men), and type 2 diabetes mellitus (T2DM) (N=124, Age range 41-82, average 65±8 years, 84 men).

Table 5.1: *Number of subjects included in this study organised by type of recording (simultaneous and sequential pressure and diameter acquisition) and clinical group.*

Clinical group	**Acquisition modality**		
	Simultaneous	Sequential	Total
Healthy controls	94	20	114
Hypertension	41	28	69
T2DM	114	11	125

5.2.2 Data acquisition

The vascular examination was performed in the morning, at least 2 hours after a light breakfast, in a quiet room with a stable temperature of 22°, after resting comfortably for at least 15 min in the supine position. All subjects were asked to abstain from cigarette smoking, caffeine and alcohol consumption and vigorous physical activity for 24 hours. Brachial Systolic and Diastolic BP (SBP_{BRA} and DBP_{BRA}, respectively) were measured with a digital electronic manometer (Omron model 705cp, Kyoto, Japan) with patients resting supine for >10 min.

The carotid pressure waveform, P, was recorded using a tonometer (PulsePen, Dia Tecne, Milan, Italy) pressed on the neck skin of the patient in correspondence of the left CCA. The two centres, Pisa University Hospital and hospital of Massa, used two different PulsePen model, sampling at 1000 Hz and 500 Hz, respectively. Diameter distension waveforms, D, were measured using B-mode ultrasound imaging of the right CCA. Similar to the pressure acquisition, two different ultrasound devices were used in the two centres: Aloka Alpha 10 (Hitachi Group, Japan) equipped with a 7.5 MHz linear probe in the Pisa University hospital and MyLab 70 (Esaote SpA, Genova, Italy) equipped with a 7.5 MHz linear probe in Massa. When the quality of the acquisition was high, the diameter (ultrasound) and pressure (tonometer) waveforms were recorded simultaneously on the right and left carotid arteries, respectively, for correspondence in heartbeats. When an accurate simultaneous acquisition was not possible, the two signals were acquired sequentially, minimising the delay between the two acquisitions. Details on the number of participants in each clinical and acquisition modality group are summarised in Table 5.1.

Intima-media thickness (IMT) was estimated on the far wall of the right CCA using a 10-MHz linear probe implemented with automatic, radiofrequencybased tracking of the arterial wall with high spatial resolution (QIMT, Esaote MyLab70 and MyLabOne, Esaote SpA, Genova, Italy) (Kozakova et al., 2017).

5.2.3 Data analysis

The main objectives of the present study were introducing a method for the non-invasive *in vivo* evaluation of the CCA wall visco-elastic propereties and providing an effective method for person-specific pressure-normalisation of c. With this objectives in mind and after the appropriate calibration and alignment of the acquired waveforms, the analysis started with the determination of elastic c and Ds in late diastole ($_{\mathrm{d}}Ds$), via the D^2P-loop method, and viscoelastic Ds is early systole ($_{\mathrm{s}}Ds$). Then, wall viscosity was evaluated through the estimation of the hysteresis area and viscoelastic constants. Finally, P-D^2 relationships were fitted with an exponential function to determine the exponential constant γ and estimate P_c (i.e., the normalising pressure) for the D^2P-loop method, thus allowing the pressure-normalisation of c (See Section 2.3.4).

Data have been analysed using a custom Matlab (The MathWorks, Inc., MA) code. The acquisition of the signals was performed according to two different protocols: 1) simultaneous and 2) sequential pressure and diameter recording. Therefore, despite sharing the main analysis steps, two versions of the same code have been compiled to account for the different underlying assumptions of the two acquisition protocols. When P and D had been acquired simultaneously, the analysis was performed only on simultaneously recorded 7-10 cardiac cycles. When recorded sequentially, to decrease potential bias given by incorrect matching of the two signals, each diameter per heartbeat was coupled with all pressure heartbeats to allow the analysis of NxM PD-loops, where N (∼8-10) and M (∼8-10) correspond to the number of recorded P and D cardiac cycles, respectively. Furthermore, only local CCA diastolic c was evaluated, while the viscosity parameters, whose accurate estimation strongly depends on the correct alignment of the P and D waveforms over the entire duration of the heartbeat, were not considered.

Waveform segmentation and pressure calibration

Firstly, CCA P and D waveforms were segmented into heartbeats by detecting the R wave of the QRS in the ECG signal. The mean heart rate (HR) was calculated as the average of the number of samples within heartbeats and knowing the sampling frequency. Then, the pressure waveform was calibrated in order to satisfy the following conditions: 1) uniform Mean BP (MBP) and 2) DBP in the arterial system (Nichols et al., 2005). Using subscript CCA and BRA for carotid and brachial arteries, respectively, these assumptions imply that $\mathrm{DBP_{BRA}} = \mathrm{DBP_{CCA}}$ and $\mathrm{MBP_{BRA}} = \mathrm{MBP_{CCA}}$, so that DBP and MBP can be used instead. MBP was estimated from $\mathrm{SBP_{BRA}}$ and DBP measurements using a form factor FF=0.43 as reported by Segers et al. (2009):

$$\mathrm{MBP} = \mathrm{DBP} + 0.43\ \mathrm{PP_{BRA}} = \mathrm{DBP} + 0.43\ (\mathrm{SBP_{BRA}} - \mathrm{DBP}) \tag{5.1}$$

where PP_{BRA} is the brachial pulse pressure ($MBP_{BRA} - DBP$).

The effect of respiration on BP has long been known (Dornhorst et al., 1952). Inspiration and expiration cyclically increase and decrease the pressure in the thorax, affecting the pressure difference across the arterial wall and, hence, the recorded pressure waveform. To overcome this issue, a straight line connecting the first and the last points of each heartbeat was subtracted to the pressure and diameter signals, thus reducing the bias related to the respiration in calculating the hysteresis area and the local wave speed.

Beat-to-beat matching and signal alignment

When dealing with simultaneous recordings, two different synchronisations have to be performed: first, the beat-to-beat synchronisation and, second, the alignment of the P and D waveforms. The beat-to-beat synchronisation accounts for the non-simultaneous starting recording time of the pressure and diameter waveforms. Comparing the R-to-R time difference in the heartbeats of the P and D signals, the first heartbeat appearing in both recordings was automatically identified.

The correct alignment of P and D waveforms is crucial for the accurate estimation of the investigated parameters. This second synchronisation compensates the different delays that may exist between the ECG recording and the pressure and diameter waveforms. Different ultrasound systems might apply different filters on the acquired arterial waveforms and ECG signals to increase the signal-to-noise ratio, thus introducing unknown delays between the two. Therefore, aligning the P and D waveform on the basis of the R wave of the ECG trace is not desirable when different acquisition systems have been used in the study.

The foot of the wave is considered as the golden standard for the alignment of arterial signals. However, noise and minor late diastolic waves can mask the foot of the wave and its identification can be complex. It has been suggested that the dicrotic notch is a more reliable reference point for the synchronisation of the pressure and diameter heartbeats (Hermeling et al., 2010; Muiesan & Paini, 2009). Here, the second derivatives of the P and D have been used to identify both reference points. As it can be seed in Figure 5.1, the second derivatives of the P and D waveforms are characterised by two main peaks: the first identifying the foot, and the second in correspondence of the dicrotic notch. The maxima of the two peaks determined the time of the foot and dicrotic notch. Then, the first alignment of P and D was performed automatically by minimising the difference between the position of the feet and dicrotic notches of the two signals. Then, the code allowed the user to check the alignment and resulting loop on screen, insert an additional shift in case of errors and discard the heartbeat in case of noise or unrepresentative data.

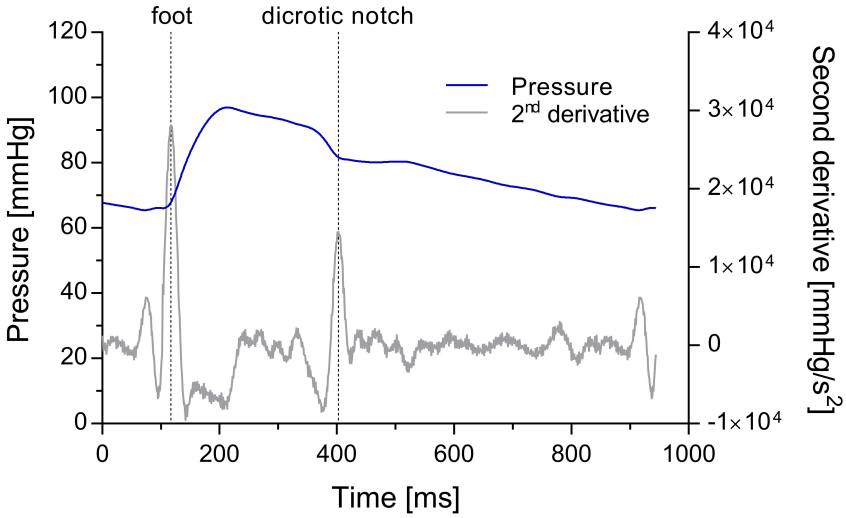

Figure 5.1: *Example of pressure heartbeat (blue) and its second derivative (grey). The second derivative is characterised by two main peaks identifying the foot and the dicrotic notch of the waveform.*

Determination of wave speed, distensibility and elastic modulus

c was estimated using the D^2P-loop method (Alastruey, 2011)(see Section 2.3.3), which assumes that, in late diastole, the rate of change of D (i.e., $\mathrm{d}D/\mathrm{d}t$) tends to a constant close to zero so that the viscous forces become negligible and elastic properties can be assessed. Following Alastruey (2011), late diastole was identified as the diastolic portion of the D^2P-loop delimited by DBP and the pressure at the dicrotic notch (Figure 5.2 in red). c was calculated as:

$$c = D_\mathrm{d}\sqrt{\frac{\mathrm{d}P}{\rho\ \mathrm{d}(D^2)}} \tag{5.2}$$

where D_d is the diastolic diameter, $\mathrm{d}P$ the change in pressure, $\mathrm{d}(D^2)$ is the change in squared diameter and ρ is the blood density assumed equal to 1060 kg/m3. To verify the impact of using sequentially acquired P and D signals on c, a preliminary study was carried out on n=25 individuals, randomly chosen between those whose P and D had been acquired simultaneously. c was determined using both sequential and simultaneous acquisition analyses. The results showed that differences between the subjects' c with the two analysis protocols were much smaller than the intra-subject variability of c across different heartbeats (See Appendix Table A11); it was concluded that the acquisition modality was unlikely to have affected results accuracy.

Known c, ${}_\mathrm{d}Ds$ was calculated as:

$${}_\mathrm{d}Ds = \frac{1}{\rho c^2} \tag{5.3}$$

Additionally, Eq. 5.2 was also applied to the early systolic portion of the D^2P-loop to evaluate Ds in early systole (${}_\mathrm{s}Ds$) (Figure 5.2) when, due to the abrupt cardiac ejection, $\mathrm{d}D/\mathrm{d}t$

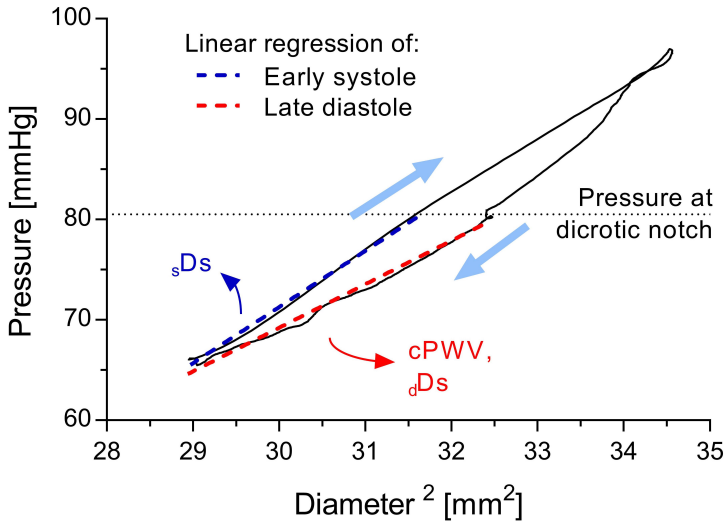

Figure 5.2: *Example of the calculation of the systolic and diastolic distensibility. A linear regression is applied to the D^2P-loop in early systole (blue dashed line) and diastole (red dashed line). Both linear regressions were performed up to the same pressure level, in proximity to the dicrotic notch pressure level.*

is approximately an order of magnitude higher than in late diastole, and viscous forces are at their maximum within the cardiac cycle. Therefore, it is expected that, unlike ${}_{\mathrm{d}}Ds$, ${}_{\mathrm{s}}Ds$ detects both elastic and viscous properties. Early systole was defined as the portion of the systolic upstroke delimited by DBP and the pressure at the dicrotic notch (Figure 5.2 in blue). This choice ensured that both ${}_{\mathrm{s}}Ds$ and ${}_{\mathrm{d}}Ds$ were calculated over the same pressure range, eliminating the issue of the pressure-dependence of arterial stiffness in the comparison.

Finally, while PWV/c is commonly used as index of arterial wall material stiffness, the Moens-Kortweg equation (Moens, 1878; Kortweg, 1878) (Eq. 5.4) suggests that PWV/c depends also on structural features of the artery (luminal diameter and wall thickness h) and rheological properties of blood (density). Indeed, it was recently shown that the Moens-Kortweg equation can be used to convert local c into the tangential elastic modulus at the pressure at which c was determined if h and D_{d} are known (Li et al., 2021).

$$\mathscr{K}_{\theta\theta\theta} = \frac{c^2\rho(D_{\mathrm{d}} + h)}{h} \tag{5.4}$$

Here, the wall thickness h was approximated with the IMT. Therefore, when applied to 'elastic' c determined in late diastole, Eq. 5.4 allows investigating the CCA wall elasticity more independently of its structural features and how these may change with ageing and pathologies.

Hysteresis area and viscous modulus

The viscous properties of the CCA wall were assessed using three parameters. Firstly, for

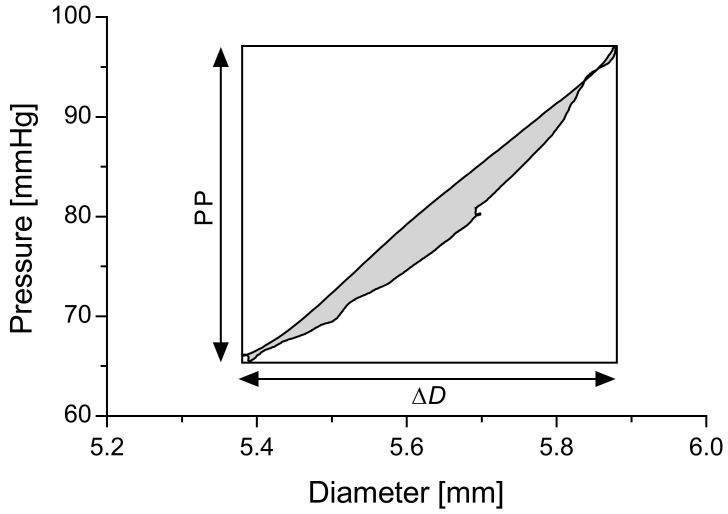

Figure 5.3: *Example of the calculation of the hysteresis index: the hysteresis area (grey area) is divided by the area of the rectangle formed by PP_{CCA} and ΔD to normalise the viscous property with respect to the change in pressure and diameter. The normalization will provide an adimensional parameter that is independent on the amplitude of the pressure and diameter waveforms and describe the distance between the systolic and diastolic parts of the loop.*

each heartbeat the hysteresis area (H_{A}) in the PD-loop was calculated as follows:

$$H_{\mathrm{A}} = \sum_{i=1}^{N} \frac{P_i + P_{i-1}}{2}(D_i - D_{i-1}) \tag{5.5}$$

where P_i and D_i are the i^{th} sampling point and N is the total number of samples of the heartbeat pressure and diameter waveforms. The magnitude of the area of hysteresis is affected by the size of the loop: i.e., the larger $\mathrm{PP_{CCA}} = \mathrm{SBP_{CCA}} - \mathrm{DBP}$) and Pulse Diameter ($\Delta D = D_{\mathrm{s}} - D_{\mathrm{d}}$), the higher H_{A}. To overcome this limitation, H_{A} was normalised with respect to $\mathrm{PP_{CCA}}$ and ΔD (Figure 5.3), introducing the hysteresis index (H_{I}), which is independent of the amplitudes of the heartbeat.

Second, the arterial viscosity was also assessed by means of the viscous term of a Voigt-type viscoelastic model, where pressure is separated into an elastic and viscous component as follow:

$$P(t) = P_{\mathrm{elastic}}(t) + P_{\mathrm{viscous}}(t) = P_{\mathrm{elastic}}(t) + \eta\frac{\mathrm{d}D(t)}{\mathrm{d}t} \tag{5.6}$$

where P_{elastic} and P_{viscous} are the elastic and viscous components of P, respectively, η is the viscous modulus, and t is time. The viscous coefficient η was estimated iteratively minimising the hysteresis area of the elastic component of P (Armentano et al., 1995a,b): i.e., minimising the cost function $H_{A_{\mathrm{elastic}}}$.

$$H_{\mathrm{A_{elastic}}} = \sum_{i=1}^{N} \frac{P_i + P_{i-1} - \eta\frac{D_i - 2D_{i-1} + D_{i-2}}{\Delta t}}{2}(D_i - D_{i-1}) \tag{5.7}$$

Note that it was assumed D_{-1}=D_N. Despite the Voigt-type viscoelastic model being the simplest description of a viscoelastic behaviour, (Valdez-Jasso et al., 2009) showed that more complex viscoelastic formulations did not improve the description of the mechanical behaviour of arteries.

Finally, it was hypothesised that, as the H_{A} increases, the relative difference between ${}_{\mathrm{s}}Ds$ and ${}_{\mathrm{d}}Ds$ ($\Delta Ds = ({}_{\mathrm{s}}Ds - {}_{\mathrm{d}}Ds)/{}_{\mathrm{d}}Ds$ %) would also increase and, therefore, provide additional insight into arterial viscosity (Figure 5.3).

Pressure-normalisation of c

As introduced in Section 2.3.4, fitting the P-D^2 relationship using an exponential function of the type

$$P_{\mathrm{estimated}} = P_{\mathrm{ref}}\, e^{\gamma_0\left(\frac{D^2}{D^2_{\mathrm{ref}}}-1\right)} \tag{5.8}$$

allows the definition of a stiffness parameter (γ_0) that is independent of inter-subject variability of BP. Furthermore, the specific choice of $P_{\mathrm{ref}} = \mathrm{DBP}$ simplifies the application of Eq. 5.8 to *in vivo* data, since the corresponding $D_{\mathrm{ref}} = D_{\mathrm{d}}$ will necessarily fall within the measured diameter range, while this might not be the case for a generic P_{ref}.

$$P_{\mathrm{estimated}} = \mathrm{DBP} e^{\gamma\left(\frac{D^2}{D^2_{\mathrm{d}}}-1\right)} \tag{5.9}$$

Note, however, that, unlike γ_0, the exponential gain γ is intrinsically dependent on the subject-specific DBP.

The Bramwell-Hill equation (Bramwell et al., 1923), of which Eq. 5.2 represents a linearisation in late diastole, relates the slope of the P-D^2 relationship to c. Combing the Bramwell-Hill equation with Eq. 5.9 leads to the following relationship between γ and c (the complete derivation of Eq. 5.10 can be found in Section 2.3.4):

$$\gamma = \frac{\rho\, c^2}{P_c} - \ln\left(\frac{P_c}{\mathrm{DBP}}\right), \tag{5.10}$$

where P_c is the pressure at which c was determined. Furthermore, knowing that combining Eqs. 5.8 and 5.9 leads to

$$\gamma_0 = \gamma - \ln\frac{\mathrm{DBP}}{P_{\mathrm{ref}}}, \tag{5.11}$$

Eq. 5.10 can be used to predict changes in c resulting from changes in BP (once more, the complete derivation of 5.12 can be found in Section 2.3.4).

$$c_{\mathrm{T}} = \sqrt{c^2\frac{P_{c_{\mathrm{T}}}}{P_c} + \frac{P_{c_{\mathrm{T}}}}{\rho}\ln\left(\frac{P_{c_{\mathrm{T}}}}{P_c}\right)} \tag{5.12}$$

where the subscript T stands for 'target' and indicates the target pressure; i.e., the pressure level to which convert the measured c.

Note that P_c inevitably depends on the specific method used for estimating c. It has been previously postulated that for PWV estimated using the foot-to-foot method (i.e., at DBP), P_c = DBP (Pucci et al., 2020; Spronck et al., 2017a), but this assumption has never been verified empirically. Furthermore, this assumption might not apply to local methods that estimate c from the relationship between arterial waveforms in a certain pressure range. To identify the optimal P_c for c estimated via the D^2P-loop method, γ was estimated directly by fitting the P-D^2 relationship. Since elastic c has been estimated in late diastole when viscous forces are at their minimum, γ was estimated by fitting the P_{elastic}-D^2 relationship with Eq. 5.9; γ was determined iteratively by minimising the difference between $P_{\text{estimated}}$ and P_{elastic} (cost function Π).

$$\Pi = \sum_{i=1}^{N} \left(P_{\text{estimated},i} - P_{\text{elastic},i}\right)^2 \ , \tag{5.13}$$

where subscript i indicates the i^{th} element of the P_{elastic} and $P_{\text{estimated}}$ heartbeat waveforms of length N. Note that P_{elastic} can be calculated after the estimation of η by inverting Eq. 5.6. Once γ and c are known, P_c is that pressure level that satisfies Eq. 5.10 and can be estimated iteratively by minimising the cost function Ω.

$$\Omega = \gamma - \frac{\rho\ c^2}{P_c} + \ln\left(\frac{P_c}{\text{DBP}}\right) \tag{5.14}$$

Finally, subject-specific c and γ can be corrected for inter-subject differences in BP using Eq. 5.12 and Eq. 5.11, respectively. P_{ref} was set to 100 mmHg.

5.2.4 Statistical analysis

The statistical analysis was performed using SPSS 23 (IBM corporation, Chicago, IL, USA) and was divided into two parts: first, the effect of age on arterial mechanics and haemodynamics has been evaluated dividing healthy controls in age-groups. Then, differences between pathologies were analysed (i.e., healthy controls, and hypertensive and T2DM patients), creating an age-matched control group of healthy individuals for this comparison.

Controls

Healthy controls were divided into five groups according to the subjects' age: <35 years, 35-49 years, 50-59 years, 60-59 years, and $\geq$ 70 years. First, ANCOVA was used to evaluate overall changes of haemodynamic parameters. Then, the post-hoc Bonferroni test was used for pairwise comparison when ANCOVA resulted significant. Sex was considered a confounder for all the outcome parameters, as was the ultrasound machine (US) (i.e., Esaote vs Aloka) for the parameters estimated via ultrasound, whether directly or because deriving from other

ultrasound-related parameters. Additional parameter-specific confounders were: DBP and HR for D_d, P_c and HR for c and Ds (both systolic and diastolic); SBP_{CCA} and HR for D_s; PP_{CCA} and HR for ΔD and γ_0 (Note that age-differences in γ were statistically analysed only after analytical correction to $P_{ref} = 100$ mmHg).

The mechanistic pressure-normalisation of c was compared with that achieved via ANCOVA, including P_c as sole confounder. Furthermore, the effect of the choice of the normalising pressure was evaluated; statistical and analytical pressure-normalisation of c were also conducted with assuming 1) P_c = MBP and 2) $P_c = SBP_{CCA}$ because commonly used for the statistical correction of PWV/c (Desamericq et al., 2015; Valbusa et al., 2019; Vogel et al., 2013) and 3) assuming P_c = DBP as suggested for foot-to-foot PWV metrics (Pucci et al., 2020; Spronck et al., 2017a).

Pathologies

Clinical groups were then compared with age-matched healthy controls: i.e., hypertensive and T2DM patients with healthy controls ≥35 years. This analysis progressed first with age and sex adjustments for all the investigated parameters and, then, with other potential parameter-specific confounders, as detailed above and as shown in Table 5.6, using ANCOVA. These also included antihypertensives, oral antidiabetic drugs, insulin and statin treatments. Post-hoc Bonferroni test was used for pair-wise comparisons between pathologies when ANCOVA was significant.

Finally, considering the 80% incidence of hypertension in T2DMs, the control-pathologies comparison was repeated with further stratification of T2DMs in normotensives and hypertensives. Results are presented as mean ± standard deviation, except for adjusted estimates that are expressed as mean (95% confidence interval). $p<0.05$ was taken as statistically significant.

5.3 Results

5.3.1 Ageing in healthy people

Heart rate, blood pressure, and carotid geometrical features

Table 5.2 presents demographics, resting HR, SBP_{BRA} and DBP of the healthy participants to this study, as well as their clustering in age groups. Distribution of men and women was not homogeneous in all age groups, but in each group the minority gender was at least 35% of the total number. Resting HR did not correlate with age and was, on average, 61±9 bpm.

Figure 5.4A shows changes in carotid SBP_{CCA} and DBP with age in healthy people. Both SBP_{CCA} and DBP positively correlated with age ($r=0.50$ $p<0.0001$ and $r=0.34$ $p<0.001$, respectively). SBP_{CCA} was, on average, just below 110 mmHg in young people (<35 years) and did not rise significantly until after 60 years of age when SBP_{CCA} was, on average, above 130 mmHg

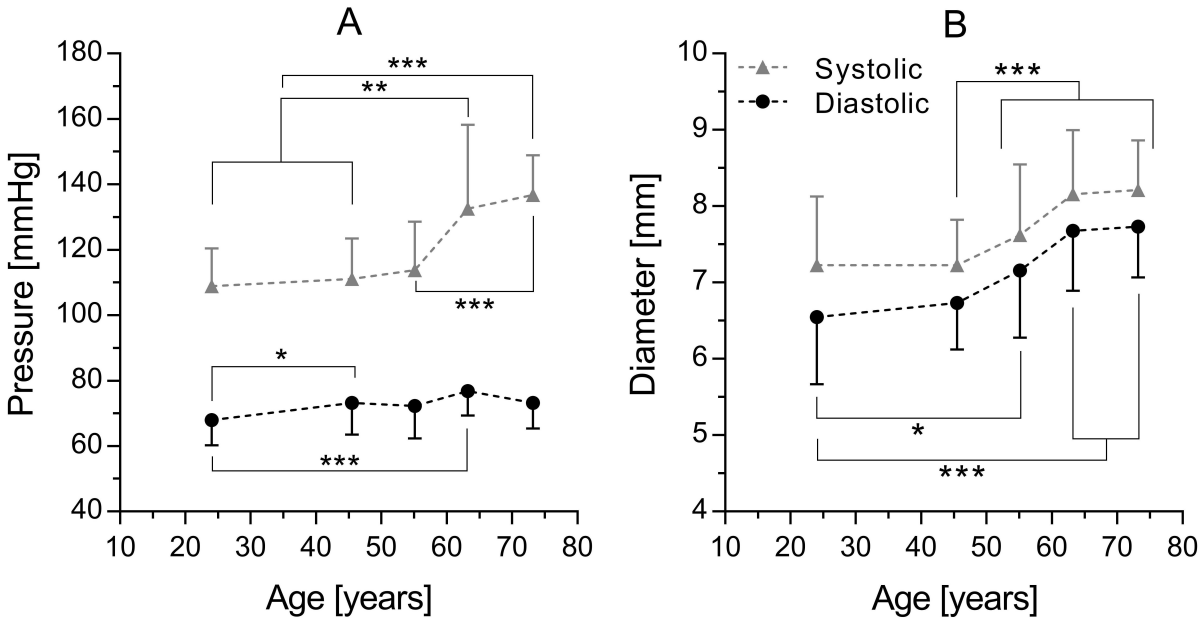

Figure 5.4: *Systolic (grey triangles) and diastolic (black circles) blood pressure (A) and carotid diameter (B) as a function of age in healthy people. As expected carotid pressure, mainly systolic, and calibre increased with age. Systolic data are presented as mean + standard deviation and diastolic data are presented as mean − standard deviation for clarity. Post-hoc Bonferroni pairwise comparison: $^{*}p<0.05$, $^{**}p<0.01$, and $^{***}p<0.001$.*

($p<0.001$). Overall changes in DBP were smaller and followed a different time course compared to SBP_{CCA}; DBP was just below 70 mmHg before 35 years of age, increased by approximately 9% by the age of 40 ($p<0.05$), and did not change thereafter. Consequently, PP_{CCA} did rose from ∼40 mmHg before 60 years to ∼50 mmHg in older adults ($p<0.001$).

Both systolic and diastolic diameter (Figure 5.4B) positively correlated with age (r=0.41

Table 5.2: *Demographic, HR and brachial pressure of the healthy population included in this study. Data are presented as mean ± standard deviation.*

Healthy controls					
Age-group	<35	35-49	50-59	60-69	≥70
Men:Women	20:19	10:11	12:16	10:6	7:4
Age [years]	24±4	46±3	55±2	63±3	73±7
HR [bpm]	64±9	59±7	61±9	61±11	61±3
SBP_{BRA} [mmHg]	110±11	114±15	115±14	134±32	138±12
DBP [mmHg]	68±8	74±10	73±9	77±7	73±7

p<0.0001, and r=0.51 p<0.0001). Differently from BP, changes in carotid diameter followed a similar pattern at the systolic and diastolic point: carotid diameter did not change significantly until 40 years, rose linearly between 45 and 65 years, and did not change thereafter. However, while age-group differences in D_d were still significant after adjusting for DBP, differences in D_s were not after SBP_{CCA} adjustment. IMT strongly correlated with age (r=0.79, p<0.0001), almost doubling across the age-range investigated in this study (from 0.428±0.080 mm before 35 years to 0.766±0.145 mm after 70 years of age).

Arterial stiffness

In healthy people, c strongly correlated with age (r=0.76, p<0.0001), ranging from 4.38±0.71 m/s in young individuals (<35 years) to 7.19±1.25 m/s in older adults (≥70 years) (Figure 5.5A). ${}_dDs$ was 53.3±15.6 MPa^{-1} in people <35 years and dropped almost linearly with age reaching 19.3±6.8 MPa^{-1} in older adults (r=−0.72, p<0.0001). Changes in ${}_sDs$ were more modest than those in ${}_dDs$ (Figure 5.5F); ${}_sDs$ was 44.5±15.3 MPa^{-1} before 35 years of age and dropped by 57% in controls ≥70 years (r=−0.61, p<0.0001).

Figure 5.5C shows age-related changes in the exponential stiffening parameter γ estimated by fitting Eq. 5.8 on the $P_{elastic}$-D^2 relationships. γ was 2.21±0.69 before <35 years and rose to 5.26±2.31 in people above 70 years (p<0.001) (Figure 5.5C). However, DBP accounted for ∼33% of the difference between the youngest and oldest age-group (Figure 5.5D); γ_0 was 2.61±0.71 before 35 years, did not change significantly until after 60 years, reaching 4.31±1.53 and 5.57±2.32 at 60-69 and ≥70 years, respectively (p<0.001 with <35 years for both).

Figure 5.6 compares SBP_{CCA} and DBP with P_c as estimated from c and γ using Eq. 5.11. On average, P_c was 77.0±12.1 mmHg, while SBP_{CCA}, DBP and MBP were 116.5±18.1, 71.8±9.2 and 91.8±11.3 mmHg, respectively. Despite a few outliers in older adults for whom P_c approached SBP_{CCA}, P_c showed good matching with DBP. Figure 5.7 A and B present correlation and Bland-Altman plot between P_c and DBP. The two pressure levels showed good agreement, with strong correlation (r=0.65, p<0.0001) and a bias of 5.2 mmHg (limits of agreement were −10.6 to 21.0 mmHg), approximately 11% of the PP_{CCA}. As visible in Figure 5.7B, the Bland-Altman plot allowed identifying a significant positive trend between the difference and average between P_c and DBP, likely reflecting increased PP_{CCA} in older adults. Indeed, the difference between P_c and DBP moderately correlated with PP_{CCA} (r=0.20, p<0.05). Nevertheless, including the 11% PP_{CCA} factor did correct the bias but did not affect the correlation in the Bland-Altman plot (Figure 5.7 C and D).

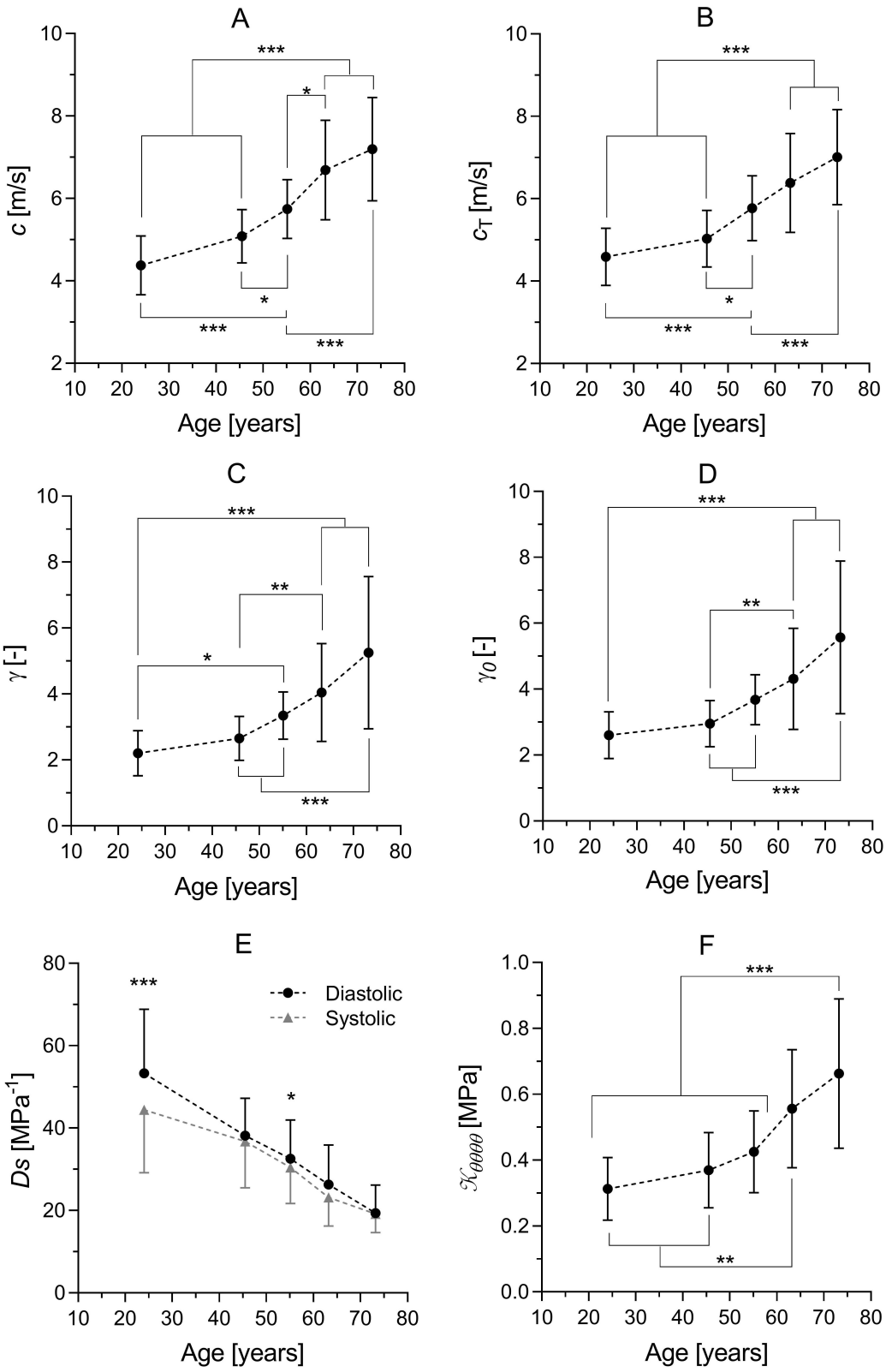

Figure 5.5: *c (A), c_T (B), γ (C), γ_0 (D), Ds in systole and diastole (E), and $\mathcal{K}_{\theta\theta\theta\theta}$ (F) as a function of age in healthy people. Stiffness metrics indicated that the onset of age-related CCA wall stiffening happens between 50 and 60 years. Data are presented as mean ± standard deviation. Post-hoc Bonferroni pairwise comparison: *p<0.05, **p<0.01, and ***p<0.001.*

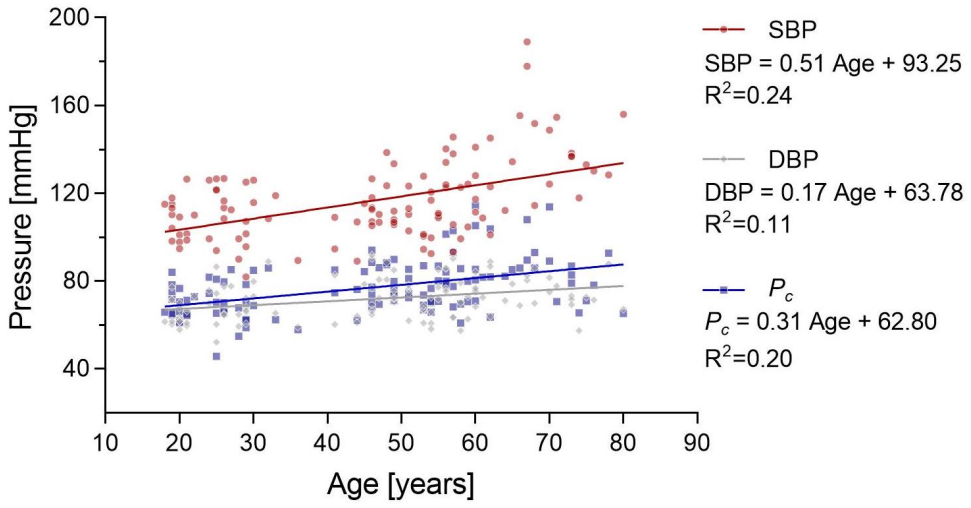

Figure 5.6: *Comparison between* P_c, $\mathrm{SBP_{CCA}}$ *and* DBP. *Except for a few outliers,* P_c *well matched* DBP.

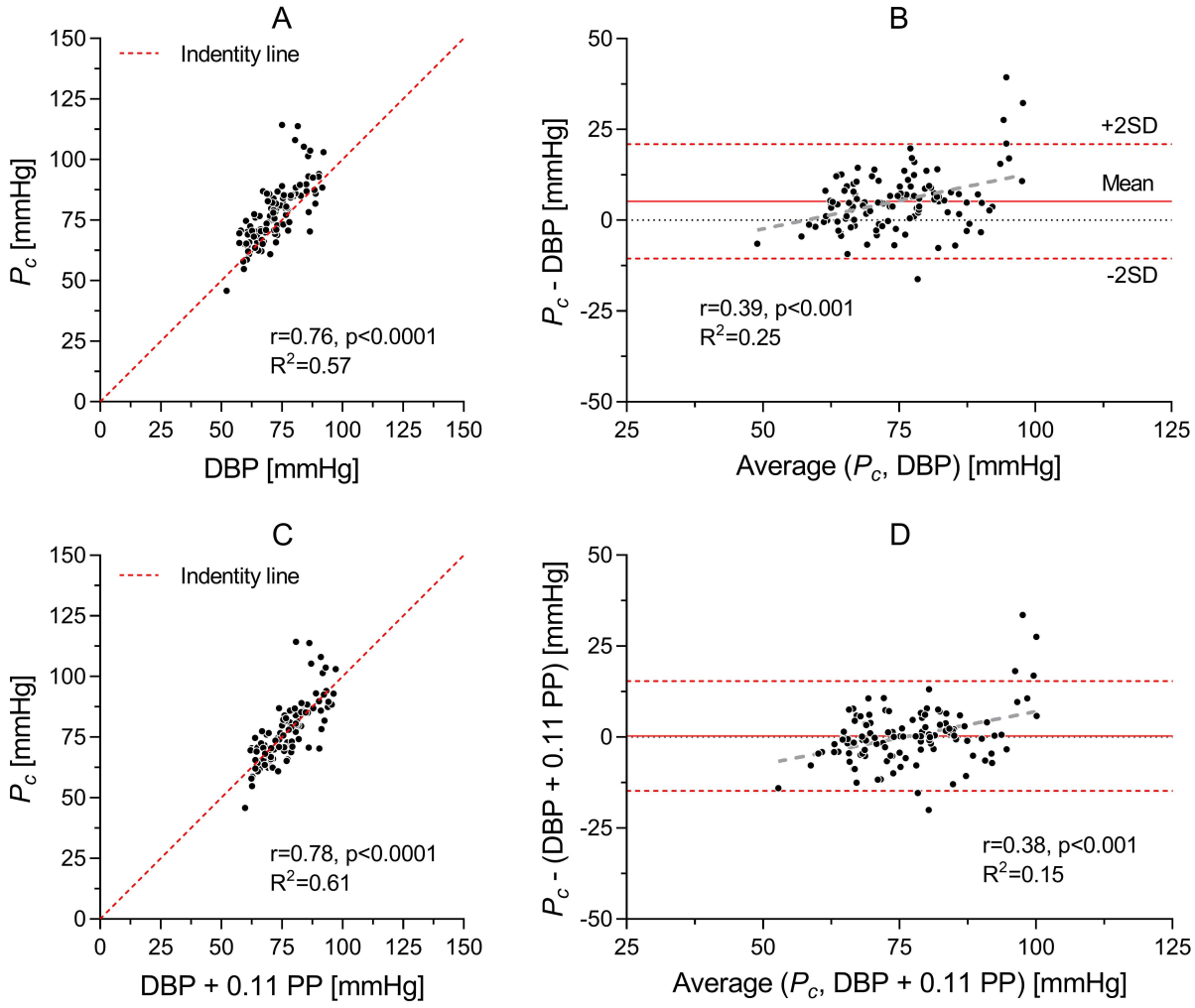

Figure 5.7: *Linear correlation and Bland-Altman plots between* P_c *and* DBP *(A and B), and between* P_c *and* $\mathrm{DBP} + 0.11\mathrm{PP_{CCA}}$ *(C and D).*

Table 5.3: *Pressure normalisation of local wave speed c in healthy controls: comparison between statistical (ANCOVA) and analytical methods. Using both methods, four different normalising pressure are considered: 1) $P_c = \mathrm{DBP}$, 2) the empirically derived $P_c = \mathrm{DBP} + 0.12\mathrm{PP_{CCA}}$, 3) $P_c = \mathrm{MBP}$, and 4) $P_c = \mathrm{SBP}$. For each age group, the corrected c is reported as mean ± standard deviation and as average percentage difference from the measured value.*

	Statistical				**Mechanistic**			
	DBP	DBP+0.11$\mathrm{PP_{CCA}}$	MBP	$\mathrm{SBP_{CCA}}$	DBP	DBP+0.11$\mathrm{PP_{CCA}}$	MBP	$\mathrm{SBP_{CCA}}$
< 35	4.43±0.87	4.47±0.87	4.58±0.83	4.60±0.75	4.58±0.73	4.59±0.69	4.62±0.64	4.64±0.59
	+1.1%	+2.1%	+4.6%	+5.0%	+4.6%	+4.8%	+5.7%	+6.0%
35-49	5.05±0.85	5.05±0.83	5.08±0.78	5.25±0.73	4.98±0.71	5.03±0.69	5.09±0.62	5.29±0.57
	−0.6%	−0.6%	-	+3.3%	−2.0%	−1.0%	-	+3.9%
50-59	5.74±0.85	5.74±0.83	5.77±0.78	5.82±0.72	5.76±0.81	5.77±0.79	5.81±0.74	5.86±0.72
	-	-	+0.5%	+1.4%	+0.3%	+0.5%	+1.2%	+2.1%
60-69	6.63±0.86	6.56±0.86	6.35±0.84	6.21±0.78	6.44±1.30	6.39±1.20	6.27±1.04	6.15±0.92
	−0.8%	−1.9%	−4.9%	−7.2%	−3.7%	−4.5%	−6.3%	−8.1%
≥70	7.18±0.85	7.12±0.84	6.88±0.82	6.59±0.78	7.13±1.22	7.01±1.15	6.77±1.06	6.45±0.96
	−0.1%	−1.0%	−4.3%	−8.3%	−0.8%	−2.5%	−5.8%	−10.3%

Table 5.3 presents the results of the pressure-normalisation of c using both statistical and mechanistic methods. Overall, statistical and mechanistic methods showed good agreement for all the considered P_c. However, the mechanistic correction always provided larger average changes in c than statistical methods for any choice of P_c. As expected, the choice of P_c largely affected the age-group-specific correction of c; the higher normalising pressure the larger the size of the correction. When P_c was set to DBP + $0.11\text{PP}_{\text{CCA}}$, BP accounted for ∼14% of the difference between people <35 years) and ≥70 years. This per cent grew to 23% and more than doubled at ∼34% when adjusting for MBP and SBP_{CCA}, respectively, and was lower at ∼10% for DBP. In agreement with results presented above for γ_0, changes in c were not significant before 50 years (after adjusting for HR, gender and US), with ∼37% of differences being related to increasing BP with age. After 50 years, c_{T} rose steadily at a rate of approximately 0.64 m/s per decade, reaching 7.95±1.13 m/s in older adults (≥70 years) (Figure 5.5B).

Finally, Figure 3.6F presents changes in $\mathscr{K}_{\theta\theta\theta\theta}$ with age. $\mathscr{K}_{\theta\theta\theta\theta}$ was 0.31±0.09 MPa in young people. Despite increasing on average to 0.37±0.11 MPa (35-49 years) and 0.43±0.12 MPa (50-59 years), changes in $\mathscr{K}_{\theta\theta\theta\theta}$ were not significant until after 60 years after accounting for DBP, sex, US and HR differences among age-groups (Figure 5.5C). By the age of 70 years, $\mathscr{K}_{\theta\theta\theta\theta}$ had more than doubled compared to the youngest age group.

5

Wall viscosity

Figure 5.8 presents examples of PD-loops in young, middle-aged and older adults and Figure 5.9 shows changes in hysteresis parameters with age. Both H_{A} and H_{I} negatively correlated with age (r=−0.47 and r=−0.48, p<0.001). H_{A} was 0.066±0.042 in young controls (<35 years), dropped to 0.027±0.024 at 35-49 years (p<0.01) and remained approximately constant thereafter. This is also visible in Figure 5.8, where only the PD-loop of the 26 years old person present clear hysteresis.

Figure 5.5B shows the comparison between systolic and diastolic distensibility. Overall, average ${}_{\text{s}}Ds$ was lower than ${}_{\text{d}}Ds$ (40.7±16.7 and 36.0±14.7 $\text{MPa}^{-}1$, respectively, p<0.001), however, ΔDs significantly decreased with age; in young individuals (<35 years), ${}_{\text{s}}Ds$ was on average 17.2±10.3% lower than diastolic distensibility (p<0.001). Such difference dropped below 6% after 40 years and was significant only in the 50-59 years decade.

The overall trend for η, the Voigt-type viscous coefficient to isolate the elastic component of the P-D relationship (Eq. 5.6), was in agreement with those of H_{A}, H_{I} and ΔDs: decreasing with age. Average η was 313.7±294.61 mmHg s/m in young people (<35 years) was approximately halved at 169.0±154.7 mmHg s/m by the age of 35-49 years, with no significant changes thereafter. It is worth noting that all viscosity parameters showed considerable variability.

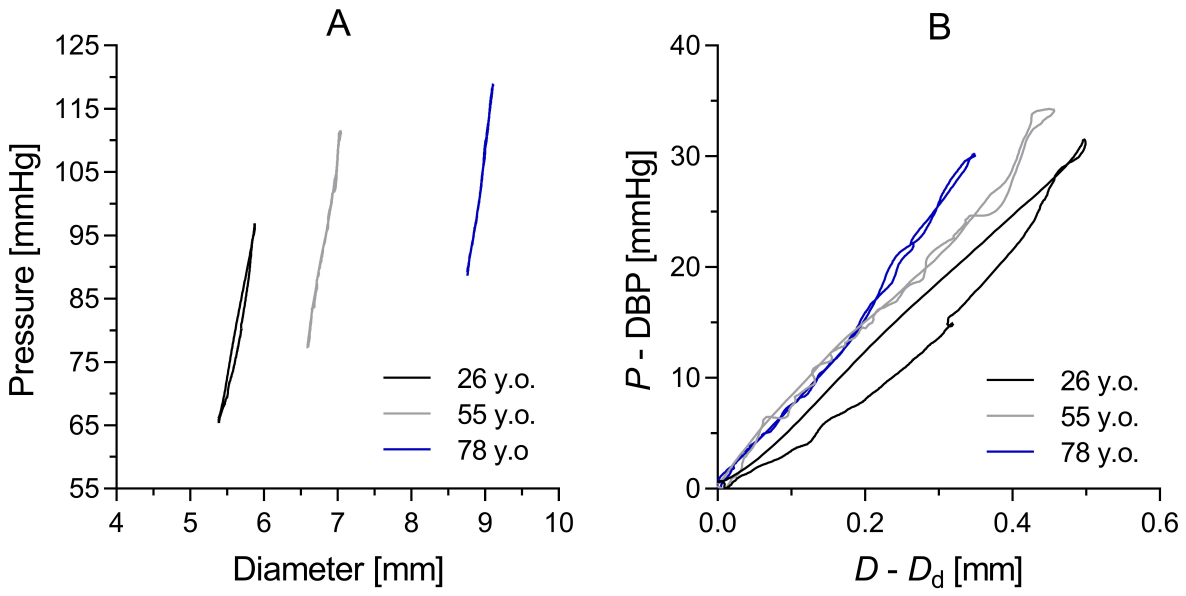

Figure 5.8: *Examples of PD-loops for three healthy controls: 26, 55, and 78 years (left, middle and right respectively). In panel B, the pressure-diameter loops were plotted by subtracting diastolic diameter and pressure from the diameter and pressure waveforms, respectively, in order to force the onset of each loop from the origin (0,0) position and hence allow for a better comparison between the loops. The slope of the PD-loop increased with age, while the hysteresis, clearly visible in the young loop, was much reduced in middle-aged and old individuals.*

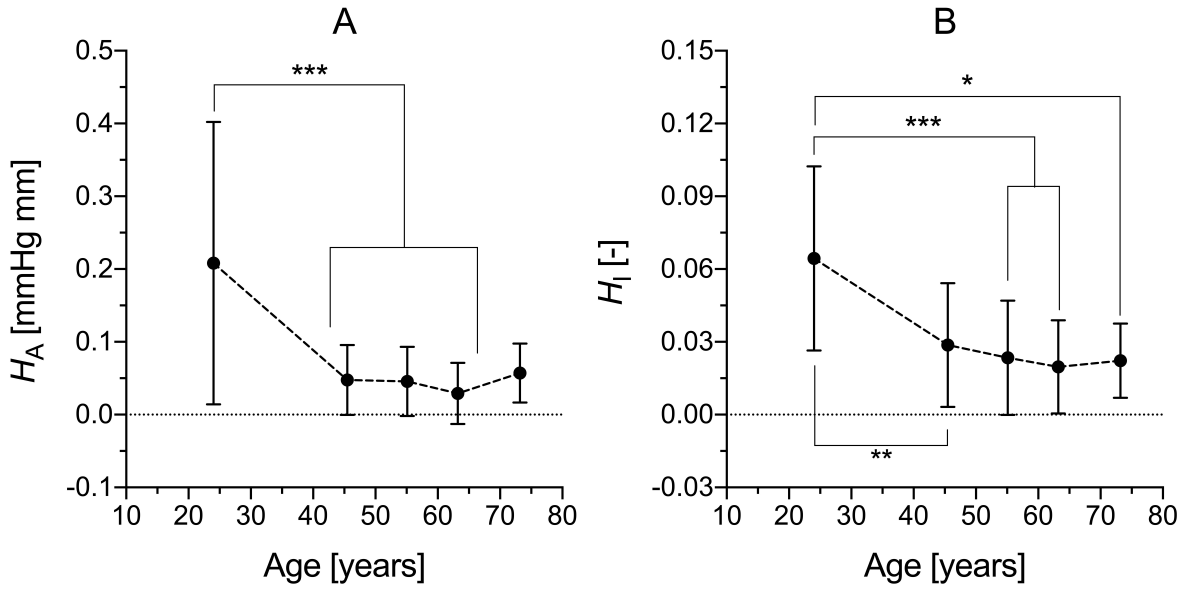

Figure 5.9: *Hysteresis area (H_A) and index (H_I) as a function of age. Hysteresis parameters were much higher in young individuals than in middle-aged and older adults. Data are presented as mean ± standard deviation. Post-hoc Bonferroni pairwise comparison: $^{*}p<0.05$, $^{**}p<0.01$, and $^{***}p<0.001$.*

5.3.2 Hypertension and type 2 diabetes

Heart rate, blood pressure, and carotid geometrical features

Table 5.4 reports the information on the drug treatments of people in each clinical group. The average age was higher in all clinical groups compared to controls ($p<0.001$ for both), as was the per cent of male subjects (67% in T2DMs and 58% in hypertensives vs 49% in controls). Dyslipidemia was present in 70% and 49% of T2DM and hypertensive patients, respectively, despite statins treatment in 61% and 25% in the two groups. Of the T2DMs, 80% and 30% were on oral antidiabetic and insulin treatment respectively, and only 8% on neither. Among T2DMs, 80% were also diagnosed with hypertension, and 91% of the latter were on antihypertensive treatment. Conversely, only 62% of the hypertensive without T2DM patients were on antihypertensives.

Table 5.5 presents the haemodynamic parameters in the three groups. HR was significantly higher in T2DMs than both in controls and hypertensives ($p<0.001$), which, in turn, had comparable average HR. HR did not correlate with age in any of the groups but in hypertensives, where it slightly decreased with age ($r=-0.34$, $p<0.01$). Despite the high incidence of hypertension in T2DMs, only hypertensive patients had higher BP than age-matched controls. Their BP was also higher than that of T2DMs ($p<0.001$ for SBP_{CCA} and $p<0.01$ for DBP). Interestingly, BP was comparable in controls and T2DMs, likely reflecting the effect of antihypertensive treatment. PP_{CCA} was also higher in hypertensives than both in controls ($p<0.001$) and T2 diabetic ($p<0.001$). After adjusting for age, sex, HR, and US machine differences, D_s and D_d, but not ΔD, were significantly higher in T2DMs than in controls and hypertensives ($p<0.01$ for

Table 5.4: *Drug treatment of the people included in this study. For each drug, data are reported as the number of people using a drug (percentage).*

Drug	T2DM N (%)	Hypertension N (%)
Antihypertensive	90 (72)	43 (62)
- Diuretics	28 (22)	4 (6)
Antidiabetics (oral)	100 (80)	0 (0)
Insulin	37 (30)	0 (0)
Statin	76 (61)	17 (25)
Antiarrhythmics	2 (2)	3 (4)
Antiplatlet	36 (29)	9 (13)

both). Average IMT was 0.65 mm in controls, and higher, although not significantly so, at 0.74 mm in both T2DM and hypertensive patients.

Arterial stiffness

Average c was 5.97±1.17 m/s in controls, and higher at 7.27±1.47 and 6.67±1.39 m/s in hypertensives and T2DMs, respectively (Table 5.5). Similarly γ was 3.58±1.48, 4.62±1.78, and 4.45±1.81 in controls, hypertensives and T2DMs, respectively. However, analytical pressure-normalisation to the reference pressure of 100 mmHg (γ_0) reduced inter-group differences, that were not significant after adjusting for age, sex, HR, US machine and drug treatments (Tables 5.5 and 5.6). As in controls, P_c was slightly higher than DBP; when compared using the Bland-Altman technique their bias was 6.70 mmHg (limits of agreement: −11.6 to 25.0 mmHg), hence P_c exceeded DBP by approximately 13% of the PP.

Table 5.7 compares the results of the mechanistic pressure-normalisation with that obtained by statistical methods (ANCOVA). Target pressures were set at the average BP level across groups (e.g., average SBP_{CCA}- DBP). As for age-group differences in healthy controls, good agreement was found between the statistical and the mechanistic pressure-normalisation for all the investigated P_c. Once more, the choice of P_c largely affected the correction of c; when assuming $P_c = \text{DBP} + 0.13\text{PP}_{\text{CCA}}$, BP alone accounted for 37% and 26% of the total difference between hypertensive and T2DMs patients, respectively, and controls. Note that after accounting for other confounders inter-group differences in c were reduced further and were not significant: 6.52 (6.13 to 6.92) m/s in controls, 6.90 (6.51 to 7.30) m/s in hypertensives, and 6.54 (6.18 to 6.90) m/s in T2DMs (Table 5.6). Neglecting the PP_{CCA} component (i.e., P_c = DBP + $0.13\text{PP}_{\text{CCA}} \approx$ DBP) only minimally affected the pressure-normalisation; the contribution of BP to differences between controls and hypertensives reduced to 31% of the total difference. Conversely, normalising against SBP_{CCA} lead to a considerably larger correction of c, especially in hypertensive people, with BP accounting for 63% of their difference with controls.

${}_{\text{s}}Ds$ was significantly lower than ${}_{\text{d}}Ds$ in all clinical groups ($p<0.001$), suggesting that the CCA wall is stiffer in systole than diastole. As for c, ${}_{\text{d}}Ds$ was also comparable in the three groups after appropriate adjustments: 28.7 (24.8 to 32.6) MPa^{-1}, 26.1 (21.8 to 30.3) MPa^{-1}, and 25.4 (22.5 to 28.3) MPa^{-1} in controls, hypertensives and T2DMs (Table 5.6). On the contrary, inter-group differences in ${}_{\text{s}}Ds$ were more accentuated, although still not significant: 27.2 (23.6 to 30.7) MPa^{-1} in controls ($p<0.05$), 22.9 (19.0 to 26.8) MPa^{-1} in hypertensives, and 22.8 (20.2 to 25.5) MPa^{-1} in T2DMs (Table 5.6).

Table 5.5: *Comparison in haemodynamic characteristics between healthy controls ≥35 and hypertensive and T2DM patients. Data are presented as mean ± standard deviation. Bonferroni post-hoc pairwise comparisons:* $^{*}p<0.05$, $^{**}p<0.01$ *and* $^{***}p<0.001$ *with controls;* $^{\dagger}p<0.05$, $^{\dagger\dagger}p<0.01$ *and* $^{\dagger\dagger\dagger}p<0.001$ *with hypertension. Adjusted parameters are presented in Table 5.6*

	Control	**Hypertension**	**T2DM**
Male:Female	37:39	40:29 ***	84:41 ***
Aloka:Esaote	41:35	24:45	112:12
Age [years]	57±10	65±10 ***	65±8 ***
HR [bpm]	60.7±8.3	62.7±9.0	70.0±10.6 ***†††
SBP_{BRA} [mmHg]	122.1±18.5	144.5±20.0 ***	128.8±18.1 †††
SBP_{CCA} [mmHg]	120.3±19.6	143.6±21.1 ***	126.9±19.0 †††
DBP [mmHg]	73.9±9.1	81.5±9.2 ***	77.2±9.7 ††
MBP [mmHg]	94.8±11.5	108.5±12.2 ***	99.5±12.1 †††
PP_{CCA} [mmHg]	46.4±17.2	62.1±18.8 **	49.6±15.6 †††
D_s [mm]	7.70±0.87	8.17±0.87	8.55±1.03 **††
D_d [mm]	7.22±0.85	7.69±0.85	8.10±1.00 **††
ΔD [mm]	0.47±0.11	0.48±0.14	0.45±0.14
IMT [mm]	0.65±0.13	0.74±0.13	0.74±0.15
c [m/s]	5.97±1.17	7.27±1.47	6.67±1.39
$\mathscr{K}_{\theta\theta\theta\theta}$ [MPa]	0.47±0.18	0.69±0.31	0.60±0.28
γ [-]	3.58±1.48	4.62±1.78	4.45±1.81
γ_0 [-]	3.89±1.50	4.83±1.79	4.72±1.81
${}_dDs$ [MPa^{-1}]	31.8±10.8	22.7±9.6	25.1±11.0
${}_sDs$ [MPa^{-1}]	29.9±10.9	19.8±8.9	22.6±9.8
ΔDs [%]	5.2±13.1	13.2±10.3 **	9.3±8.8
H_A [mmHg mm]	0.43±0.44	1.22±1.09 **	0.79±0.81
H_I [-]	0.023±0.022	0.048±0.037 **	0.036±0.026
η [mmHg s/m]	161.9±185.7	403.8±435.4 **	286.6±325.5

Table 5.6: *Adjusted haemodynamic characteristics between healthy controls ≥35 years and hypertensive and T2DM patients. Age and sex were considered confounders for all other parameters. Adjusted values are presented as mean [95% confidence interval]. Other parameter-specific adjustments: ultrasound machine (US),* HR *and* SBP_{CCA} *for* D_s*;* US, HR *and* DBP *for* D_d*;* US, HR *and* PP_{CCA} *for* ΔD*;* US *for* IMT*;* US, HR, P_c *and drug treatments for* c, $\mathscr{K}_{\theta\theta\theta\theta}$, ${}_dDs$, *and* ${}_sDs$*;* US, HR *and drug treatments for* γ_0*;* US *and drug treatments for* H_A *and* η*; drug treatments for* H_I.

	Control	**Hypertension**	**T2DM**
HR [bpm]	59.4 [57.1-61.6]	62.1 [59.9-64.4]	70.6 [68.9-72.3]
SBP_{BRA} [mmHg]	126.6 [122.5-130.8]	142.9 [138.8-147.1]	126.9 [123.8-130.1]
SBP_{CCA} [mmHg]	125.3 [120.9-129.7]	141.9 [137.5-146.2]	124.8 [121.5-128.1]
DBP [mmHg]	73.8 [71.6-76.0]	81.7 [79.5-83.9]	77.2 [75.5-78.9]
MBP [mmHg]	96.7 [94.0-99.5]	108.0 [105.2-110.7]	98.6 [96.5-100.7]
PP_{CCA} [mmHg]	51.5 [47.9-55.0]	60.2 [56.6-63.8]	47.6 [44.9-50.3]
D_s [mm]	7.99 [7.77-8.20]	7.98 [7.76-8.20]	8.48 [8.31-8.66]
D_d [mm]	7.49 [7.28-7.70]	7.58 [7.36-7.80]	8.00 [7.83-8.18]
ΔD [mm]	0.46 [0.43-0.50]	0.44 [0.41-0.47]	0.48 [0.45-0.51]
IMT [mm]	0.68 [0.65-0.72]	0.71 [0.67-0.74]	0.74 [0.70-0.77]
c [m/s]	6.52 [6.13-6.92]	6.90 [6.51-7.30]	6.54 [6.18-6.90]
$\mathscr{K}_{\theta\theta\theta\theta}$ [MPa]	0.55 [0.46-0.64]	0.61 [0.52-0.70]	0.60 [0.50-0.69]
γ_0 [-]	4.43 [3.89-4.97]	4.76 [4.23-5.29]	4.43 [3.94-4.93]
${}_dDs$ [MPa^{-1}]	28.7 [24.8-32.6]	26.1 [21.8-30.3]	25.4 [22.5-28.3]
${}_sDs$ [MPa^{-1}]	27.2 [23.6-30.7]	22.9 [19.0-26.8]	22.8 [20.2-25.5]
ΔDs [%]	5.2 [1.1-9.4]	13.9 [9.6-18.3]	9.0 [6.0-12.1]
H_A [mmHg mm]	0.52 [0.19-0.86]	1.23 [0.87-1.58]	0.75 [0.51-0.99]
H_I [-]	0.025 [0.014-0.036]	0.048 [0.037-0.060]	0.034 [0.026-0.042]
η [mmHg s/m]	226.5 [94.0-359.0]	476.9 [336.0-617.9]	248.1 [154.3-341.9]

Table 5.7: *Pressure normalisation of local wave speed c in the three clinical groups: comparison between statistical (ANCOVA) and analytical methods. Using both methods, four different normalising pressure are considered: 1)* P_c = DBP, *2) the empirically derived* P_c = DBP + $0.13\text{PP}_{\text{CCA}}$, *3)* P_c = MBP, *and 4)* $P_c = \text{SBP}_{\text{CCA}}$. *For each age group, the corrected c is provided as mean ± standard deviation and as the average percentage difference from the measured value.*

	P_c	Control	Hypertension	T2DM
Statistical	DBP+$0.13\text{PP}_{\text{CCA}}$	6.15±1.33 +3.0%	7.04±1.34 −3.2%	6.69±1.29 +0.3%
	DBP	6.07±1.35 +1.7%	7.15±1.36 −1.6%	6.68±1.33 +0.1%
	MBP	6.24±1.24 +4.5%	6.83±1.29 −6.1%	6.71±1.21 +0.7%
	SBP_{CCA}	6.29±1.18 +5.4%	6.74±1.22 −7.3%	6.76±1.15 +1.3%
Mechanistic	DBP+$0.13\text{PP}_{\text{CCA}}$	6.19±1.15 +3.7%	7.01±1.39 −3.6%	6.71±1.31 +0.6%
	DBP	6.17±1.23 +3.4%	7.07±1.45 −2.8%	6.70±1.35 +0.4%
	MBP	6.19±1.02 +3.7%	6.90±1.27 −5.1%	6.75±1.27 +1.2%
	SBP_{CCA}	6.30±0.88 +5.5%	6.78±1.18 −6.7%	6.78±1.25 +1.6%

Finally, $\mathscr{K}_{\theta\theta\theta\theta}$ was, on average, accentuated in hypertensives and T2DMs at 0.69±0.31 and 0.60±0.28 MPa, respectively, compared to controls (0.47±0.18 MPa), but as for c reflecting structural stiffness rather than plain material stiffness, differences in $\mathscr{K}_{\theta\theta\theta\theta}$ were mostly attributable to BP, sex and age differences among groups, rather than actual differences in wall stiffness.

Wall viscosity

Examples of P-D loops for representative control, hypertensive and T2DM people are shown in Figure 5.10. All indices of wall viscosity were significantly higher in hypertensive patients than in controls; H_{A} and the normalised H_{I} were 0.52 (0.19 to 0.86) mmHg mm and 0.025 (0.014 to 0.036), respectively in controls, and approximately twice as high in hypertensives at 1.23 (0.87 to 1.58) mmHg mm and 0.048 (0.037 to 0.060) ($p<0.01$ for both). H_{A} and H_{I} in T2DMs did not differ from either of the other two groups, displaying intermediate levels of viscosity (Tables 5.5 and 5.6). Considering the high incidence of hypertension in T2DMs, the

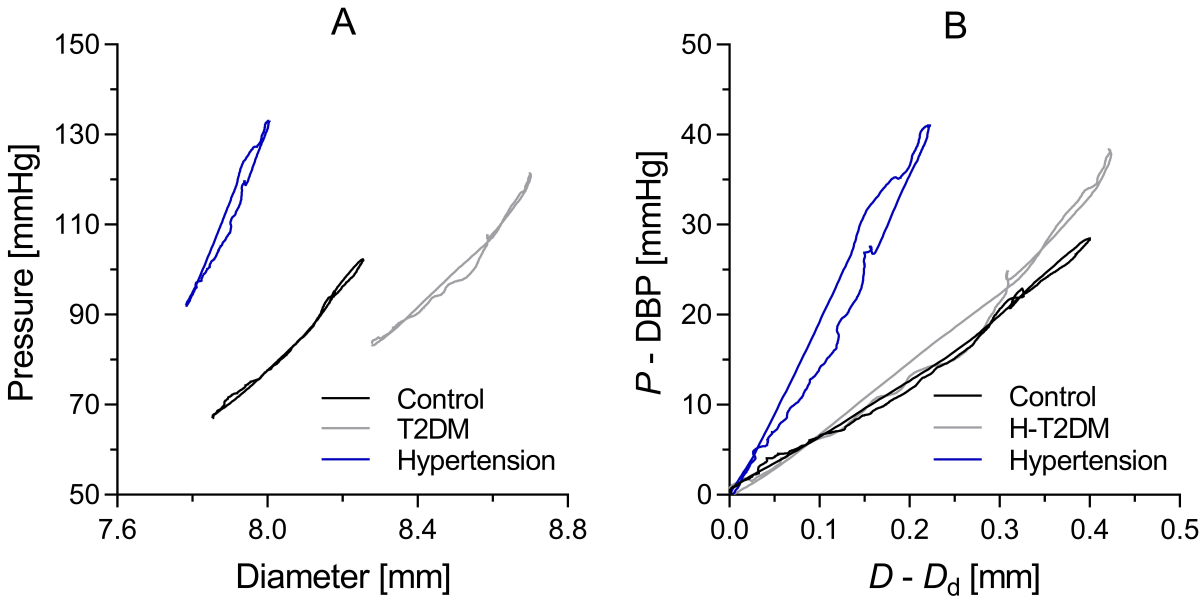

Figure 5.10: *Examples of PD-loops for a healthy control, a hypertensive patient, and a T2DM patient (all >60 years). In panel B, the pressure-diameter loops were plotted by subtracting diastolic diameter and pressure from the diameter and pressure waveform, respectively, in order to force the onset of each loop from the origin (0,0) position and hence allow for a better comparison between the loops. Unlike in controls, hysteresis persists also in older individuals with hypertension.*

group was further stratified in normotensive (N-T2DMs, N=25) and hypertensive (H-T2DMs, N=99) T2DMs and their viscosity indices compared with controls and hypertensives. Results are presented in Table 5.8. After appropriate adjustments, H_A was 0.25 (−0.19 to 0.68) mmHg mm in N-T2DMs, significantly lower than in H-T2DMs (1.02, 0.71 to 1.33 mmHg mm)($p<0.05$) and in plain hypertensives (1.21, 0.086 to 1.55 mmHg mm)($p<0.05$). H_I was also lower in N-T2DMs (0.019, 0.005 to 0.034) than in hypertensives (0.049, 0.037 to 0.060)($p<0.05$), but not than in H-T2DMs (0.042, 0.032 to 0.052). No differences were found between controls and NT2DMs and between plain hypertensives and H-T2DMs.

In agreement with the results of the hysteresis, hypertensives patients showed higher differences between Ds in systole and diastole; after age, sex and treatment adjustments, ΔDs was 13.9 (9.6 to 18.3)% in hypertensives and les than half in controls at 5.2 (1.1 to 9.4)% ($p<0.01$), but not significantly different in all T2DMs (9.6, 6.0 to 12.1%). When T2DMs were further stratified according to the presence of hypertension, average values did suggest similar findings to those reported for the hysteresis, but differences were not significant (Table 5.8). In the overall population, ΔDs significantly correlated with both H_I and H_A ($r=0.53$ and $r=0.46$, $p<0.001$), suggesting that ΔDs is indeed related to arterial viscosity. Indeed, differences ΔDs among

Table 5.8: *Comparison in viscous parameters between healthy controls ≥35 years, plain hypertensive, plain T2DM (N-T2DMs), and hypertensive T2DM (H-T2DMs) patients. Data are presented as mean ± standard deviation and adjusted values as mean [95% confidence interval]. ANCOVA post-hoc pairwise comparisons: $^{**}p<0.01$ and $^{***}p<0.001$ with controls; $^{\dagger}p<0.05$ with hypertension; $^{\ddagger}p<0.05$ with N-T2DM.*

	Control	**Hypertension**	**N-T2DM**	**H-T2DM**
ΔDs [%]	5.2±13.1	13.2±10.3 **	8.7±7.9	9.5±9.1
	4.2 [−0.5-9.0]	13.9 [9.6-18.2]	6.9 [1.2-12.5]	10.2 [6.2-14.1]
H_{A} [mmHg mm]	0.43±0.44	1.22±1.09 ***	0.45±0.29 †	0.88±0.88 ‡
	0.27 [−0.11-0.65]	1.21 [0.86-1.55]	0.25 [−0.19-0.68]	1.02 [0.71-1.33]
H_{I} [-]	0.023±0.022	0.048±0.037 **	0.023±0.015 †	0.039±0.027
	0.018 [0.006-0.031]	0.049 [0.037-0.060]	0.019 [0.005-0.034]	0.042 [0.032-0.052]
η [mmHg s/m]	161.9±185.7	403.8±435.4 **	199.8±172.6 †	327.3±336.8
	165.8 [14.9-316.7]	472.1 [331.6-612.6]	127.7 [−45.1-300.5]	313.3 [191.1-435.5]

groups were not significant when adjusting for either H_{I} or H_{A}.

5.4 Discussion

This Chapter aimed at introducing methods for a) evaluating arterial viscoelasticity *in vivo* by discerning between viscoelastic distensibility in systole and 'elastic' distensibility in diastole, considering the implications for the concept of arterial stiffness, and b) accounting for the effect inter-subjects BP differences on local wave speed c. The novel techniques have been used to investigate changes in the viscoelastic mechanical properties of the human CCA associated with ageing and pathologies affecting the cardiovascular system (hypertension and T2DM), beyond BP. The main findings are: 1) distensibility in both systole and diastole decreased with age in controls, but their relative difference (ΔDs) was significantly higher in young people than in middle-aged and older individuals (when this was mostly negligible). All other viscosity indices, H_{A} in the P-D loop, H_{I} and the viscous coefficient η, also decreased with age in controls. 2) Elevated BP (i.e., hypertension) can alter the normal decline in wall viscosity with age, with ΔDs, H_{A}, H_{I}, and η being significantly higher in plain hypertensives than controls. 3) Diastolic indices of arterial stiffness, reflecting the elastic property of the wall tissue, indicated a significant stiffening with age, but did not differ significantly between clinical groups after accounting for BP differences and other confounders. Conversely, as a result of the increased viscosity of the

wall tissue in response to elevated BP, inter-group differences viscoelastic Ds in systole were more accentuated, although still not significant.

5.4.1 Ageing

Previous studies have shown the correlation between ageing and stiffening of elastic arteries using both regional (The Reference Values for Arterial Stiffness' Collaboration, 2010) and local (Borlotti et al., 2012; Li et al.; Uejima et al., 2020) methods for the estimation of PWV/c. The results presented here confirm previous findings indicating a strong correlation between c and age, and with c increasing by ∼64% across the investigated age range. It is worth noting, however, that changes of c with age were accompanied by BP changes, that necessarily contributed to differences between age-groups. In agreement with previous studies, BP changes mainly interested SBP that increased by ∼20 mmHg across the investigated age-range, while changes in DBP were milder and reached their peak in middle-aged individuals (Gurven et al., 2012; Shimura & Kubo, 2019; Wang et al., 2019). The pressure-normalisation method proposed here indicated that the D^2P-loop method provides a 'almost diastolic' measure of c: DBP accounted for ∼87-89% of P_c compared to ∼11-13% of SBP. Mechanistic pressure-normalisation of c estimated that pressure accounted for approximately 23% of changes in local wave speed. The BP effect was mostly visible in the first two age-groups (<35 years and 35-49 years), where DBP increased by more than 9% and BP accounted for almost 40% of the difference in c. As a result, changes in c was modest until the age of 50 years, when c started rising at a steady pace of ∼0.64 m/s per decade.

It was recently shown that the tangential elastic modulus at ∼DBP can be estimated from measures of local c, wall thickness and diameter (Li et al., 2021). The tangential elastic modulus presents the advantage of being an index of pure material stiffness, independent from geometrical features of the artery. Conversely, as indicated by the Moens-Kortweg equation (Kortweg, 1878; Moens, 1878), c is a function of the material stiffness and of the thickness-to-diameter ratio, hence, reflecting structure-dependent stiffness. Interestingly, $\mathscr{K}_{\theta\theta\theta\theta}$ did not change significantly until after 60 years, thus suggesting that earlier changes in c might reflect an increase of the thickness-to-diameter ratio rather than an actual stiffening of the wall tissue. It is worth noting, however, that the total wall thickness is challenging to assess *in vivo*; here, IMT was used as a surrogate of wall thickness. Although the adventitia is less affected than both intima and media by age-related arterial remodelling, result presented here might be biased by this approximation.

While arterial stiffening with age has long been known, the methodology proposed here indicated a decrease of the PD-loop hysteresis with age, suggesting a decrease in carotid wall

viscosity. While this finding agrees with the results found by Learoyd & Taylor (1966) >50 years ago in an *ex vivo* study on the human arteries (including the carotid), to the limit of the author's knowledge, has not been previously reported in *in vivo* studies. Arterial wall viscosity is commonly associated with the muscular component of the arterial wall as higher viscous properties have been found in arteries with a higher concentration of smooth muscle cells (SMCs) (Apter et al., 1966; Zatzman et al., 1954). Therefore, these results possibly reflect well established age-related microstructural changes of the arterial media described in Chapter 4, with SMCs migrating to the intima while abandoning their contractile phenotype (Learoyd & Taylor, 1966; Tesauro et al., 2017). As expected, changes in wall viscosity were also paralleled by a drop of ΔDs with increasing age; in agreement with Giannattasio et al. (2008), we found a significantly higher Ds in the late diastole compared to early systole (∼12% difference), but correlation with age of ${}_{\mathrm{s}}Ds$ was weaker than that of ${}_{\mathrm{d}}Ds$. These results suggest that ${}_{\mathrm{s}}Ds$ describe a combination of elastic and viscous properties.

Arterial viscosity is often overlooked in *in vivo* investigations and has been previously quantified in a handful of studies. Boutouyrie et al. (1998) studied arterial wall viscosity, as expressed by the PA-loop hysteresis, in mice both *in vivo* and *in vitro* under different level of smooth muscle tone, and found a higher viscosity *in vitro* independently on the of the pressure level, suggesting that the viscous effect might be relatively small *in vivo*. Furthermore, they found that increased smooth muscle tone was associated with increased hysteresis *in vivo*, however, their *in vitro* suggested that this might have been mediated, at least in part, by changes in PP. Using a similar signal alignment method to that used in this study, Hermeling et al. (2010) studied pressure-diameter relationships in 21 patients (age 64±12 years) finding negligible hysteresis. Given the different scope of their work, the clinical background of the subjects included was not specified. Nevertheless, the results presented in this study are in agreement and indicate that H_{I} in healthy middle-aged and old individual is, indeed, small. By contrast, in younger subjects, a higher hysteresis area is associated with markedly increased difference between diastolic and systolic distensibility.

5.4.2 Hypertension and type 2 diabetes

Given the pressure-dependence of arterial stiffness, increased PWV is expected in both hypertensives and T2DMs whose BP is typically higher than that of healthy normotensives. However, several studies have reported that increased PWV was independent of pressure differences among clinical groups. Zhang et al. (2011) reported a significantly higher cfPWV, carotid-radial PWV, and carotid-ankle PWV in Chinese normotensive T2DMs when compared to age-matched healthy

controls. Laugesen et al. (2013) reported a higher average cfPWV in T2DMs than in controls with similar values of 24h ambulatory BP in the two groups. In this study, diastolic indices of arterial stiffness (c and ${}_{\mathrm{d}}Ds$), that best describe the 'purely elastic' properties of the arterial wall (Alastruey, 2011), were, indeed, accentuated (higher c and lower ${}_{\mathrm{d}}Ds$) in T2DM and hypertensive patients than in controls. However, differences were not significant after adjusting for confounding factors (mainly BP, age, and sex). Similarly, exponential stiffness parameters (γ and γ_0) were also comparable in the three clinical groups. Similar findings have been reported previously when the elastic exponential P-D^2 relationship of the CCA was estimated by iteratively minimising the area of hysteresis in the PD-loop of normotensive and hypertensive people (Armentano et al., 1995a). Conversely, all the viscosity indices (H_{A}, H_{I}, η and ΔDs) were significantly higher in hypertensives than in controls, so that differences in ${}_{\mathrm{s}}Ds$, describing a combination of both elastic and viscous wall response, were greater than those in diastolic stiffness, if not significant. Therefore, in agreement with Armentano et al. (1995a), the results of this Chapter indicate increased wall viscosity *in vivo* in humans associated with hypertension possibly contributing to increased wall stiffness in systole. Further, similar differences were also observed in T2DM, with H_{A} significantly higher in H-T2DMs than in N-T2DMs, while comparable viscosity indices were found among normotensives (controls vs N-T2DMs) and hypertensives (plain vs H-T2DMs).

Most methods, as the foot-to-foot technique, estimate PWV from early systole when viscous forces reach their maximum. Therefore, the positive correlation between H_{A} and ΔDs found here suggests that reported differences in PWV between hypertensive, T2DM and healthy people might reflect, at least in part, different levels of wall viscosity rather than purely elastic mechanical properties of the arterial wall. Additionally, regional and local PWVs must be compared with caution, as they describe average properties of relatively long sections and properties of a single location of the arterial tree, respectively. Therefore, changes in local c might not reflect changes in regional PWV as ageing and pathologies act differently in different regions of the arterial tree (Armentano et al., 1995a; Borlotti et al., 2012).

Additionally, while T2DM *per se* did not significanlty affect the cartoid wall viscoelasticity, it is worth noting the finding of higher diastolic and systolic carotid diameters in T2DM patients compared to controls and hypertensive patients, independently of BP, confirming a previous observation of Prof. Palombo's group (Kozakova et al., 2019). They also reported a direct relation of matrix metalloproteinases 12 (MMP-12) with interleukin 6 and 8 (IL-6 and IL-8), and a direct correlation of MMP-12 with carotid interadventitial diameter independent of age and blood pressure. Being MMP-12a potent elastase highly expressed in macrophages, these previous findings support the hypothesis that these differences in diameter may be dependent on

enhanced expression of the inflammatory mediators inducing MMPs activation with a consequent extracellular matrix alteration.

5.4.3 Pressure-normalisation of local wave speed

Despite the clinical evidence of correlation between wave speed and arterial stiffness, pressure-dependency may confound the differentiation between various pathologies with varying arterial pressures. It may also confound the differentiation between the effect pressure and that of ageing. Therefore, a technique to normalise with respect to pressure would be highly advantageous and sought after. Most clinical studies address this issue using statistical regression methods to account for BP differences among groups (typically considering DBP, MBP or SBP as confounding factor) (Desamericq et al., 2015; Valbusa et al., 2019; Vogel et al., 2013). However, using statistical methods presents three major limitations: first and foremost, they fail in providing patient-specific corrections of c and are consequently not ideal in clinical practice. Second, as elevated BP is associated with vascular damage and arterial stiffening, to a certain extent, in large population studies PWV and c are expected to show correlation with BP even after pressure-normalisation. Therefore, discerning between the short-term and long-term effects of exposure to high BP using statistical regressions is a complex goal to achieve that may not be attainable. Third, as demonstrated in this Chapter, the choice of normalising pressure strongly affects the correction of PWV/c against BP differences.

The mechanistic method proposed here is based on the observation that, in the physiological range of pressure, the pressure-area relationship of arteries can be expressed as an exponential function and allows to directly predict changes in c associated with changes in P_c, which is the pressure at which c was determined. The technique also allows to directly estimate γ from c. Similar methods had been previously developed for the pressure-normalisation of regional PWV (Pucci et al., 2020; Shirai et al., 2006; Spronck et al., 2017b), but, unlike the one proposed here, they are based on the exponential approximation of the pressure-diameter relationship through the parameter β (see Chapter 1.3.1). However, as the behaviour of long arterial pathways, along which regional PWV is calculated, cannot be described by a single pressure-diameter relationship, P_β (i.e. the equivalent of P_c for the pressure-diameter exponential parameter β) defining the pressure at which the regional PWV is determined was not empirically calculated but deduced from qualitative methodological observations (e.g. $P_\beta \approx$ DBP for foot-to-foot PWV).

The results in this chapter showed that on average, for c estimated using the D^2P-loop method, P_c exceeded DBP by ∼11-13% of the PP. Hence, P_c is determined for its 87-89% by DBP and only for its 11-13% by SBP. This result is not surprising considering that D^2P-loop method

estimates c from a linear regression of the P-D^2 relationship in late diastole (from DBP to the dicrotic notch). In agreement with a previous study (Spronck et al., 2017c), mechanistic BP-correction of c showed good agreement with that obtained via statistical methods. Furthermore, in this study, the impact of the choice of the normalising pressure has been evaluated; while neglecting the ∼11-13% PP_{CCA} component of P_c only mildly affected the pressure-normalisation of c, using MBP and, even more so, SBP_{CCA} lead to a considerable over-correction of c in hypertensive patients. Therefore, while SBP and MBP are commonly chosen as confounding factors for regional PWV (Desamericq et al., 2015; Valbusa et al., 2019; Vogel et al., 2013), these might lead to wrong interpretations of pathology associated changes in arterial mechanics and DBP is likely more appropriate for most PWV/c estimation methods, typically providing diastolic measures of arterial stiffness (e.g., foot-to-foot detection).

Limitations

The participants included in this study have been recruited in two different centres in Italy equipped with different US machines. Palombo et al. (2012) experimentally studied the consistency between the two US systems and reported systematic differences in the diameter distensions acquired with the two devices. While these differences were accounted for via statistical methods, the data in Palombo et al. (2012) indicate that c values estimated via a linearisation of the Bramwell-Hill equation between SBP and DBP differ by approximately 10% between MyLabOne and Aloka ultrasound tracking systems. It is worth considering that different US systems likely apply different filters to increase the signal-to-noise ratio. These filter inevitably cause undesirable delays of the arterial waveforms with respect to the ECG signal. To address this issue, pressure-diameter waveforms were aligned on the basis of their foot and dicrotic notch. Additionally, inter-group differences in wall viscosity indices were comparable when considering the entire cohort (Aloka and Esaote) or only subjected recruited in Pisa (Aloka only) (Table A12).

The hysteresis area enclosed in the PD-loop is a complex parameter to evaluate as sensitive to the P and D signal alignment and to noise. In this study, signals were aligned by taking the second derivative peaks corresponding to the foot of the wave and the dicrotic notch as reference points. These two points are clearly identifiable in most of the pressure and diameter waveforms and provide an effective signal alignment (Hermeling et al., 2010; Muiesan & Paini, 2009). However, due to the superimposed noise and to the relatively small amplitude of the hysteresis area, some subjects exhibited slightly negative H_I values. While this phenomenon is acceptable from an experimental perspective, the hysteresis loop is expected to be always positive as the system loses energy due to viscosity (systolic and diastolic works can be defined as the area underneath the systolic and diastolic portions of the PD-loop). We opted for accepting

also negative H_I as neglecting these might result in a biased correction of noise, while noise is expected to act symmetrically on H_I.

5.5 Chapter conclusions

The methods proposed in this Chapter allowed to investigate the viscoelastic properties of the CCA wall in a cohort of healthy people and patients with hypertension and T2DM, accounting for the acute effect of BP differences at the time of data collection between age and clinical groups. The analysis indicated that ageing is the major determinant of chronic CCA wall stiffening, while neither T2DM nor hypertension induce significant chronic effect on its stiffness. Since hypertension and T2DM have been previously associated with a BP-independent increase in regional PWV, the results presented in this Chapter suggest that the clinical assessment of arterial mechanics should aim to improve the location-specificity of the information provided. Furthermore, adoption of mechanistic approaches to account for the effect of BP at the time of the clinical examination would likely improve the interpretation of the measured stiffness metrics.

The analysis proposed here allowed also to discriminate between arterial elastic and viscous properties. Hypertension seemed to alter the normal decline of wall viscosity with age and this contributed to decrease the wall distensibility in systole. While wall viscosity is commonly neglected *in vivo*, this finding warrant more further investigations into the mechano-biological aetiology of this altered behaviour.

CHAPTER 6

Non-invasive investigation of the impact of bariatric surgery on the human carotid haemodynamics

The contents of this chapter are largely based on:

Giudici, A., Palombo, C., Morizzo, C., Kozakova, M., Losso, L., Nannipieri, M., Berta, R., Hughes, A.D., Cruickshank, J.K., & Khir, A.W. (2020). Weight Loss After Bariatric Surgery Significantly Improves Carotid and Cardiac Function in Apparently Healthy People with Morbid Obesity. *Obesity Surgery*, *20*, 3776-3783.

6.1 Introduction

Chapter 5 investigated age and pathology induced changes in the carotid arteries haemodynamics and mechanics. Age was identified as the major determinant of carotid stiffening, while hypertension may alter the normal progression of arterial ageing by acting mainly on the viscous wall properties rather than on its 'purely' elastic stiffness. This Chapter focuses on another non-cardiovascular pathology that dramatically elevates the cardiovascular risk: obesity. Obesity, clinically diagnosed when a person's body mass index (BMI) exceeds 30 kg/m^2, is a global epidemic; while it affects only 13% of the population worldwide, its incidence in Europe and North America is close to 30% (Roser & Ritchie, 2019). As a result, obesity accounts for 0.7-2.8% of the total healthcare expenditure (Withrow & Alter, 2011) and has an estimated death-rate of 4 million/year (The GBD 2015 Obesity Collaborators, 2017).

Increased body weight is associated with increased BP, dyslipidemia and glucose intolerance, and rises the incidence of T2DM, hypertension and cardiovascular diseases (Hubert et al., 1983; Safar et al., 2006). It is not surprising, therefore, that obesity is associated with increased arterial stiffness (Sutton-Tyrrell et al., 2001); Balkestein et al. (1999) reported that a 15% decrease of BMI was associated with a 10% increase of arterial compliance. Similar findings were reported for cfPWV and brachial-ankle PWV (Petersen et al., 2016). However, most studies are limited by the relatively small BMI change achievable with diet regulation and lifestyle changes. Moreover, changes in body weight are typically associated with BP changes so that, in most studies, it is not clear to what extent the reduction in stiffness observed after weight loss merely reflects a parallel decrement in BP. Therefore, pressure-normalisation techniques for PWV/c are essential when investigating the relationship between body weight and arterial stiffness.

Bariatric surgery is the most effective treatment for morbid obesity in terms of weight loss, disappearance or improvement of diabetes, hypertension, or dyslipidemia; the number of procedures per year steadily increases (Angrisani et al., 2015). Allowing for an average BMI decrease ~25% within 1-year, bariatric surgery can provide insight into the effect of drastic weight loss on haemodynamics and arterial mechanics. Nevertheless, to the limit of the author's knowledge, no study has examined the effect of bariatric surgery on local arterial stiffness and cardiovascular haemodynamics.

This Chapter aimed to investigate changes in local carotid haemodynamics of 'otherwise healthy' people with third-degree obesity (BMI $\geq$ 40kg/m^2) in response to a two-stage treatment of 1-month diet regulation and bariatric surgery using non-invasive methods. Furthermore, the pressure-normalisation method proposed in Section 2.3.4 and used in Chapters 5 allowed assessing

whether observed differences in wall stiffness were independent of BP changes throughout the treatment.

6.2 Methods

6.2.1 Study population

This prospective study was conducted in the University Hospital of Pisa (Tuscany, Italy) and included 26 patients (45±10 years, 5 men) with third-degree obesity (BMI $\geq$ 40 kg/m^2) referred for bariatric surgery. The final study population comprised 32 recruited patients, however 2 patients dropped out of the study after the diet period, and 4 were excluded for inadequate carotid distension waveforms. All were free of hypertension, diabetes mellitus, atrial fibrillation, heart failure, or previous ischemic cardiac and cerebral events. Patients with any significant systemic disease were excluded. Five patients had impaired glucose tolerance at an oral glucose tolerance test before the study. The analysis of non-invasive human data was approved by the Brunel Research Ethics Committee (Reference: 6124-LR-Feb/2017-6443-1).

All subjects were evaluated at three time-points: 1) baseline, 2) after 1 month's diet and before the surgical procedure (post-diet), and 3) 5-11 months (average 8 months) after bariatric surgery (post-surgery). Body weight, height, and BP were measured at each time-point, and allowing for >10 min of rest before the measurement.

BMI and BSA were computed using standard formulas (Du Bois & Du Bois, 1915):

$$\text{BMI} = \frac{\text{body mass}}{\text{height}^2} \ , \quad \text{and} \tag{6.1}$$

$$\text{BSA} = 0.20247 \ \text{height}^{0.725} \ \text{weight}^{0.425} \ . \tag{6.2}$$

6.2.2 Ultrasound acquisitions

All carotid artery ultrasound acquisitions were performed by a single trained operator (Carmela Morizzo). *U* and *D* waveforms were recorded at the level of the right common CCA using an Aloka Alpha 10 Prosound system (Hitachi, Japan) equipped with a 10.0 MHz linear array probe at a frequency of 1kHz as reported previously (Uejima et al., 2019). The operator manually positioned a perpendicular line (with respect to the CCA longitudinal axis) approximately 1.5 cm proximal to the carotid bulb and placed the cursors on the anterior and posterior vessel walls to allow the tracking. Each acquisition lasted for 20 seconds, but the operator was allowed to discard unrepresentative and noisy heartbeats after checking the waveforms on screen. The approved heartbeats were then ensemble averaged providing the final average diameter distension and blood velocity waveforms.

6.2.3 Data analysis

Estimation of local wave speed and distensibility

CCA ${}_{\mathrm{n}}c$ was estimated using the lnDU-loop method (see Section 2.3.2) (Feng & Khir, 2010). Briefly, when the waves travelling in an artery are unidirectional (i.e., either travelling from the heart to the periphery or vice versa), the relationship between U and the natural logarithm of D is linear, and its slope is proportional to ${}_{\mathrm{n}}c$. In the carotid artery this condition is met in early systole, when the wave produced by the contraction of the left ventricle travels from the heart towards the brain and reflections form distal bifurcations have not reached the CCA yet. Therefore, ${}_{\mathrm{n}}c$ can be estimated from the slope of the linear regression of the U-ln$D$ relationship in early systole as described in Eq. 6.3.

$$ {}_{\mathrm{n}}c = \frac{1}{2}\frac{\mathrm{d}U}{\mathrm{d}(\ln D)} \ , \tag{6.3} $$

where dU and d(ln D) are changes in carotid blood flow velocity and the natural logarithm of the diameter. Following results presented in Chapter 5 that showed that c values estimated in late diastole/early systole reflect measures of arterial stiffness close to DBP, the effect of BP changes during the treatment on ${}_{\mathrm{n}}c$ was accounted using the mechanistic pressure-normalisation method proposed in Section 2.3.4 and assuming $P_c = \mathrm{DBP}$.

$$ {}_{\mathrm{n}}c_{\mathrm{T}} = \sqrt{{}_{\mathrm{n}}c^2\frac{\mathrm{DBP_T}}{\mathrm{DBP}} + \frac{\mathrm{DBP_T}}{\rho}\ln\left(\frac{\mathrm{DBP_T}}{\mathrm{DBP}}\right)} \ . \tag{6.4} $$

The target DBP (DBP$_{\mathrm{T}}$) was set to 80 mmHg. Arterial distensibility Ds was directly calculated from ${}_{\mathrm{n}}c$ and assuming $\rho = 1060$ kg/m^3.

$$ Ds = \frac{1}{\rho\ {}_{\mathrm{n}}c^2} \ . \tag{6.5} $$

Similarly, the pressure-normalised Ds_{T} was calculated using Eq. 6.5 and ${}_{\mathrm{n}}c_{\mathrm{T}}$.

Wave separation and wave intensity analysis

Once the local wave speed is known, WIA allows for the separation of U and D waveforms into their forward and backward components (refer to Section 2.3.2 for the full derivation of these equations) (Feng & Khir, 2010). Increments in the forward (+) and backward (−) components of the D and U waveforms can be computed as:

$$ \mathrm{d}D_{\pm} = \frac{1}{2}\left(\mathrm{d}D \pm \frac{D_{\mathrm{d}}}{2\ {}_{\mathrm{n}}c}\mathrm{d}U\right) \ , \quad \text{and} \tag{6.6} $$

$$ \mathrm{d}U_{\pm} = \frac{1}{2}\left(\mathrm{d}U \pm \frac{2\ {}_{\mathrm{n}}c}{D_{\mathrm{d}}}\mathrm{d}P\right) \ . \tag{6.7} $$

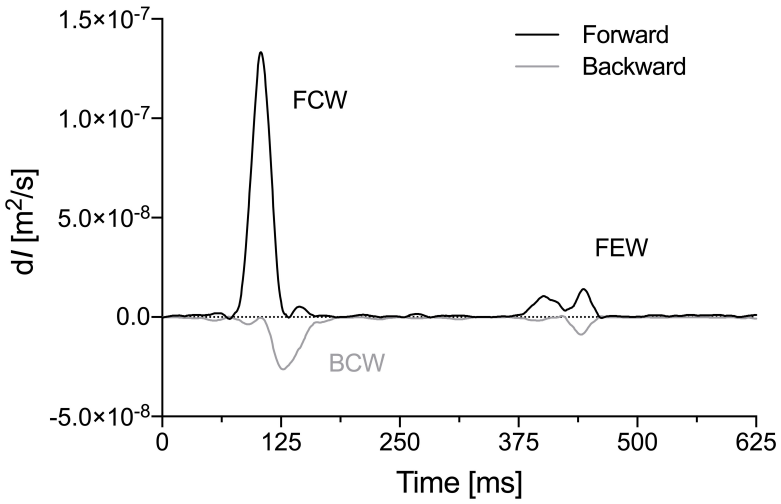

Figure 6.1: *Example of non-invasive wave intensity graph in the common carotid artery chosen from one of the patients included in this study. Black and grey lines indicate the intensity of waves travelling in the forward and backward directions, respectively.*

Finally, the forward and backward non-invasive wave intensity was calculated as the product between increments in forward and backward U and D.

$$_{\mathrm{n}}\mathrm{d}I_{\pm} = \mathrm{d}D_{\pm}\mathrm{d}U_{\pm} \tag{6.8}$$

By definition, $\mathrm{d}I_{-}$ is always negative, while $\mathrm{d}I_{+}$ is always positive. As in Figure 6.1, the forward wave intensity is characterised by two main waves; the first a large forward compression wave (FCW) related to the ejection phase of the heart. The second is later, a forward expansion wave (FEW) prior to aortic valve closure, and contemporaneous with the end of the ejection. $\mathrm{d}I_{-}$ is mainly characterised by a small peak from a backward compression wave (BCW) resulting from reflection of the FCW from downstream arterial sites during early systole. These three intensity peaks have been characterised in terms of underlying area and arrival time. The reflection index, quantifying the portion of the forward traveling wave that is reflected back from the periphery to the heart, was calculated as the ratio between BCW and FCW areas.

6.2.4 Statistical analysis

SPSS 23 (IBM corporation, Chicago, IL, USA) was used for the statistical analysis. Data are reported as mean ± standard deviation. Changes in anthropometric, BP measurements were evaluated using repeated measures ANOVA, as was $_{\mathrm{n}}c$ after analytical pressure-normalisation. If a significant change was found, the three treatment steps were compared using paired sample t-tests. $p \leq 0.05$ was considered as statistically significant. Similar analyses were also performed on the wave intensity parameters FCW area, BCW area, FEW area, and relative timing.

6.3 Results

6.3.1 Treatment outcome

Table 6.1 summarises the effect of the treatment on body mass and carotid haemodynamic parameters. At baseline, average body weight, BMI and BSA were 129.9±27.0 kg, 47.9±7.1 kg/m^2, and 2.29±0.28 m^2, respectively. After one month of caloric intake regulation, BMI decreased by approximately 5% and BSA by ∼2%. Additionally, BP decreased slightly (5.5%

Table 6.1: *Participant characteristics and carotid haemodynamic indices at baseline, post-diet, and post-surgery. Values are mean ± standard deviation.* $^{*}p<0.05$, $^{**}p<0.01$, *and* $^{***}p<0.001$ *with respect to basal value;* $^{\dagger}p<0.05$, $^{\dagger\dagger}p<0.01$, *and* $^{\dagger\dagger\dagger}p<0.001$ *with respect to diet.*

	Baseline	**Post-diet**	**Post-surgery**
Body weight [kg]	129.9±27.0	123.6±24.8 **	90.5±21.3 **††
BMI [kg/m^2]	47.9±7.1	45.5±6.7 **	33.4±6.9 **††
BSA [m^2]	2.29±0.28	2.24±0.26 **	1.96±0.24 **††
HR [bpm]	76.4 ± 10.2	68.8 ± 9.7 ***	60.6 ± 9.6 ***†††
SBP_{BRA} [mmHg]	122.2±13.3	116.3±12.4 **	115.7±16.8 *
DBP [mmHg]	81.5±7.5	78.1±6.2 **	77.0±9.0 *
MBP [mmHg]	91.7±8.2	87.6±7.1 **	86.7±10.5 *
PP_{BRA} [mmHg]	40.7±10.0	38.2±9.4	38.7±10.4
D_s [mm]	8.23 ± 1.22	8.11 ± 1.11	7.95 ± 1.18 *
D_d [mm]	7.76 ± 1.18	7.63 ± 1.06	7.41 ± 1.10 *
ΔD [mm]	0.47 ± 0.11	0.48 ± 0.13	0.54 ± 0.16 **††
$\Delta D/D_d$ [%]	6.08 ± 1.41	6.35 ± 1.69	7.30 ± 1.93 *
U_{max} [m/s]	0.53 ± 0.10	0.55 ± 0.13	0.51 ± 0.09
U_{min} [m/s]	0.06 ± 0.06	0.07 ± 0.07	0.07 ± 0.07
${}_nc$ [m/s]	6.27 ± 1.35	5.52 ± 0.93 **	4.74 ± 1.09 ***†††
${}_nc_T$ [m/s]	6.20 ± 1.28	5.61 ± 0.86 **	4.89 ± 1.10 ***†††
Ds [MPa^{-1}]	27.5 ± 11.2	33.6 ± 10.9 **	50.0 ± 27.0 ***†††
Ds_T [MPa^{-1}]	28.0 ± 11.9	32.4 ± 11.3 **	47.3 ± 27.4 ***†††

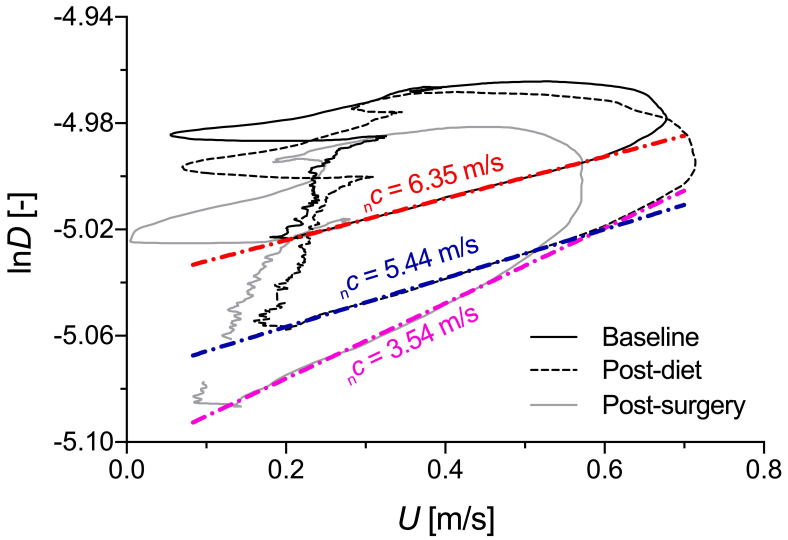

Figure 6.2: *Evolution during the treatment of the* lnDU*-loop of a representative patient included in this study. The increased slope of the relationship in early systole signifies a decrease of the local wave speed. Such changes were produced by an increased diameter distension with no changes in* ΔU*.*

for both SBP_{BRA} and DBP). 8 months after surgery, BMI and BSA furtherly dropped by 26% and 13%, leading to a total 30±8% and 14±4% with respect to the baseline value. Interestingly, no further changes in BP were observed 8 months after the surgery. On the other hand, HR, 76.4±10.2 bpm, significantly decreased during the treatment, by 10% post-diet and a further 12% post-surgery.

6.3.2 Local wave speed

Table 6.1 presents changes in vascular function indices at the three time-points considered in this study. Baseline ${}_{n}c$ was 6.27±1.35 m/s and decreased by 10±14% post-diet and 23±15% post-surgery. Normalisation against DBP reduced such differences to 7±15% and 20±15%. Figure 7.3 shows changes in the shape of the lnDU-loop at the three time-points in a representative patient included in this study (note that, from Eq. 6.3, ${}_{n}c$ is proportional to the inverse of the slopes shown in Figure 6.2). U_{max}, U_{min} and, consequently, ΔU did not change at any of the time points (Table 6.1). Conversely, while both D_s and D_d significantly decreased during the treatment ($p<0.05$), ΔD and $\Delta D/D_d$ were significantly higher post-surgery than at baseline, thus explaining observed changes in ${}_{n}c$. Interestingly, while brachial BP significantly decreased only in the first month of diet, changes in D_s and D_d were significant only 8-months after surgery, thus suggesting that observed changes were independent of BP. Similarly, increased ΔD was not accompanied by significant changes in PP (Table 6.1).

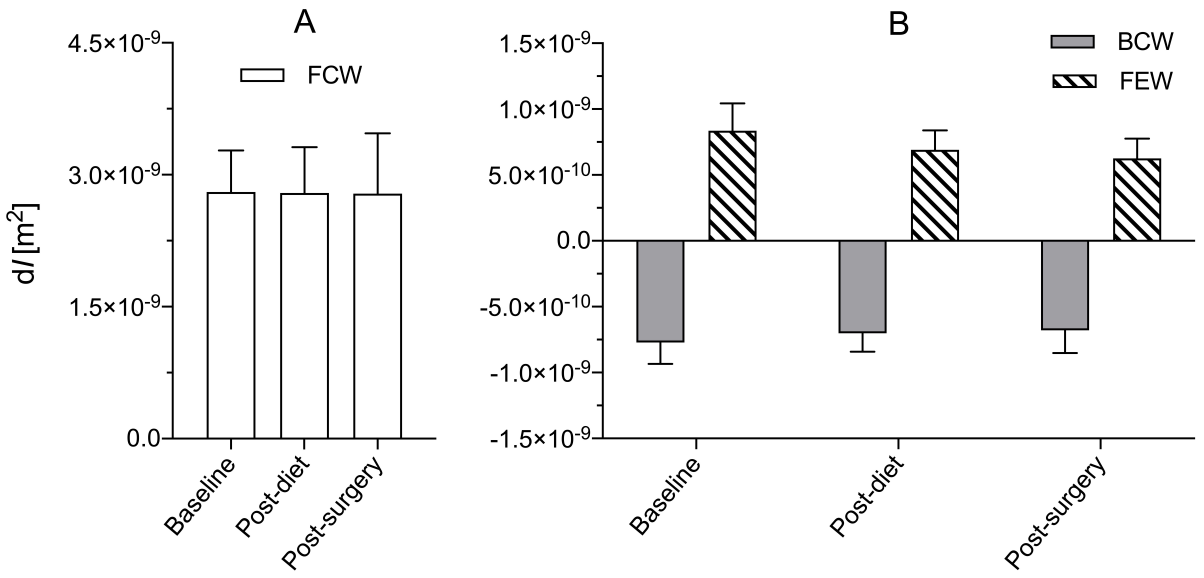

Figure 6.3: *Average forward compression wave (*FCW*) (A), backward compression wave (*BCW*) and forward expansion wave (*FEW*) (B) area at baseline, post-diet and post-surgery. Results are mean ±95% confidence interval.* BCW *and* FEW *are shown separately (panel B) for clarity.*

6.3.3 Wave intensity

Wave intensity did not show statistically significant changes between different time-points of the study (Figure 6.3). FCW was very similar across the three time-points. On the other hand, BCW fell slightly from 7.71±1.60 10^{-10} m^2 at baseline to 6.34±1.90 10^{-10} m^2 at 8 months, the end of the study. The trend for the FEW was similar: 8.37±2.02 10^{-10} m^2 basally and 6.25±1.49 10^{-10} m^2 at 8 months. Consequently, both the reflection index BCW/FCW and the ratio FEW/FCW decreased after the surgery, but these differences were not statistically significant.

As predicted by changes in local wave speed, the arrival time of the waves was significantly affected by the surgical procedure. The time lag between FCW and BCW was higher in the post-surgery recording than at baseline. The baseline time lag between FCW and BCW was 33.0±10.7 ms, which increased to 40.8±12.2 ($p<0.05$) and 43.5±14.4 ($p<0.01$) after 1-month of diet and 8-months after bariatric surgery, respectively.

6.4 Discussion

Arterial stiffness and body weight are generally positively correlated, and weight loss has been associated with decrease in cfPWV and baPWV (Cooper et al., 2012). However, this is the first study to have examined changes in local carotid wave speed ($_nc$) after bariatric surgery,

evaluating the effect of extensive weight loss on carotid haemodynamics in 26 patients with third-degree obesity but without other morbidity, particularly defined hypertension or diabetes. Data were compared between baseline, post-diet, and post bariatric surgery.

As much as 40 kg weight loss or 11.7 kg/m^2 BMI, almost 30% of basal BMI, were associated with improvements in carotid function; the ∼25% reduced ${}_{\mathrm{n}}c$ at ∼8 months post-surgery was due to increased relative distension of the carotid wall. Borlotti et al. (2012) reported values of ${}_{\mathrm{n}}c$ in the carotid artery just above 4 m/s using the lnDU-loop method in a healthy 40 years old sample. Di Lascio et al. (2014) found an average c of 5.64±1.7 m/s in 50.5±20 year olds using the foot-to-foot method with accelerometric sensors positioned on the carotid. In Chapter 5 of this thesis, the PD^2-loop method was used to determine c from carotid pressure-diameter relationships; c was 5.08±0.63 m/s and 6.69±1.17 m/s in healthy controls aged 40-49 and 60-69 years, respectively. Therefore, the results presented in this study indicate that increased carotid stiffness is a likely consequence of obesity; the predominantly female cohort of middle-aged people displayed a vascular age that was almost two decades higher than their demographic age. More importantly, the results suggest that obesity-related arterial stiffening can be reversed to the healthy range if body weight is effectively reduced. This finding is in agreement with those of other groups (Balkestein et al., 1999), but here shown to be independent of the BP change. As further support to this hypothesis, only three patients did not show a decrease in ${}_{\mathrm{n}}c$ between the basal and the post-surgery measurements, and 2 of these already had basal ${}_{\mathrm{n}}c$ within the normal range.

Recently, Streese et al. (2019) examined changes in Cardio-Ankle Vascular Index (CAVI) and baPWV 6 weeks and 4 years after bariatric surgery. Neither measures changed significantly, in apparent disagreement with findings presented here. Similarly, Galkine et al. (2018) studied changes in CAVI after bariatric surgery in patients with at least one comorbidity, reporting an increase in CAVI at 1-year and no difference from baseline at 4-years follow-up. As previously discussed in Chapter 5, a likely explanation for this disparity is that CAVI and baPWV are regional indices of arterial stiffness, including long muscular arterial pathways, while the lnDU-loop method provides a local measure of wave speed c. Given the difference in wall composition and stiffness of different sites along the arterial bed, local stiffness might be affected differently. In addition, the majority of participants included in their studies was hypertensive, while those included in this study were not.

As previously discussed in this thesis, PWV/c is intrinsically pressure-dependent (Spronck et al., 2015). In this study, $\mathrm{SBP_{BRA}}$ and DBP decreased by ∼6 and 4 mmHg, respectively, during the 1-month diet with a 2.4 kg/m2 BMI decrease. Cooper et al. (2012) reported a reduction

in SBP_{BRA} and DBP following 1-year lifestyle intervention of diet and physical activity only about half that observed here. Balkestein et al. (1999) reported a decrease in MBP comparable to those found in this study, but with twice the change in BMI following a 10-week energy restricted diet and exercise programme. However, the degree of obesity in their studies was much less than that of the participants to this study (baseline BMI = 32.9 and 32.3 kg/m^2), and the relationship between change in BMI and change in MBP may not be linear. Although the change in BP was significant, its relatively small amplitude was responsible for only ∼3% of the ${}_{n}c$ reduction. Furthermore, 8-months post-surgery, when BMI had decreased further by 11.1 kg/m^2, SBP_{BRA} and DBP had not reduced further but there was a further fall in ${}_{n}c$. Other recent results suggest SBP_{BRA} and DBP did significantly decrease 6 months after bariatric surgery (Gluszewska et al., 2019; Hawkins et al., 2018). However, the lack of BP changes with time after the intervention in this study suggests that much of the average 0.78 m/s reduction in ${}_{n}c$ comparing diet to 8-months follow-up is related to changes in arterial wall mechanics. On the contrary, in agreement with previous findings (Cooper et al., 2012), HR did drop considerably throughout the treatment (−15.8 bpm from baseline to post-surgery). While HR is a known confounder for PWV/c, its effect is expected to be marginal; a previous study estimated a 10 bpm change in HR would affect cfPWV by ∼ ±2% (Tan et al., 2016), an order of magnitude lower than differences in ${}_{n}c$ observed in this study.

Interestingly, no correlation was found between the magnitude of intra-subject changes in BMI (or weight) and vascular parameters. Sutton-Tyrrell et al. (2001) found a higher correlation between aortic stiffness and visceral adiposity than between aortic stiffness and body weight. They hypothesised that the correlation between aortic stiffness and body weight might actually reflect a correlation between body weight and visceral adiposity. Therefore, it is possible that other parameters contributing to determining the body weight may affect changes in vascular parameters.

WIA, analysed for the first time in this context, did not provide as clear a trend as found for ${}_{n}c$. FCW area did not change, while BCW and FEW showed consistent but small decreases. The reduced reflection index may indicate improved transmission of waves to the periphery; however, this difference was not significant (p=0.214) and could be by chance. The sample size might have been too small to detect clinically significant differences. The difference of arrival time of BCW with respect to FCW suggests, as in the lower ${}_{n}c$, that waves travel slower after weight loss, indicating further potential benefits.

Limitations

This study is a before-after comparison without a formal control group, but medically-treated

patients with third-degree obesity never lose the amount of weight found after surgery in this study. However, it is theoretically possible that time-dependent changes could occur with this design, but is most unlikely. The sample size was relatively small but prospective and no patients had hypertension or T2DM, a unique feature of this cohort to date allowing assessing cardiovascular changes related to obesity alone. It is possible that diabetes and hypertension might make weight-related arterial stiffening less reversible.

6.5 Chapter conclusions

In this study, the effect of intensive weight loss on the CAA haemodynamics has been evaluated in a cohort of severely obese patients undergoing a two-phase treatment consisting in 1-month of diet followed by bariatric surgery. The results of this study suggest that the increase in local c due to excessive body weight can be reversed to physiological values if the BMI is effectively reduced, independently of BP, and further support the use of bariatric surgery for the treatment of severe obesity. Note that observed changes in CCA function happened in a relatively short time-frame; future studies should focus on 1) investigating whether observed improvements are maintained over a longer follow-up period, and 2) further deepening our understanding of the their underlying physiological mechanisms.

CHAPTER 7

Non-invasive determination of pressure using cuff pressure and local vessel diameter and flow velocity

Part of this Chapter was published in:

Giudici A., Palombo C., Morizzo C., Kozakova M., Cruickshank J.K., Wilkinson I.B., & Khir A.W. (2021). Transfer-function free technique for the non-invasive determination of the human arterial pressure waveform. *Physiological Reports* (In press).

7.1 Introduction

According to the European Societies of Hypertension and Cardiology, the current definition of hypertension entails having a brachial systolic blood pressure SBP_{BRA} ≥140 mmHg and/or diastolic blood pressure DBP≥90 mmHg (Williams et al., 2018). Indeed. studies have shown the ability of peripheral pressure to predict adverse cardiovascular outcomes (Dart et al., 2006). In contrast to central aortic blood pressure, which can only be measured invasively, SBP_{BRA} and DBP can easily be assessed non-invasively via cuff measurement and represent, therefore, the gold standard in daily clinical practice.

DBP and MBP are relatively constant throughout most of the arterial tree (Kroeker & Wood, 1955; Pauca et al., 2001) but SBP increases when moving distally from the ascending aorta (Reference Values for Arterial Measurements Collaboration, 2014; Segers et al., 2009), most likely due to wave reflections and higher wall stiffness in distal arteries compared to the aorta. In Chapter 3, distal stiffening was observed even within the pig thoracic aorta. Further, the entity of the central-to-distal pressure amplification is age, sex and pathology-dependent (McEniery et al., 2014; Reference Values for Arterial Measurements Collaboration, 2014), likely reflecting the differential effect of ageing and cardiovascular pathologies (Borlotti et al., 2012; Armentano et al., 1995a; Mitchell et al., 2010; Zhang et al., 2013) on the mechanical properties of proximal and distal arteries. Therefore, brachial pressure poorly describe pressure in other regions of the arterial tree.

Several studies have shown the added predictive value of central blood pressure for future cardiovascular events and stroke mortality, beyond brachial pressure and independent from established cardiovascular risk factors (Cheng et al., 2013; Chirinos et al., 2013). Indeed, it is expected that central blood pressure reflects the haemodynamic load on the left ventricle more accurately than brachial pressure (Roman et al., 2007). These findings promoted the development of methods to non-invasively estimate aortic pressure.

Transfer functions (TFs) are the most commonly used technique for the non-invasive determination of aortic pressure. These functions describe the relationship between the input pressure (i.e., the pressure in the aorta) and an output pressure (i.e., the pressure measured at a peripheral site), and their inverse function can be used to estimate central aortic pressure from a peripheral pressure waveform (Costello et al., 2015; Ghasemi et al., 2017). While several commercial devices have been produced to absolve this task (Ding et al., 2011) and empirical evidence suggests that TFs accurately predict the systolic-diastolic pressure range in the aorta, the estimated waveforms preserve high-frequency features of the peripheral pressure waveform (Millasseau et al., 2003; Segers et al., 2005).

To overcome this issue, alternative methods have been designed to directly estimate pressure from local arterial waveforms acquired non-invasively, using a local estimate of c, reflecting local wall stiffness, to operate conversions between arterial waveforms. Similar to TFs, these methods typically rely on the assumption that DBP and MBP are the same in most arterial locations. Vennin et al. (2015) proposed a method to reconstruct the aortic pressure waveform from the non-invasive acquisition of aortic blood flow velocity, peripheral SBP, DBP and diastolic pressure exponential decay. Dividing the pressure waveform in sections, such method relies on c and the water hammer equation (Khir et al., 2001) (see Section 2.3.1 Eq. 2.39) to convert the systolic ejection of the velocity waveform into the pressure upstroke. While this method provided plausible estimations of aortic pressure both in computational and *in vivo* settings, the pressure waveform involved in the determination of c (Davies et al., 2005) (1.3.1) was recorded invasively. This renders the technique unsuitable for routine examinations, although the relative accuracy is yet to be determined if c is estimated non-invasively.

Beulen et al. (2011) used simultaneous ultrasound measurement of blood flow velocity and diameter distension to estimate pressure in flexible tubes. The flow-area method (Rabben et al., 2004) was used to determine c non-invasivley, and the relationship between c and distensibility, described by the Bramwell-Hill equation (Bramwell et al., 1923) (Eq. 2.57), was used to calculate pressure by integrating changes in tube cross-sectional area with respect to the diastolic reference. This method assumes that c is constant across the SBP-DBP range. While this assumption is correct in the case of flexible tubes that exhibit a linear pressure-area relationship, the latter is nearly exponential in arteries (Gavish & Izzo, 2016), implying that c does increase with increasing pressure. Section 2.3.4 showed that the relationship between γ, the parameter that defines the exponential pressure-area relationship of arteries, and c is mediated by the blood density ρ and P_c, i.e., pressure at which c was determined. This relationship, therefore, relaxes the assumption that c is constant over the systolic-diastolic pressure range. In Chapter 5, P_c was empirically estimated to be close to DBP when c was determined using the D^2P-loop method in late diastole.

This Chapter aimed to evaluate the effectiveness of a new method to non-invasively estimate arterial pressure from local ultrasound acquisitions of arterial diameter and blood velocity waveforms and peripheral cuff BP. It was postulated that ${}_{\mathrm{n}}c$, non-invasively estimated using the $\ln DU$-loop in early systole (close to DBP), would provide an estimate of arterial stiffness at DBP. If this assumption were to be proven reasonable, the new method would allow determining γ from ${}_{\mathrm{n}}c$ and peripheral non-invasive DBP, thus allowing the conversion of the diameter distension waveform into a pressure waveform via the exponential P-D^2 relationship. In this proof-of-

concept study, the novel method was validated at the CCA where pressure at the CCA can be acquired non-invasively via applanation tonometry.

7.2 Methods

7.2.1 Study population and acquisition protocol

The data used in this study were acquired at the University Hospital of Pisa (Tuscany, Italy). The protocol of the study followed the principles of the Declaration of Helsinki and was approved by the institutional ethics committee "Comitato Etico di Area Vasta Nord Ovest" (reference number: 3146/2010). The initial study population included 251 people undergoing standard out-patient cardiovascular risk assessment, but 21 were excluded for missing blood velocity acquisition data, and other 27 for unrepresentative data. The final study population included 203 people (122 men, 51±17 years, age range 16-78 years), all free of major cardiovascular events, atrial fibrillation, malignancy or chronic inflammatory disease. The analysis of non-invasive human data was approved by the Brunel Research Ethics Committee (Reference: 6124-LR-Feb/2017-6443-1).

P, D, and U waveforms of CCA were acquired simultaneously by a single experienced operator (Carmela Morizzo). Simultaneous ultrasound acquisition of D and U were performed on the right CCA using a 10.0-MHz linear array probe with radiofrequency data output at the frequency of 1 kHz connected to a Hitachi Aloka Alpha10 Prosound system as reported previously (Uejima et al., 2020). Given the impossibility of placing a pressure tonometer on the right CCA due to the presence of the ultrasound probe, P was acquired at the left CCA using a PulsePen (DiaTecne, Milan, Italy) with sampling frequency 1 kHz (as reported in Chapter 5).

$\mathrm{SBP_{BRA}}$ and DBP were measured by an electronic digital manometer (Omron, model 705cp, Kyoto, Japan), before the ultrasound/tonometer acquisition and after the person had rested in a supine position for >10 min. The calibration of the tonometer pressure waveforms was performed as described in Section 5.2.3 (i.e., assuming uniform DBP and MBP in the arterial tree). Brachial MBP was estimated using a form factor (FF) of 0.43 (Segers et al., 2009).

$$\mathrm{MBP} = \mathrm{DBP} + 0.43\ \mathrm{PP_{BRA}} = \mathrm{DBP} + 0.43\ (\mathrm{SBP_{BRA}} - \mathrm{DBP})\ . \tag{7.1}$$

7.2.2 Non-invasive wave speed ${}_{\mathrm{n}}c$ and exponential gain ${}_{\mathrm{n}}\gamma$

The local CCA wave speed was estimated using the lnDU-loop method (Feng & Khir, 2010) (See Section 2.3.2 for complete derivation). Briefly, when arterial waves are unidirectional (i.e. travelling only from the heart towards the periphery or vice versa), the relationship between the U and the natural logarithm of D is linear and proportional to the wave speed (Eq. 2.50 and

reported here as Eq: 7.2).

$$ {}_{\mathrm{n}}c = \pm \frac{1}{2} \frac{\mathrm{d}U_{\pm}}{\mathrm{d}(\ln D_{\pm})} \ , \tag{7.2} $$

where subscripts + and − indicate forward (from the heart to the periphery) and backward (from the periphery to the heart) direction of wave travel. In early systole, a forward travelling compression wave is created by the contraction of the left ventricle, and no reflected wave has arrived yet from peripheral sites. Therefore, the assumption of the unidirectionality of the waves is reasonable, and ${}_{\mathrm{n}}c$ can be determined with Eq. 7.2 (Figure 7.1B).

In Section 2.3.4, it was illustrated how the exponential parameter γ can be estimated from c if the reference pressure P_c is known. As the mechanical behaviour of arteries is highly non-linear, arterial stiffness and c are intrinsically stress/pressure dependent. Therefore, P_c indicates the pressure level at which the propagation of waves in the arterial tree corresponds exactly to c. Since the lnDU-loop estimates ${}_{\mathrm{n}}c$ in early systole (i.e. in a similar pressure interval to that of late diastole), it was hypothesised that P_c=DBP would provide reasonable estimates of γ. Therefore, the non-invasive exponential gain ${}_{\mathrm{n}}\gamma$ was calculated as

$$ {}_{\mathrm{n}}\gamma = \frac{\rho \ {}_{\mathrm{n}}c^2}{\mathrm{DBP}} \ , \tag{7.3} $$

using brachial DBP and $\rho = 1060$ kg/m^3 (see Eq. 2.68 and Eq. 2.69).

7.2.3 Non-invasive estimation of pressure

Assuming a uniform DBP throughout the arterial system, the diameter waveform can be converted in pressure waveform using the exponential P-D^2 relationship described in Section 2.3.4 and ${}_{\mathrm{n}}\gamma$.

$$ {}_{\mathrm{n}}P = \mathrm{DBP} e^{{}_{\mathrm{n}}\gamma \left(\frac{D^2}{D_{\mathrm{d}}^2} - 1 \right)} \ . \tag{7.4} $$

Since DBP, D and ${}_{\mathrm{n}}\gamma$ are all determined non-invasively from ultrasound acquisition and cuff measurement of peripheral pressure, ${}_{\mathrm{n}}P$ does not require any invasive measurement to be estimated.

The non-invasive $\mathrm{SBP_{CCA}}$ (${}_{\mathrm{n}}\mathrm{SBP_{CCA}}$) was estimated as the average of the maximum pressures of all the ${}_{\mathrm{n}}P$ heartbeats, and the non-invasive MBP (${}_{\mathrm{n}}$MBP) was the average of the ${}_{\mathrm{n}}P$ waveform between the first and last R wave in the ECG signal (i.e., excluding incomplete heartbeats).

Figure 7.1 shows an example of the process used for the non-invasive estimation of pressure; U (Panel A) and D (Panel C) waveforms are used to build the lnDU-loop and estimate ${}_{\mathrm{n}}c$ in early systole. ${}_{\mathrm{n}}c$ is then used to estimate ${}_{\mathrm{n}}\gamma$ (Eq. 7.3) and convert D into ${}_{\mathrm{n}}P$ (Eq. 7.4).

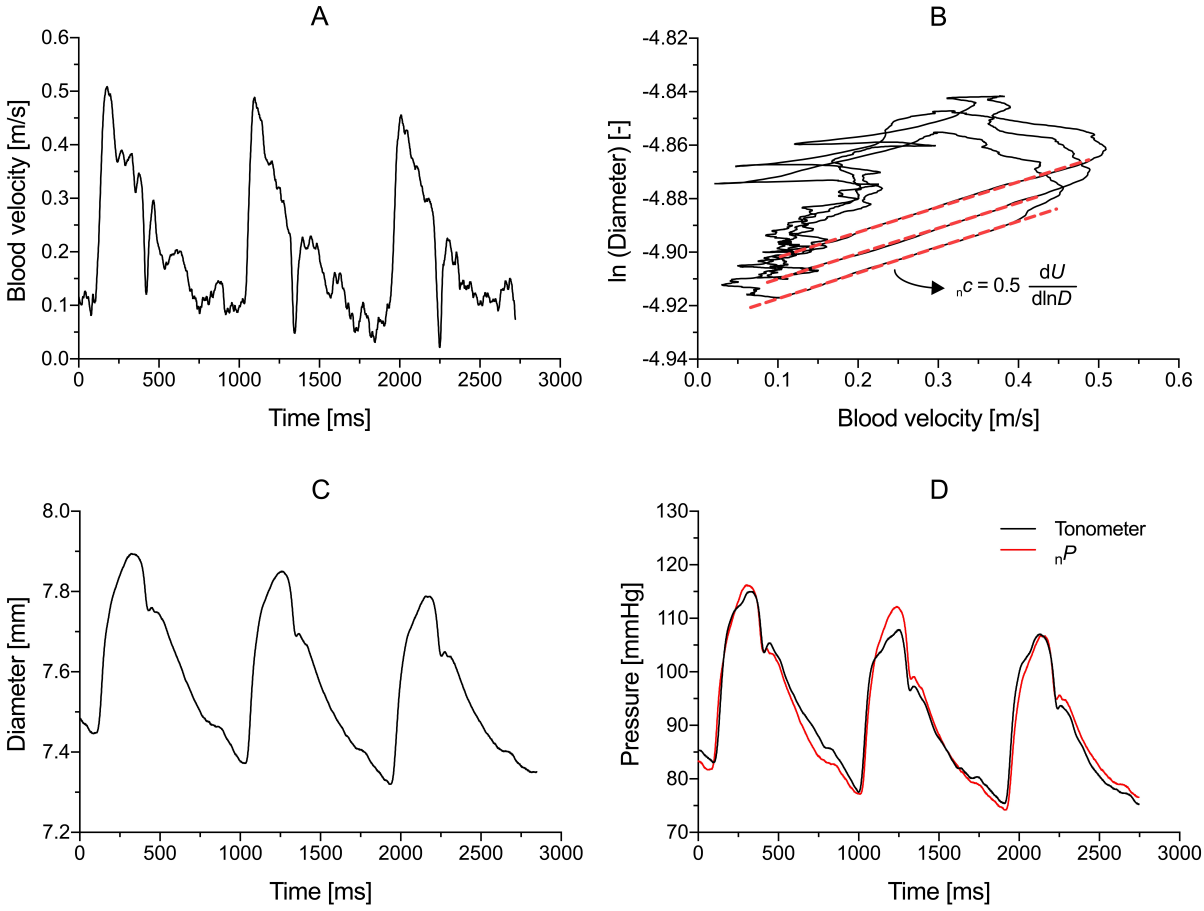

Figure 7.1: *Graphical representation of the process used to non-invasively estimate the pressure from acquisition of blood flow velocity U (A) and diameter distension D (C). The $\ln DU$-loop is used to estimate the local wave speed $_nc$ (B). $_nc$ then used to calculate $_n\gamma$ and convert the diameter waveform into the pressure waveform through the exponential function (Eq. 7.4). In panel D, the non-invasive pressure waveform is compared with the tonometer the tonometer pressure waveform.*

7.2.4 Tonometer-based local wave speed c and exponential gain γ

To provide a mean of comparison for $_n\gamma$, the exponential gain γ was also determined fitting the P-D^2 relationship (refer to Section 5.2.3 for more details). Similarly, the late diastolic D^2P-loop c was used for comparison with $_nc$ (refer to Section 5.2.3 for more details). As for $_nP$, carotid SBP_{CCA} was estimated as the average of the maximum pressures of all the tonometric P heartbeats, and MBP was the average of the P waveform between the first and last R wave in the ECG signal.

7.2.5 Statistical analysis

The statistical analysis was performed using SPSS 23 (IBM corporation, Chicago, IL, USA). Non-invasive and tonometer-based SBP_{CCA}, MBP, c and γ were compared using paired samples t-test and Bland-Altman plots (Bland & Altman, 1986), taking ± 2 standard deviations as limits of agreement between the two measures. The non-invasive carotid FF was calculated as

$$_{n}FF = (_{n}SBP_{CCA} - DBP)/(_{n}MBP_{CCA} - DBP) \ , \tag{7.5}$$

was used as an additional parameter to quantify the accuracy of the estimation of the pressure waveform and compared to FF calculated from the left CCA tonometry.

$$FF = (SBP_{CCA} - DBP)/(MBP_{CCA} - DBP) \ . \tag{7.6}$$

The analysis was first conducted on the entire population. Then the age-effect was evaluated by stratifying the population in three age-groups, young (<35 years), middle-aged (35-59 years) and older adults (≥70 years), and comparing non-invasive and tonometer parameters in the within groups.

Data are generally reported as mean ± standard deviation. Linear regression and correlation analysis were performed where appropriate. $p<0.05$ was considered statistically significant.

7.3 Results

The haemodynamic characteristics of the people included in this study are reported in Table 7.1. SBP_{BRA} and DBP were 122.1±16.8 mmHg and 75.2±10.4 mmHg, respectively. Using a form factor 0.43 lead to MBP = 95.4 ± 12.0 mmHg.

Non-invasive wave speed $_{n}c$ was on average 5.67±1.45 m/s, and strongly correlated with D^2P-loop c (r=0.72, p<0.001) that was on average 5.69±1.36 m/s (Figure 7.2A). The bias between the two methods was −0.02 m/s, with limits of agreement −1.91 to 1.87 m/s (Figure 7.2B). The average $_{n}\gamma$ was 3.60±1.75, comparable to the average fitted γ (mean difference −0.08, limit of agreement: −2.58 to 2.74)(Figure 7.2C-D). For both c and γ, the Bland-Altman plots did not show relevant clustering (Figure 7.2B-D).

Figure 7.3 presents correlation and Bland-Altman plots between measured tonometer pressure P and estimated pressure $_{n}P$. On average, $_{n}P$ slightly overestimated the tonometer P; $_{n}SBP_{CCA}$ and $_{n}$MBP were 4.1 (Limit of agreement −40.7% to 49.0%) mmHg and 2.4 (−17.3% to 22.1%) mmHg higher than SBP_{CCA} and MBP. $_{n}$FF matched well the shape of the tonometer waveform (0.46±0.03 vs 0.45±0.04).

Table 7.1: *Measured and non-invasively estimated haemodynamic characteristics of the people included in the study. Comparison between non-invasive and tonometer-based parameters:* $^{*}p<0.05$, $^{**}p<0.01$ *and* $^{***}p<0.001$

	All	**≤35**	**35-59**	**≥60**
Number (Male %)	203 (60%)	47 (59%)	78 (53%)	78 (68%)
Age [years]	51±17	24±5	51±6	67±5
SBP_{BRA} [mmHg]	122.1±16.8	111.4±11.7	120.9±14.7	129.8±17.6
DBP [mmHg]	75.2±10.3	67.0±8.5	77.8±9.4	77.5±9.5
c [m/s]	5.69±1.36	4.19±0.50	5.62±0.92	6.66±1.23
${}_{n}c$ [m/s]	5.67±1.45	4.45±0.73*	5.58±1.12	6.49±1.50
γ [-]	3.51±1.56	1.99±0.51	3.19±0.96	4.38±1.45
${}_{n}\gamma$ [-]	3.60±1.75 ***	2.43±0.80 ***	3.33±1.30	4.53±1.98
SBP_{CCA} [mmHg]	120.3±17.3	110.5±13.0	118.5±15.0	128.1±18.1
${}_{n}SBP_{CCA}$ [mmHg]	124.1±23.6 *	122.2±25.6 **	120.4±18.9	127.5±23.3
MBP [mmHg]	95.4±12.0	86.1±8.4	96.3±11.0	100.0±11.7
${}_{n}$MBP [mmHg]	97.6±13.6 **	91.7±12.1 ***	97.6±11.8	100.3±13.7
FF [-]	0.45±0.04	0.45±0.03	0.46±0.04	0.45±0.04
${}_{n}$FF [-]	0.46±0.03 ***	0.46±0.03	0.46±0.03*	0.46±0.03 **

7.3.1 Effect of ageing

Table 7.1 presents the stratification of the population in three age groups: young people (≤35 years), middle-aged adults (36-59 years), and older adults (≥60 years). Figure 7.4 shows the correlations and Bland-Altman plots between ${}_{n}c$ and c in the three age groups. ${}_{n}c$ significantly differed from c in the youngest age-group only, where the bias between the two techniques was 0.26 m/s (limits of agreement: −1.08 to 2.61 m/s, $p<0.05$) and correlation was only moderate ($r=0.45$, $p<0.01$). Conversely, ${}_{n}c$ and c strongly correlated in middle-aged and older adults ($r= 0.68$ and 0.70, $p<0.001$ for both) and differences were non-significant: −0.04 (−1.72 to 1.63) m/s and −0.17 (−2.36 to 2.02) m/s, respectively. Similarly, ${}_{n}\gamma$ was significantly higher ($p<0.001$) than and mildly correlated with γ in young people (Bland-Altman: 0.44, −1.09 to 1.98, $p<0.001$). On the contrary, differences were non-significant in middle-aged (0.14, −1.93 to 2.22) and older (0.15, −2.86 to 3.16) adults (Figure 7.5). However, unlike for c, the correlation between ${}_{n}\gamma$ and γ was strong only in middle-aged subject.

Figure 7.6 and 7.7 present correlation and Bland-Altman plots for SBP_{CCA} and MBP. As for c and γ, the non-invasive pressure estimation performed better in middle-aged and older adults,

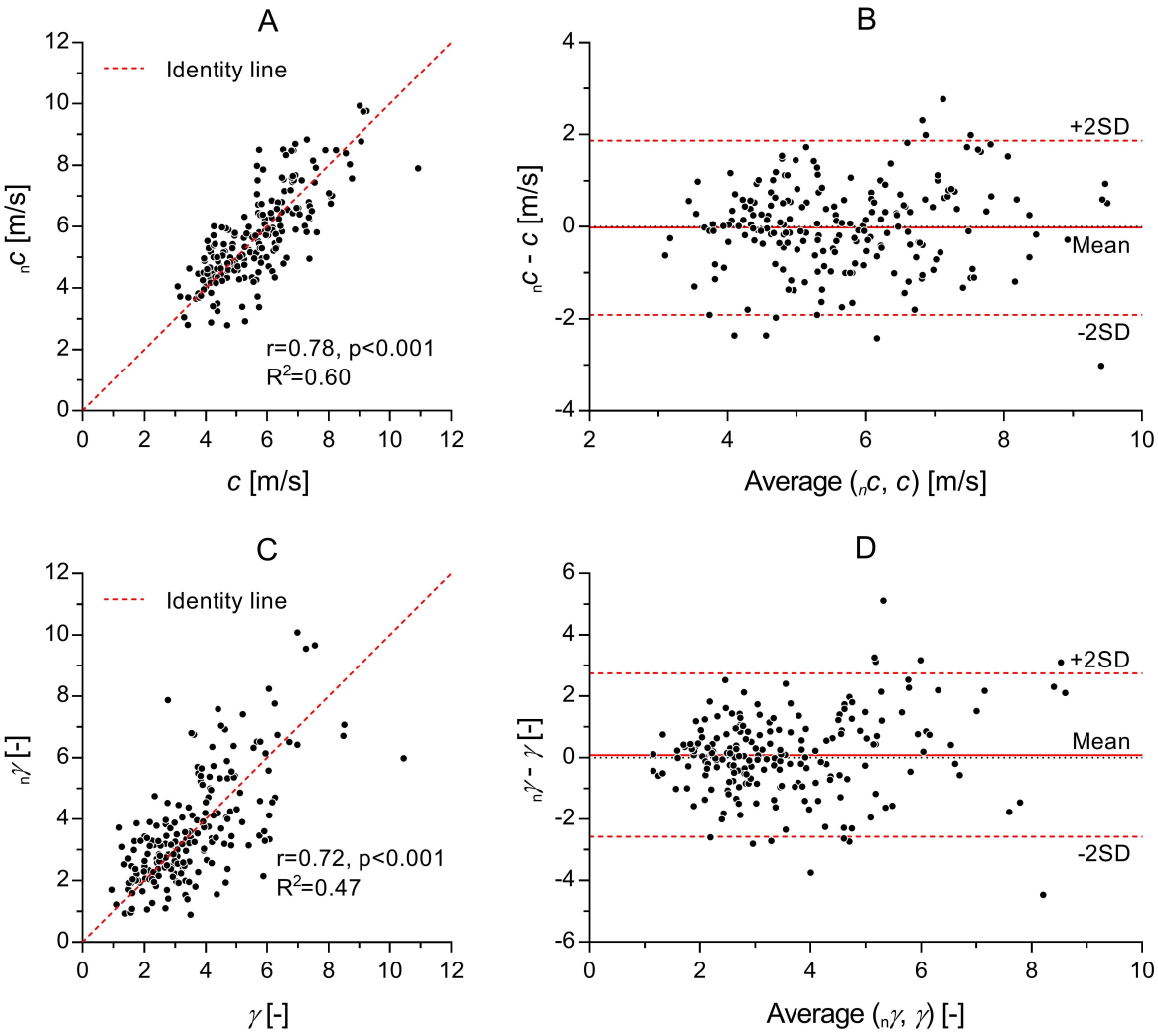

Figure 7.2: *Correlation analysis and Bland-Altman plot between c estimated with D^2P-loop and ${}_{n}c$ estimated with the lnDU-loop (A and B), and between the fitted γ and ${}_{n}\gamma$ estimated from ${}_{n}c$ (C and D). On the left side (A, C, E), the dashed red line represents the identity line. In the Bland-Altman plots (B, D, F), the red dashed line represents the average difference between the two measures and the two solid red line the limit of agreement between the two measures (±2 standard deviation).*

where the average error for ${}_{n}\mathrm{SBP}_{\mathrm{CCA}}$ and ${}_{n}\mathrm{MBP}$ were 1.8 (limits of agreement: −29.9 to 33.6, p=0.31) mmHg and 1.3 (limites of agreement: −12.6 to 15.2, p=0.11) mmHg, and −0.6 (limits of agreement: −42.8 to 41.6, p=0.80) mmHg and 0.3 (limits of agreement: −18.5 to 19.1, p=0.76) mmHg, respectively. It is worth noting that correlation between ${}_{n}P$ and P was stronger at MBP (r=0.81 and r=0.71 in 30-59 and ≥60 years, respectively, for both) than at $\mathrm{SBP}_{\mathrm{CCA}}$ (r=0.58 and r=0.50, respectively, p¡0.001 for both). On the other hand, in young people the accuracy of the non-invasive pressure estimation was lower; on average ${}_{n}\mathrm{MBP}$ was 5.5 mmHg higher than MBP (limit of agreement: −12.4 to 23.5 mmHg, p<0.001) and ${}_{n}\mathrm{SBP}_{\mathrm{CCA}}$ 11.7 mmHg higher

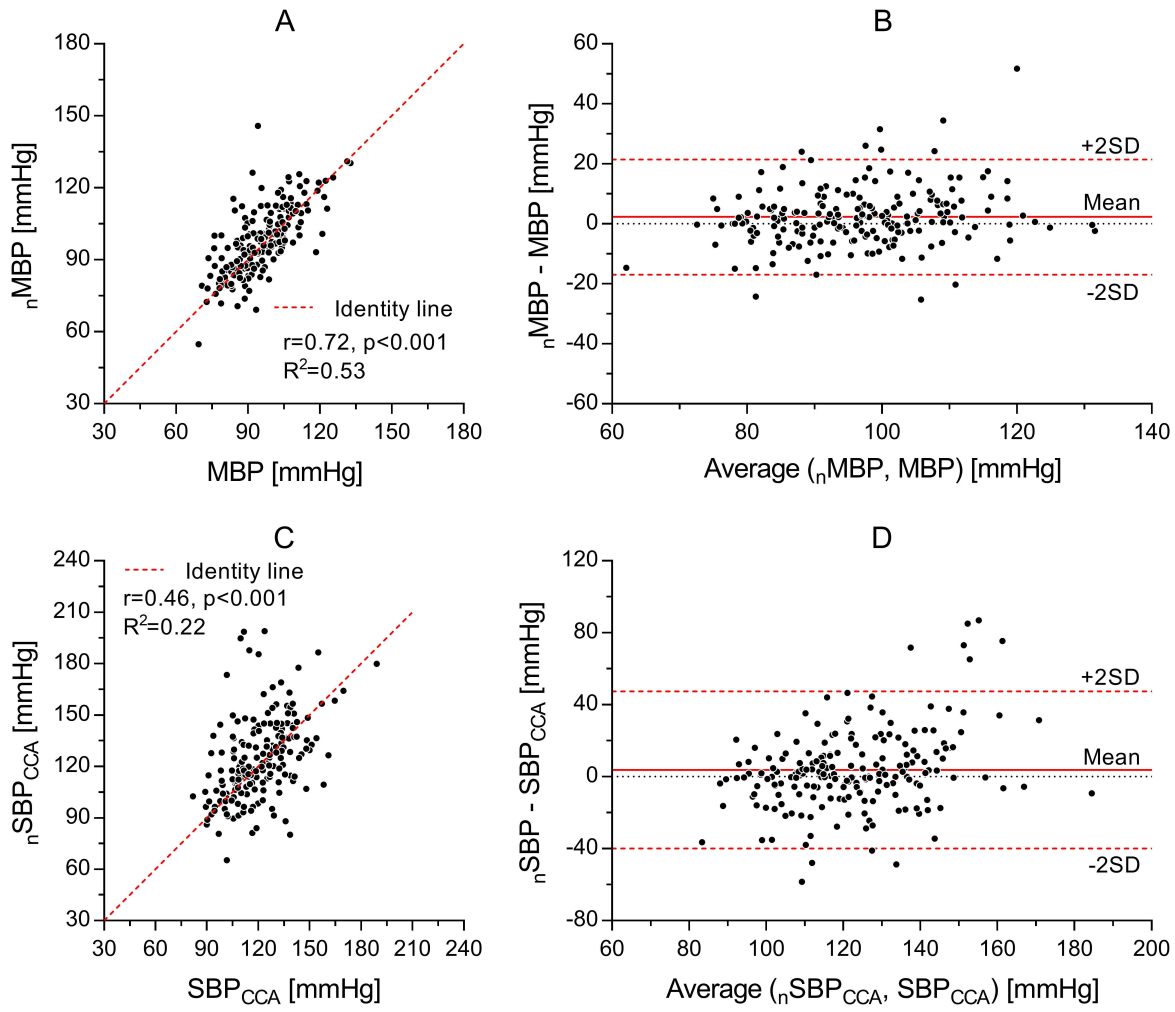

Figure 7.3: *Correlation analysis and Bland-Altman plot between tonometer* MBP *and* $_{\text{n}}$MBP *(A and B), and between tonometer* SBP_{CCA} *and* $_{\text{n}}\text{SBP}_{\text{CCA}}$ *(C and D). On the left side (A, C, E), the dashed red line represents the identity line. In the Bland-Altman plots (B, D, F), the red dashed line represents the average difference between the two measures and the two solid red line the limit of agreement between the two measures (±2 standard deviation).*

than SBP_{CCA} (−34.6 to 58.0 mmHg, p<0.01). Overall, $_{\text{n}}$FF showed good agreement tonometer FF in all groups, despite begin significantly different in middle-aged and older adults.

7.4 Discussion

This Chapter proposed a new technique where local non-invasive arterial measurements of diameter distension and blood flow velocity waveforms are used to estimate the non-invasive wave speed $_{\text{n}}c$, which is then used to determine the parameters of the exponential function that converts the diameter waveform into a pressure waveform. This proof-of-concept study had two main objectives: 1) test the hypothesis that γ cab be estimated from $_{\text{n}}c$ and DBP, and 2) validate

the new method using measurements of blood velocity and arterial diameter waveforms taken at the right CCA, and pressure at the left CCA using applanation tonometry simultaneously. The results indicated a good agreement between ${}_{\mathrm{n}}\gamma$ and γ fitted on the measured P-D^2 relationship, leading, on average, to a good matching between ${}_{\mathrm{n}}P$ and P. Agreement between tonometer and estimated metrics was particularly good in middle-aged and older adults, while ${}_{\mathrm{n}}P$ significantly overestimated the tonometer P in young individuals.

In the past two decades, several commercial TF-based devices have been developed to estimate pressure non-invasively in the aorta. Although they are the most commonly used, their accuracy is still called into question. Ding et al. (2011) compared invasively measured central aortic pressure with estimates provided by two commercial devices, SphygmoCor and Omron HEM- 9000AI, both relying on the measurement of radial pressure waveforms calibrated with cuff measurement of brachial pressure. The first underestimated aortic SBP by 15 mmHg and the limits of agreement in the Bland-Altman plot were approximately −33 to 3 mmHg. The Omron device performed slightly better on average, with limits of agreement of approximately ±20 mmHg. Laugesen et al. (2014) showed that calibrating the radial pressure waveform with oscillometric brachial pressure did reduce, on average, the underestimation of the SphygmoCor synthesised central SBP, but retained similarly wide limits of agreement (±22 mmHg). Only the calibration using invasively measured aortic SBP and DBP considerably improved the accuracy (±11 mmHg).

The method proposed in this Chapter overestimated $\mathrm{SBP}_{\mathrm{CCA}}$ and MBP by 3.8 and 2.3 mmHg in the overall study population. This differences were largely attributable to young subjects, where $\mathrm{SBP}_{\mathrm{CCA}}$ and MBP were overestimated by ∼11% and ∼7%, respectively, while smaller and non-significant differences were found in middle-aged and older adults. However, limits of agreement for $\mathrm{SBP}_{\mathrm{CCA}}$ were wider than that reported for commercial devices (−36.8 to 38.0 mmHg in middle-aged and older adults). These results might be due to the fact that the brachial pressure waveform was not acquired in this study. Conversely, the MBP used for calibrating the tonometer pressure waveform was estimated using average FF previously reported for the brachial artery (Segers et al., 2005). Here, carotid FF, determined from the acquired tonometer waveforms, averaged 0.44 but ranged between 0.36 and 0.57, and a similar variability was reported for the brachial artery (Grillo et al., 2020). Hence, neglecting the age-dependence and inter-subjects variability of the brachial FF likely affected the accuracy of the calibration of the tonometer pressure waveforms. Grillo et al. (2020) recently proposed an alternative method for the estimation of brachial MBP from DBP and sex, resulting in subject-specific brachial FF. They showed that the method more effectively predicts age-differences in brachial

FF in middle-aged and older adults. However, as conceded by the authors, the accuracy of the proposed formula remains sub-optimal and unable to capture the high inter-subject variability of the brachial FF. When applied to the data presented here, estimation of MBP from DBP and sex did not improve the agreement between ${}_{\mathrm{n}}P$ and tonometer P in young subjects, nor did in middle-aged and older adults.

The accurate estimation of SBP is undoubtedly important, however little attention is generally given to the shape and high-frequency components of the pressure waveform synthesised from distal measurements. The pressure waveform at any given arterial location is determined by the amalgamation of forward travelling pressure waves; a compression wave generated by the left ventricle contraction, and an expansion wave generated by the slowing down of ventricular ejection speed (Park et al., 2020), and reflected pressure waves originating by at discontinuity points (i.e. bifurcations and tapering) downstream in the arterial tree (Abdullateef et al., 2020; Khir & Parker, 2005). Given the complex structure of the arterial tree, the magnitude and timing of reflected waves are highly location-dependent, making the estimation of pressure at any location from pressure acquired elsewhere in the arterial tree a complicated task. Indeed, Segers et al. (2005) found that that the agumentation index (AIx), an estimate of the relative magnitude of the reflected wave, calculated from the TF-synthesised aortic pressure strongly correlated with that of the radial pressure waveform used in the estimation but only mildly correlated with the carotid AIx acquired via tonometry. This result contradicts previous findings showing that carotid AIx strongly correlates with that of invasively measure aortic pressure waveforms (Chen et al., 1996), thus raising some concerns on the accuracy of TF-based aortic waveforms (Millasseau et al., 2003; Segers et al., 2005).

The magnitude and timing of reflected waves in central arteries has been positively associated with ventricular function (Park et al., 2020) and the incidence of cardiovascular events (Wang et al., 2010; Sugawara et al., 2009). Therefore, findings by Segers et al. (2005) suggest that the pressure waveform estimated via TF might carry information on reflections at peripheral sites but be less than ideal to evaluate the subject-specific cardiac risk. Conversely, a previous study from Li & Khir (2011) showed good agreement between wave intensity analysis, using standard invasive P and U and non-invasive D and U methods, i.e. analysis of the propagation and reflection of waves in the arterial system, suggesting that the information on the complex interaction between forward and reflected waves carried by the diameter waveform is, indeed, similar to that provided by pressure. Therefore, local diameter likely represents a better candidate for the non-invasive estimation of pressure.

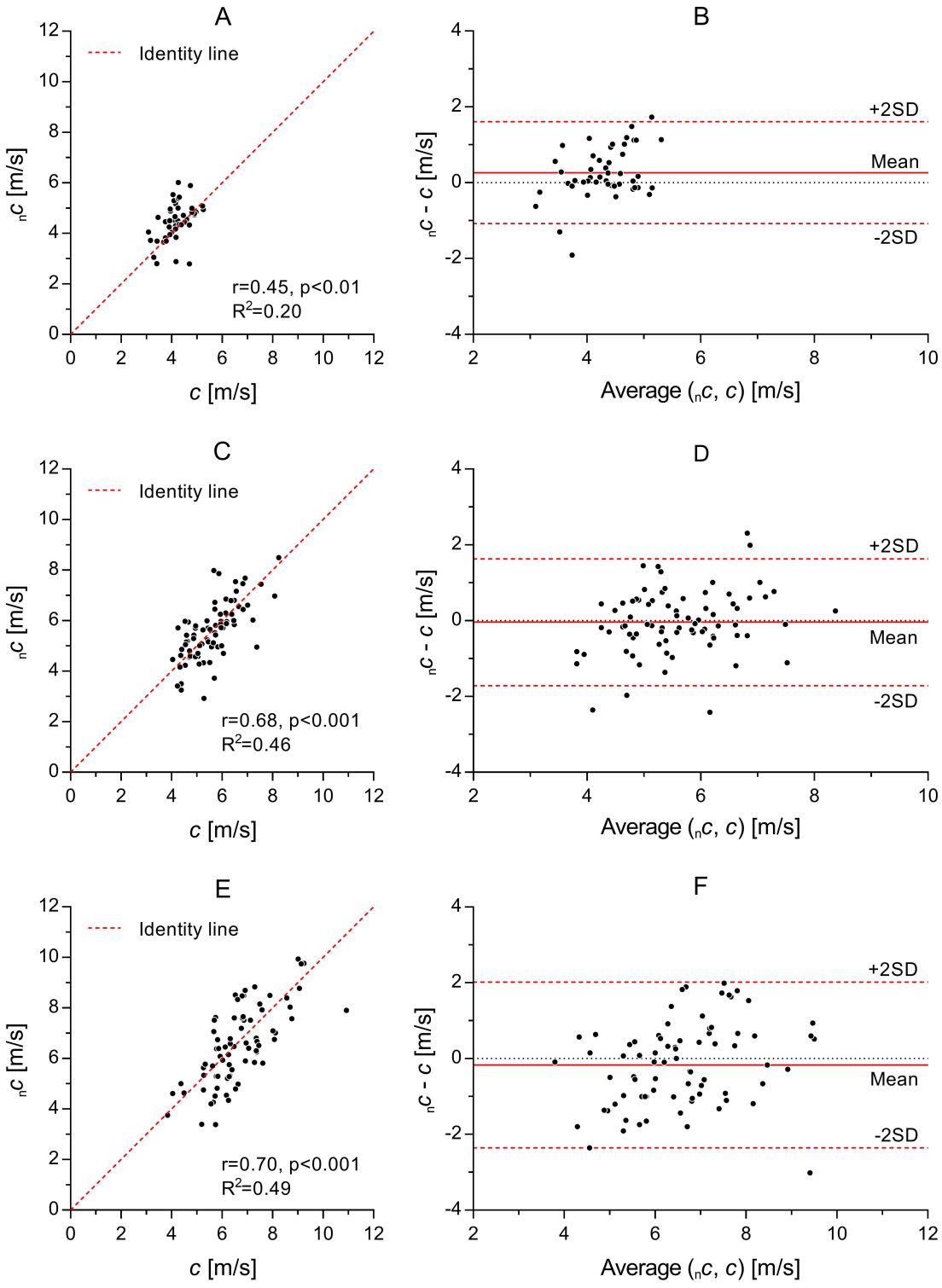

Figure 7.4: *Correlation analysis and Bland-Altman plot between c estimated with D^2P-loop and ${}_nc$ estimated with the lnDU-loop in young people (A and B), middle-aged adults (C and D) and older adults (E and F). On the left side (A, C, E), the dashed red line represents the identity line. In the Bland-Altman plots (B, D, F), the red dashed line represents the average difference between the two measures and the two solid red line the limit of agreement between the two measures (±2 standard deviation).*

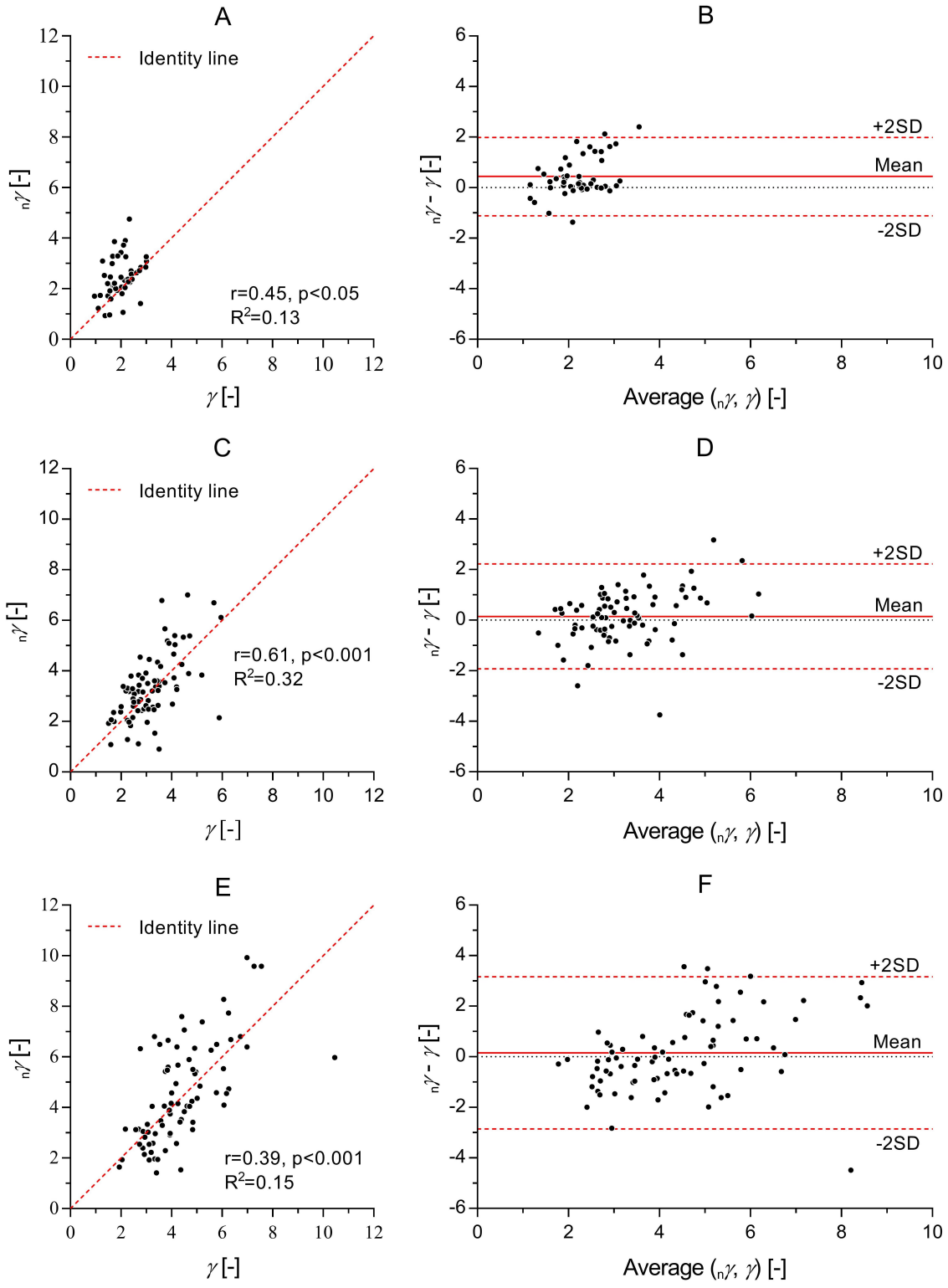

Figure 7.5: *Correlation analysis and Bland-Altman plot between the fitted γ and ${}_{n}\gamma$ estimated from ${}_{n}c$ in young people (A and B), middle-aged adults (C and D) and older adults (E and F). On the left side (A, C, E), the dashed red line represents the identity line. In the Bland-Altman plots (B, D, F), the red dashed line represents the average difference between the two measures and the two solid red line the limit of agreement between the two measures (±2 standard deviation).*

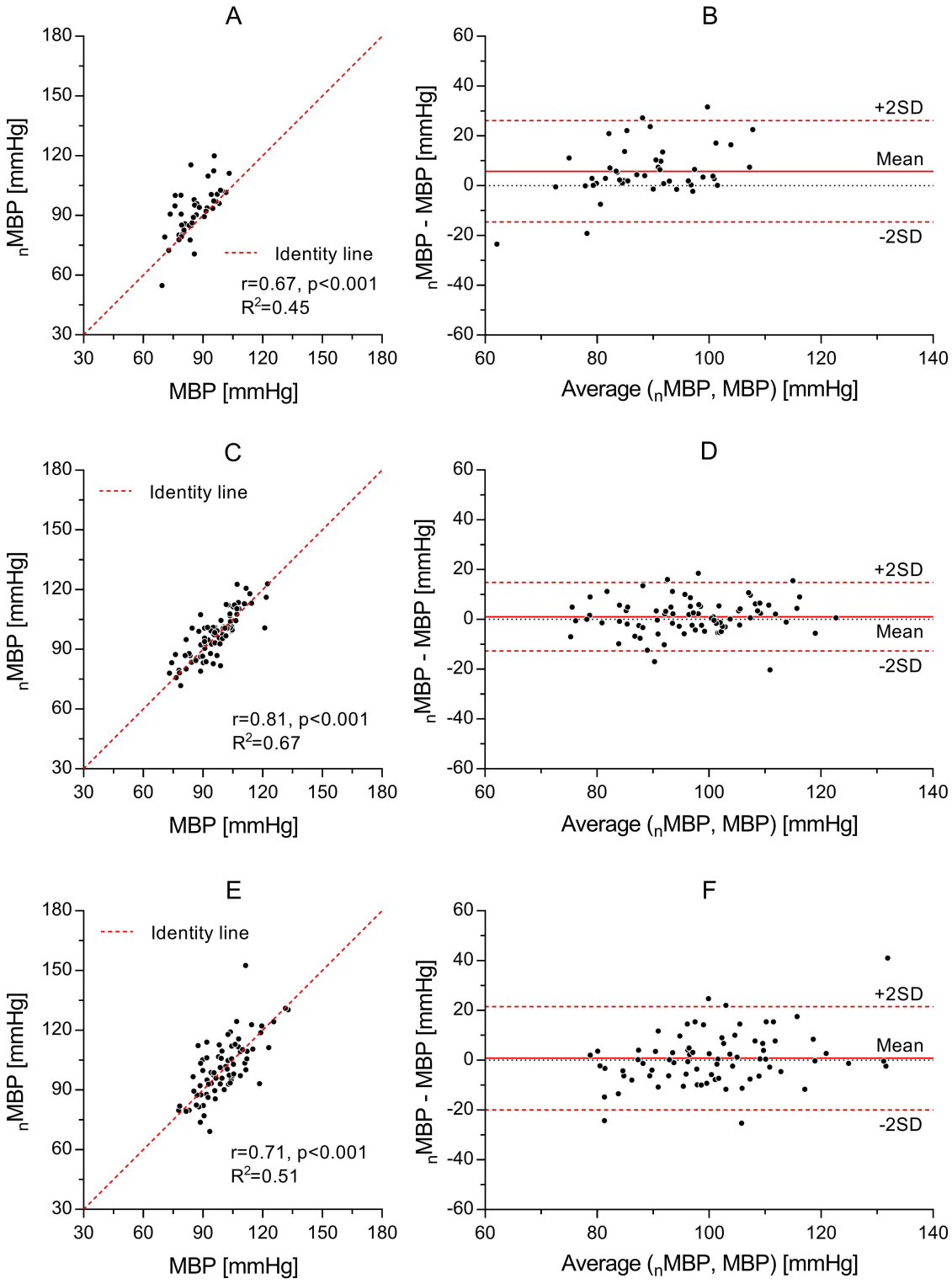

Figure 7.6: *Correlation analysis and Bland-Altman plot between tonometer* MBP *and* $_{n}$MBP *in young people (A and B), middle-aged adults (C and D) and older adults (E and F). On the left side (A, C, E), the dashed red line represents the identity line. In the Bland-Altman plots (B, D, F), the red dashed line represents the average difference between the two measures and the two solid red line the limit of agreement between the two measures (±2 standard deviation).*

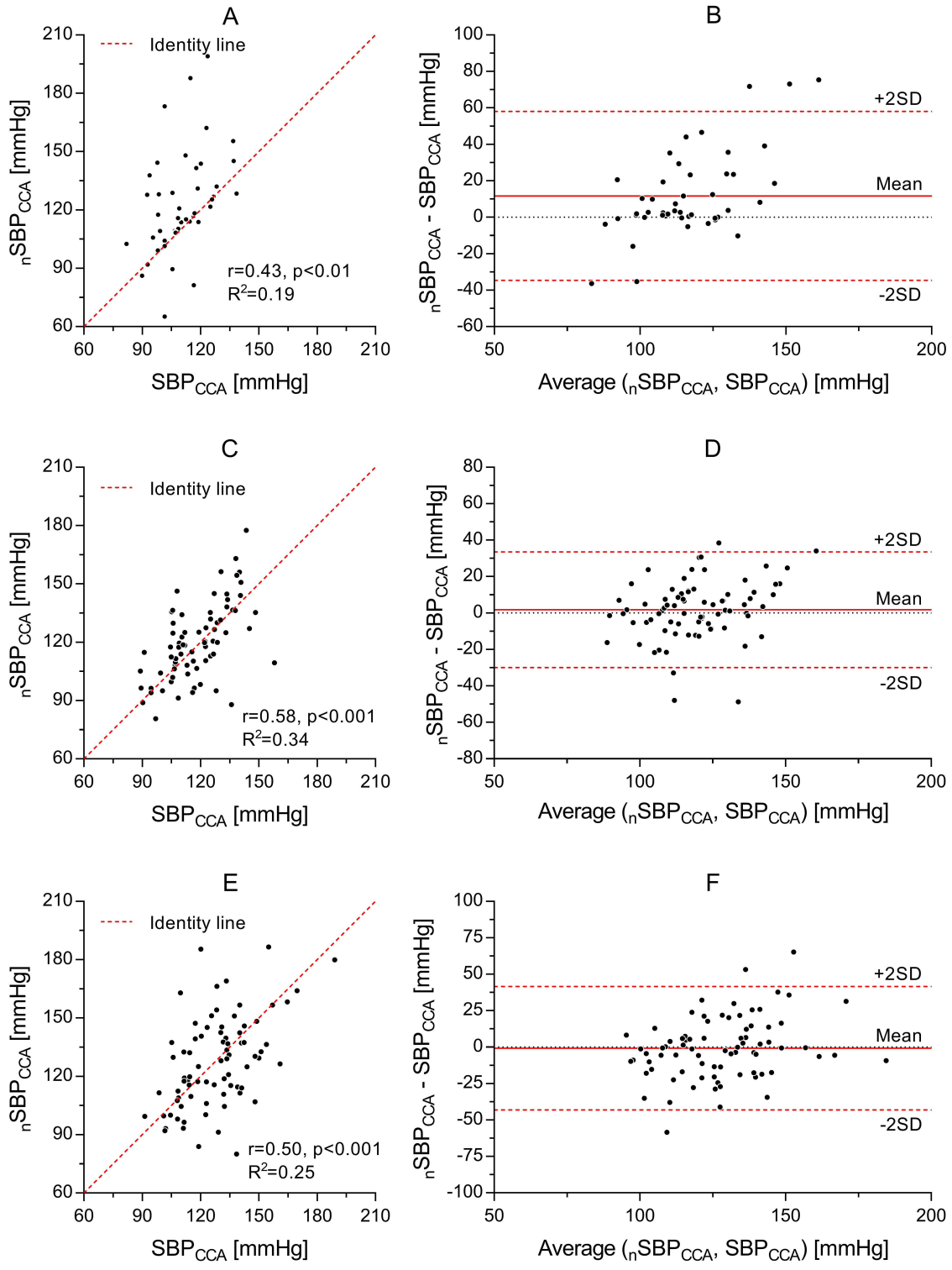

Figure 7.7: *Correlation analysis and Bland-Altman plot between tonometer* $\mathrm{SBP_{CCA}}$ *and* $_{\mathrm{n}}\mathrm{SBP_{CCA}}$ *in young people (A and B), middle-aged adults (C and D) and older adults (E and F). On the left side (A, C, E), the dashed red line represents the identity line. In the Bland-Altman plots (B, D, F), the red dashed line repesents the average difference between the two measures and the two solid red line the limit of agreement between the two measures (±2 standard deviation).*

Methods that non-invasively estimate pressure from local arterial waveforms aim at providing more accurate alternatives to TFs, following the rationale that local waveforms necessarily carry more representative information on local haemodynamics than peripheral pressure and rely on local wave speed to convert diameter distension or blood flow velocity waveforms into pressure. Vennin et al. (2015) used the water hammer equation (see Section 2.3.1 Eq. 2.39) to convert the upstroke of the flow velocity waveform into the pressure upstroke, and then modelled the elastic recoil in diastole with an exponential decay function and the pressure peak in late systole. The method yielded good results both in a one-dimensional computational model of the arterial tree and *in vivo*. However, the use of invasively measured aortic P for the estimation of c using the sum of squares method (Davies et al., 2005) makes this technique less likely to be used clinically. The accuracy of this proof of concept remains to be examined when using a non-invasive estimation of c.

Recently, Mariscal-Harana et al. (2021) developed a comprehensive approach to convert the aortic flow waveform into central aortic pressure. Their method relies chiefly on MRI acquisitions of the geometrical features of the aorta and supra-aortic arteries, flow at the ascending and descending thoracic aorta, and a peripheral BP measurement (i.e., brachial SBP and DBP). Haemodynamic data are then used to estimate parameters necessary to solve the 1-D equations of blood flow in the modelled network of arterial segments replicating the patient-specific aorta and supra-aortic arteries. Additional acquisition of the flow in each supra-aortic artery and of the CCA tonometer pressure waveform via tonometer further improves the formulation of the 1-D aortic model. When validated against invasively measured aortic pressure, their method showed higher accuracy than the method proposed here; agreement between estimated and measured aortic SBP was -0.0 (limits of agreement: ~ -19.4 to 19.4) mmHg. However, the high cost and limited avaialbility of MRI could pose a limit to the applicability of their technique in routine examinations and standard cardiovascular risk assessment (Negoita et al., 2018).

On the contrary, ultrasound scanner are widely diffused and commonly used for standard cardiovascular risk assessment. Beulen et al. (2011) were the first to use the relationship between c, estimated noninvasively from ultrasound A and Q, and arterial distensibility to convert the arterial diameter/area distension waveform into P. It is worth noting, however, that the underlying assumption in their method is that c is constant in the investigated pressure range, yielding to a linear P-D^2 relationship. While such assumption is reasonable for the flexible tubes used for the validation of the method, arteries exhibit an approximately exponential behaviour (Fung, 1967) and c is strongly pressure-dependent (Spronck et al., 2015). Application of their method on the data presented here led to the underestimation of $\mathrm{SBP_{CCA}}$ and preserved the

FF of the D^2 waveform (0.48±0.03), calculated as $(D_m^2 - D_d^2)/(D_s^2 - D_d^2)$ (D_m is the average of the diameter waveform within a cardiac cycle), higher than that of the P waveform (0.45±0.04). On the contrary, it was shown that, in agreement with the proposed hypothesis, c determined by the lnDU-loop describes the slope of the P-D^2 relationship only in the proximity of DBP, but allows the estimation of γ that, together with local D_d and DBP defines the exponential relationship between P and D^2. Hence, the proposed method relaxes the assumption that c is pressure independent. As a result, the $_n$FF closely matched that calculated on the tonometer pressure acquisition (Table 7.1) and $_n$SBP$_{CCA}$, on average, did not underestimate SBP$_{CCA}$.

7.4.1 Considerations on the age-effect

Interestingly, the accuracy of the method proposed was lower in young people. An accurate estimation of $_nc$ represents the cardinal point for the effectiveness of the proposed method. This is even more true when considering that, due to the quadratic dependence of γ from c, a 10% under or overestimation of c translates into a ∼20% error in γ. Here, the agreement between $_nc$ and c estimated using the D^2P-loop method was in line with that reported in other studies for similar comparisons between techniques (limits of agreement: $\sim \pm 2$ m/s) (Di Lascio et al., 2014). However, $_nc$ was, on average, ∼6% higher than c in young people, while average differences in the other age-groups were small and non-significant. This age-dependence might be related to several factors: first, it has been shown that the accuracy of the lnDU-loop method is strongly affected by reflections originating from peripheral sites. Borlotti et al. (2014) demonstrated that the slope of the early systolic part of the lnDU-loop is altered by the arrival of reflected waves, resulting in a decrease of $_nc$ in the presence of a backward compression wave (BCW) or vice versa in the case of a backward expansion wave (BEW). It is well known that the reflection reaching the CCA is a BCW (Borlotti et al., 2012; Willemet et al., 2016), so that $_nc$ is expected to be, on average, lower than c. On the contrary, here $_nc$ and c were not significantly different in middle-aged and older adults, and $_nc$ was even higher than c in young individuals, thus suggesting that other factors might affect differences between the two techniques.

Chapter 5 analysed changes in arterial wall viscosity characterising both ageing and cardiovascular pathologies, considering the impact the viscoelastic behaviour of the arterial tissue has on differences between systolic and diastolic Ds. Young people showed the highest level of viscosity of the entire cohort, implying a much stiffer response in systole than in diastole. In young controls, Ds was reduced by ∼17% in systole compared to diastole. This per cents translate into ∼10% when comparing systolic and diastolic c. Considering that the lnDU-loop estimates wave speed in early systole, $_nc$ is likely affected by both viscous and elastic properties,

and that differences found here in young individuals might, at least in part, reflect findings on arterial viscosity described in the previous chapter. However, similar differences would then be expected in hypertensive people, also showing higher systolic stiffness compared to that in diastole. Interestingly, such trend was not observed here; differences between ${}_{\mathrm{n}}c$ and c were similar in controls, hypertensives and T2DMs. It is worth considering that an increase in the magnitude of the wave reflections has been reported with both ageing (Borlotti et al., 2012) and hypertension (Su et al., 2016), so that the effects of viscosity and wave reflections in hypertensives might partially compensate each other.

Finally, once more, the calibration of the pressure waveforms was performed assuming brachial artery FF=0.43, as reported by Segers et al. (2009), for all subjects. However, FF its age, sex, and hypertension dependence and its high inter-subjects variability likely affected results reported here (Grillo et al., 2020; Segers et al., 2009).

Limitations

As all the non-invasive methods for the estimation of pressure, both based on TFs and local arterial waveforms, the accuracy of this method strongly depends on the level of accuracy of the measurement of peripheral BP, with brachial cuff measurement typically under and overestimating $\mathrm{SBP_{BRA}}$ and DBP, respectively (Picone et al., 2017). However, differently from other methods, the technique proposed here only requires DBP, so that the effect on pulse pressure ($\mathrm{SBP_{BRA}}-\mathrm{DBP}$) is expected to be marginal. Further, as mention above, this study lacked the acquisition of the brachial pressure waveform allowing the determination of a subject-specific FF and, hence, ensuring a more accurate calibration of the CCA pressure waveform. On the contrary, the effect on the calibration of the tonometer pressure waveform is certainly non-negligible. Even more so when considering that, as reported by Grillo et al. (2020), estimating MBP by a single formula is prone to considerable error. Therefore, future work should be directed to validate the technique against invasive pressure measurements.

Finally, ultrasound and tonometer acquisitions could not be carried out simultaneously on the same CCA, but the two signals were acquired simultaneously on contralateral arteries. It is, therefore, possible that some differences might occur between the haemodynamics of the right and left CCA, although these are expected to be small and unlikely affected the validity of the results presented here.

7.5 Chapter conclusions

This proof-of-concept study introduced a new method where local arterial wall stiffness, estimated non-invasively *in vivo* by the local c, is used to operate an exponential conversion of the local diameter distension waveform into pressure. While the novel method has been validated at the CCA against pressure acquired via tonometry, the encouraging result presented here suggests that *local* ultrasound acquisition of blood velocity and diameter waveforms could provide an alternative to TF-methods for the non-invasive estimation of aortic pressure in routine examinations (Negoita et al., 2018). This technique could, therefore, enhance the characterisation of the ventricular afterload, potentially improving our ability to predict the cardiovascular risk. Further work is warranted to validate the new technique against invasive pressure measurements and to test its effectiveness in estimating central aortic pressure.

CHAPTER 8

General discussion and conclusions

8.1 General discussion

8.1.1 Methodological considerations

The attention given to the concept of arterial stiffness has steadily grown over the years, as scientific evidence has demonstrated the predictive value of PWV for cardiovascular events (Ben-Shlomo et al., 2014; Boutouyrie et al., 2002; Tomiyama et al., 2016), longitudinal increase in BP and incidence of hypertension (Najjar et al., 2008), fatal stroke in hypertension (Laurent et al., 2003), and cognitive decline (Chiesa et al., 2019; Laugesen et al., 2013). This clinical work was accompanied also by an effort to standardise the clinical assessment of arterial stiffness, aiming at enhancing comparability between different centres/countries (Laurent et al., 2006; Salvi et al., 2008; Van Bortel et al., 2012). Despite the compelling evidence of the pivotal role of arterial stiffness in determining the CV risk, current guidelines for the management of hypertension discourage the use of PWV in routine clinical practice as considered impractical (Williams et al., 2018), suggesting that more concerted work is needed to improve the *in vivo* quantification of arterial stiffness. This doctoral work is to be considered as part of this effort and focuses on the improvement of the quantification of arterial stiffness and more broadly mechanics/function using both invasive and non-invasive techniques.

The pressure-dependence of arterial stiffness

The intrinsic pressure-dependence of arterial stiffness has long been known (Gavish & Izzo, 2016; Learoyd & Taylor, 1966). As pressure increases, arterial collagen, that appears as wavy and crimped bundles of fibres in the unloaded arterial wall, is gradually straightened and recruited (Chow et al., 2014; Krasny et al., 2017b). This process produces a shift in the load-bearing from compliant elastin to stiffer collagen fibres that ultimately results in the non-linear pseudoelastic behaviour of the arterial wall (Burton, 1954; Fonck et al., 2007). Chapter 3 of this thesis focused on further characterising this process; layer-specific uniaxial tensile testing was combined with a novel modelling framework that, by accounting for the layers' residual deformations, allows incorporating the layer-specific mechanical behaviour into a tri-layered model of a cylindrical arterial segment. Simulation of physiological loads provided valuable insight into the role arterial layers play in aortic mechanics at different distending pressures, suggesting that when moving from the normotensive to the hypertensive pressure range, the 90-180% wall stiffening is structurally justified by a shift in the load-bearing from the compliant media to the stiffer adventitia that ranged between 2 and 13% depending on the aortic region and species. In agreement with previous findings (Burton, 1954; Wolinsky & Glagov, 1964), this results suggest that pressure-dependence of arterial stiffness is a direct consequence of functional tri-layered

structure of the wall, where the media provides compliance in the physiological pressure range while the adventitia serves as protective layer against the risk of rupture at supra-physiological pressures, and highlights the fact that considerable wall stiffening results from the increase BP alone without actual changes in wall composition.

Arterial ageing is associated with important changes in the wall structure that, from a passive mechanics standpoint, can be summarised as: a) degradation and fragmentation of the elastin matrix, and b) increased content and cross-linking of collagen fibres (Greenwald, 2007). Chapter 4 aimed at evaluating the consequences of said structural changes on the pressure-stiffness relationship of human donor's aortae *ex vivo*; the results indicated that, in response to an equal increase in BP, the aortic wall of older individuals (above 70 years of age) stiffens, on average, ∼4 times more than that of young people (<30 years). This finding indicates that the pressure-dependence of arterial stiffness is complicated further by being, in-turn, age-dependent.

As a result, assessing intrinsic arterial stiffness (i.e., related to the wall structure independently of acute differences is BP) *in vivo* is not trivial; in contrast with *ex vivo* mechanical testing that allows characterising the entire mechanical response of the arterial wall, arterial waveforms provide a limited view of a small part of this non-linear behaviour. Most clinical studies account for the acute pressure-dependence of PWV/c by means of statistical methods, typically including SBP or MBP in multivariate regression analyses (Desamericq et al., 2015; Valbusa et al., 2019; Vogel et al., 2013). This strategy, however, is not patient-specific, so that its use is limited to clinical studies and precluded to clinical practice. Subject-specific mechanistic pressure-normalisation methods for PWV/c (Ma et al., 2018; Shirai et al., 2006; Spronck et al., 2015) aim at addressing this limitation, and rely, chiefly, on the observation that the pressure-diameter and pressure-area relationships of arteries are nearly exponential in the physiological range of pressure (see Chapter 3 and 4).

The mechanistic method proposed here (see Chapter 2) suggests that the pressure-area exponential parameter γ can be estimated from c if the reference pressure P_c, indicating the pressure at which c was determined, is known. Application of the method in a cohort of healthy, hypertensive and diabetic people (Chapter 5) yielded comparable results to those obtained with classical cross-sectional statistical adjustments and indicated that the choice of P_c coincided with that of the normalising pressure in statistical methods.

Furthermore, results in Chapter 5 and 7 empirically demonstrated that, for local loops methods, P_c is close to DBP. This finding does not come as a surprise when considering that both the D^2P-loop and the lnDU-loop methods determine c from the relationship between arterial waveforms in early systole/late diastole, hence, close to DBP, and suggests that, similarly, regional

foot-to-foot PWVs most likely reflects arterial stiffness in diastole, as previously postulated (Pucci et al., 2020; Spronck et al., 2017a). Therefore, despite PWV/c typically shows stronger correlations with SBP and MBP than DBP (Shirai et al., 2019), the latter likely represents the best choice when accounting for the acute effect of BP on arterial stiffness, while caution should be used with higher normalising pressures that might also remove chronic effects of long terms exposure to high BP.

The effect of wall viscosity on arterial stiffness

Several *ex vivo* studies have demonstrated that the arterial wall is characterised by a typical viscoelastic behaviour (Learoyd & Taylor, 1966; Remington, 1954), and this viscoelastic nature has commonly been attributed to the presence of the VSMCs in the wall (Apter et al., 1966; Learoyd & Taylor, 1966; Zatzman et al., 1954). Nonetheless, the arterial wall viscosity is commonly neglected in clinical studies, on the ground that its effect might be relatively small *in vivo* (Boutouyrie et al., 1998). In agreement with previous studies (Armentano et al., 1995a,b), analysis of PD-loop hysteresis in Chapter 5 of this thesis indicated that carotid wall viscosity can be detected *in vivo*. Further, it was shown that such property can significantly affect differences between arterial stiffness, as distensibility, in early systole and late diastole. Under the assumption that the different dynamics of wall abrupt distension in systole and slow recoil in diastole might reflect its combined visco-elastic and elastic properties, respectively, results presented in Chapter 5 warrant more caution in considering systolic indices of stiffness as reflecting the wall's elasticity alone.

Non-invasive estimation of arterial pressure

Despite brachial measurements of BP are still considered the gold-standard for the diagnosis of hypertension (Williams et al., 2018), central arterial pressure, the pressure in the aorta, has gained more and more relevance in recent years (McEniery et al., 2014), as this likely provides more relevant information on the cardiac function (Park et al., 2020). However, the invasivity of the direct measurement of central arterial pressure, requiring the insertion of a pressure catheter in the aorta via a peripheral arterial access point, limits its use in clinical practice. In Chapter 7 of this thesis, the viability of a new method for the non-invasive estimation of pressure in arteries was evaluated. The technique relies on the γ-c relationship described above to perform an exponential conversion of the diameter into a pressure waveform. The proposed method showed encouraging results at the common carotid artery. Further development of the technique could improve our ability of estimating pressure in arteries by replacing commonly used transfer function methods (Pauca et al., 2001), relying on distal haemodynamic parameters

that might poorly relate with local haemodynamics (Segers et al., 2005), with a method based, uniquely, on local arterial waveforms.

8.1.2 Clinical considerations

In agreement with previous work (Haskett et al., 2010; Mattace-Raso et al., 2010), the results presented in this thesis, combing both *ex vivo* (Chapter 4) and *in vivo* studies (Chapter 5), indicate that age is a major determinant of large arteries stiffening. In Chapter 4, constitutive modelling of the response of the aortic wall to uniaxial ring tests provided valuable insights into the age-related remodelling process, suggesting that, in agreement with microscopy observations (Jadidi et al., 2020), elastin degradation might start relatively early with age (30-39 years). Loss of integrity of the elastin network then triggers the collagen remodelling process, likely to replace the elastin function. Constitutively, collagen remodelling resulted particularly evident from 60 years onward. Further, the results suggest that, up to the age of 50, age-related remodelling effectively preserved the elastic function of the aortic wall, but this steadily declined thereafter (Figure 4.7). Indeed, with age, large arteries lose their ability to smooth the pulsatile action of the heart, likely explaining the increased PP in older adults observed in Chapter 5 and several clinical studies (Gurven et al., 2012; Shimura & Kubo, 2019; Wang et al., 2019).

This trend was also observed in terms of wall stiffness, with the onset of arterial ageing identified, statistically, *ex vivo* at approximately 60 years of age (Figures 4.3 and 4.4B and Table 4.3). Similar results were found when assessing arterial stiffness *in vivo* using c and γ, although age-related carotid wall stiffening appeared to occur approximately one decade earlier ($\sim$50 years) (Figures 5.5B, C and D). However, important considerations concern the use of PWV/c as an index of arterial stiffness. The Moens-Kortweg equation (Kortweg, 1878; Moens, 1878) indicates that c is a function of both the wall material stiffness (i.e., the elastic modulus), geometrical features (i.e., wall thickness to diameter ratio), and blood rheological properties (i.e., blood density). Indeed, it was recently shown that this relationship could be used to effectively estimates the wall circumferential tangential elastic modulus from a non-invasive measurement of wave speed (Li et al., 2021). It is worth noting that, in Chapter 5, once c was converted to actual material stiffness (tangential elastic modulus) (Figure 5.5F), significant wall stiffening was observed only after 60 years of age, in agreement with findings in the *ex vivo* study in Chapter 4. Therefore, earlier changes in c possibly reflect those in arterial geometrical features rather than pure mechanical properties and discourage the blind use of PWV/c as proxy of arterial stiffness without considering changes in arterial calibre and wall thickness.

On the other hand, in agreement with previous studies (Armentano et al., 1995a; Bussy et al.,

2000), CCA stiffening with hypertension and diabetes, known cardiovascular risk factors, was mainly related to the acute effect of increased BP. Intrinsic CCA elastic stiffness of hypertensive and T2DM patients did not differ from that of controls. Chapter 3 provided a detailed analysis of the structural basis behind the acute effect of BP on the wall stiffness; the differential involvement of arterial layers in the microscopic wall response at different distending pressures determines the dependence of wall stiffness on BP (Figure 3.20). These findings highlight the fact that arterial stiffness should always be considered in relation to BP at the time of the measurement. Among the cardiovascular risk factors analysed in this PhD work, only obesity significantly increased CCA wall stiffness (as c). The study in Chapter 6 showed that this alteration of the normal wall mechanics is reversible if the body mass is effectively reduced via bariatric surgery. It is worth noting that changes in c happened in a relatively limited time frame (<1 year) and in the absence of big changes in BP.

Interestingly, exposure to high BP appeared to significantly affect arterial viscosity (Chapter 5), with potential clinical implications on the wall viscoelastic stiffness in early systole (Table 5.5). Despite the exact underlying mechanism allowing the VSMCs to modulate the wall viscosity is still poorly understood (Boutouyrie et al., 1998), a recent study (Spronck et al., 2019) (available in pre-print) showed that mice with a specific genetic background reacted to induced hypertension with increased VSMCs contractility; this allows maintaining the wall stress in the physiological range without triggering the fibrosis to increase wall thickness and reduce wall stress. Therefore, these findings could possibly reflect a defensive mechanism enacted by the VSMCs in response to increased BP.

8.2 Limitations and experimental considerations

8.2.1 *Ex vivo* studies

In Chapter 3, the complex layer-specific anisotropic behaviour of the arterial wall has been investigated by subjecting samples to uniaxial tensile testing in both the circumferential and axial directions. This approach introduces three main issues: 1) the mechanical coupling between the circumferential and axial response of the arterial wall cannot be directly assessed, 2) the necessity of flattening a naturally arched shaped circumferential sample into a straight strip inevitably introduces unphysiological deformations that depend on the radial coordinate, and 3) the loading condition poorly mimics physiological loads. More complex testing methods could improve the quantification of the wall mechanical properties; planar biaxial testing represents a valuable alternative addressing the first limitation mentioned above. However, this technique

similarly induces unphysiological deformations in the sample and the increased complexity of the experimental procedure limits the size of the loads that can be applied. On the other hand, tension-inflation tests closely mimic the physiological loading conditions but complicate the investigation of layer-specific mechanics. In Chapter 3, point 2 and 3 above were addressed by computationally assembling the three layers into a cylindrical blood vessel that would 1) account for the effects of layer-specific residual stresses and 2) allow the simulation of a physiological loading condition. While this modelling approach likely improved the quantification of the arterial wall mechanics, it is worth considering layers were modelled as thin membranes (thin-walled modelling approach). A more complex modelling approach of the three-dimensional layer-specific residual deformations that would account for the layers bending stiffness and opening angles (Holzapfel et al., 2007) could improve the tractation of the problem. It could be argued, however, that the uncertainty in the determination of the required geometrical parameters (i.e., layer-specific OA and deformation in the axial-radial plane) could lead to inaccuracy.

In Chapter 4, the effect of ageing on the mechanical properties of the human aortic wall has been investigated via ring tests. This choice has been dictated by the limited amount of arterial tissue available for the study and the necessity to conduct non-destructive testing. In addition to the three limitations mentioned above for uniaxial tests, ring tests do not allow to assess the wall response to axial loads. While circumferential properties are more relevant to the pulsatile haemodynamics, a thorough characterisation of the aortic wall mechanics requires the acquisition of axial data. For example, when fitting the wall circumferential stress-stretch curves, the SEF parameters defining the wall anisotropicity have been assumed on the basis of information available in the literature. Fitting biaxial mechanical data would provide a more accurate estimation of the model parameters.

8.2.2 *In vivo* studies

In Chapters 5 and 7, carotid mechanics and haemodynamics have been investigated by assessing simultaneously acquired tonometer pressure and ultrasound wall distension/blood velocity waveforms at the left and right CCAs, respectively. Although the two contralateral CCAs show similar waveforms (Giannattasio et al., 2008), ideally, the methods used in the analysis should be applied to data acquired at the same location. However, simultaneous ultrasound and tonometer acquisitions at the same location are currently impossible, and the error introduced by the contralateral acquisition protocol is expected to be negligible.

Additionally, the calibration of the CCA tonometer pressure waveform has been performed

based on MBP estimated from brachial SBP and DBP using a standardised constant FF = 0.43. However, in agreement with previous studies (Grillo et al., 2020; Segers et al., 2009), FF of the CCA showed high inter-subject variability. Further, it was shown that estimation of the subject-specific brachial MBP from easily measurable parameters, such as age, brachial SBP and DBP, and gender, provides sub-optimal accuracy (Grillo et al., 2020). Therefore, a more accurate estimation of MBP from the brachial tonometer waveforms would likely improve the accuracy of the results. While this limitation is expected to have a marginal effect on population-based results in Chapter 5, the impact on the subject-specific estimation of pressure in Chapter 7 could be non-negligible, and validation of the non-invasive technique for the estimation of arterial pressure against invasively measured pressure is required.

The cohort analysed in Chapter 5 came from two Italian hospitals (Pisa and Massa, Tuscany, Italy). While, on one side, this granted access to a larger cohort, it also implied that acquisitions were performed by different operators and using different ultrasound systems (Hitachi Aloka Alpha 10 and Esaote MyLab 70, respectively). A previous study from Prof. Palombo's group found systematic differences in the diameter tracking obtained with the two ultrasound systems (Palombo et al., 2012). Furthermore, the two systems likely applied different and unknown filtering to increase the signal-to-noise ratio, with the direct effect of causing systematic delays of the acquired signals with respect to the ECG waveforms. For this reason, the alignment of the pressure and diameter waveforms was not performed on the basis of the QRS complex of the ECG waveform but using peaks of the second derivative of the pressure and diameter waveforms, corresponding to the foot of the wave and dicrotic notch, as fiducial points for the alignment. Further, a dichotomous variable was used to include the ultrasound system as a confounder for all the parameters derived from ultrasound data. Finally, inter-clinical group differences in all viscosity parameters, which are expected to be strongly affected by the incorrect alignment of pressure-diameter data, were nearly unchanged when only data acquired with Hitachi Aloka Alpha 10 was considered.

The pressure-normalisation performed in Chapters 5 and 6 and the non-invasive pressure estimation method in Chapters 7 are based on the assumption of the existence of a perfectly exponential pressure-area relationship in arteries in the physiological range of pressures. While empirical data support this hypothesis (Gavish & Izzo, 2016), the true subject-specific pressure-area relationship is obviously not exactly exponential, especially in highly compliant arteries of young individuals and at low pressures (Vande Geest et al., 2004). It is therefore possible that the accuracy of the pressure-normalisation and non-invasive pressure estimation methods, as well as the results presented in this thesis (e.g., absence of pressure-independent changes in carotid

function in hypertensive patients) might have been affected by this assumption. For example, it can be shown that by simply opting for an exponential pressure-diameter relationship rather than pressure-area relationship the second term under the square root in Eq. 2.73 (also appearing as Eqs. 5.12 and 6.4) becomes multiplied by a factor 1/2. Hence, for a given normalising pressure, the pressure correction obtained through an exponential pressure-diameter modelling is slightly lower than that resulting from an exponential pressure-area relationship (i.e., the main contribution arises from the first term in Eq. 2.73). Nevertheless, a previous study has proven that exponential pressure-area modelling accurately predicted changes in carotid c following BP reduction with antihypertensive drugs (Spronck et al., 2015). Therefore, it is unlikely that the assumption made herein largely affected the validity of the results presented in this thesis.

8.3 Conclusions

Cardiovascular diseases are the leading cause of death worldwide. Large arteries play a fundamental role in the cardiovascular system, and their function directly affects the cardiac workload. Therefore, devising techniques to effectively characterise the arterial wall behaviour in physiological and pathological conditions has been and remains fundamental in cardiovascular research. Using a combination of novel and established techniques, this thesis aimed to improve our understanding of the behaviour of the wall of elastic arteries. This aim has been achieved by combining invasive *ex vivo* studies and non-invasive clinical investigations. On one side, the scientific value of the proposed invasive experimental methods consists of allowing a precise and comprehensive characterisation of the wall behaviour, from the level of the individual layers to its macroscopic response, while relying on simple, widely available and inexpensive experimental techniques. In Chapter 3, layer-specific uniaxial testing combined with layer-specific and tri-layered wall constitutive modelling allowed investigating the role intima, media and adventitia play in arterial mechanics at different aortic locations and at different levels of distending pressure. While the media provides compliance in the resting physiological pressure range, the contribution of the adventitia to the wall mechanics grows with increasing pressure, providing protection against high-physiological and supra-physiological loads. Furthermore, the role of the adventitia gains more and more relevance when moving from proximal to distal locations in the aorta and, more generally, in the arterial tree. Chapter 4 expanded this work, investigating how ageing affects the behaviour of the thoracic aorta. The two most important findings were that age-related aortic remodelling: 1) causes a significant stiffening of the wall tissue from ~60 years onward, and 2) exacerbates the pressure-dependence of the arterial stiffness. These changes then compromise the elastic function of large arteries.

On the other hand, the proposed non-invasive techniques could provide valuable tools to evaluate the performance of the arterial wall in clinical settings, and cardiovascular risk. Indeed, these techniques have the advantage of relying, once more, on widely diffused and inexpensive data acquisition techniques (ultrasound scanning and tonometry), making them available to most laboratories and cardiovascular clinics. In Chapter 5, CCA pressure-diameter/area relationships were used to investigate the effect of age, hypertension and T2DM on the wall visco-elastic behaviour, independently of inter-subject differences in BP at the time of data acquisition. In agreement with the results of Chapter 4, age did affect the elasticity of the CCA independently from the concomitant increase in BP (mainly systolic). Conversely, this was not the case for neither hypertension nor T2DM; differences in wall stiffness with age-matched controls were mainly attributable to differences in BP at the time of measurement. Among the cardiovascular risk factors evaluated in this Thesis, only morbid obesity significantly affected local CCA c, independently from BP (Chapter 6). Interestingly, the observed alteration of the physiological CCA haemodynamics/mechanics associated with excessive body weight was entirely reversible if body weight was successfully controlled via bariatric surgery. Results in Chapter 5 do, however, suggest that exposure to high BP might affect the wall viscosity, reversing its normal decline with age and decreasing wall distensibility in systole compared to diastole. Finally, following from the theoretical background in Chapter 2 and from the exponential pressure-area modelling work performed in Chapter 5, Chapter 7's objective consisted of evaluating the viability of a novel technique to non-invasively estimate blood pressure in arteries from ultrasound acquisitions of blood velocity and diameter distension waveforms. Given the pivotal role of BP in arterial function, this technique could prove helpful when assessing the healthy/pathological state of non-superficial arteries.

8.3.1 Future directions

This Section will provide possible future directions that are the natural continuation of the studies presented in this thesis.

Ex vivo studies

When applied to animal aortic samples, the experimental/modelling framework developed in Chapter 3 provided valuable insight into the mechanical behaviour of the tri-layered aortic wall. In future studies, the proposed methodology should be applied to human arterial samples, as it would prove extremely useful in furthering our understanding of the mechanics of arterial ageing (as seen in Chapter 4) and vascular pathologies, such as hypertension and aneurysms. Furthermore, while the technique was conceived to allow detailed analysis of the wall behaviour

using mechanical data measured using simple and inexpensive experimental methods, the growing use of sophisticated microscopy techniques, such as two-photon fluorescence (Sugita & Matsumoto, 2013, 2016; Krasny et al., 2017b,a; Chow et al., 2014), warrants further work to incorporate layer-specific microstructural data obtained via microscopy into the model. This would improve its ability to accurately describe the wall behaviour at the level of its microscopic constituents.

In vivo studies

The studies in Chapter 5 and 6 used non-invasive approaches to quantify carotid mechanics and haemodynamics. While these studies provided valuable insight into changes in carotid function with ageing, hypertension, T2DM, and intensive weight loss following bariatric surgery, future studies should focus on understanding the mechano-biological processes that are at their basis. For example, viscous wall properties are commonly associated with VSMCs. If the physiological decline in wall viscosity with age is altered by hypertension as suggested in Chapter 5 and in previous work (Armentano et al., 1995a), future studies should attempt to characterise this process at a cellular level. A viable approach for such investigations could be altering the sympathetic activity using drugs (Shirai et al., 2011) or appropriate physical manoeuvres (Faconti et al., 2019; Pucci et al., 2020) to observe if and how the smooth muscle tone affects the relationships between arterial waveforms (e.g., PD-loop).

The pressure-normalisation method for local wave speed used in Chapters 5 and 6 is based on the assumption of the existence of an exponential pressure-area relationship. While this assumption is strongly supported by empirical evidence, future studies should aim to experimentally validate the normalisation technique by inducing acute changes in BP in a cohort of individuals and comparing predicted and measured changes in c. It is worth considering, however, that BP-lowering drugs (Shirai et al., 2011) and manoeuvers (Faconti et al., 2019; Pucci et al., 2020) often alter also the sympathetic activity and, hence, the muscular tone of elastic arteries, thus possibly affecting arterial stiffness independently of BP. Therefore, while these studies are relatively easy to conceive, in practice it is hard to ensure that observed changes in c are entirely attributable to BP. Alternatively, the validity of the proposed technique could be validated *ex vivo* using animal aortae connected to a mock circulatory loop where pressure can be easily controlled by controlling components in the system (Li et al., 2021).

The study described in Chapter 7 was conceived as a proof-of-concept, proposing a novel technique for the non-invasive determination of pressure in arteries from ultrasound data. As acknowledged in the limitations, the technique was validated against pressure acquired via tonometry, which is a well-established technique but requires calibration using unreliable

peripheral SBP and DBP measures. Therefore, future studies should investigate the effectiveness of the proposed pressure-estimation method against invasively measured pressure. Furthermore, the ultimate goal of the proposed technique is to provide an alternative to TF methods for the estimation of pressure in the aorta. Future studies should investigate the effectiveness of the technique in estimating aortic pressure (Giudici et al., 2020). Finally, the method was developed to address the limited ability of TF techniques to predict the shape and high frequencies of the aortic pressure waveform. Therefore, the added value of an enhanced determination of these features to predict cardiovascular risk should be evaluated.

Appendix

A1 The relationship between $\mathscr{C}_{\theta\theta\theta\theta}$ and $\mathscr{K}_{\theta\theta\theta\theta}$

The tangential elastic modulus $\mathscr{K}_{\theta\theta\theta\theta}$ is defined as

$$\mathscr{K}_{\theta\theta\theta\theta} = \frac{\partial t_{\theta\theta}}{\partial \epsilon_{\theta\theta}} \ . \tag{A1}$$

Considering that $\epsilon_{\theta\theta} = \lambda_\theta - 1$, Eq. A1 can be rewritten as

$$\mathscr{K}_{\theta\theta\theta\theta} = \frac{\partial t_{\theta\theta}}{\partial \lambda_\theta} \ , \tag{A2}$$

Then, knowing that

$$\partial \lambda_\theta^2 = \frac{\partial \lambda_\theta}{\partial \lambda_\theta} \partial \lambda_\theta^2 = 2\lambda_\theta \partial \lambda_\theta \ , \tag{A3}$$

Eq. A2 becomes Considering that $\epsilon_{\theta\theta} = \lambda_\theta - 1$, Eq. A1 can be rewritten as

$$\mathscr{K}_{\theta\theta\theta\theta} = 2\lambda_\theta \frac{\partial t_{\theta\theta}}{\partial \lambda_\theta^2} \ , \tag{A4}$$

Supposing that the wall behaviour is determined by a SEF Ψ, the circumferential Cauchy stress is

$$t_{\theta\theta} = -p + 2\lambda_\theta^2 \frac{\partial \Psi}{\partial \lambda_\theta^2} \ , \tag{A5}$$

so that

$$\mathscr{K}_{\theta\theta\theta\theta} = 2\lambda_\theta \frac{\partial}{\partial \lambda_\theta^2} \left(2\lambda_\theta^2 \frac{\partial \Psi}{\partial \lambda_\theta^2} \right) = 2\lambda_\theta \left[\frac{\partial \Psi}{\partial \lambda_\theta^2} + 2\lambda_\theta^2 \frac{\partial^2 \Psi}{(\partial \lambda_\theta^2)^2} \right] \ . \tag{A6}$$

Using Eq. A5, Eq. A6 can be reformulated as

$$\mathscr{K}_{\theta\theta\theta\theta} = \frac{1}{\lambda_\theta} \left[(t_{\theta\theta} + p) + 4\lambda_\theta^4 \frac{\partial^2 \Psi}{(\partial \lambda_\theta^2)^2} \right] \ . \tag{A7}$$

Finally, the small-on-large circumferential stiffness $\mathscr{C}_{\theta\theta\theta\theta}$ (Baek et al., 2007) is defined as

$$\mathscr{C}_{\theta\theta\theta\theta} = 2\left(t_{\theta\theta} + p\right) + 4\lambda_\theta^4 \frac{\partial^2 \Psi}{\partial \left(\lambda_\theta^2\right)^2} \ , \tag{A8}$$

and using Eq. A7

$$\mathscr{C}_{\theta\theta\theta\theta} = \lambda_\theta \mathscr{K}_{\theta\theta\theta\theta} \ . \tag{A9}$$

A2 Supplementary tables

Table A1: *HGO-SEF intact wall and layer-specific parameters of the ascending aortae of the lambs included in this study.*

	Ascending aorta - Lambs					
Sample number	μ [kPa]	k_1 [kPa]	k_2 [-]	α [°]	τ [-]	R^2
Wall I	6.54	51.22	0.00	36.62	0.18	0.99
Wall II	12.24	46.79	4.10	31.36	0.24	1.00
Wall III	5.85	34.17	0.03	32.10	0.17	0.99
Wall IV	5.63	45.65	0.13	36.38	0.21	0.99
Wall V	6.83	48.48	0.60	37.10	0.22	0.99
Wall VI	5.58	39.01	0.19	34.13	0.20	0.99
Wall VII	7.12	43.65	0.43	39.36	0.21	0.98
Wall VIII	12.24	46.62	5.07	30.61	0.29	1.00
Wall IX	3.19	32.24	0.14	30.61	0.20	0.99
Wall X	9.30	36.59	3.44	49.24	0.31	0.97
Intima I	26.33	51.53	1.31	38.63	0.21	0.99
Intima II	27.22	50.40	3.40	47.31	0.30	1.00
Intima III	17.06	47.94	0.17	38.29	0.19	0.99
Intima IV	32.67	87.52	1.08	40.30	0.27	1.00
Intima V	17.34	42.01	0.73	35.58	0.22	1.00
Intima VI	22.58	55.89	0.29	28.05	0.31	1.00
Intima VII	16.59	54.45	0.78	32.73	0.23	1.00
Intima VIII	25.41	75.43	0.03	52.37	0.27	1.00
Intima IX	9.48	47.99	0.17	34.93	0.17	0.99
Intima X	27.15	55.95	4.13	58.91	0.31	1.00
Media I	11.46	59.42	0.05	31.69	0.27	0.99
Media II	12.38	48.89	0.42	26.08	0.28	1.00
Media III	9.46	55.49	0.00	38.27	0.19	0.98
Media IV	10.22	54.06	0.58	34.81	0.24	1.00
Media V	6.14	46.21	0.04	35.25	0.20	0.99
Media VI	8.49	35.45	0.05	34.70	0.17	1.00
Media VII	6.31	22.70	0.12	30.74	0.16	1.00
Media VIII	11.84	52.75	0.13	37.28	0.26	1.00
Media IX	6.90	42.58	0.15	30.14	0.25	0.98
Media X	11.07	33.93	1.80	53.99	0.31	0.99
Adventitia I	7.35	54.77	6.27	41.71	0.26	0.96
Adventitia II	6.91	54.77	6.27	41.71	0.26	0.99
Adventitia III	7.00	17.81	5.06	25.24	0.24	0.99
Adventitia IV	6.23	33.70	3.60	20.44	0.29	1.00
Adventitia V	7.14	35.81	1.73	27.00	0.25	0.99
Adventitia VI	7.45	24.42	4.64	24.98	0.28	1.00
Adventitia VII	4.38	17.78	3.03	10.68	0.27	0.99
Adventitia VIII	5.52	29.37	4.40	15.39	0.29	0.99
Adventitia IX	5.30	25.52	2.11	9.45	0.29	0.99
Adventitia X	4.92	5.63	4.78	8.06	0.28	0.98

Table A2: *HGO-SEF intact wall and layer-specific parameters of the upper thoracic aortae of the lambs included in this study.*

Upper thoracic aorta - Lambs							
	Sample number	μ [kPa]	k_1 [kPa]	k_2 [-]	α [°]	τ [-]	R^2
Wall	I	14.18	57.70	5.27	63.22	0.31	0.98
	II	8.80	39.87	1.43	35.76	0.22	0.99
	III	15.53	53.32	5.31	49.18	0.30	0.99
	IV	6.97	77.60	1.21	18.14	0.27	0.97
	V	9.20	70.70	0.13	40.84	0.23	0.98
	VI	15.62	163.88	0.00	61.28	0.32	0.93
	VII	12.11	16.37	4.08	45.87	0.14	0.97
	VIII	7.91	36.22	2.17	47.45	0.29	0.97
	IX	3.53	31.95	0.25	35.90	0.22	0.98
	X	10.25	21.70	2.83	33.55	0.31	0.99
Intima	I	13.51	64.91	0.00	35.77	0.17	0.98
	II	16.27	61.58	0.00	41.21	0.18	0.97
	III	16.00	69.50	0.12	38.93	0.20	0.98
	IV	11.36	95.20	0.00	36.07	0.21	0.98
	V	16.81	51.77	0.00	38.17	0.17	0.99
	VI	13.97	82.87	0.00	39.78	0.18	0.96
	VII	27.11	75.23	0.75	40.80	0.27	0.99
	VIII	16.00	69.50	0.12	38.93	0.20	0.98
	IX	9.65	66.07	0.00	40.11	0.20	0.96
	X	18.17	59.66	0.19	39.53	0.23	0.99
Media	I	7.36	66.27	0.44	41.76	0.26	0.96
	II	10.70	48.90	0.17	40.70	0.24	0.99
	III	8.75	62.65	0.81	37.00	0.21	0.97
	IV	7.99	34.11	0.30	24.47	0.22	1.00
	V	9.65	46.70	0.00	38.14	0.18	0.99
	VI	11.77	46.51	0.00	36.31	0.15	0.99
	VII	7.82	30.35	0.20	21.15	0.22	1.00
	VIII	4.68	34.81	0.00	29.26	0.22	0.99
	IX	5.17	27.86	0.27	8.22	0.29	1.00
	X	11.17	39.21	0.38	44.65	0.29	0.99
Adventitia	I	11.24	49.07	5.50	47.86	0.24	0.97
	II	8.70	7.72	13.63	29.05	0.22	0.99
	III	9.23	17.07	10.39	25.40	0.30	1.00
	IV	6.13	30.08	5.21	33.04	0.30	0.99
	V	18.16	19.95	8.57	57.27	0.24	0.99
	VI	13.01	2.96	10.47	48.28	0.10	0.93
	VII	8.59	16.70	11.02	45.99	0.30	0.98
	VIII	5.99	19.49	10.61	31.63	0.30	0.99
	IX	9.73	2.31	3.54	33.63	0.14	0.98
	X	2.33	30.87	14.79	50.91	0.29	0.99

Table A3: *HGO-SEF intact wall and layer-specific parameters of the lower thoracic aortae of the lambs included in this study.*

	Lower thoracic aorta - Lambs						
	Sample number	μ [kPa]	k_1 [kPa]	k_2 [-]	α [°]	τ [-]	R^2
Wall	I	10.44	151.89	0.00	44.57	0.27	0.91
	II	9.18	98.35	0.63	34.84	0.22	0.98
	III	9.15	55.42	1.25	40.52	0.20	0.97
	IV	13.08	52.52	8.44	44.07	0.21	0.96
	V	14.28	109.02	8.75	45.82	0.15	0.93
	VI	5.97	180.31	0.02	40.93	0.22	0.92
	VII	15.22	119.61	9.04	41.28	0.16	0.93
	VIII	15.41	3.06	10.38	51.84	0.05	0.97
	IX	21.37	1.78	17.52	53.30	0.00	0.97
	X	12.38	44.09	3.73	45.97	0.15	0.95
Intima	I	18.21	51.02	0.00	32.82	0.10	0.99
	II	25.26	70.70	0.00	35.25	0.10	1.00
	III	19.36	46.84	1.59	25.21	0.25	0.99
	IV	16.30	91.53	0.00	32.99	0.17	0.99
	V	12.25	49.97	0.00	30.13	0.19	0.99
	VI	13.34	83.91	0.00	31.82	0.17	0.99
	VII	28.30	102.02	0.00	36.71	0.21	0.99
	VIII	8.78	73.31	0.00	39.56	0.22	0.97
	IX	13.61	71.22	0.27	40.18	0.23	0.98
	X	9.57	46.83	0.26	31.90	0.21	0.99
Media	I	11.32	37.50	0.09	33.99	0.18	1.00
	II	13.90	49.01	0.00	33.41	0.14	1.00
	III	10.54	47.91	0.03	32.86	0.18	0.99
	IV	8.68	31.68	0.53	29.30	0.21	1.00
	V	14.66	47.09	0.00	33.48	0.15	1.00
	VI	11.77	54.74	0.27	32.33	0.18	1.00
	VII	14.06	67.19	0.28	35.17	0.22	1.00
	VIII	7.58	34.52	0.43	38.50	0.20	0.99
	IX	7.05	38.74	0.03	35.37	0.18	0.99
	X	8.63	35.61	0.00	34.84	0.15	1.00
Adventitia	I	18.58	57.78	10.93	44.06	0.14	0.95
	II	5.48	44.58	4.27	22.98	0.26	0.98
	III	10.01	14.36	9.58	36.94	0.32	1.00
	IV	8.87	18.18	14.54	38.14	0.29	0.99
	V	11.48	16.06	15.27	45.51	0.24	0.97
	VI	13.44	2.87	22.61	48.77	0.15	0.97
	VII	10.00	9.31	22.87	42.73	0.27	1.00
	VIII	5.64	26.41	28.98	53.40	0.29	1.00
	IX	11.99	3.58	22.24	52.46	0.16	0.97
	X	5.89	11.69	14.72	38.97	0.29	1.00

Table A4: *HGO-SEF intact wall and layer-specific parameters of the ascending aortae of the pigs included in this study.*

	Ascending aorta - Pigs						
	Sample number	μ [kPa]	k_1 [kPa]	k_2 [-]	α [°]	τ [-]	R^2
Wall	I	-	-	-	-	-	-
	II	20.16	159.09	3.19	39.41	0.21	0.99
	III	24.00	140.86	3.78	40.22	0.23	1.00
	IV	24.91	102.24	2.81	42.68	0.27	1.00
	V	14.59	96.19	4.63	32.62	0.26	1.00
	VI	23.01	145.93	11.00	36.53	0.23	1.00
	VII	20.74	115.43	8.42	33.68	0.24	1.00
	VIII	18.33	86.28	6.34	31.68	0.25	1.00
	IX	23.73	127.80	4.25	37.20	0.22	1.00
	X	22.55	95.45	3.32	35.15	0.25	1.00
Intima	I	-	-	-	-	-	-
	II	26.95	60.83	2.59	51.17	0.18	0.99
	III	34.66	78.57	4.74	49.68	0.28	1.00
	IV	26.82	88.21	1.80	54.03	0.29	1.00
	V	22.08	49.21	6.07	32.50	0.29	1.00
	VI	16.38	144.37	1.87	44.87	0.30	0.99
	VII	28.08	127.65	0.00	50.30	0.24	1.00
	VIII	25.79	95.51	0.00	54.38	0.27	1.00
	IX	37.51	136.22	0.86	45.38	0.27	1.00
	X	31.73	96.28	0.95	39.93	0.28	1.00
Media	I	-	-	-	-	-	-
	II	27.04	145.43	1.22	35.10	0.24	1.00
	III	25.53	120.67	2.36	41.67	0.25	1.00
	IV	22.99	107.82	0.91	44.96	0.27	1.00
	V	14.94	85.15	2.24	30.49	0.25	1.00
	VI	25.00	143.39	4.57	34.95	0.22	1.00
	VII	22.08	111.47	4.99	32.14	0.25	1.00
	VIII	13.41	87.78	2.56	31.26	0.24	1.00
	IX	24.74	129.26	2.59	33.91	0.24	1.00
	X	21.04	93.20	0.77	32.10	0.24	1.00
Adventitia	I	-	-	-	-	-	-
	II	11.95	44.65	9.59	26.53	0.28	1.00
	III	14.91	79.36	4.01	26.71	0.25	1.00
	IV	18.32	100.04	1.75	43.91	0.26	0.99
	V	8.13	43.68	4.54	22.60	0.25	0.99
	VI	13.18	71.99	10.23	23.88	0.26	1.00
	VII	10.01	103.42	8.76	28.90	0.24	1.00
	VIII	9.35	56.84	8.10	24.38	0.28	1.00
	IX	11.33	127.58	2.24	29.56	0.23	0.99
	X	8.91	109.69	2.82	33.80	0.23	0.99

Table A5: *HGO-SEF intact wall and layer-specific parameters of the upper thoracic aortae of the pigs included in this study.*

	Upper thoracic aorta - Pigs						
	Sample number	μ [kPa]	k_1 [kPa]	k_2 [-]	α [°]	τ [-]	R^2
Wall	I	12.21	189.08	4.80	41.26	0.20	0.98
	II	22.18	157.01	10.20	42.26	0.22	0.99
	III	32.32	38.18	36.83	47.45	0.14	0.96
	IV	15.63	146.84	7.39	37.87	0.23	0.99
	V	18.73	90.58	21.75	48.82	0.27	0.97
	VI	26.97	156.44	26.24	45.65	0.21	0.99
	VII	19.30	132.51	15.98	40.75	0.23	1.00
	VIII	15.23	179.25	14.55	43.50	0.21	0.97
	IX	19.45	184.87	12.30	43.13	0.21	0.98
	X	28.70	103.91	21.09	44.24	0.25	0.99
Intima	I	29.56	62.43	12.23	41.24	0.25	0.99
	II	36.89	126.71	13.38	46.16	0.23	0.99
	III	34.17	81.89	19.49	43.29	0.26	0.99
	IV	25.50	86.30	6.72	37.07	0.26	0.99
	V	18.85	55.78	8.66	45.66	0.28	0.98
	VI	31.07	119.23	17.48	40.84	0.24	0.99
	VII	22.79	120.98	4.33	40.17	0.21	0.98
	VIII	22.79	120.98	4.33	32.95	0.23	1.00
	IX	26.93	78.89	15.39	44.71	0.26	1.00
	X	20.91	125.28	11.04	30.41	0.23	1.00
Media	I	24.65	126.15	5.29	34.78	0.26	1.00
	II	20.11	176.60	2.84	37.42	0.21	1.00
	III	14.48	199.99	1.94	39.42	0.20	0.99
	IV	14.59	119.99	4.96	37.45	0.22	0.99
	V	11.48	135.62	1.28	36.04	0.23	0.99
	VI	19.77	200.36	7.71	40.34	0.21	1.00
	VII	21.80	103.44	6.51	27.04	0.26	1.00
	VIII	21.54	128.99	6.13	30.41	0.26	1.00
	IX	18.95	163.62	3.57	33.01	0.23	1.00
	X	36.02	107.97	18.15	30.10	0.22	1.00
Adventitia	I	18.40	82.57	30.90	45.36	0.24	0.96
	II	18.05	80.31	20.99	45.37	0.27	1.00
	III	24.03	45.80	41.32	51.14	0.24	0.98
	IV	10.61	92.13	17.49	39.23	0.23	0.98
	V	18.26	24.84	53.10	44.92	0.26	1.00
	VI	25.98	34.42	50.83	46.02	0.22	0.99
	VII	15.59	95.28	28.22	39.45	0.23	1.00
	VIII	17.33	51.53	48.31	46.06	0.22	0.96
	IX	27.28	84.41	28.61	47.52	0.25	0.99
	X	9.55	25.06	103.71	40.43	0.20	0.98

Table A6: *HGO-SEF intact wall and layer-specific parameters of the lower thoracic aortae of the pigs included in this study.*

	Lower thoracic aorta - Pigs						
	Sample number	μ [kPa]	k_1 [kPa]	k_2 [-]	α [°]	τ [-]	R^2
Wall	I	24.29	170.04	34.29	46.98	0.20	0.93
	II	-	-	-	-	-	-
	III	19.74	197.38	15.57	43.90	0.21	0.97
	IV	23.59	97.58	31.35	46.33	0.15	0.96
	V	6.50	188.11	20.46	43.33	0.22	0.95
	VI	15.59	300.18	45.54	42.97	0.18	0.97
	VII	10.57	232.25	16.56	39.70	0.20	0.97
	VIII	11.53	170.70	22.96	40.55	0.21	0.97
	IX	11.80	262.82	26.91	41.60	0.18	0.95
	X	23.47	212.88	83.83	45.52	0.16	0.96
Intima	I	24.05	100.49	22.15	45.84	0.25	0.97
	II	-	-	-	-	-	-
	III	26.61	128.92	14.77	41.72	0.22	0.96
	IV	16.88	98.90	2.57	38.33	0.22	0.98
	V	14.49	101.17	13.73	41.53	0.24	0.98
	VI	26.18	114.89	29.07	32.24	0.22	1.00
	VII	20.05	174.78	5.81	27.62	0.24	1.00
	VIII	20.83	153.24	4.90	30.90	0.21	1.00
	IX	19.84	197.39	9.84	26.61	0.24	1.00
	X	20.91	125.28	11.04	30.41	0.23	1.00
Media	I	24.50	206.06	3.39	38.41	0.22	1.00
	II	-	-	-	-	-	-
	III	25.66	190.86	1.90	38.24	0.20	1.00
	IV	18.45	139.71	1.83	35.10	0.23	1.00
	V	17.52	123.72	6.55	26.47	0.27	1.00
	VI	44.02	146.77	33.86	32.84	0.21	1.00
	VII	27.17	135.19	9.00	27.36	0.23	1.00
	VIII	25.36	184.26	4.74	30.95	0.20	1.00
	IX	36.10	162.18	9.06	28.27	0.20	1.00
	X	36.02	107.97	18.15	30.10	0.22	1.00
Adventitia	I	7.81	262.93	45.87	42.65	0.24	0.91
	II	-	-	-	-	-	-
	III	19.79	139.99	46.34	49.50	0.25	0.98
	IV	23.44	37.75	46.33	43.98	0.26	1.00
	V	6.80	40.05	84.34	46.61	0.20	0.99
	VI	12.18	202.28	82.94	42.72	0.14	0.93
	VII	14.13	35.20	60.55	37.61	0.23	1.00
	VIII	5.32	53.97	96.79	40.42	0.18	0.99
	IX	12.47	15.93	80.49	39.03	0.22	1.00
	X	9.55	25.06	103.71	40.43	0.20	0.98

Table A7: *Inter-regional differences (AA=ascending aorta, UTA=upper thoracic aorta, and LTA=lower thoracic aorta) in the HGO-SEF parameters of the intact wall and isolated layers of the lamb aorta. N.S.=non-significant, Rm-ANOVA=repeated measures analysis of variance.*

		Lambs			
	Parameter	Rm-ANOVA	AA-UTA	AA-LTA	UTA-LTA
Wall	μ	N.S.	-	-	-
	k_1	N.S.	-	-	-
	k_2	N.S.	-	-	-
	α	N.S.	-	-	-
	τ	p<0.01	N.S.	N.S.	p<0.05
Intima	μ	N.S.	-	-	-
	k_1	p<0.05	p<0.001	N.S.	N.S.
	k_2	N.S.	-	-	-
	α	p<0.05	N.S.	N.S.	p<0.05
	τ	N.S.	-	-	-
Media	μ	N.S.	-	-	-
	k_1	N.S.	-	-	-
	k_2	N.S.	-	-	-
	α	N.S.	-	-	-
	τ	N.S.	-	-	-
Adventitia	μ	p<0.05	N.S.	p<0.05	N.S.
	k_1	N.S.	-	-	-
	k_2	p<0.01	p<0.01	p<0.01	N.S.
	α	p<0.001	p<0.01	p<0.001	N.S.
	τ	N.S.	-	-	-

Table A8: *Inter-regional differences (AA=ascending aorta, UTA=upper thoracic aorta, and LTA=lower thoracic aorta) in the HGO-SEF parameters of the intact wall and isolated layers of the pig aorta. N.S.=non-significant, Rm-ANOVA=repeated measures analysis of variance.*

		Pigs			
	Parameter	Rm-ANOVA	AA-UTA	AA-LTA	UTA-LTA
Wall	μ	p<0.01	N.S.	p<0.05	N.S.
	k_1	p<0.001	N.S.	p<0.01	N.S.
	k_2	p<0.05	p<0.05	p<0.05	N.S.-
	α	p<0.001	p<0.05	p<0.001	N.S.
	τ	p<0.01	N.S.	p<0.01	N.S.
Intima	μ	N.S.	-	-	-
	k_1	p<0.05	N.S.	p<0.05	N.S.
	k_2	p<0.001	p<0.01	p<0.05	N.S.
	α	p<0.01	N.S.	p<0.05	N.S.
	τ	p<0.001	p<0.05	p<0.01	N.S.
Media	μ	N.S.	-	-	-
	k_1	p<0.01	p<0.05	p<0.05	N.S.
	k_2	N.S.	-	-	-
	α	p<0.05	N.S.	p<0.05	N.S.
	τ	N.S.	-	-	-
Adventitia	μ	N.S.	-	-	-
	k_1	N.S.	-	-	-
	k_2	p<0.001	p<0.01	p<0.001	p<0.01
	α	p<0.01	p<0.05	p<0.01	N.S.
	τ	N.S.	-	-	-

Table A9: *Inter-layer differences in the HGO-SEF parameters of the three regions (AA=ascending aorta, UTA=upper thoracic aorta, and LTA=lower thoracic aorta) of the lamb aorta. N.S.=non-significant, Rm-ANOVA=repeated measures analysis of variance.*

		Lambs			
	Parameter	Rm-ANOVA	Intima-Media	Intima-Adventitia	Media-Adventitia
AA	μ	p<0.001	p<0.001	p<0.001	p<0.01
	k_1	p<0.001	p<0.05	p<0.001	p<0.001
	k_2	p<0.001	p<0.05	p<0.001	p<0.001
	α	p<0.001	N.S.	p<0.01	p<0.01
	τ	N.S.	-	-	-
UTA	μ	p<0.001	p<0.001	p<0.05	N.S.
	k_1	p<0.001	p<0.01	p<0.001	p<0.001
	k_2	p<0.001	N.S.	p<0.001	p<0.001
	α	N.S.	-	-	-
	τ	N.S.	-	-	-
LTA	μ	p<0.01	p<0.01	p<0.05	N.S.
	k_1	p<0.001	p<0.01	p<0.001	p<0.01
	k_2	p<0.001	N.S.	p<0.001	p<0.001
	α	p<0.001	N.S.	p<0.01	p<0.01
	τ	p<0.01	N.S.	p<0.05	p<0.05

Table A10: *Inter-layer differences in the HGO-SEF parameters of the three regions (AA=ascending aorta, UTA=upper thoracic aorta, and LTA=lower thoracic aorta) of the pig aorta. N.S.=non-significant, Rm-ANOVA=repeated measures analysis of variance.*

		Pigs			
	Parameter	Rm-ANOVA	Intima-Media	Intima-Adventitia	Media-Adventitia
AA	μ	p<0.001	N.S.	p<0.001	p<0.001
	k_1	p<0.05	N.S.	N.S.	p<0.05
	k_2	p<0.01	N.S.	p<0.05	p<0.01
	α	p<0.001	p<0.001	p<0.001	p<0.01
	τ	N.S.	-	-	-
UTA	μ	p<0.05	N.S.	p<0.01	N.S.
	k_1	p<0.001	p<0.05	p<0.05	p<0.01
	k_2	p<0.001	p<0.05	p<0.01	p<0.001
	α	p<0.001	p<0.05	p<0.05	p<0.001
	τ	N.S.	-	-	-
LTA	μ	p<0.001	p<0.05	p<0.01	p<0.01
	k_1	N.S.	-	-	-
	k_2	p<0.001	N.S.	p<0.001	p<0.001
	α	p<0.001	N.S.	p<0.001	p<0.001
	τ	N.S.	-	-	-

Table A11: *Comparison between local carotid wave speed (c) calculated using the sequential and simultaneous analysis protocol. SD: standard deviation.*

Subject	**Synchronous analysis**		**Sequential analysis**	**Difference**	
	Average	SD	Average	Absolute	%
I	4.05	0.38	4.13	0.07	1.78
II	6.06	0.95	5.64	-0.42	-6.98
III	4.04	0.24	3.96	-0.08	-1.93
IV	5.81	0.45	5.83	0.02	0.37
V	4.16	0.22	4.28	0.12	2.95
VI	7.10	0.81	6.97	-0.13	-1.89
VII	5.75	0.40	5.84	0.09	1.65
VIII	5.43	0.26	5.76	0.33	6.09
IX	6.16	0.28	6.19	0.07	1.20
X	4.16	0.31	4.05	-0.11	-2.68
XI	7.66	0.74	7.63	-0.03	-0.34
XII	9.08	0.77	9.05	-0.03	-0.28
XIII	6.18	0.62	6.33	0.15	2.39
XIV	5.92	0.25	5.87	-0.05	-0.78
XV	6.01	0.56	5.93	-0.08	-1.33
XVI	8.26	0.99	8.24	-0.01	-0.27
XVII	4.18	0.82	4.10	-0.08	-1.80
XVIII	6.63	0.37	6.31	-0.32	-4.77
XIX	6.12	1.03	6.09	-0.03	-0.46
XX	6.38	0.94	6.60	0.22	3.39
XXI	3.07	0.22	3.03	-0.04	-1.24
XXII	5.03	0.56	5.23	0.20	4.02
XXIII	5.95	0.26	6.19	0.24	4.02
XVI	5.03	0.11	5.00	-0.03	-0.57
XXIII	6.63	0.11	6.61	-0.02	-0.32
Aerage	**5.79**	**0.53**	**5.80**	**0.00**	**0.09**
SD	1.40	0.29	1.39	0.16	2.86

Table A12: *Comparison in viscous parameters between healthy controls ≥35 years, plain hypertensive, plain T2DM (N-T2DMs), and hypertensive T2DM (H-T2DMs) patients recruited in the hospital of Pisa. All diameter data acquisitions were performed with Aloka Prosound 10 (Hitachi). Data are presented as mean ± standard deviation and adjusted values as mean [95% confidence interval]. ANCOVA post-hoc pairwise comparisons: $^{**}p<0.01$ and $^{***}p<0.001$ with controls; $^{\dagger}p<0.05$ and $^{\dagger\dagger}p=0.059$ with hypertension.*

	Control	**Hypertension**	**N-T2DM**	**H-T2DM**
	N = 41	N = 20	N = 21	N = 89
ΔDs [%]	4.9±14.3	12.6±9.8 **	8.4±7.9	9.4±9.1
	3.5 [−2.3-9.3]	13.4 [7.4-19.5]	5.3 [−0.8-11.4]	10.6 [6.6-14.6]
H_{A} [mmHg mm]	0.40±0.41	1.10±1.24 **	0.45±0.30 †	0.85±0.86
	0.47 [0.02-0.90]	1.30 [0.85-1.76]	0.28 [−0.18-0.74]	0.82 [0.53-1.12]
H_{I} [-]	0.024±0.023	0.047±0.046 **	0.023±0.015 ††	0.038±0.027
	0.019 [0.004-0.035]	0.048 [0.032-0.064]	0.017 [0.001-0.033]	0.042 [0.031-0.052]
η [mmHg s/m]	178.8±204.3	466.1±559.5 **	207.2±173.3 †	324.6±338.9
	199.6 [13.2-385.7]	535.0 [342.8-727.2]	134.4 [−59.1-327.9]	317.2 [192.3-442.1]

A3 Supplementary figures

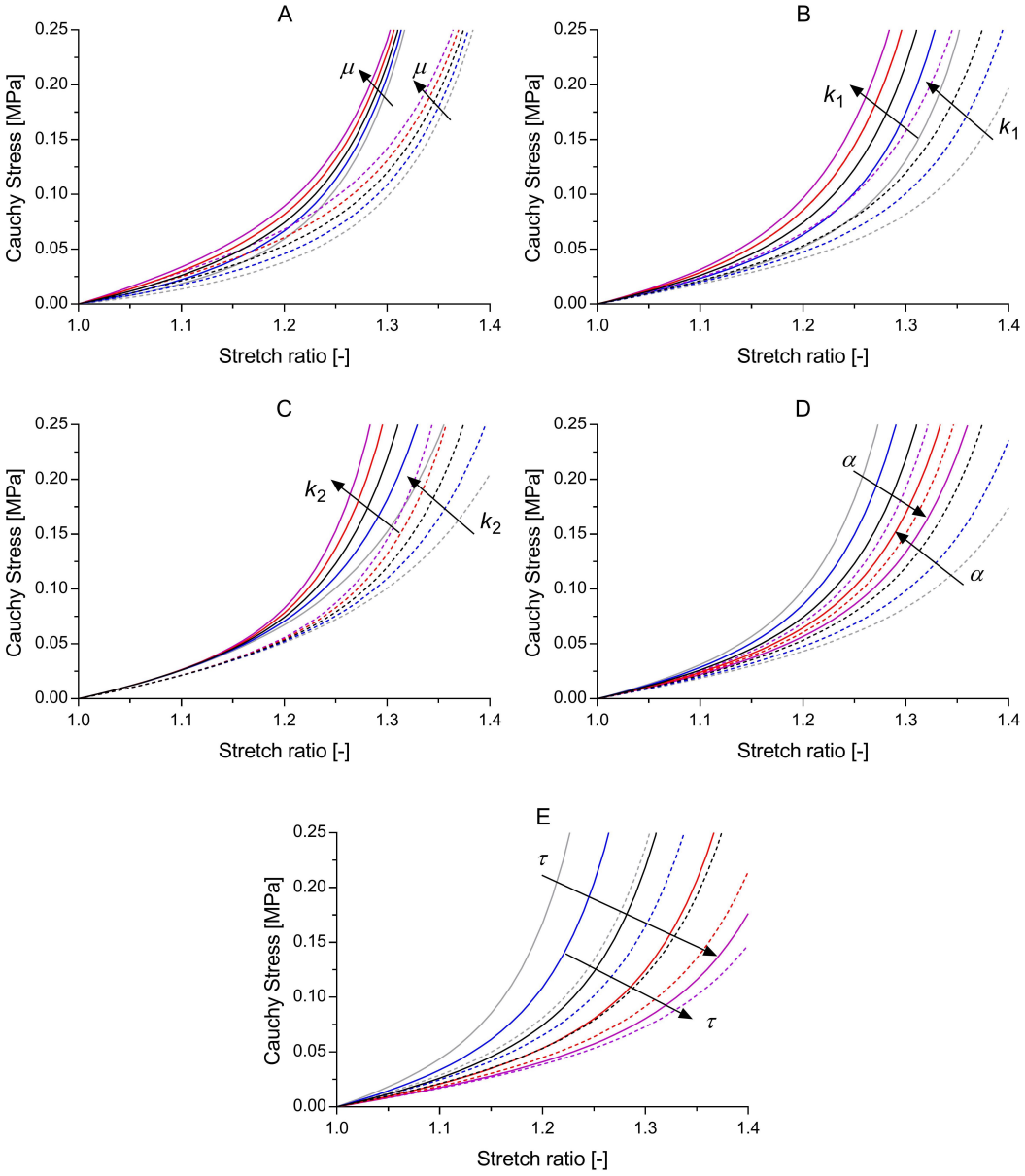

Figure A1: *Effect of changes in HGO-SEF model parameters on the modelled behaviour of the arterial wall. Black curves are equal in all five graphs and correspond to the behaviour of HGO-SEF when μ=20 kPa, k_1=125 kPa, k_2=20, α=40°, and τ=0.20. Coloured lines corresponds to varying of ±25% or ±50% one of the model parameters as indicated by the arrows (except for Panel D, where changes in α were ±10% or ±20%). Solid lines represent the results of a tensile test in the circumferential direction while holding the axial stretch constant at 1. Dashed lines represent the results of a tensile test in the axial direction while holding the circumferential stretch constant at 1.*

List of publications

Peer-reviewed journal publications

- Giudici, A.*, Palombo, C.*, Kozakova M., Morizzo C., Losso, L., Nannipieri, M., Berta, R., Hughes, A.D., Cruickshank, J.K., & Khir, A.W. (2020) Weight loss after bariatric surgery significantly improves carotid and cardiac function in apparently healthy people with morbid obesity. *Obesity Surgery*, *30*, 3776-3783.

- Giudici A., Wilkinson, I.B., & Khir, A.W. (2021). Review of the techniques used for investigating the role elastin and collagen play in arterial wall mechanics. *IEEE Reviews in Biomedical Engineering*, *14*, 256-269.

- Li*, Y., Giudici, A.*, Wilkinson, I.B., & Khir, A.W. (2021). Towards the non-invasive determination of arterial wall distensible properties: new approach using old formulae. *Journal of Biomechanics*, *115*, 110102.

- Giudici, A., Khir, A.W., Szafron, J.M. & Spronck, B. (2021). From uniaxial testing of isolated layers to a tri-layered arterial wall: A novel constitutive modelling framework. *Annals of Biomedical Engineering* (accepted).

- Giudici, A., Palombo, C., Kozakova, M., Morizzo, C., Penno, G., Jamagidze, G., Della Latta, D., Chiappino, D., Cruicshank, J.K.& Khir, A.W. (2021). Non-invasive Carotid Pressure-Diameter Loops to Identify Viscoelastic Properties in Ageing, Hypertension and Type 2 Diabetes. *Journal of Hypertension* (In press).

- Giudici, A., Palombo, C., Morizzo, C., Kozakova, M., Cruickshank, J.K., Wilkinson, I.B. & Khir, A.W. (2021). Transfer-function free technique for the non-invasive determination of the human arterial pressure waveform. *Physiological Reports* (In press).

- Giudici, A., Khir A.W., Reesink, K.D., Delhaas, T. & Spronck B. (2021). Five years of cardio-ankle vascular index and modified cardio-ankle vascular index: how close are we to a pressure-independent index of arterial stiffness? *Journal of Hypertension* (In press).

* Equal contribution

Conference papers

- Giudici, A., Hacham, W., & Khir, A.W. (2018). Theoretical and experimental reflection coefficients in flexible tubes as a function of the mach number. *IEEE Computing in Cardiology* (Maastricht, The Netherlands).

Conference proceedings - oral presentations

- Giudici, A., Palombo, C., Morizzo, C., Danieli, N., Losso, L., Della Latta, D., Kozakova, M., Chiappino, D., Cruickshank, J.K., & Khir, A.W. (2019). Evaluating carotid artery dynamics using pressure/diameter waveforms to determine stiffness and viscoelastic properties. *Journal of Hypertension*, *37*, e60-e61 (Milan, Italy).

- Giudici, A., Li, Y., Connolly, K., Cleary, S., McEniery, C., Yasmin, Wilkinson, I.B., & Khir, A.W. (2019). Aortic stiffness in healthy humans: effect of age *BioMedEng19*, September 2019 (London, UK).

- Giudici, A., Khir, A.W., & Spronck, B. (2020). Tri-layered constitutive modelling of the arterial wall based on layer-specific uniaxial testing: Novel insights into region-specific aortic mechanics. *ECCR* (Virtual conference).

- Giudici, A., Khir, A.W., & Spronck, B. (2020). Tri-layered constitutive modelling of the arterial wall: Evaluation of a new approach based on uniaxial testing of isolated layers. *Artery Research* (Virtual conference - presentation for the Artery19 Research Travel Grant).

- Giudici, A., Spronck, B., & Khir, A.W. (2021). Regional differences in aortic function: Tri-layered modelling of the pig aorta. *ESBiomech 2021* (Virtual conference).

Conference proceedings - poster presentations

- Giudici, A., Hacham, W., & Khir, A.W. (2018). Effect of Mach number on the reflection coefficient estimated by wave intensity analysis. *BioMedEng18* (London, UK).

- Hacham, W., Giudici, A., Khir, A.W.. Wave speed estimated by using PU-loop technique in the presence of continuous flow. *BioMedEng18* (London, UK).

- Giudici, A., Wilkinson, I.B., & Khir, A.W. (2018). Regional differences in layer-specific residual stresses in the bovine descending thoracic aorta. *Artery Research*, *24*(C), 127-128 (Guimarães, Portugal).

- Giudici, A., Palombo, C., Morizzo, C., Losso, L., & Khir, A.W. (2018). Low carotid arterial stiffness in young Type1 diabetic patients compared with age-matched controls. *Artery Research*, *24*(C):123 (Guimarães, Portugal).

- Giudici, A., Kozakova, M., Losso, L., Palombo, C., Cruickshank, J.K., & Khir, A.W. (2019). Restored physiological local carotid pulse wave velocity after bariatric surgery in obese subjects. *Artery Research*, *25*(S1), S67 (Budapest, Hungary).

- Giudici, A., Cretu, I., Negoita, M., Wilkinson, I.B., & Khir, A.W. (2020). A transfer-function-free technique for the non-invasive estimation of central arterial pressure. *Artery Research*, *26*(S1), S24 (Virtual conference).

Bibliography

Abdullateef, S., Mariscal-Harana, J., & Khir, A. W. (2020). Impact of tapering of arterial vessels on blood pressure, pulse wave velocity, and wave intensity analysis using one-dimensional computational model. *International Journal for Numerical Methods in Biomedical Engineering*, *18*, e3312.

Akhtar, R., Sherratt, M. J., Watson, R. E. B., Kundu, T., & Derby, B. (2009). Mapping the micromechanical properties of cryo-sectioned aortic tissue with scanning acoustic microscopy. *Materials Research Society symposia proceedings. Materials Research Society*, *1132E*(1132-Z03-07), ukpmcpa27262.

Alastrué, V., Peña, E., Martínez, M. A., & Doblaré, M. (2007). Assessing the use of the "opening angle method" to enforce residual stresses in patient-specific arteries. *Annals of biomedical engineering*, *35*(10), 1821–1837.

Alastruey, J. (2011). Numerical assessment of time-domain methods for the estimation of local arterial pulse wave speed. *Journal of Biomechanics*, *44*(5), 885–891.

Alford, P., Humphrey, J., & Taber, L. (2008). Growth and remodeling in a thick-walled artery model: effects of spatial variations in wall constituents. *Biomechanics and Modeling in Mechanobiology*, *7*(4), 245–262.

Angrisani, L., Santonicola, A., Iovino, P., Formisano, G., Buchwald, H., & Scopinaro, N. (2015). Bariatric Surgery Worldwide 2013. *Obesity Surgery*, *25*(10), 1822–1832.

Apter, J. T., Rabinowitz, M., & Cummings, D. H. (1966). Correlation of visco-elastic properties of large arteries with microscopic structure. *Circulation research*, *19*(1), 104–121.

Armentano, R., Megnien, J. L., Simon, A., Bellenfant, F., Barra, J., & Levenson, J. (1995a). Effects of Hypertension on Viscoelasticity of Carotid and Femoral Arteries in Humans. *Hypertension*, *26*(1), 48–54.

Armentano, R. L., Barra, J. G., Levenson, J., Simon, A., & Pichel, R. H. (1995b). Arterial Wall Mechanics in Conscious Dogs: Assessment of Viscous, Inertial, and Elastic Moduli to Characterize Aortic Wall Behavior. *Circulation research*, *76*(3), 468–478.

Armentano, R. L., Levenson, J., Barra, J. G., Fischer, E. I., Breitbart, G. J., Pichel, R. H., & Simon, A. (1991). Assessment of elastin and collagen contribution to aortic elasticity in conscious dogs. *AJP - Heart and Circulatory Physiology*, *260*(6), H1870–H1877.

Azinfar, L., Ravanfar, M., Wang, Y., Zhang, K., Duan, D., & Yao, G. (2017). High resolution imaging of the fibrous microstructure in bovine common carotid artery using optical polarization tractography. *Journal of Biophotonics*, *10*(2), 231–241.

Baek, S., Gleason, R. L., Rajagopal, K. R., & Humphrey, J. D. (2007). Theory of small on large: Potential utility in computations of fluid-solid interactions in arteries. *Computer Methods in Applied Mechanics and Engineering*, *196*(31-32), 3070–3078.

Balkestein, E. J., Van Aggel-Leijssen, D. P., Van Baak, M. A., Struijker-Boudier, H. A., & Van Bortel, L. M. (1999). The effect of weight loss with or without exercise training on large artery compliance in healthy obese men. *Journal of hypertension*, *17*(12), 1831–1835.

Bellini, C., Ferruzzi, J., Roccabianca, S., Di Martino, E. S., & Humphrey, J. D. (2014). A microstructurally motivated model of arterial wall mechanics with mechanobiological implications. *Annals of Biomedical Engineering*, *42*(3), 488–502.

Ben-Shlomo, Y., Spears, M., Boustred, C., May, M., Anderson, S. G., Benjamin, E. J., Boutouyrie, P., Cameron, J., Chen, C.-H., Cruickshank, J. K., Hwang, S.-J., Lakatta, E. G., Laurent, S., Maldonado, J., Mitchell, G. F., Najjar, S. S., Newman, A. B., Ohishi, M., Pannier, B., Pereira, T., Vasan, R. S., Shokawa, T., Sutton-Tyrell, K., Verbeke, F., Wang, K.-L., Webb, D. J., Hansen, T. W., Zoungas, S., McEniery, C. M., Cockcroft, J. R., & Wilkinson, I. B. (2014). Aortic Pulse Wave Velocity Improves Cardiovascular Event Prediction. *Journal of the American College of Cardiology*, *63*(7), 636–646.

Bergel, D. H. (1961). The dynamic elastic properties of the arterial wall. *The Journal of physiology*, *156*(3), 458–469.

Beulen, B. W. A. M. M., Bijnens, N., Koutsouridis, G. G., Brands, P. J., Rutten, M. C. M., & Van de Vosse, F. N. (2011). Towards noninvasive blood pressure assessment in arteries by using ultrasound. *Ultrasound in Medicine and Biology*, *37*(5), 788–797.

Bezie, Y., Lacolley, P., Laurent, S., & Gabella, G. (1998a). Connection of Smooth Muscle Cells to Elastic Lamellae in Aorta of Spontaneously Hypertensive Rats. *Hypertension*, *32*(1), 166–169.

Bezie, Y., Lamaziere, J.-M. D., Laurent, S., Challande, P., Cunha, R. S., Bonnet, J., & Lacolley, P. (1998b). Fibronectin Expression and Aortic Wall Elastic Modulus in Spontaneously Hypertensive Rats. *Arteriosclerosis, Thrombosis, and Vascular Biology*, *18*(7), 1027–1034.

Bia, D., Aguirre, I., Zocalo, Y., Devera, L., Fischer, E. C., & Armentano, R. (2005). Regional Differences in Viscosity, Elasticity, and Wall Buffering Function in Systemic Arteries: Pulse Wave Analysis of the Arterial Pressure-Diameter Relationship. *Revista Espanola de Cardiologia (Internet)*, *58*(2), 167–174.

Bland, M. J., & Altman, D. G. (1986). Statistical methods for assessing agreement between two methods of clinical measurement. *The Lancet*, *327*(8476), 307–310.

Bloom, D. E., Cafiero, E., Jané-Llopis, E., Abrahams-Gessel, S., Bloom, L. R., Fathima, S., Feigl, A. B., Gaziano, T., Hamandi, A., Mowafi, M., Pandya, A., Prettner, K., Rosenberg, L., Seligman, B., Stein, A. Z., & Weinstein, C. (2011). The Global Economic Burden of Noncommunicable Diseases. (September).

Borlotti, A., Khir, A. W., Rietzschel, E. R., Buyzere, M. L. D., Vermeersch, S., & Segers, P. (2012). Noninvasive determination of local pulse wave velocity and wave intensity: changes with age and gender in the carotid and femoral arteries of healthy human. *Journal of Applied Physiology*, *113*(5), 727–735.

Borlotti, A., Li, Y., Parker, K. H., & Khir, A. W. (2014). Experimental evaluation of local wave speed in the presence of reflected waves. *Journal of biomechanics*, *47*(1), 87–95.

Boulesteix, T., Pena, A. M., Pagès, N., Godeau, G., Sauviat, M. P., Beaurepaire, E., & Schanne-Klein, M. C. (2006). Micrometer scale Ex Vivo multiphoton imaging of unstained arterial wall structure. *Cytometry Part A*, *69A*(1), 20–26.

Boutouyrie, P., Boumaza, S., Challande, P., Lacolley, P., & Laurent, S. (1998). Smooth muscle tone and arterial wall viscosity: An in vivo/in vitro study. *Hypertension*, *32*(2), 360–364.

Boutouyrie, P., Tropeano, A. I., Asmar, R., Gautier, I., Benetos, A., Lacolley, P., & Laurent, S. (2002). Aortic stiffness is an independent predictor of primary coronary events in hypertensive patients: A longitudinal study. *Hypertension*, *39*(1), 10–15.

Bramwell, J. C., Hill, A. V., & McSwiney, B. A. (1923). The velocity of the pulse wave in man in relation to age as measured by the hot-wire sphygmograph. *Heart*, *10*, 233–255.

British Heart Foundation (2020). Heart statistics - Heart and Circulatory Diseases in the UK - BHF.

Burton, A. C. (1954). Relation of structure to function of the tissues of the wall of blood vessels. *Physiological reviews*, *34*(4), 619–642.

Bussy, C., Boutouyrie, P., Lacolley, P., Challande, P., & Laurent, S. (2000). Intrinsic stiffness of the carotid arterial wall material in essential hypertensives. *Hypertension*, *35*(5), 1049–1054.

Butcher, H. R. J. (1960). The elastic properties of human aortic intima, media and adventitia:Â the initial effect of thromboendarterectomy'. *Annals of Surgery*, *151*, 480–489.

Canham, P. B., Finlay, H. M., Dixon, J. G., Boughner, D. R., & Chen, A. (1989). Measurements from light and polarised light microscopy of human coronary arteries fixed at distending pressure. *Cardiovascular research*, *23*(11), 973–982.

Carew, T. E., Vaishnav, R. N., & Patel, D. J. (1968). Compressibility of the arterial wall. *Circulation research*, *23*(1), 61.

Cavinato, C., Helfenstein-Didier, C., Olivier, T., Rolland du Roscoat, S., Laroche, N., & Badel, P. (2017). Biaxial loading of arterial tissues with 3D in situ observations of adventitia fibrous microstructure: A

method coupling multi-photon confocal microscopy and bulge inflation test. *Journal of the mechanical behavior of biomedical materials*, *74*, 488–498.

Chen, C. H., Ting, C. T., Nussbacher, A., Nevo, E., Kass, D. A., Pak, P., Wang, S. P., Chang, M. S., & Yin, F. C. (1996). Validation of carotid artery tonometry as a means of estimating augmentation index of ascending aortic pressure. *Hypertension*, *27*(2), 168–175.

Chen, H., Liu, Y., Slipchenko, M. N., Zhao, X., Cheng, J.-X., & Kassab, G. S. (2011). The layered structure of coronary adventitia under mechanical load. *Biophysical Journal*, *101*(11), 2555–2562.

Chen, H., Slipchenko, M. N., Liu, Y., Zhao, X., Cheng, J.-X., Kassab, G. S., & Lanir, Y. (2013). Biaxial deformation of collagen and elastin fibers in coronary adventitia. *Journal of applied physiology*, *115*(11), 1683–1693.

Cheng, H. M., Chuang, S. Y., Sung, S. H., Yu, W. C., Pearson, A., Lakatta, E. G., Pan, W. H., & Chen, C. H. (2013). Derivation and validation of diagnostic thresholds for central blood pressure measurements based on long-term cardiovascular risks. *Journal of the American College of Cardiology*, *62*(19), 1780–1787.

Cheng, H. M., Sung, S. H., Shih, Y. T., Chuang, S. Y., Yu, W. C., & Chen, C. H. (2012). Measurement of central aortic pulse pressure: Noninvasive brachial cuff-based estimation by a transfer function vs. a novel pulse wave analysis method. *American Journal of Hypertension*, *25*(11), 1162–1169.

Chiesa, S. T., Masi, S., Shipley, M. J., Ellins, E. A., Fraser, A. G., Hughes, A. D., Patel, R. S., Khir, A. W., Halcox, J. P., Singh-Manoux, A., Kivimaki, M., Celermajer, D. S., & Deanfield, J. E. (2019). Carotid artery wave intensity in mid- to late-life predicts cognitive decline: the Whitehall II study. *European Heart Journal*, *40*(28), 2300–2309.

Chirinos, J. A., Segers, P., Gillebert, T. C., De Buyzere, M. L., Van Daele, C. M., Khan, Z. A., Khawar, U., De Bacquer, D., & Rietzschel, E. R. (2013). Central pulse pressure and its hemodynamic determinants in middle-aged adults with impaired fasting glucose and diabetes: The asklepios study. *Diabetes Care*, *36*(8), 2359–2365.

Chow, M.-J., Turcotte, R., Lin, C. P., & Zhang, Y. (2014). Arterial extracellular matrix: a mechanobiological study of the contributions and interactions of elastin and collagen. *Biophysical Journal*, *106*(12), 2684–2692.

Chuong, C. J., & Fung, Y. C. (1984). Compressibility and constitutive equation of arterial wall in radial compression experiments. *Journal of Biomechanics*, *17*(1), 35–40.

Chuong, C. J., & Fung, Y. C. (1986). On residual stresses in arteries. *Journal of Biomechanical Engineering*, *108*(2), 189–192.

Clark, J., & Glagov, S. (1985). Transmural organization of the arterial media: the lamellar unit revisited. *Arteriosclerosis, Thrombosis, and Vascular Biology*, *5*(1), 19–34.

Cohuet, G., Challande, P., Osborne-Pellegrin, M., Arribas, S. M., Dominiczak, A., Louis, H., Laurent, S., & Lacolley, P. (2001). Mechanical Strength of the Isolated Carotid Artery in SHR. *Hypertension*, *38*(5), 1167–1171.

Cooper, J. N., Buchanich, J. M., Youk, A., Brooks, M. M., Barinas-Mitchell, E., Conroy, M. B., & Sutton-Tyrrell, K. (2012). Reductions in arterial stiffness with weight loss in overweight and obese young adults: Potential mechanisms. *Atherosclerosis*, *223*(2), 485–490.

Costello, B. T., Schultz, M. G., Black, J. A., & Sharman, J. E. (2015). Evaluation of a brachial cuff and suprasystolic waveform algorithm method to noninvasively derive central blood pressure. *American Journal of Hypertension*, *28*(4), 480–486.

Cox, R. H. (1972). A model for the dynamic mechanical properties of arteries. *Journal of Biomechanics*, *5*(2), 135–152.

Cox, R. H. (1977). Effects of age on the mechanical properties of rat carotid artery. *The American Journal of Physiology*, *233*(2), H256–H263.

Cox, R. H. (1978). Passive mechanics and connective tissue composition of canine arteries. *The American Physiology Society*, *234*(5), H533–H541.

Cox, R. H. (1982). Comparison of mechanical and chemical properties of extra- and intralobar canine pulmonary arteries. *AJP - Heart and Circulatory Physiology*, *242*(2), H245–H253.

Cruickshank, J. K., Riste, L., Anderson, S. G., Wright, J. S., Dunn, G., & Gosling, R. G. (2002). Aortic Pulse-Wave Velocity and Its Relationship to Mortality in Diabetes and Glucose Intolerance: An Integrated Index of Vascular Function? *Circulation*, *106*(16), 2085–2090.

Dart, A. M., Gatzka, C. D., Kingwell, B. A., Willson, K., Cameron, J. D., Liang, Y. L., Berry, K. L., Wing, L. M., Reid, C. M., Ryan, P., Beilin, L. J., Jennings, G. L., Johnston, C. I., McNeil, J. J., MacDonald, G. J., Morgan, T. O., & West, M. J. (2006). Brachial blood pressure but not carotid arterial waveforms predict cardiovascular events in elderly female hypertensives. *Hypertension*, *47*(4), 785–790.

Davies, J. E., Whinnett, Z. I., Francis, D. P., Willson, K., Foale, R. A., Malik, I. S., Hughes, A. D., Parker, K. H., & Mayet, J. (2005). Use of simultaneous pressure and velocity measurements to estimate arterial wave speed at a single site in humans. *American Journal of Physiology: Heart Circulation Physiology*, *290*, H878–H885.

de Lucio, M., García, M. F., García, J. D., Rodríguez, L. E. R., & Marcos, F. Ã. (2020). On the importance of tunica intima in the aging aorta: a three-layered in silico model for computing wall stresses in abdominal aortic aneurysms. *Computer Methods in Biomechanics and Biomedical Engineering*, *22*, 1–18.

Deplano, V., Boufi, M., Boiron, O., Guivier-Curien, C., Alimi, Y., & Bertrand, E. (2016). Biaxial tensile tests of the porcine ascending aorta. *Journal of biomechanics*, *49*, 2031–2037.

Desamericq, G., Tissot, C. M., Akakpo, S., Tropeano, A. I., Millasseau, S., & MacQuin-Mavier, I. (2015). Carotid-femoral pulse wave velocity is not increased in obesity. *American Journal of Hypertension*, *28*(4), 546–551.

Deveja, R. P., Iliopoulos, D. C., Kritharis, E. P., Angouras, D. C., Sfyris, D., Papadodima, S. A., & Sokolis, D. P. (2018). Effect of Aneurysm and Bicuspid Aortic Valve on Layer-Specific Ascending Aorta Mechanics. *Annals of Thoracic Surgery*, *106*(6), 1692–1701.

Di Lascio, N., Bruno, R., Stea, F., Bianchini, E., Gemignani, V., Ghiadoni, L., & Faita, F. (2014). Non-invasive assessment of carotid PWV via accelerometric sensors: validation of a new device and comparison with established techniques. *European Journal of Applied Physiology*, *114*(7), 1503–1512.

Díaz, C., Peña, J. A., Martínez, M. A., & Peña, E. (2021). Unraveling the multilayer mechanical response of aorta using layer-specific residual stresses and experimental properties. *Journal of the Mechanical Behavior of Biomedical Materials*, *113*, 104070.

Ding, F. H., Fan, W. X., Zhang, R. Y., Zhang, Q., Li, Y., & Wang, J. G. (2011). Validation of the noninvasive assessment of central blood pressure by the sphygmocor and omron devices against the invasive catheter measurement. *American Journal of Hypertension*, *24*(12), 1306–1311.

Dingemans, K. P., Teeling, P., Lagendijk, J. H., & Becker, A. E. (2000). Extracellular matrix of the human aortic media: an ultrastructural histochemical and immunohistochemical study of the adult aortic media. *The Anatomical record*, *258*(1), 1–14.

Dobrin, P. B. (1978). Mechanical properties of arteries. *Physiological Reviews*, *58*(2), 397–460.

Dobrin, P. B., & Canfield, T. R. (1984). Elastase, collagenase, and the biaxial elastic properties of dog carotid artery. *AJP - Heart and Circulatory Physiology*, *247*(1), H124–H131.

Dornhorst, A., Howard, P., & Leathart, G. (1952). Respiratory Variationsin Blood Pressure. *Circulation*, *VI*, 553–558.

Driessen, N. J. B., Wilson, W., Bouten, C. V. C., & Baaijens, F. P. T. (2004). A computational model for collagen fibre remodelling in the arterial wall. *Journal of Theoretical Biology*, *226*(1), 53–64.

Du Bois, D., & Du Bois, E. (1915). The measurement of the surface area of man. *Arch Intern Med*, *15*, 868–881.

Duprey, A., Khanafer, K., Schlicht, M., Avril, S., Williams, D., & Berguer, R. (2010). In Vitro Characterisation of Physiological and Maximum Elastic Modulus of Ascending Thoracic Aortic Aneurysms Using Uniaxial Tensile Testing. *European Journal of Vascular & Endovascular Surgery*, *39*(6), 700–707.

Euler, L. (1775). Principia pro motu sanguinis per arterias determinando. *Opera postuma mathematica et physica anno 1844 detecta*, *2*, 814–823.

Faconti, L., Farukh, B., McNally, R., Webb, A., & Chowienczyk, P. (2019). Arterial Stiffness Can Be Modulated by Pressure-Independent Mechanisms in Hypertension. *Journal of the American Heart Association*, *8*(15), e012601.

Farand, P., Garon, A., & Plante, G. E. (2007). Structure of large arteries: Orientation of elastin in rabbit aortic internal elastic lamina and in the elastic lamellae of aortic media. *Microvascular Research*, *73*(2), 95–99.

Fata, B., Carruthers, C. A., Gibson, G. A., Watkins, S. C., Gottlieb, D., Mayer, J. E., & Sacks, M. S. (2012). Regional biomechanical and microstructural alterations of the ovine main pulmonary artery during postnatal growth. *ASME 2012 Summer Bioengineering Conference*, (pp. 477–478).

Fata, B., Zhang, W., Amini, R., & Sacks, M. S. (2014). Insights into regional adaptations in the growing pulmonary artery using a meso-scale structural model: Effects of ascending aorta impingement. *Journal of Biomechanical Engineering*, *136*(2), 021009.

Feng, J., & Khir, A. W. (2010). Determination of wave speed and wave separation in the arteries using diameter and velocity. *Journal of Biomechanics*, *43*(3), 455–462.

Ferruzzi, J., Achille, P. D., Tellides, G., & Humphrey, J. D. (2018). Combining in vivo and in vitro biomechanical data reveals key roles of perivascular tethering in central artery function. *PLoS ONE*, *13*(9), 1–21.

Fischer, G., & Llaurado, J. (1966). Collagen and Elastin Content in Canine Arteries Selected from Functionally Different Vascular Beds. *Circulation Research*, *19*(2), 394–399.

Flamini, V., Kerskens, C., Moerman, K. M., Simms, C. K., & Lally, C. (2010). Imaging arterial fibres using diffusion tensor imaging: feasibility study and preliminary results. *EURASIP Journal on Advances in Signal Processing*, *2010*(1), 1–13.

Flamini, V., Kerskens, C., Simms, C., & Lally, C. (2013). Fibre orientation of fresh and frozen porcine aorta determined non-invasively using diffusion tensor imaging. *Medical engineering & physics*, *35*(6), 765–776.

Fonck, E., Prod'hom, G., Roy, S., Augsburger, L., Rüfenacht, D. A., & Stergiopulos, N. (2007). Effect of elastin degradation on carotid wall mechanics as assessed by a constituent-based biomechanical model. *American Journal of Physiology - Heart and Circulatory Physiology*, *292*(6), 2754–2763.

Fung, Y. C. (1967). Elasticity of soft tissues in simple elongation. *The American journal of physiology*, *213*(6), 1532–1544.

Fung, Y. C., Fronek, K., & Patitucci, P. (1979). Pseudoelasticity of arteries and the choice of its mathematical expression. *The American journal of physiology*, *237*(5), H620–H631.

Galkine, A., Dzenkeviciute, V., Sapoka, V., Urbanavicius, V., Petrulioniene, Z., Brimas, G., & Laucevicius, A. (2018). Effects of body weight reduction on arterial stiffness and endothelial function after bariatric surgery in morbidly obese patients: A 4-year clinical study. *Acta Endocrinologica*, *14*(4), 491–497.

Gasser, T. C., Ogden, R. W., & Holzapfel, G. A. (2006). Hyperelastic modelling of arterial layers with distributed collagen fibre orientations. *Journal of the Royal Society Interface*, *3*, 15–35.

Gavish, B., & Izzo, J. L. (2016). Arterial Stiffness: Going a Step Beyond. *American Journal of Hypertension*, *29*(11), 1223–1233.

GBD 2015 Mortality and Causes of Death Collaborators (2016). Global, regional, and national life expectancy, all-cause mortality, and cause-specific mortality for 249 causes of death, 1980-2015: a systematic analysis for the Global Burden of Disease Study 2015. *The Lancet*, *388*(10053), 1459–1544.

Ghasemi, Z., Kim, C. S., Ginsberg, E., Gupta, A., & Hahn, J. O. (2017). Model-Based Blind System Identification Approach to Estimation of Central Aortic Blood Pressure Waveform from Noninvasive Diametric Circulatory Signals. *Journal of Dynamic Systems, Measurement and Control, Transactions of the ASME*, *139*(6), 1–10.

Giannattasio, C., Salvi, P., Valbusa, F., Kearney-Schwartz, A., Capra, A., Amigoni, M., Failla, M., Boffi, L., Madotto, F., Benetos, A., & Mancia, G. (2008). Simultaneous Measurement of Beat-to-Beat Carotid Diameter and Pressure Changes to Assess Arterial Mechanical Properties. *Hypertension*, *52*(5), 896–902.

Giudici, A., Cretu, I., Negoita, M., Wilkinson, I. B., & Khir, A. W. (2020). P.04 A Transfer-Function-Free Technique for the Non-Invasive Estimation of Central Arterial Pressure. *Artery Research*, *26*(Supplement 1), S24.

Gluszewska, A., Gryglewska, B., Gąsowski, J., Bilo, G., Zarzycki, B., Dzieża-Grudnik, A., Major, P., Budzyński, A., Faini, A., Parati, G., & Grodzicki, T. (2019). European journal of internal medicine. *European journal of internal medicine*, *60*, 39–45.

Graham, Akhtar, Kridiotis, Derby, Kundu, Trafford, & Sherratt (2011). Localised micro-mechanical stiffening in the ageing aorta. *Mechanism of Ageing and Developement*, *132*(10), 459–467.

Graham, H. K., Hodson, N. W., Hoyland, J. A., Millward-Sadler, S. J., Garrod, D., Scothern, A., Griffiths, C. E. M., Watson, R. E. B., Cox, T. R., Erler, J. T., Trafford, A. W., & Sherratt, M. J. (2010). Tissue section AFM: In situ ultrastructural imaging of native biomolecules. *Matrix Biology*, *29*(4), 254–260.

Greenwald, S. E. (2007). Ageing of the conduit arteries. *The Journal of Pathology*, *211*(2), 157–172.

Greenwald, S. E., Moore, J. J. E., Rachev, A., Kane, T. P. C., & Meister, J. J. (1997). Experimental investigation of the distribution of the residual strains in the arterial wall. *Transaction of the ASME*, *119*, 438–444.

Grillo, A., Salvati, P., Furlanis, G., Baldi, C., Rovina, M., Salvi, L., Faini, A., Bilo, G., Fabris, B., Carretta, R., Benetos, A., & Parati, G. (2020). Mean arterial pressure estimated by brachial pulse wave analysis and comparison with currently used algorithms. *Journal of Hypertension*, *38*(11), 2161–2168.

Gundiah, N., Babu, A. R., & Pruitt, L. A. (2013). Effects of elastase and collagenase on the nonlinearity and anisotropy of porcine aorta. *Physiological Measurement*, *34*, 1657–1673.

Gurven, M., Blackwell, A. D., Rodríguez, D. E., Stieglitz, J., & Kaplan, H. (2012). Does blood pressure inevitably rise with age?: Longitudinal evidence among forager-horticulturalists. *Hypertension*, *60*(1), 25–33.

Halloran, B. G., Davis, V. A., McManus, B. M., Lynch, T. G., & Baxter, B. T. (1995). Localization of aortic disease is associated with intrinsic differences in aortic structure. *Journal of Surgical Research*, *59*, 17–22.

Han, H. C., & Fung, Y. C. (1991). Species dependence of the zero-stress state of aorta: Pig versus rat. *Journal of Biomechanical Engineering*, *113*(4), 446–451.

Han, H. C., & Fung, Y. C. (1995). Longitudinal strain of canine and porcine aortas. *Journal of Biomechanics*, *28*(5), 637–641.

Harkness, M. L. R., Harkness, R. D., & McDonald, D. A. (1957). The collagen and elastin content of the arterial wall in the dog. *Proceedings of the Royal Society of London. Series B - Biological Sciences*, *146*(925), 541–551.

Harvey, A., Montezano, A. C., Lopes, R. A., Rios, F., & Touyz, R. M. (2016). Vascular fibrosis in aging and hypertension: molecular mechanisms and clinical implications. *Canadian Journal of Cardiology*, *32*(5), 659–668.

Haskett, D., Johnson, G., Zhou, A., Utzinger, U., & Vande Geest, J. (2010). Microstructural and biomechanical alterations of the human aorta as a function of age and location. *Biomechanics and Modeling in Mechanobiology*, *9*(6), 725–736.

Hawkins, D., Faler, B., Choi, Y., & Prasad, B. (2018). Time Course of Blood Pressure Decrease After Bariatric Surgery in Normotensive and Hypertensive Patients. *Obesity Surgery*, *28*(7), 1845–1851.

Hayashi, K., Handa, H., Nagasawa, S., Okumura, A., & Moritake, K. (1980). Stiffness and elastic behavior of human intracranial and extracranial arteries. *Journal of Biomechanics*, *13*(2), 175–184.

Hermeling, E., Hoeks, A. P. G., Winkens, M. H. M., Waltenberger, J. L., Reneman, R. S., Kroon, A. A., & Reesink, K. D. (2010). Noninvasive Assessment of Arterial Stiffness Should Discriminate Between Systolic and Diastolic Pressure Ranges. *Hypertension*, *55*(1), 124–130.

Hollander, Y., Durban, D., Lu, X., Kassab, G. S., & Lanir, Y. (2011a). Constitutive modeling of coronary arterial media-comparison of three model classes. *Journal of Biomechanical Engineering*, *133*(6), 061008.

Hollander, Y., Durban, D., Lu, X., Kassab, G. S., & Lanir, Y. (2011b). Experimentally validated microstructural 3D constitutive model of coronary arterial media. *Journal of Biomechanical Engineering*, *133*(3), 031007.

Holzapfel, G., Sommer, G., Auer, M., Regitnig, P., & Ogden, R. (2007). Layer-specific 3D residual deformations of human aortas with non-atherosclerotic intimal thickening. *Annals of Biomedical Engineering*, *35*(4), 530–545.

Holzapfel, G. A., Gasser, C. T., Sommer, G., & Regitnig, P. (2005). Determination of layer-specific mechanical properties of human coronary arteries with nonatherosclerotic intimal thickening and related constitutive modeling. *The American Journal of Physiology*, *289*(5), 2048–58.

Holzapfel, G. A., & Ogden, R. W. (2010a). Constitutive modelling of arteries. *The Royal Society Publishing*, *466*, 1551–1596.

Holzapfel, G. A., & Ogden, R. W. (2010b). Modelling the layer-specific three-dimensional residual stresses in arteries, with an application to the human aorta. *Journal of the Royal Society: Interface*, *7*, 787–799.

Holzapfel, G. A., Stadler, M., & Schulze-Bauer, C. A. (2002). A layer-specific three-dimensional model for the simulation of balloon angioplasty using magnetic resonance imaging and mechanical testing. *Annals of Biomedical Engineering*, *30*(6), 753–767.

Hubert, H. B., Feinleib, M., McNamara, P. M., & Castelli, W. P. (1983). Obesity as an independent risk factor for cardiovascular disease: a 26-year follow-up of participants in the Framingham Heart Study. *Circulation*, *67*(5), 968–977.

Humphrey, J., & Na, S. (2002). Elastodynamics and arterial wall stress. *Annals of Biomedical Engineering*, *30*(4), 509–523.

Humphrey, J. D., Eberth, J. F., Dye, W. W., & Gleason, R. L. (2009). Fundamental role of axial stress in compensatory adaptations by arteries. *Journal of biomechanics*, *42*, 1–8.

Jadidi, M., Habibnezhad, M., Anttila, E., Maleckis, K., Desyatova, A., MacTaggart, J., & Kamenskiy, A. (2020). Mechanical and structural changes in human thoracic aortas with age. *Acta Biomaterialia*, *103*, 172–188.

Jerius, H., Bagwell, C. A., Beall, A., Karolyi, D., & Brophy, C. (2000). Vascular smooth muscle mechanics in isolated perfused segments of carotid arteries. *Surgery*, *127*(2), 148–154.

Kawasaki, T., Sasayama, S., Yagi, S. I., Asakawa, T., & Hirai, T. (1987). Non-invasive assessment of the age related changes in stiffness of major branches of the human arteries. *Cardiovascular Research*, *21*(9), 678–687.

Khir, A. W., O'Brien, A., Gibbs, J. S. R., & Parker, K. H. (2001). Determination of wave speed and wave separation in the arteries. *Journal of Biomechanics*, *34*(9), 1145–1155.

Khir, A. W., & Parker, K. H. (2005). Wave intensity in the ascending aorta: effects of arterial occlusion. *Journal of Biomechanics*, *38*(4), 647–655.

Kim, J., & Baek, S. (2011). Circumferential variations of mechanical behavior of the porcine thoracic aorta during the inflation test. *Journal of Biomechanics*, *44*(10), 1941–1947.

Kohn, J. C., Lampi, M. C., & Reinhart-King, C. A. (2015). Age-related vascular stiffening: causes and consequences. *Frontiers in genetics*, *6*, 112.

Korotkoff, N. S. (1905). A contribution to the problem of methods for the determination of blood pressure. *Rep. Imp. Mil. Med. Acad.*, *11*, 365–367.

Kortweg, D. J. (1878). Uber die fortpflanzungsgeshwindigkeit des schalles in elastiischen rohren. *Ann Phys Chem*, *5*, 52–537.

Kozakova, M., Morizzo, C., Goncalves, I., Natali, A., Nilsson, J., & Palombo, C. (2019). Cardiovascular organ damage in type 2 diabetes mellitus: The role of lipids and inflammation. *Cardiovascular Diabetology*, *18*(1), 1–11.

Kozakova, M., Morizzo, C., La Carrubba, S., Fabiani, I., Della Latta, D., Jamagidze, J., Chiappino, D., Di Bello, V., & Palombo, C. (2017). Associations between common carotid artery diameter, Framingham risk score and cardiovascular events. *Nutrition, Metabolism and Cardiovascular Diseases*, *27*(4), 329–334.

Krasny, W., Magoariec, H., Morin, C., & Avril, S. (2017a). Kinematics of collagen fibers in carotid arteries under tension-inflation loading. *Journal of the mechanical behavior of biomedical materials*.

Krasny, W., Morin, C., Magoariec, H., & Avril, S. (2017b). A comprehensive study of layer-specific morphological changes in the microstructure of carotid arteries under uniaxial load. *Acta Biomaterialia*, *57*, 342–351.

Kroeker, E. J., & Wood, E. H. (1955). Comparison of simultaneously recorded central and peripheral arterial pressure pulses during rest, exercise and tilted position in man. *Circulation research*, *3*(6), 623–632.

Krug, J. W., Rose, G., Clifford, G. D., & Oster, J. (2013). ECG-based gating in ultra high field cardiovascular magnetic resonance using an independent component analysis approach. *Journal of Cardiovascular Magnetic Resonance*, *15*(1), 104.

Laugesen, E., Høyem, P., Stausbøl-Grøn, B., Mikkelsen, A., Thrysøe, S., Erlandsen, M., Christiansen, J. S., Knudsen, S. T., Hansen, K. W., Kim, W. Y., Hansen, T. K., & Poulsen, P. L. (2013). Carotid-femoral pulse wave velocity is associated with cerebral white matter lesions in type 2 diabetes. *Diabetes Care*, *36*(3), 722–728.

Laugesen, E., Rossen, N. B., Peters, C. D., Mæng, M., Ebbehøj, E., Knudsen, S. T., Hansen, K. W., Bøtker, H. E., & Poulsen, P. L. (2014). Assessment of central blood pressure in patients with type 2 diabetes: A comparison between sphygmocor and invasively measured values. *American Journal of Hypertension*, *27*(2), 169–176.

Laurent, S., Cockcroft, J., Van Bortel, L., Boutouyrie, P., Giannattasio, C., Hayoz, D., Pannier, B., Vlachopoulos, C., Wilkinson, I., & Struijker-Boudier, H. (2006). Expert consensus document on arterial stiffness: methodological issues and clinical applications. *European heart journal*, *27*(21), 2588–2605.

Laurent, S., Girerd, X., Mourad, J. J., Lacolley, P., Beck, L., Boutouyrie, P., Mignot, J. P., & Safar, M. (1994). Elastic modulus of the radial artery wall material is not increased in patients with essential hypertension. *Arteriosclerosis and Thrombosis*, *14*(7), 1223–1231.

Laurent, S., Katsahian, S., Fassot, C., Tropeano, A.-I., Gautier, I., Laloux, B., & Boutouyrie, P. (2003). Aortic Stiffness Is an Independent Predictor of Fatal Stroke in Essential Hypertension. *Stroke*, *34*(5), 1203–1206.

Laurent, S., Marais, L., & Boutouyrie, P. (2016). The Noninvasive Assessment of Vascular Aging. *Canadian Journal of Cardiology*, *32*(5), 669–679.

Learoyd, B. M., & Taylor, M. G. (1966). Alterations with Age in the Viscoelastic Properties of Human Arterial Walls. *Circulation research*, *XVIII*, 278–292.

Li, B., & Daggett, V. (2002). Molecular basis for the extensibility of elastin. *Journal of Muscle Research and Cell Motility*, *23*(5-6), 561–573.

Li, Y., Borlotti, A., Hickson, S. S., McEniery, C. M., Wilkinson, I. B., & Khir, A. W. (????). Using magnetic resonance imaging measurements for the determination of local wave speed and arrival time of reflected waves in human ascending aorta. *2010 Annual International Conference of the IEEE Engineering in Medicine and Biology*, *2010*, 5153–5156.

Li, Y., Giudici, A., Wilkinson, I. B., & Khir, A. W. (2021). Towards the non-invasive determination of arterial wall distensible properties: new approach using old formulae. *Journal of Biomechanics*, (p. 110102).

Li, Y., & Khir, A. W. (2011). Experimental validation of non-invasive and fluid density independent methods for the determination of local wave speed and arrival time of reflected wave. *Journal of Biomechanics*, *44*(7), 1393–1399.

Lillie, M. A., Armstrong, T. E., Gérard, S. G., Shadwick, R. E., & Gosline, J. M. (2012). Contribution of elastin and collagen to the inflation response of the pig thoracic aorta: assessing elastin's role in mechanical homeostasis. *Journal of biomechanics*, *45*(12), 2133–2141.

Lillie, M. A., Shadwick, R. E., & Gosline, J. M. (2010). Mechanical anisotropy of inflated elastic tissue from the pig aorta. *Journal of biomechanics*, *43*, 2070–2078.

Ma, Y., Choi, J., Hourlier-Fargette, A., Xue, Y., Chung, H. U., Lee, J. Y., Wang, X., Xie, Z., Kang, D., Wang, H., Han, S., Kang, S.-K., Kang, Y., Yu, X., Slepian, M. J., Raj, M. S., Model, J. B., Feng, X., Ghaffari, R., Rogers, J. A., & Huang, Y. (2018). Relation between blood pressure and pulse wave velocity for human arteries. *Proceedings of the National Academy of Sciences of the United States of America*, *115*(44), 11144–11149.

Mahomed, F. A. (1872). The physiology and clinical use of the sphygmograph. *Med. Time Gaz.*, *1*, 62.

Mancia, G., Fagard, R., Narkiewicz, K., Redon, J., Zanchetti, A., Böhm, M., Christiaens, T., Cifkova, R., De Backer, G., Dominiczak, A., Galderisi, M., Grobbee, D. E., Jaarsma, T., Kirchhof, P., Kjeldsen, S. E., Laurent, S., Manolis, A. J., Nilsson, P. M., Ruilope, L. M., Schmieder, R. E., Sirnes, P. A., Sleight, P., Viigimaa, M., Waeber, B., & Zannad, F. (2013). 2013 ESH/ESC guidelines for the management of arterial hypertension.

Marey, E. J. (1863). *Physiologie médicale de la circulation du sang: basée sur l'étude graphique des mouvements du coeur et du pouls artériel avec application aux maladies de l'appareil circulatoire*.

Mariscal-Harana, J., Charlton, P. H., Vennin, S., Aramburu, J., Florkow, M. C., van Engelen, A., Schneider, T., de Bliek, H., Ruijsink, B., Valverde, I., Beerbaum, P., Grotenhuis, H., Charakida, M., Chowienczyk, P., Sherwin, S. J., & Alastruey, J. (2021). Estimating central blood pressure from aortic flow: development and assessment of algorithms. *American journal of physiology. Heart and circulatory physiology*, *320*(2), H494–H510.

Marque, V., Kieffer, P., Atkinson, J., & Lartaud-Idjouadiene, I. (1999). Elastic Properties and Composition of the Aortic Wall in Old Spontaneously Hypertensive Rats. *Hypertension*, *34*(3), 415–422.

Matsumoto, T., Tsuchida, M., & Sato, M. (1996). Change in intramural strain distribution in rat aorta due to smooth muscle contraction and relaxation. *American Journal of Physiology - Heart and Circulatory Physiology*, *271*(4 Pt 2), 1711–1716.

Mattace-Raso, F. U., Hofman, A., Verwoert, G. C., Wittemana, J. C., Wilkinson, I., Cockcroft, J., McEniery, C., Yasmina, Laurent, S., Boutouyrie, P., Bozec, E., Hansen, T. W., Torp-Pedersen, C., Ibsen, H., Jeppesen, J., Vermeersch, S. J., Rietzschel, E., de Buyzere, M., Gillebert, T. C., van Bortel, L., Segers, P., Vlachopoulos, C., Aznaouridis, C., Stefanadis, C., Benetos, A., Labat, C., Lacolley, P., Stehouwer, C. D., Nijpels, G., Dekker, J. M., Ferreira, I., Twisk, J. W., Czernichow, S., Galan, P., Hercberg, S., Pannier, B., Guérin, A., London, G., Kennedy Cruickshank, J., Anderson, S. G., Paini, A., Rosei, E. A., Muiesan, M. L., Salvetti, M., Filipovsky, J., Seidlerova, J., & Dolejsova, M. (2010). Determinants of pulse wave velocity in healthy people and in the presence of cardiovascular risk factors: 'Establishing normal and reference values'. *European Heart Journal*, *31*(19), 2338–2350.

McEniery, C. M., Cockcroft, J. R., Roman, M. J., Franklin, S. S., & Wilkinson, I. B. (2014). Central blood pressure: Current evidence and clinical importance. *European Heart Journal*, *35*(26), 1719–1725.

Meinders, J. M., & Hoeks, A. P. (2004). Simultaneous assessment of diameter and pressure waveforms in the carotid artery. *Ultrasound in Medicine and Biology*, *30*(2), 147–154.

Millasseau, S. C., Patel, S. J., Redwood, S. R., Ritter, J. M., & Chowienczyk, P. J. (2003). Pressure wave reflection assessed from the peripheral pulse: Is a transfer function necessary? *Hypertension*, *41*(5), 1016–1020.

Mitchell, G. F., Parise, H., Benjamin, E. J., Larson, M. G., Keyes, M. J., Vita, J. A., Vasan, R. S., & Levy, D. (2004). Changes in Arterial Stiffness and Wave Reflection With Advancing Age in Healthy Men and Women: The Framingham Heart Study. *Hypertension*, *43*(6), 1239–1245.

Mitchell, G. F., Wang, N., Palmisano, J. N., Larson, M. G., Hamburg, N. M., Vita, J. A., Levy, D., Benjamin, E. J., & Vasan, R. S. (2010). Hemodynamic correlates of blood pressure across the adult age spectrum: Noninvasive evaluation in the framingham heart study. *Circulation*, *122*(14), 1379–1386.

Moens, A. I. (1878). *Die Pulskurve*. Leiden, Netherlands.

Muiesan, M., & Paini, A. (2009). Local carotid artery pulse wave velocity: foot to foot or dicrotic notch? *Journal of Hypertension*, *27*(10), 1962–1963.

Najjar, S. S., Scuteri, A., Shetty, V., Wright, J. G., Muller, D. C., Fleg, J. L., Spurgeon, H. P., Ferrucci, L., & Lakatta, E. G. (2008). Pulse Wave Velocity Is an Independent Predictor of the Longitudinal Increase in Systolic Blood Pressure and of Incident Hypertension in the Baltimore Longitudinal Study of Aging. *Journal of the American College of Cardiology*, *51*(14), 1377–1383.

Negoita, M., Hughes, A. D., Parker, K. H., & Khir, A. W. (2018). A method for determining local pulse wave velocity in human ascending aorta from sequential ultrasound measurements of diameter and velocity. *Physiological measurement*, *39*(11), 114009.

Nichols, W. W., O'Rourke, M. F., & McDonald, D. A. (2005). *McDonald's blood flow in arteries: theoretical, experimental and clinical principles*. London; New York: Hodder Arnold, 5th ed.

O'Connell, M. K., Murthy, S., Phan, S., Xu, C., Buchanan, J., Spilker, R., Dalman, R. L., Zarins, C. K., Denk, W., & Taylor, C. A. (2008). The three-dimensional micro- and nanostructure of the aortic medial lamellar unit measured using 3D confocal and electron microscopy imaging. *Matrix Biology*, *27*(3), 171–181.

Palombo, C., Kozakova, M., Guraschi, N., Bini, G., Cesana, F., Castoldi, G., Stella, A., Morizzo, C., & Giannattasio, C. (2012). Radiofrequency-based carotid wall tracking: A comparison between two different systems. *Journal of Hypertension*, *30*(8), 1614–1619.

Park, C. M., Hughes, A. D., Henein, M. Y., & Khir, A. W. (2020). Mechanisms of Aortic Flow Deceleration and the Effect of Wave Reflection on Left Ventricular Function. *Frontiers in Physiology*, *11*, 578701.

Parker, K. (2009). An introduction to wave intensity analysis. *Medical & Biological Engineering & Computing*, *47*(2), 175–188.

Parker, K. H., Jones, C. J., Dawson, J. R., & Gibson, D. G. (1988). What stops the flow of blood from the heart? *Heart and vessels*, *4*(4), 241–245.

Patel, D. J., De Freitas, F. M., Greenfield, J. C., & Fry, D. L. (1963). Relationship of radius to pressure along the aorta in living dogs. *Journal of Applied Physiology*, *18*(6), 1111–1117.

Pauca, A. L., O'Rourke, M. F., & Kon, N. D. (2001). Prospective Evaluation of a Method for Estimating Ascending Aortic Pressure From the Radial Artery Pressure Waveform. *Hypertension*, *38*(4), 932–937.

Peña, J. A., Corral, V., Martínez, M. A., & Peña, E. (2017). Over length quantification of the multiracial mechanical properties of the ascending, descending and abdominal aorta using Digital Image Correlation. *Journal of the mechanical behavior of biomedical materials*, *77*, 434–445.

Peña, J. A., Martinez, M. A., & Peña, E. (2015). Layer-specific residual deformations and uniaxial and biaxial mechanical properties of thoracic porcine aorta. *Journal of the Mechanical Behaviour of Biomedical Materials*, *50*, 55–69.

Petersen, K. S., Clifton, P. M., Lister, N., & Keogh, J. B. (2016). Effect of weight loss induced by energy restriction on measures of arterial compliance: A systematic review and meta-analysis. *Atherosclerosis*, *247*, 7–20.

Picone, D. S., Schultz, M. G., Otahal, P., Aakhus, S., Al-Jumaily, A. M., Black, J. A., Bos, W. J., Chambers, J. B., Chen, C. H., Cheng, H. M., Cremer, A., Davies, J. E., Dwyer, N., Gould, B. A., Hughes, A. D., Lacy, P. S., Laugesen, E., Liang, F., Melamed, R., Muecke, S., Ohte, N., Okada, S., Omboni, S., Ott, C., Peng, X., Pereira, T., Pucci, G., Rajani, R., Roberts-Thomson, P., Rossen, N. B., Sueta, D., Sinha, M. D., Schmieder, R. E., Smulyan, H., Srikanth, V. K., Stewart, R., Stouffer, G. A., Takazawa, K., Wang, J., Westerhof, B. E., Weber, F., Weber, T., Williams, B., Yamada, H., Yamamoto, E., & Sharman, J. E. (2017). Accuracy of Cuff-Measured Blood Pressure: Systematic Reviews and Meta-Analyses. *Journal of the American College of Cardiology*, *70*(5), 572–586.

Polzer, S., Gasser, T. C., Novak, K., Man, V., Tichy, M., Skacel, P., & Bursa, J. (2015). Structure-based constitutive model can accurately predict planar biaxial properties of aortic wall tissue. *Acta biomaterialia*, *14*, 133–145.

Prim, D. A., Mohamed, M. A., Lane, B. A., Poblete, K., Wierzbicki, M. A., Lessner, S. M., Shazly, T., & Eberth, J. F. (2018). Comparative mechanics of diverse mammalian carotid arteries. *PLoS One*, *13*(8), e0202123.

Prockop, D. J., & Kivirikko, K. I. (1995). Collagens: molecular biology, diseases, and potentials for therapy. *Annual Revision of Biochemistry*, *64*, 403–434.

Pucci, G., Bart, S., Avolio, A., Tap, L., Vaudo, G., Anastasio, F., Van Den Meiracker, A., & Mattace-Raso, F. (2020). Age-specific acute changes in carotid-femoral pulse wave velocity with head-up tilt. *Marican Journal of Hypertension*, *33*(12), 1112–1118.

Rabben, S. I., Stergiopulos, N., Hellevik, L. R., Smiseth, O. A., Slørdahl, S., Urheim, S., & Angelsen, B. (2004). An ultrasound-based method for determining pulse wave velocity in superficial arteries. *Journal of Biomechanics*, *37*(10), 1615–1622.

Rachev, A., & Greenwald, S. E. (2003). Residual strains in conduit arteries. *Journal of Biomechanics*, *36*(5), 661–670.

Raspanti, M., Protasoni, M., Manelli, A., Guizzardi, S., Mantovani, V., & Sala, A. (2006). The extracellular matrix of the human aortic wall: Ultrastructural observations by FEG-SEM and by tapping-mode AFM. *Micron*, *37*(1), 81–86.

Reference Values for Arterial Measurements Collaboration (2014). Establishing reference values for central blood pressure and its amplification in a general healthy population and according to cardiovascular risk factors. *European Heart Journal*, *35*(44), 3122–3133.

Rego, B. V., & Sacks, M. S. (2017). A functionally graded material model for the transmural stress distribution of the aortic valve leaflet. *Journal of Biomechanics*, *54*, 88–95.

Remington, J. W. (1954). Hysteresis Loop Behavior of the Aorta and Other Extensible Tissues. *American Journal of Physiology-Legacy Content*, *180*(1), 83–95.

Rezakhaniha, R., Agianniotis, A., Schrauwen, J. T. C. J., Griffa, A., Sage, D., Bouten, C. V. C. C., Vosse FN Frans, v. d., Unser, M., & Stergiopulos, N. (2012). Experimental investigation of collagen waviness and orientation in the arterial adventitia using confocal laser scanning microscopy. *Biomechanics and Modeling in Mechanobiology*, *11*, 461–473.

Riemann, G. (1860). Ueber die Fortzflanzung ebener Luftwellen von endlicher Schwingungsweite. In *Gesammelte mathematische Werke und wissenschaftlcher. Nachlass*, (pp. 145–176). Liepzig, teubner bg ed.

Ritchie, H., & Roser, M. (2019). Causes of Death - Our World in Data.

Riva-Rocci, S. (1896). Un nuovo sfigmomanometro. *Gazz. Med. di Torino*, *50*, 981–1017.

Roman, M. J., Devereux, R. B., Kizer, J. R., Lee, E. T., Galloway, J. M., Ali, T., Umans, J. G., & Howard, B. V. (2007). Central pressure more strongly relates to vascular disease and outcome than does brachial pressure: The strong heart study. *Hypertension*, *50*(1), 197–203.

Roser, M., & Ritchie, H. (2019). Obesity - Our World in Data.

Safar, M. E., Czernichow, S., & Blacher, J. (2006). Obesity, Arterial Stiffness, and Cardiovascular Risk. *Journal of the American Society of Nephrology*, (pp. S109–S110).

Salvi, P., Magnani, E., Valbusa, F., Agnoletti, D., Alecu, C., Joly, L., & Benetos, A. (2008). Comparative study of methodologies for pulse wave velocity estimation. *Journal of Human Hypertension*, *22*, 669–677.

Sánchez Muñoz-Torrero, J. F., Calderón-García, J. F., De Nicolás-Jiménez, J. M., García-Ortiz, L., Rodilla-Salas, E., Gómez-Marcos, M. A., Suárez-Fernandez, C., Cordovilla-Guardia, S., & Rico-Martín, S. (2018). Automatic or manual arterial path for the ankle-brachial differences pulse wave velocity. *PLOS ONE*, *13*(11), e0206434.

Sassani, S. G., Tsangaris, S., & Sokolis, D. P. (2015). Layer- and region-specific material characterization of ascending thoracic aortic aneurysms by microstructure-based models. *Journal of Biomechanics*, *48*(14), 3757–3765.

Schrauwen, J. T. C., Vilanova, A., Rezakhaniha, R., Stergiopulos, N., van de Vosse, F. N., & Bovendeerd, P. H. M. (2012). A method for the quantification of the pressure dependent 3D collagen configuration in the arterial adventitia. *Journal of structural biology*, *41*(7), 1579–1591.

Schriefl, A. J., Schmidt, T., Balzani, D., Sommer, G., & Holzapfel, G. A. (2015). Selective enzymatic removal of elastin and collagen from human abdominal aortas: uniaxial mechanical response and constitutive modeling. *Acta biomaterialia*, *17*, 125–136.

Schriefl, A. J., Wolinski, H., Regitnig, P., Kohlwein, S. D., & Holzapfel, G. A. (2013). An automated approach for three-dimensional quantification of fibrillar structures in optically cleared soft biological tissues. *Journal of the Royal Society Interface*, *10*(80), 20120760.

Schriefl, A. J., Zeindlinger, G., Pierce, D. M., Regitnig, P., & Holzapfel, G. A. (2012). Determination of the layer-specific distributed collagen fibre orientations in human thoracic and abdominal aortas and common iliac arteries. *Journal of the Royal Society, Interface / the Royal Society*, *9*(71), 1275–1286.

Segers, P. (2017). A lesson in vigilance: Pressure dependency of a presumed pressure-independent index of arterial stiffness. *Journal of Hypertension*, *35*(1), 33–35.

Segers, P., Mahieu, D., Kips, J., Rietzschel, E., De Buyzere, M., De Bacquer, D., Bekaert, S., De Backer, G., Gillebert, T., Verdonck, P., & Van Bortel, L. (2009). Amplification of the pressure pulse in the upper limb in healthy, middle-aged men and women. *Hypertension*, *54*(2), 414–420.

Segers, P., Rietzschel, E., Heireman, S., Debuyzere, M., Gillebert, T., Verdonck, P., & Van Bortel, L. (2005). Carotid Tonometry Versus Synthesized Aorta Pressure Waves for the Estimation of Central Systolic Blood Pressure and Augmentation Index. *American Journal of Hypertension*, *18*(9), 1168–1173.

Shafigh, M., Fatouraee, N., & Seddighi, A. S. (2013). Determining the biomechanical properties of human intracranial blood vessels through biaxial tensile test and fitting them to a hyperelastic model. *Engineering Solid Mechanics*, *1*, 43–56.

Sharman, J. E., Stowasser, M., Fassett, R. G., Marwick, T. H., & Franklin, S. S. (2008). Central blood pressure measurement may improve risk stratification. *Journal of Human Hypertension*, *22*(12), 838–844.

Shimada, T., Sato, F., Zhang, L., Ina, K., & Kitamura, H. (1993). Three-dimensional visualization of the aorta and elastic cartilage after removal of extracellular ground substance with a modified NaOH maceration method. *Journal of electron microscopy*, *42*(5), 328–333.

Shimura, K., & Kubo, A. (2019). Characteristics of age-related changes in blood pressure, oxyhemoglobin saturation, and physique in Bolivians residing at different altitudes: presentation of basic data for health promotion. *Journal of Physical Therapy Science*, *31*(10), 807–812.

Shirai, K., Song, M., Suzuki, J., Kurosu, T., Oyama, T., Nagayama, D., Miyashita, Y., Yamamura, S., & Takahashi, M. (2011). Contradictory effects of β1- and α1- aderenergic receptor blockers on Cardio-Ankle Vascular Stiffness Index (CAVI): CAVI is independent of blood pressure. *Journal of Atherosclerosis and Thrombosis*, *18*(1), 49–55.

Shirai, K., Suzuki, K., Tsuda, S., Shimizu, K., Takata, M., Yamamoto, T., Maruyama, M., & Takahashi, K. (2019). Comparison of cardio-ankle vascular index (CAVI) and CAVI0 in large healthy and hypertensive populations. *Journal of Atherosclerosis and Thrombosis*, *26*(7), 603–615.

Shirai, K., Takata, M., Takahara, A., & Shimizu, K. (2018). Medical science is based on evidence (answer to Spronck et al.'s refutation: Physics cannot be disputed). *Journal of Hypertension*, *36*(4), 958–960.

Shirai, K., Utino, J., Otsuka, K., & Takata, M. (2006). A novel blood pressure-independent arterial wall stiffness parameter; cardio-ankle vascular index (CAVI). *Journal of Atherosclerosis and Thrombosis*, *13*(2), 101–107.

Sokolis, D. P. (2007). Passive mechanical properties and structure of the aorta: Segmental analysis. *Acta Physiologica*, *190*(4), 277–289.

Sokolis, D. P. (2019). Regional distribution of layer-specific circumferential residual deformations and opening angles in the porcine aorta. *Journal of Biomechanics*, *96*, 109335.

Sokolis, D. P., Kefaloyannis, E. M., Kouloukoussa, M., Marinos, E., Boudoulas, H., & Karayannacos, P. E. (2006). A structural basis for the aortic stress-strain relation in uniaxial tension. *Journal of Biomechanics*, *39*(9), 1651–1662.

Sokolis, D. P., Savva, G. D., Papadodima, S. A., & Kourkoulis, S. K. (2017). Regional distribution of circumferential residual strains in the human aorta according to age and gender. *Journal of the Mechanical Behavior of Biomedical Materials*, *67*, 87–100.

Sommer, G., Regitnig, P., Költringer, L., & Holzapfel, G. A. (2010). Biaxial mechanical properties of intact and layer-dissected human carotid arteries at physiological and supraphysiological loadings. *American Journal of Physiology - Heart and Circulatory Physiology*, *298*(3), 898–912.

Spina, M., Garbisa, S., Hinnie, J., Hunter, J. C., & Serafini-Fracassini, A. (1983). Age-related changes in composition and mechanical properties of the tunica media of the upper thoracic human aorta. *Arteriosclerosis, Thrombosis, and Vascular Biology*, *3*(1), 64–76.

Spronck, B. (2018). Stiff vessels approached in a flexible way: Advancing quantification and interpretation of arterial stiffness. *Artery Research*, *21*(December), 63–68.

Spronck, B., Avolio, A. P., Tan, I., Butlin, M., Reesink, K. D., & Delhaas, T. (2017a). Arterial stiffness index beta and cardio-ankle vascular index inherently depend on blood pressure but can be readily corrected. *Journal of Hypertension*, *35*(1), 98–104.

Spronck, B., Caulk, A., Ramachandra, A., Murtada, S.-I., Rojas, A., He, C.-S., Bersi, M., Tellides, G., & Humphrey, J. (2019). Genetic Background Dominates Fibrotic Aortic Remodeling During Angiotensin-Induced Hypertension in Mice. *bioRxiv*, (p. 727800).

Spronck, B., Delhaas, T., Butlin, M., Reesink, K. D., & Avolio, A. P. (2017b). Options for Dealing with Pressure Dependence of Pulse Wave Velocity as a Measure of Arterial Stiffness: An Update of Cardio-Ankle Vascular Index (CAVI) and CAVI0. *Pulse*, *5*(1-4), 106–114.

Spronck, B., Delhaas, T., De Lepper, A. G., Giroux, J., Goldwasser, F., Boutouyrie, P., Alivon, M., & Reesink, K. D. (2017c). Patient-specific blood pressure correction technique for arterial stiffness: Evaluation in a cohort on anti-angiogenic medication. *Hypertension Research*, *40*(8), 752–757.

Spronck, B., Ferruzzi, J., Bellini, C., Caulk, A. W., Murtada, S.-I., & Humphrey, J. D. (2020). Aortic remodeling is modest and sex-independent in mice when hypertension is superimposed on aging. *Journal of Hypertension*, *38*(7), 1312–1321.

Spronck, B., Heusinkveld, M., Vanmolkot, F., Roodt, J. O., Hermeling, E., Delhaas, T., Kroon, A., & Reesink, K. (2015). Pressure-dependence of arterial stiffness: potential clinical implications. *Journal of Hypertension*, *33*(2), 330–338.

Stella, J. A., & Sacks, M. S. (2007). On the biaxial mechanical properties of the layers of the aortic valve leaflet. *Journal of Biomechanical Engineering*, *129*(5), 757–766.

Stergiopulos, N., Vulliémoz, S., Rachev, A., Meister, J. J., & Greenwald, S. E. (2001). Assessing the homogeneity of the elastic properties and composition of the pig aortic media. *Journal of Vascular Research*, *38*(3), 237–246.

Streese, L., Königstein, K., Goricki, L., Infanger, D., Wölnerhanssen, B., Peters, T., Schmidt-Trucksäss, A., & Hanssen, H. (2019). Short- and Long-Term Effects of Bariatric Surgery on Vascular Phenotype. *Obesity surgery*, *29*(4), 1301–1308.

Su, J., Manisty, C., Parker, K. H., Mellemkjaer, S., Howard, L., Simonsen, U., & Hughes, A. (2016). Wave intensity analysis provides novel insights into pulmonary hypertension. *Artery Research*, *16*, 51–52.

Sugawara, M., Niki, K., Ohte, N., Okada, T., & Harada, A. (2009). Clinical usefulness of wave intensity analysis. *Medical and Biological Engineering and Computing*, *47*(2), 197–206.

Sugita, S., & Matsumoto, T. (2013). Quantitative measurements of the distribution and alignment of collagen fibers in unfixed aortic tissue. *Journal of biomechanics*, *46*(7), 1403–1407.

Sugita, S., & Matsumoto, T. (2016). Multiphoton microscopy observations of 3D elastin and collagen fiber microstructure changes during pressurization in aortic media. *Biomechanics and Modeling in Mechanobiology*, *16*(3), 763–773.

Sutton-Tyrrell, K., Newman, A., Simonsick, E. M., Havlik, R., Pahor, M., Lakatta, E., Spurgeon, H., & Vaitkevicius, P. (2001). Aortic Stiffness Is Associated With Visceral Adiposity in Older Adults Enrolled in the Study of Health, Aging, and Body Composition. *Hypertension*, *38*(3), 429–433.

Tan, I., Spronck, B., Kiat, H., Barin, E., Reesink, K. D., Delhaas, T., Avolio, A. P., & Butlin, M. (2016). Heart Rate Dependency of Large Artery Stiffness. *Hypertension*, *68*(1), 236–242.

Tesauro, M., Mauriello, A., Rovella, V., Annicchiarico-Petruzzelli, M., Cardillo, C., Melino, G., & Di Daniele, N. (2017). Arterial ageing: from endothelial dysfunction to vascular calcification. *Journal of Internal Medicine*, *281*(5), 471–482.

The GBD 2015 Obesity Collaborators (2017). Health effects of overweight and obesity in 195 countries over 25 years. *New England Journal of Medicine*, *377*(1), 13–27.

The Reference Values for Arterial Stiffness' Collaboration (2010). Determinants of pulse wave velocity in healthy people and in the presence of cardiovascular risk factors: 'establishing normal and reference values'. *European heart journal*, *31*(19), 2338–2350.

Timmins, L. H., Wu, Q., Yeh, A. T., Moore, J. E. J., & Greenwald, S. E. (2010). Structural inhomogeneity and fiber orientation in the inner arterial media. *American Journal of Physiology - Heart and Circulatory Physiology*, *298*(5), 1537–1545.

Tomiyama, H., Matsumoto, C., Shiina, K., & Yamashina, A. (2016). Brachial-Ankle PWV: Current Status and Future Directions as a Useful Marker in the Management of Cardiovascular Disease and/or Cardiovascular Risk Factors. *Journal of Atherosclerosis and Thrombosis*, *23*(2), 128–146.

Tsamis, A., Krawiec, J. T., & Vorp, D. A. (2013). Elastin and collagen fibre microstructure of the human aorta in ageing and disease: a review. *Journal of the Royal Society*, *10*(83), 1–22.

Tsamis, A., & Stergiopulos, N. (2007). Arterial remodeling in response to hypertension using a constituent based model. *American Physiological Society*, *293*(5), H3130–H3139.

Ueda, I., Tagawa, T., Watanabe, S., Yamakawa, K., Yasu, T., & Ueda, S. (2008). Comparability and reproducibility of the carotid-femoral pulse wave velocity measurements using a multi-element carotid tonometry sensor. *Journal of Human Hypertension*, *22*(10), 699–703.

Uejima, T., Dunstan, F. D., Arbustini, E., Łoboz-Grudzień, K., Hughes, A. D., Carerj, S., Favalli, V., Antonini-Canterin, F., Vriz, O., Vinereanu, D., Zamorano, J. L., Popescu, B. A., Evangelista, A., Lancellotti, P., Lefthériotis, G., Kozakova, M., Palombo, C., & Fraser, A. G. (2019). Age-specific reference values for carotid arterial stiffness estimated by ultrasonic wall tracking. *Journal of human hypertension*, *34*(3), 214–222.

Uejima, T., Dunstan, F. D., Arbustini, E., Łoboz-Grudzień, K., Hughes, A. D., Carerj, S., Favalli, V., Antonini-Canterin, F., Vriz, O., Vinereanu, D., Zamorano, J. L., Popescu, B. A., Evangelista, A., Lancellotti, P., Lefthériotis, G., Kozakova, M., Palombo, C., & Fraser, A. G. (2020). Age-specific reference values for carotid arterial stiffness estimated by ultrasonic wall tracking. *Journal of Human Hypertension*, *34*(3), 214–222.

Urry, D. W., Luan, C. H., & Peng, S. Q. (1995). Molecular biophysics of elastin structure, function and pathology. *Ciba Foundation symposium*, *192*, 4–22.

Vaishnav, R. N., & Vossoughi, J. (1983). Estimation of the residual strains in aortic segments. *Proceedings of the Second Southern Biomedical Engineering Conference*, (pp. 330–333).

Valbusa, F., Angheben, A., Mantovani, A., Zerbato, V., Chiampan, A., Bonapace, S., Rodari, P., Agnoletti, D., Arcaro, G., Fava, C., Bisoffi, Z., & Targher, G. (2019). Increased aortic stiffness in adults with chronic indeterminate Chagas disease. *PLoS ONE*, *14*(8), e0220689.

Valdez-Jasso, D., Haider, M. A., Banks, H. T., Santana, D. B., German, Y. Z., Armentano, R. L., & Olufsen, M. S. (2009). Analysis of Viscoelastic Wall Properties in Ovine Arteries. *IEEE Transactions on Biomedical Engineering*, *56*(2), 210–219.

Van Bortel, L. M., Laurent, S., Boutouyrie, P., Chowienczyk, P., Cruickshank, J. K., De Backer, T., Filipovsky, J., Huybrechts, S., Mattace-Raso, F. U., Protogerou, A. D., Schillaci, G., Segers, P., Vermeersch, S., & Weber, T. (2012). Expert consensus document on the measurement of aortic stiffness in daily practice using carotid-femoral pulse wave velocity. *Journal of Hypertension*, *30*(3), 445–448.

Van Loon, P., Klip, W., & Bradley, E. L. (1977). Length-force and volume-pressure relationships of arteries. *Biorheology*, *14*(4), 181–201.

Vande Geest, J. P., Sacks, M. S., & Vorp, D. A. (2004). Age dependency of the biaxial biomechanical behavior of human abdominal aorta. *Journal of biomechanical engineering*, *126*(6), 815–822.

Vennin, S., Mayer, A., Li, Y., Fok, H., Clapp, B., Alastruey, J., & Chowienczyk, P. (2015). Noninvasive calculation of the aortic blood pressure waveform from the flow velocity waveform: a proof of concept. *American journal of physiology. Heart and circulatory physiology*, *309*(5), H969–H976.

Vogel, T., Leprêtre, P. M., Brechat, P. H., Lonsdorfer-Wolf, E., Kaltenbach, G., Lonsdorfer, J., & Benetos, A. (2013). Effect of a short-term intermittent exercise-training programme on the pulse wave velocity and arterial pressure: A prospective study among 71 healthy older subjects.

Wan, W., Dixon, J. B., & Gleason, R. L. (2012). Constitutive modeling of mouse carotid arteries using experimentally measured microstructural parameters. *Biophysical Journal*, *102*(12), 2916–2925.

Wang, G., Wang, L., Yang, S., Zhang, P., Chen, X., Yao, Q., Gong, X., Qi, Y., Jiang, Z., & Han, H. (2017). Arterial wall remodelling under sustained axial twisting in rats. *Journal of Biomechanics*, *60*, 124–133.

Wang, K. L., Cheng, H. M., Sung, S. H., Chuang, S. Y., Li, C. H., Spurgeon, H. A., Ting, C. T., Najjar, S. S., Lakatta, E. G., Yin, F. C., Chou, P., & Chen, C. H. (2010). Wave reflection and arterial stiffness in the prediction of 15-year all-cause and cardiovascular mortalities: A community-based study. *Hypertension*, *55*(3), 799–805.

Wang, R., Vetrano, D. L., Liang, Y., & Qiu, C. (2019). The age-related blood pressure trajectories from young-old adults to centenarians: A cohort study. *International Journal of Cardiology*, *296*, 141–148.

Wang, Y., Zeinali-Davarani, S., & Zhang, Y. (2016). Arterial mechanics considering the structural and mechanical contributions of ECM constituents. *Journal of biomechanics*, *49*(12), 2358–2365.

Wasano, K., & Yamamoto, T. (1983). Tridimensional architecture of elastic tissue in the rat aorta and femoral artery–a scanning electron microscope study. *Journal of electron microscopy*, *32*(1), 33–44.

Weisbecker, H., Pierce, D. M., Regitnig, P., & Holzapfel, G. A. (2012). Layer-specific damage experiments and modeling of human thoracic and abdominal aortas with non-atherosclerotic intimal thickening. *Journal of the Mechanical Behavior of Biomedical Materials*, *12*, 93–106.

Weisbecker, H., Viertler, C., Pierce, D. M., & Holzapfel, G. A. (2013). The role of elastin and collagen in the softening behavior of the human thoracic aortic media. *Journal of biomechanics*, *46*(11), 1859–1865.

Wells, S. M., Lowell, B. L., & Lee, S. A. (1998). In vivo and in vitro mechanical properties of the sheep thoracic aorta in the perinatal period and adulthood. *American Journal of Physiology*, *274*(5 PART 2).

Willemet, M., Vennin, S., & Alastruey, J. (2016). Computational assessment of hemodynamics-based diagnostic tools using a database of virtual subjects: Application to three case studies. *Journal of Biomechanics*, *49*(16), 3908–3914.

Williams, B., Mancia, G., Spiering, W., Agabiti Rosei, E., Azizi, M., Burnier, M., Clement, D. L., Coca, A., de Simone, G., Dominiczak, A., Kahan, T., Mahfoud, F., Redon, J., Ruilope, L., Zanchetti, A., Kerins, M., Kjeldsen, S. E., Kreutz, R., Laurent, S., Lip, G. Y. H., McManus, R., Narkiewicz, K., Ruschitzka, F., Schmieder, R. E., Shlyakhto, E., Tsioufis, C., Aboyans, V., & Desormais, I. (2018). 2018 ESC/ESH Guidelines for the management of arterial hypertension. *European heart journal*, *39*(33), 3021–3104.

Withrow, D., & Alter, D. A. (2011). The economic burden of obesity worldwide: A systematic review of the direct costs of obesity.

Wittek, A., Karatolios, K., Fritzen, C. P., Bereiter-Hahn, J., Schieffer, B., Moosdorf, R., Vogt, S., & Blase, C. (2016). Cyclic three-dimensional wall motion of the human ascending and abdominal aorta characterized by time-resolved three-dimensional ultrasound speckle tracking. *Biomechanics and Modeling in Mechanobiology*, *15*(5), 1375–1388.

Wolinsky, H., & Glagov, S. (1964). Structural basis for the static mechanical properties of the aortic media. *Circulation research*, *14*, 400–413.

Wolinsky, H., & Glagov, S. (1969). Comparison of abdominal and thoracic aortic medial structure in mammals. *Circulation Research*, *25*(6), 677–686.

World Health Organization (2017). Cardiovascular Diseases (CVDs).

Zatzman, M., Stacy, R. W., Randall, J., & Eberstein, A. (1954). Time Course of Stress Relaxation in Isolated Arterial Segments. *The American journal of physiology*, *177*(2), 299–302.

Zhang, M., Bai, Y., Ye, P., Luo, L., Xiao, W., Wu, H., & Liu, D. (2011). Type 2 diabetes is associated with increased pulse wave velocity measured at different sites of the arterial system but not augmentation index in a Chinese population. *Clinical Cardiology*, *34*(10), 622–627.

Zhang, Y., Agnoletti, D., Protogerou, A. D., Topouchian, J., Wang, J. G., Xu, Y., Blacher, J., & Safar, M. E. (2013). Characteristics of pulse wave velocity in elastic and muscular arteries: A mismatch beyond age. *Journal of Hypertension*, *31*(3), 554–559.

Zheng, X., & Ren, J. (2016). Effects of the three-dimensional residual stresses on the mechanical properties of arterial walls. *Journal of theoretical biology*, *393*, 118–126.

Zhou, B., Prim, D. A., Romito, E. J., McNamara, L. P., Spinale, F. G., Shazly, T., & Eberth, J. F. (2018). Contractile Smooth Muscle and Active Stress Generation in Porcine Common Carotids. *Journal of Biomechanical Engineering*, *140*(1), 14501–14506.

Zou, Y., & Zhang, Y. (2009). An experimental and theoretical study on the anisotropy of elastin network. *Annals of biomedical engineering*, *37*(8), 1572–1583.

Zulliger, M. A., & Stergiopulos, N. (2007). Structural strain energy function applied to the ageing of the human aorta. *Journal of Biomechanics*, *40*(14), 3061–3069.